Computation Based Understanding And Prediction Of Technologically Important Indigenous Materials

Thesis submitted for the degree of

Doctor of Philosophy (Science)

in

Physics (Theoretical)

by

Shiladitya Karmakar

Department of Physics
University of Calcutta

2023

To

my parents...

Acknowledgements

First and foremost, I express my sincere and humble gratitude to my supervisor Prof. Tanusri Saha-Dasgupta for her spontaneous support and constant guidance throughout every step of my PhD journey. The present computational work could not have been accomplished without her kind help and valuable suggestions. Her deep involvement in research work and passion for science has greatly motivated and inspired me during these years. I am forever grateful for her mentorship and for believing in my potential. I am sincerely thankful to my collaborators, Prof. Debashree Ghosh and Dr. Pradip Chakraborty for their suggestions and fruitful discussions.

I take this opportunity to thank my senior lab members Dr. Dhani Nafday, Dr. Dipayan Sen, Dr. Uttam Pal, Dr. Edwine Tendong, Dr. Ransell D'Souza, Dr. Anita Halder, and Dr. Shreya Das who took a genuine interest in my work and provided the most needed guidance without reservation whenever necessary. I also thank my fellow lab members Samir, Aishwaryo, Koushik, Manoj, Rajdeep, Arnab and Prosanta for their spontaneous help, company, and encouragement. I convey my earnest thanks to the senior members from the group of Prof. Indra Dasgupta and Prof. Debashree Ghosh at the Indian Association for the Cultivation of Sciences, Kolkata where I spent the initial stages of my PhD life.

I am grateful to S. N. Bose National Centre for Basic Sciences, Department of Science and Technology, India for the fellowship, financial support, providing the infrastructure and funding my trip to Jawaharlal Nehru Centre For Advanced Scientific Research, Bangalore, and Weizmann Institute of Science, Israel. I wish to thank all the members and staff of S. N. Bose Centre for their cooperation during the course of my research work. My sincere thanks goes to the Technical Research Centre and Computer Services cell for providing the computational facility to carry out my research work.

My sincere gratitude to all my teachers I come across in my life inside as well as outside classroom. Last, but not the least, I dont have enough words to convey my gratitude and thanks to my parents, who always stand beside me.

Abstract

The present thesis focuses on the modeling and simulation of two broad classes of materials that are technologically important and indigenous. The first class of materials is Spin Crossover (SCO) molecular materials exhibiting light-induced excited spin state trapping (LIESST) and SCO coordination polymers exhibiting thermally activated spin transition suitable for designing molecular device-based applications. The other class of material deals with layered two-dimensional (2D) materials like 2D transition metal carbide known as MXene and elemental 2D material of group-VI element Tellurium (Te) known as tellurene exhibiting thermoelectric properties promising for renewable energy harvesting technology. In the context of SCO material, our findings reveal that Time-dependent Density Functional Theory (TDDFT) with a suitable choice of exchange-correlation functional is a reasonable approach for estimating the low-temperature relaxation rates of LIESST process in real complexes, consisting of several tens to hundreds of atoms. Next, we apply our method to study the microscopic origin of 14-order of magnitude jump in the relaxation rate of Fe(II) SCO complexes coordinated by mono-dentate, bi-dentate, and multi-dentate ligands. The calculated rate constants are in excellent agreement with measured values. The large variation in rate constant is rationalized in terms of the change in metal-ligand covalency. Next, we study the spin-transition in three Fe(II) based coordination polymers where Fe(II) SCO centers are connected via tetrazole-based bridging ligands forming 1D and 2D coordination networks. We investigate how cooperativity among Fe(II) centers build upon increasing the length of the bridging ligands. To explore the thermoelectric materials, we investigate Titanium (Ti) and Molybdenum (Mo) based MXene compounds considering five ordered alloyed structures $Ti_{3-x}Mo_xC_2$ with x = 0.5, 1, 1.5, 2, 2.5 with -OH, -O, or -F passivation. Three narrow gap semiconducting compounds are identified, namely, $Ti_2MoC_2F_2$, $TiMo_2C_2F_2$, and $TiMo_2C_2(OH)_2$ for subsequent study of thermoelectric properties within the semi-classical Boltzmann transport formalism. Our study highlights the potential of $Ti_2MoC_2F_2$ as a thermoelectric material within a large temperature range of 300-800K upon p-type carrier doping and figure of merit (ZT) was found to reach a high value of 3.1 and an efficiency of $\sim$27% at 800 K. Our exercise should motivate the experimental study of yet-to-be synthesized MXene compound, Ti_2MoC_2. Next, we investigate the influence of biaxial strain on the β-phase of Tellurene (β-Te), which had been discussed already for its potential in thermoelectric applications. Realistic estimates of strain that may be imposed on β-Te are obtained through van der Waals heterostructuring with other known 2D materials. We find that through strain engineering, the thermoelectric performance of β-Te in p-type doping can be significantly improved and made comparable to that of the known binary or ternary layered compound at room temperature, and can outperform the known binary or ternary layered

compounds at high to moderate temperature. Our computational study on prediction of new materials with targeted and improved properties should form a useful guide for future experiments.

List of Publications

1. * Light-induced excited spin-state trapping in spin crossover model system.
   Shiladitya Karmakar, Debashree Ghosh, and Tanusri Saha-Dasgupta.
   International Journal of Quantum Chemistry 120.6 (2020), e26122.

2. * First-principles prediction of enhanced thermoelectric properties of double transition metal MXenes: $Ti_{3-x}Mo_xC_2T_2$; (x = 0.5, 1, 1.5, 2, 2.5, T = -OH/ -O/ -F).
   Shiladitya Karmakar and Tanusri Saha-Dasgupta.
   Physical Review Materials 4.12 (2020), p. 124007.

3. * High-performance thermoelectric properties of strained two-dimensional tellurium.
   Shiladitya Karmakar and Tanusri Saha-Dasgupta.
   Physical Review Materials 5.12 (2021), p. 124006.

4. * Trend in light-induced excited-state spin trapping in Fe (II)-based spin crossover systems.
   Shiladitya Karmakar, Pradip Chakraborty, and Tanusri Saha-Dasgupta.
   Physical Chemistry Chemical Physics 24.17 (2022), pp. 10201-10209.

5. * Trend in cooperativity in spin-crossover of metal-organic polymers.
   Shiladitya Karmakar, Pradip Chakraborty, and Tanusri Saha-Dasgupta.
   (Under Preparation)

6. Giant Rashba effect and non-linear anomalous Hall conductivity in a two-dimensional molybdenum-based Janus structure.
   Shiladitya Karmakar, Rajdeep Biswas, and Tanusri Saha-Dasgupta.
   Physical Review B 107.7 (2023), p. 075403.

7. Establishing Magnetic Coupling in Spin-crossover-2D Hybrid Nanostructures via Interfacial Charge-transfer Interaction.
   Shatabda Bhattacharya, Shubhadip Moulick, Chinmoy Das, Shiladitya Karmakar, Hirokazu Tada, Tanusri Saha-Dasgupta, Pradip Chakraborty, Atindra Nath Pal. (Under Review)

Thesis will be based on the references marked by *

Contents

List of Figures

List of Tables

Chapter 1

Introduction

"When nature finishes to produce its own species, man begins using natural things and in harmony with this very nature to create an infinity of species." -Leonardo da Vinci

Materials have been instrumental in shaping human history since the dawn of civilization.[1–4] The importance of materials in human civilization is so much that it is often divided into ages according to the materials that dominated the society, starting from the stone age to the bronze age, iron age and to modern time of silicon age. During the stone age, humans learned to use natural materials, stones as grinding or cutting tools for agriculture. Materials like fiber and resin helped humans to invent knives and axes by attaching blades to sticks. This brought the Neolithic (or first agricultural) revolution in society transforming the hunting and gathering lifestyle of humans. The discovery of smelting techniques to extract metals from mineral ores was realized accidentally in stone age pottery kilns, ushered in bronze, and the subsequent iron age. The adoption of iron caused radical changes in agriculture as well as weaponry leading to the establishment of countries, empires and the beginning of written literature. Around 4000 years later such developments in metallurgy culminated in the industrial revolution. But the profound change in the evolution of human civilization was noticed at the end of the 19th century with the advent of two events, one is the birth of semiconducting materials [5] and the other is the discovery of the electron by J. J. Thomson in 1897 [6]. The latter led to the development of the vacuum tube and spurred the discovery of solid-state transistors at Bell Labs by William Shockley, John Bardeen, and Walter Brattain in 1947 [7]. In the present silicon age, not only computers and mobile phones, but also commerce, transportation, and communication i.e., every aspect of human life are now underpinned by microelectronic devices. Moore's law [8, 9] ensures that the capabilities of such devices are expected to grow exponentially with decreasing cost and size anticipating more automation and convenience in our daily life. Clearly, major advances in human civilization have been guided by a fundamental development in science

and technology driven by materials.

But the silicon revolution governed by Moores law will be forced to seize soon as it poses profound problems for society.[10] As living standards improve, the Internet of Things (IoT) will be widespread causing the market of microelectronics devices to expand worldwide rapidly. It is predicted by many studies that more than half of the worlds energy will be consumed by information technologies within a couple of decades. For example, exascale supercomputer El Capitan at Lawrence Livermore National Laboratory[11] is expected to need 30 megawatts of power to be operational at full capacity in 2023, which is about the same consumption as 12,000 households. Secondly, the cost of the semiconductor chip fabrication plant doubles every four years as predicted by Rocks law, and had already reached about 14 billion US dollars in 2015. Moreover, devices made of environment-friendly materials are expected to avoid negative impacts on the environment as well as human health. So, the question one can ask is that what kinds of materials lie ahead beyond the present silicon age? It was the far-sight of the great genius of Renaissance Leonardo da Vinci, which suggests that the future age is going to be the age of designed materials.[12] Apparently, future materials must be designed in such a way that it will address the issue of high energy demand in cost-effective and eco-friendly way.

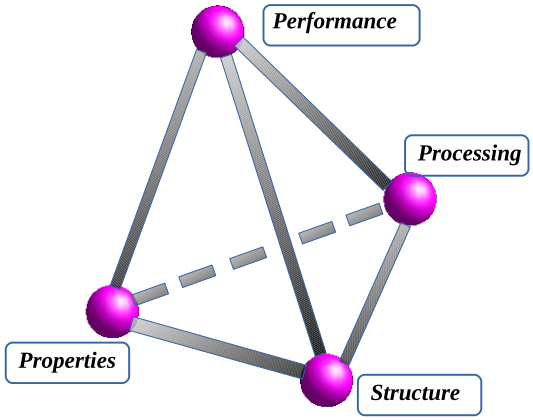

Figure 1.1: Schematic of material science tetrahedron encompassing four interdependent aspects

The "Designed Materials Age" requires new knowledge which encompasses four interdependent, distinct aspects of materials science: processing, structure, properties, and performance forming four corners of materials science tetrahedron (Figure-1.1)[13]. To design a material with a certain performance, one needs to decide on a set of properties. Based on that one predict a structure manifesting such properties. The structures are finally manufactured by processing. In recent years, major advances in materials science have been achieved through the active usage of computer simulations to understand the close interplay between struc-

ture and properties and hence predict newly designed materials. Simulations with ab-initio techniques that utilize various structural and chemical aspects of the material systems can become the motivation for related experimental research which will verify the structure-property relationship. This allows theory and experiment to work hand in hand leading to the processing of high-performance materials. In the present thesis, using ab-initio techniques we will computationally investigate two different classes of materials that are technologically important and indigenous. The first class of materials is molecular materials suitable for designing molecular device-based applications and the second class deals with thermoelectric materials which have drawn significant attention in modern-day technology. We will primarily use density functional theory to explore the electronic properties of both classes of materials in the ground state and time-dependent density functional theory to determine the excited states of molecular systems. For thermoelectric materials, we will further solve Boltzmann transport equations to calculate electron and lattice transport properties inputting the band structure from density functional theory calculation. Before proceeding towards details of studied materials belonging to these two broad classes, we would like to discuss the technological importance of these material classes in the following section.

1.1 Technological Applications of Materials studied

1.1.1 Spin Crossover materials

Molecule-based devices require the design of molecular analogs of transistors that are capable of working at low addressing power and short addressing time. Molecular materials showing spin crossover (SCO) are the potential candidates to fulfill those demands and find applications in the following technology sector.

SCO complex may act as a molecular switch, in which two stable spin states distinguish between the on and off positions. Interconversion between the states requires abrupt spin crossover in response to the input, such as temperature, pressure, or light irradiation. Clearly, the molecule can act as a NOT operator in logic operations, where one input produces one output (Figure-1.2). Hence SCO complex might be a key to todays continuous urge for the miniaturization of current technology and thus can be a route to continue Moores law.

SCO materials exhibiting abrupt spin transition around room temperature with wide hysteresis loop are ideal for memory storage devices since it has the ability to be observed in two different states (bistability) in a certain range of temperature. Multi-functional materials showing electrical conductivity as well as SCO are advantageous since the spin state can be read by measuring the conductivity. Tristable (three stable states at a given temperature) and multiply bistable

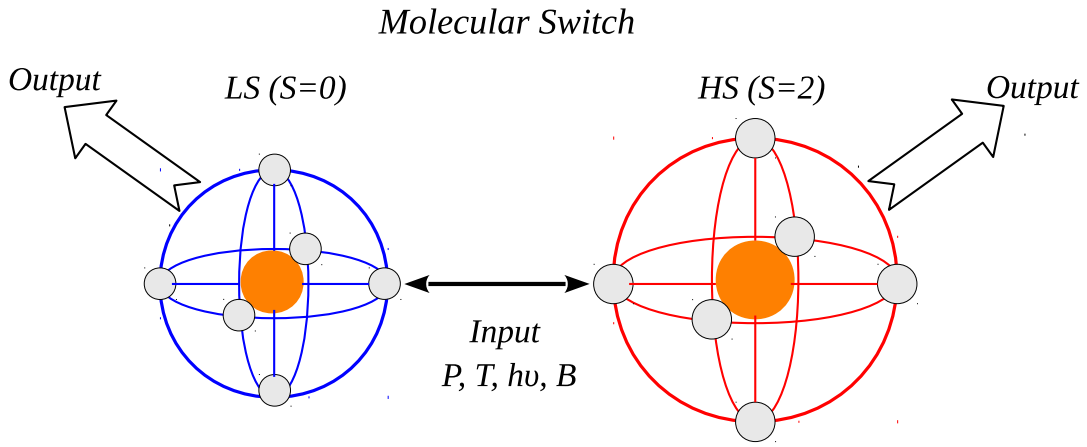

Figure 1.2: Schematic of molecular switch adapted from ref.[14]

(bistability at some temperatures) materials like $[Fe(dppL4)_2][Ni(mnt)_2].MeNO_2$ (where dppL4 is 2,6-Bis(pyrazolyl)pyridine and mnt is maleonitriledithiolate) are promising for multi switches and ternary data storage devices [15].

SCO driven by pressure, temperature, and light irradiation have applications as pressure, temperature, and sensors respectively [16]. Materials with well-defined phase diagrams are advantageous since they can be used as combined temperature and pressure sensors which detect temperature changes at a constant pressure, as well as pressure changes at a constant temperature [17].

1.1.2 Thermoelectric materials

The phenomenon of thermoelectricity was discovered way back in 1823 when German physicist Thomas Seebeck observed the deflection of a compass needle close to two metal junctions that were kept at different temperatures.[18] Direct conversion from heat to electricity at the junction of two conductors was later named as Seebeck effect. Together with the Peltier effect [19], discovered in 1834, and the Thomson effect [20], in 1851, the Seebeck effect constitutes the physical processes that manifest in a TE material. TE devices consist of several thermo-couples made of n-type (carrier e^-) and p-type (carrier holes) materials connected electrically in series and thermally in parallel as shown in Figure-. When a temperature gradient is applied to a material, the mobile charge carriers tend to diffuse from the hot to the cold end. The accumulated charge carriers result in a net charge (-ve for e^-s, +ve for holes) at the cold end, producing an electrostatic potential difference (ΔV). Subsequently, an equilibrium is achieved between the chemical potential for diffusion and the electrostatic repulsion due to the accumulated charge. ΔV is directly proportional to the temperature difference, ΔT, $\Delta V = S\Delta T$ where S is the Seebeck coefficient and can power an

electric load through the external circuit. Such thermoelectric generators (TEG) find applications in a multitude of technology fields.

Apart from the earth's limited source of fossil fuels and human-induced global climate change, one of the striking reasons for the emerging energy crisis in the twenty-first century is that the large amounts of the generated heat energy cannot be effectively used getting wasted in the environment, by the means of emissions of factory boilers, car exhausts, friction, etc. The average useful energy from fossil fuels from different sectors is shown schematically in figure-1.3. A key solution to this growing energy crisis will be energy-harvesting technologies which can effectively recycle and partially or fully harvest this wasted thermal energy (>60%). TEG allows the direct conversion between thermal and electrical energy and hence can be deployed to generate electricity by recovering the waste heat utilizing the Seebeck effect. This unique capability makes them a promising candidate for renewable as well as sustainable energy harvesting technology.

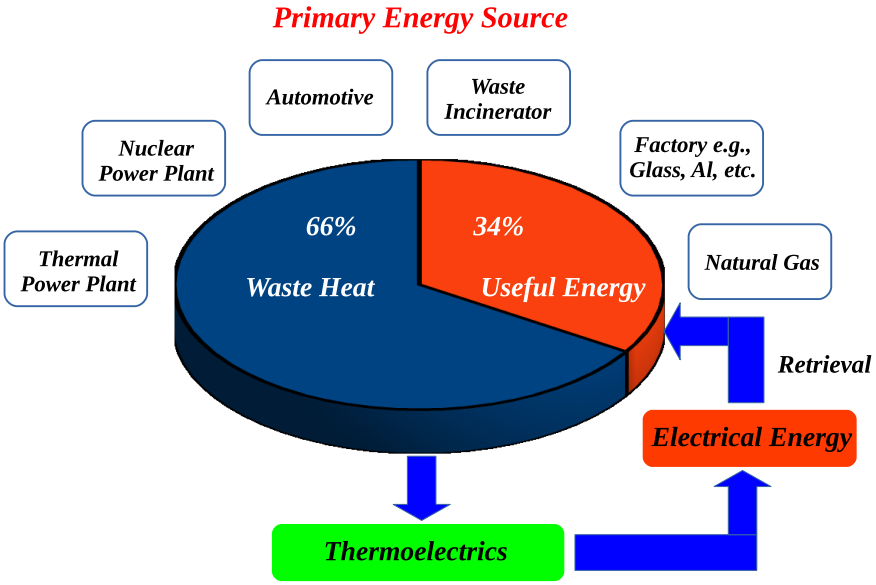

Figure 1.3: Schematic representation of different sectors contributing to large amounts of wasted thermal energy. The figure is adapted from Ref.[21]

Radioisotope TE generators have been used successfully over the last four decades in space missions [22] which require a continuous supply of electric power for weeks to months. It converts the thermal energy gradient by radioactive decay into electric energy. Plutonium (^{238}Pu) serves as the best radioisotope with half life $\sim$ 88 years.

In the Peltier cooler, the external circuit provides d.c. power supply, which drives the electric current (I) and heat flow (Q), thereby cooling the top surface due to the Peltier effect (Q = STI), which can be utilized in the air condition

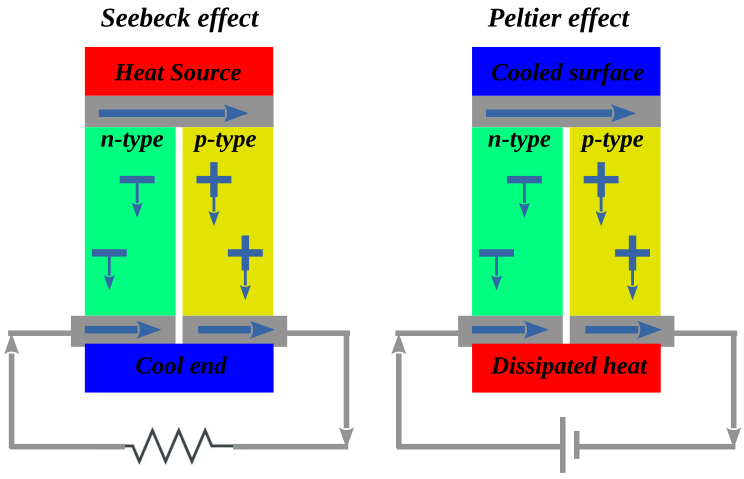

Figure 1.4: Schematic of thermocouples used in TE devices. The figure is adapted from Wikipedia. (see text for details)

system [23]. TE climate-control seat systems have been developed and currently are functional to provide rapid cooling and heating in the summer and winter, respectively [24]. The speed and operating life of electronic devices (circuits) decreases gradually with increasing temperature giving rise to the necessity of a cooling system. TE-powered cooling systems (known as Peltier coolers) can outperform conventional fan-based cooling systems. These are now extensively used in electronic microprocessors such as CPUs for personal computers to boost performance speeds. TE refrigerator is both quiet and light compared to ordinary refrigerators since it needs no compressor. Moreover, it produces no hazardous bi-products, such as chlorofluorocarbon (CFC) gas, used in old refrigerators.

One of the advantages of using TE devices is that they possess no moving or mechanical parts making them able to function for a substantially long time without the need for repair. Moreover, the lack of moving parts ensures the soundless operation of the devices. Although TE technology has been known for two centuries, it has only been applied in narrow fields because of its low conversion efficiency (typically less than 6%)[25] constituting the main disadvantage of TE devices. The efficiency of TE device at a given temperature, T, is estimated by a dimensionless quantity called a figure of merit (ZT) which depends on transport properties of the materials, where $\mathrm{ZT}=\sigma \mathrm{S}^2 T/\kappa$, σ, S, $\kappa=\kappa_e+\kappa_l$ being the electrical conductivity, Seebeck coefficient, and total thermal conductivity having contribution from both charge carriers (κ_e) and lattice vibration (κ_l). Therefore, ideal thermoelectric materials must exhibit a large S, a high σ, and a low κ_l to produce a large potential difference across the junction, so as to minimize the Joule heating effect and to maintain a large temperature gradient, respectively. TE technology will have a larger commercial market when the efficiency reaches

that of conventional mechanical applications.

1.2 Phenomena and Material Background

1.2.1 Spin-Crossover compounds

SCO represents a spin-state transition at the molecular level [26–28]. Switching of spin states is driven by external stimuli such as temperature, pressure, applied magnetic field, and light irradiation (Figure-1.4). This is accompanied by a change in magnetic properties, electrical conductivity, and other physical properties (like refractive index, etc.) of the complex [27]. The phenomenon was first discovered more than 90 years ago in iron(III) tris-dithiocarbamate compounds in which Fe ions switch between low spin (S = 1/2) state and high spin (S = 5/2) state [29]. In 1961, Co(II) based SCO compound ($Co(L)_2X_2$, where L = bis-[2,6-pyridindialdihydrazone] and X is a transcoordinated anion) was synthesized [30] and followed by the discovery of SCO in a Fe(II) compound, $(Fe(phen)_2(SCN)_2$, where phen = 1,10-phenanthroline), involving the transition from LS (S = 0) to HS (S = 2) state [31].

Several SCO complexes have been synthesized, characterized, and studied which involve TM ions with 4 to 7 d -electrons, such as Fe^{2+}, Fe^{3+}, Co^{2+}, or Co^{3+} with the help of experimental techniques, like magnetic susceptibility, M*ö*ssbauer spectroscopy, x-ray crystallography, and extended x-ray absorption fine structure [27]. But most studies on SCO compounds are based on earth-abundant metal Fe(II)-based compounds with 6 d -electrons. SCO transition can be identified by the change in the bond length of the TM ion to its ligand atoms (often nitrogen or carbon); for Fe(II) complexes, this bond length is typically ~ 0.2 $\mathring{A}$ shorter in the LS state than in the HS state whereas for others the change is comparably small (for Co(II) complexes, around $\sim 0.1\mathring{A}$). This leads to SCO transitions in Fe(II) complexes being pronounced and abrupt, whereas they are more subtle in other complexes. Hence SCO transition in Fe(II) complexes is easier to follow and more suitable for application purposes as a result of their robust and prompt switching. Moreover, switches made out of Fe(II) SCO complexes prove to be particularly appealing in terms of sustainable technology. Furthermore, mechanochemistry has recently been applied to the synthesis of SCO materials, thus demonstrating that these materials may be synthesized using the techniques of Green Chemistry [32].

SCO transition can be qualitatively understood using ligand-field theory [28]. The theory describes the energy levels of the spin-polarized d -electrons in a crystal field potential provided by the ligand atoms. For Fe(II) complexes, Fe(II) ion sits inside an octahedral crystal field which breaks the degeneracy of d orbitals. $d_{x^2y^2}$ and d_{z^2} orbitals have lobe that points towards the ligand atom and affected most by electrostatic interaction and gain energy to form e_g level whereas other

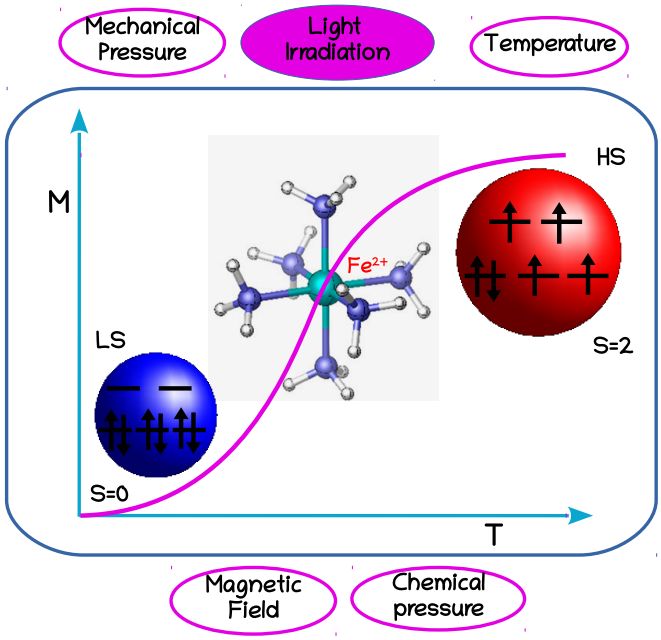

Figure 1.5: Schematic picture of the SCO in a typical Fe(II) metal-organic complex (A typical model complex $[Fe(NH)_3]^2$ is shown in the background, with Fe, N, and H atoms depicted by cyan, blue, and white spheres, respectively). The transition in the magnetization M from the molecular low-spin (LS) S = 0 state to the high-spin (HS) S = 2 state can be triggered by various external perturbations, such as temperature (T), mechanical or chemical pressure, light irradiation, magnetic field, and substrate effect. The 6 d -electrons on the Fe(II) ion, shown by arrows, can fully occupy the t_{2g} levels, resulting in a diamagnetic S = 0 state, or when the t_{2g}-e_g energy splitting is reduced, they can partially occupy both levels, leading to a paramagnetic S = 2 state. The figure is adapted from ref.[28]

d_{xz}, d_{yz} and d_{xy} orbitals have lobe that point in between ligand atoms and remain less affected forming t_{2g} level. Now how 6 d electrons occupy these levels is decided by the interplay between e_g - t_{2g} energy splitting also known as crystal field splitting Δ and exchange interactions manifested in the compound. If by external stimuli Δ is increased, all electrons will fully occupy t_{2g} level, giving rise to diamagnetic low-spin S = 0 state (${t_{2g}}^6{e_g}^0$). If Δ is reduced, exchange interactions will dominate and will populate the levels with electrons having parallel spin (so-called Hunds rule coupling) maximizing the magnetic moment resulting in partially occupied t_{2g} as well as e_g energy levels, giving rise to paramagnetic high-spin S = 2 states (${t_{2g}}^4{e_g}^2$). Clearly, SCO systems display bi-stability, as the energetics of the LS and HS states can be externally modified.

The energy gap between HS and LS states is thermally accessible leading the HS state to be stable at high temperatures and the LS state stable at low temper-

atures. In 1984, Decurtins et al. [33] demonstrated that the crystalline sample of $[Fe(ptz)_6](BF_4)_2$ (ptz = 1-propyltetrazole) at 10K can transit from stable LS state to metastable HS state upon irradiation by green light. The system remains trapped in a photoinduced HS state for days to weeks if the temperature is maintained at T $\leq$ 50K. This phenomenon is known as light-induced excited spin-state trapping (LIESST). LIESST effect is of potential technical use as optical switches and magneto-optical storage. Later, reverse-LIESST effect [34] was found, which converted the compound back to LS state upon shining red light ensuring reversibility of the LIESST process. But the process is limited by the fact that trapping to metastable HS state usually happens at rather low temperatures. A microscopic understanding of this phenomenon is thus needed.

The mechanism of LIESST can be understood in terms of the relaxation model proposed by Hauser et al[35–37]. Here electronic states are modeled as potential energy curves (PEC) i.e., electronic energy (E) calculated as a function of nuclear coordinate (R_{Fe-N}) as shown in figure-1.5. During SCO, drastic change occurs in the FeN_6 octahedra of corresponding compounds causing its average Fe-N bond length (R_{Fe-N}) to be changed by $\sim 0.2\mathring{A}$. Fe(II) $3d^6$ system in LS singlet ground state ($^1A_1$) is first photo-excited (λ=514.5 nm) to an excited singlet state ($^1T_1$). Then spin transition occurs through a relaxation process involving a number of intersystem crossing (ISC) and internal conversion (IC) steps. Typically, a system relaxes to the intermediate states ($^3T_1$) and finally back to the metastable HS quintet state ($^5T_2$) where it gets trapped at cryogenic temperature (typically T < 50K), before relaxing back to LS ground state ($^1A_1$). The reverse-LIESST effect occurs by irradiating (λ=820 nm) the compound prepared at low temperature in the metastable HS state. The excitation induces the transition from $^5T_2$ to ^5E states and then the excited ^5E state relaxes to the $^1A_1$ ground state via the $^3T_1$ state.

Now we are particularly interested to estimate the relaxation rate between the stable LS state and the metastable HS state since it will qualitatively give an idea of how long the system can be trapped in the photoinduced HS state. This will be beneficial to tune the efficiency of the devices made out of the LIESST compound. According to Fermi's Golden Rule, the HS→LS relaxation rate constant can be expressed as,[35]

$$k_{HL}(T) = \frac{2\pi}{\hbar^2\omega}\beta_{HL}^2 F_p(T) \tag{1.1}$$

which consists of electronic contribution encoded in electronic coupling matrix element, β_{HL}, and the nuclear contribution expressed in terms of thermally averaged Franck-Condon factor $F_p(T)$.

From first-order perturbation theory [38], one can write the electronic contribution as

$$\beta_{HL} = \langle \Phi_{LS}|H_{SO}|\Phi_{HS}\rangle = \sum_j \langle S|H_{SO}|j\rangle\langle j|H_{SO}|Q\rangle\left(\frac{1}{\Delta E_{S,j}} + \frac{1}{\Delta E_{j,Q}}\right) \tag{1.2}$$

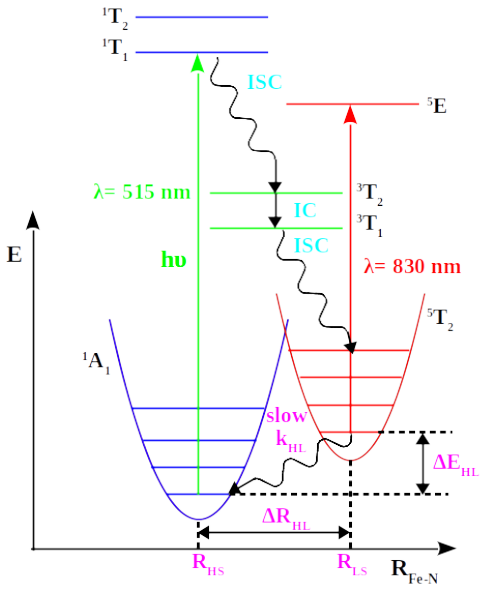

Figure 1.6: Schematic of the mechanism of LIESST and reverse LIESST effects of iron (II) SCO complexes. The figure is adapted from ref.[16] (see text for details)

where the only non-vanishing matrix elements with both LS singlet (S) and high-spin quintet (Q) are those of triplet (T) multiplicity having configuration of $t_{2g}^5 e_g$, intermediate between the singlet configuration of t_{2g}^6 and quintet configuration of $t_{2g}^4 e_g^2$. $\Delta E_{S(Q),j}$ is the energy difference between S(Q) and T, at the equilibrium configuration of S(Q).

At very low temperatures, the Franck-Condon factor becomes,[35]

$$F_p(T \to 0) = \frac{s^p e^{-s}}{p!} \tag{1.3}$$

where, s is the Huang-Rhys factor and p is the reduced energy gap. s and p refer to the horizontal and vertical displacement of the HS and LS ground states from each other respectively. The expressions for s and p are given as:

$$s = \frac{f \Delta Q_{HL}^2}{2\hbar\omega} \tag{1.4}$$

$$p = \frac{\Delta E_{HL}}{\hbar\omega} \tag{1.5}$$

where, $\Delta Q_{HL} = \sqrt{6}\Delta R_{H-L}$

The electronic contribution thus can be computed from knowledge of energy differences $\Delta E_{S(Q),j}$, and SOC matrix elements. Similarly, the nuclear contribution can be computed from the horizontal (for s) and vertical (for p) displacements

of the HS and LS ground states relative to each other, vibrational frequencies (ω) and force constant (f) associated with the excited states.

Clearly, the computation of the relaxation rate of the LIESST mechanism requires an accurate description of both ground and excited states. Considering a model SCO system, we first test the applicability of the wave function and density functional theory (DFT)-based approaches to calculate the electronic structure of the Fe(II) based SCO complex. This has been discussed in Chapter 3 of the present thesis. After establishing our tool, we turn into a real problem. From optical spectroscopy measurement, Hauser et al [39] demonstrated that the low-temperature HS-LS relaxation rate can vary 12 orders of magnitude for different Fe(II) based LIESST compounds. Several compounds are chosen such that the core FeN_6 octahedra is taken as fixed but ligands may vary from monodentate to bidentate to multidentate coordination. Such tunability of relaxation rate has not been explained properly in terms of a structural point of view and inspired us to study the structure-property relationship manifested in such compounds. This has been discussed in Chapter 4 of the present thesis.

1.2.2 Coordination Polymers

Although the fundamental origin of SCO phenomena is molecular, intermolecular interactions play a key role in making SCO a spin transition. When the magnitude of intermolecular interactions overcomes certain threshold value, SCO phenomena becomes cooperative leading to spin transition. Depending on the nature and strength of the interaction, a) the transition may be gradual and continuous over an extended temperature range, b) it may be abrupt, seen as a sharp first-order transition. c) In case of a first-order transition, it may be accompanied by a hysteresis loop. d) In a few cases, the transition may be incomplete at either or both ends of the spin states. In cases of hysteresis, LS $\rightarrow$ HS transition (warming mode) temperature Tc_1, is higher than HS $\rightarrow$ LS transition (cooling mode) temperature Tc_2. Between Tc_1 and Tc_2, the state of the system, LS or HS, depends on its history, and hence on the information which has been stored. Clearly, the presence of hysteresis in spin transition confers a memory effect in the devices. In a molecular crystal, isolated molecular units are connected by weak van der Waals interaction or hydrogen bonding that are not sufficient to give rise to cooperativity. To design strongly cooperative SCO compounds, active SCO sites must be linked to each other by chemical bridges through which the intersite interactions may be efficiently propagated. This makes the coordination polymeric compounds with repeating coordination entities having extended solid structures the suitable candidate.

Pioneering work on coordination polymers was done by Alfred Warner which include cyanide complexes Prussian blue and Hofmann clathrates[40]. Most studied SCO materials showing cooperativity are linear 1-dimensional coordination

polymers which are materials extending through repeating coordination entities in 1-dimension forming chain-like structures, with weak links between individual chains. But coordination compound can also extend through repeating coordination entities in 2 or 3 dimensions. The dimensionality of a coordination polymer is defined by the number of directions in space the array extends to. A one-dimensional structure extends in a straight line (for example along the x-axis); a two-dimensional structure extends in a plane (two directions, x and y axes); and a three-dimensional structure extends in all three directions (x, y, and z axes). Strategic crystal engineering that makes use of multidentate ligands, connected by spacers, facilitates to increase the dimensionality from 1-d to 2-d or 3-d.

Pressure-induced SCO transition in 2-d coordination polymer was first reported in 1990 for $[Fe(btr)_2(NCS)_2].H_2O$[41]. In this compound, the active sites i.e., Fe(II) ions are bridged by the 4,4-bis-1,2,4-triazole ligand (btr), resulting in a two-dimensional structure with weak links of van der Waals or hydrogen bonds among these infinite layers. Very abrupt spin transitions, both in the warming and cooling modes, as well as a thermal hysteresis of 21 K were observed, with Tc_1=144.5 K and Tc_1=123.5 K. $[Fe(btr)_3\ [(ClO_4)_2]$[42] represents the first 3-d SCO coordination polymer. Among the 1-d coordination polymers, triazole-based Fe(II) chain compounds have drawn significant attention. A schematic representation of a linear, 1-d coordination polymer is shown in figure-1.7. [Fe(4R-1,2,4-triazole)$_3$]A_2.solv, where A is the counterion and solv denotes the solvent molecule consisting of linear chains in which the adjacent Fe(II) ions in the chain are linked by three triazole ligands. The coordination linkers, which are 1,2,4-triazole blocks form efficient chemical bonds to transmit a cooperative effect, leading to a hysteresis loop of width ranging $\sim$ 2-20 K.[43] In a seminal experimental study by Kahn et al.[44] thermal hysteresis at room temperature was demonstrated in $[Fe(Htrz)_{3-3x},(4\text{-}NH_2trz)_{3x}](ClO_4)_2.nH_2O$ with x = 0.05.

Bimetallic 1-d chain compounds like $Fe(aqin)_2(\mu 2\text{-}M(CN)_4)$, M = Ni(II) or Pt(II), have been synthesized which were found to show abrupt HS-LS SCO.[45] Experimental and simulation studies by Linares et al.[46] on $[Fe_xCo_{1-x}(btr)_2(NCS)_2].H_2O$ with x = 0.847 showed large hysteresis loops in SCO phenomena induced thermally as well as through pressure. Their study on $[Fe_xNi_{1-x}(btr)_2(NCS)_2].H_2O$ with x = 0.66 showed large hysteresis in pressure-induced SCO.

Balde et al. [47] considered coordination polymers with the general formula $[FeL_{eq}(L_{ax})]$solvent where L_{eq} = 3,3-[1,2-phenylene bis(iminomethylidyne)]bis(2, 4-pentanedionato)(2-)-N,N,O^2 ,O^2 and 3 different components for L_{ax} such as 4,4-bipyridine(bipy), 1,2-bis(4-pyridyl)ethane (bpea), and 1,3-bis(4-pyridyl)propane (bppa). Cooperative SCO was previously reported for the bipy linker, which showed thermal hysteresis, and bpea and bppa-based compounds showed multi-step transitions.

Novel 1-d Fe(II) SCO coordination polymers with 3,3-azopyridine as an axial ligand have been synthesized which were found to show kinetic trapping effects

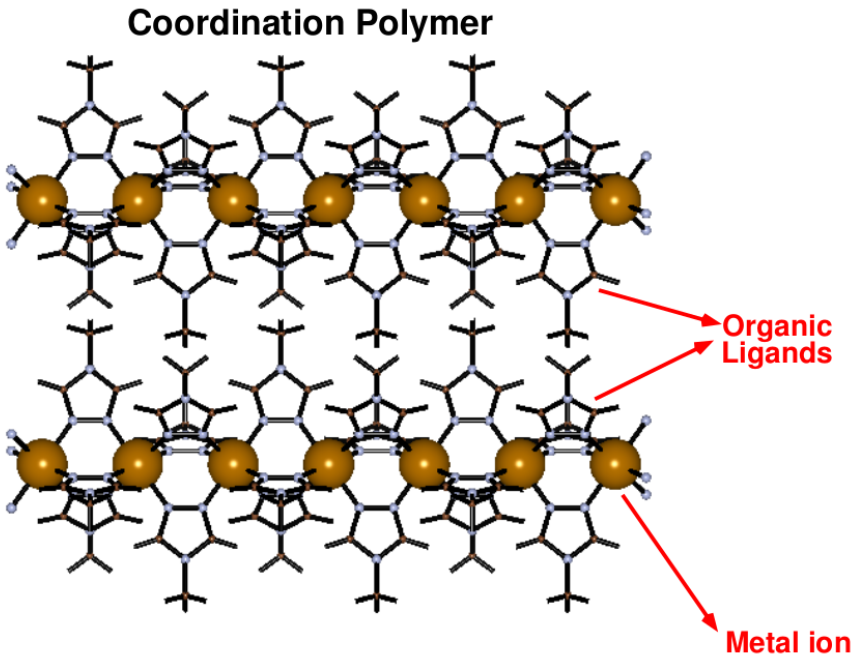

Figure 1.7: Schematic representation of linear, 1-d coordination polymer in which chains of metals are linked by organic ligands. The figure is adapted from ref.[50]

and spin transition above room temperature.[48] Combination of rigid links and a hydrogen bond network between 1-d Fe(II) chains has been recently shown as a promising tool to trigger SCO with hysteresis loops having widths as large as $\sim$ 43 K.[49]

Admitting the suitability of such compounds in exhibiting cooperativity there are several issues that need attention. The key questions are, (a) understanding the microscopic mechanism, i.e., what is the driving force for the cooperativity and the hysteresis; and (b) how the cooperativity can be tuned or modified to suit the specific need. These understandings are expected to provide an advancement of the field in terms of possible commercialization of this technologically important property which relies on critical parameters of cross-over being close to ambient conditions, and a large enough hysteresis width. Motivated by this, we investigate three metal-organic polymers with Fe^{2+} as TM ion and tetrazole-based organic ligands consisting of two, four, and six-carbon(C) linkers-based bridging ligands.

Experimentally, SCO compounds with two and six-C linker show hysteresis of width ($\Delta T_{1/2}$) 29K and 2K respectively with $T_{1/2}$ around 126K. This indicates that the cooperativity among Fe(II) centers must be different for the three polymers. Our motivation is to understand how cooperativity among Fe centers affects while we increase the length of the linkers. Banerjee et al.[51] discussed

the microscopic origin of cooperativity in the Fe-triazole system as the interplay of magnetic and elastic interactions existing between Fe centers. In Chapter 5 we calculate the Fe-Fe magnetic exchange interaction (J) and spin-state dependent elastic interaction (E_v) from DFT calculation and will finally discuss the driving force responsible for cooperativity in these SCO compounds.

1.2.3 Thermoelectric materials

Most of the commercially available thermoelectric materials are doped semiconductors such as Bi_2Te_3, $Si_{1-x}Ge_x$, and PbTe have ZT around 1.[52] But for practical purposes, ZT of around 3-4 with TE conversion efficiency 30 % is required.[53] The difficulty of designing high-performance TE materials arises from the fact that the electron transport properties are strongly coupled via charge carrier concentration. As evident from figure-1.8 that the charge-carrier concentration influences the transport properties such that increased carrier concentration increases σ, electron thermal conductivity κ_e but decreases the S whereas lattice thermal conductivity κ_l remains unaffected being solely controlled by phonon transport arising from lattice vibration. Hence, there must be an optimal carrier concentration for which ZT can be maximized. Clearly, the largest value for ZT is obtained midway between these two extremes (metal or insulator) at a carrier concentration of about $10^{19}/cm^{-3}$ implying that highly doped (degenerate) semiconductors are the potential candidates. Best thermoelectrics therefore require a material that exhibits unusual phonon-glass electron-crystal like features [54]. The electron-crystal requirement stems from the fact that crystalline semiconductors have been the best at meeting the compromises required from the electronic transport properties (σ, S and κ_e). The phonon-glass requirement stems from the need for as low a κ_l as possible.

In 1993, Hicks and Dresselhaus suggested that TE performance can be substantially improved through nanostructuring the materials due to the quantum confinement of charge carriers in low-dimensional materials.[56] For reduced-dimensionality materials such as quantum-dot, quantum-well structures, and 2D materials, the thermal conductivity has been considerably reduced without significantly affecting the power factor. High values of ZT, ranging from 1.6 at 300K to 3 at 550K, are reported for Bi-doped n-type PbSeTe/PbTe quantum-dot superlattice (QDSL) samples grown by molecular beam epitaxy (MBE). According to theoretical calculation, when the diameter of Bi_2Te_3 nanowires is $5\mathring{A}$,[57] the ZT value reaches 14, and graphdiyne has a ZT value of 4.8 at 300 K.[58] On the other hand, layered materials have been proved to be potential thermoelectrics since 1950, when tetradymites (M_2X_3, M = Bi/Sb, X = Te/Se) were identified as the class of semiconductors with the highest TE efficiency and their TE performance has been further improved over the decades via materials engineering. According to optimal working temperature, the layered TE materials

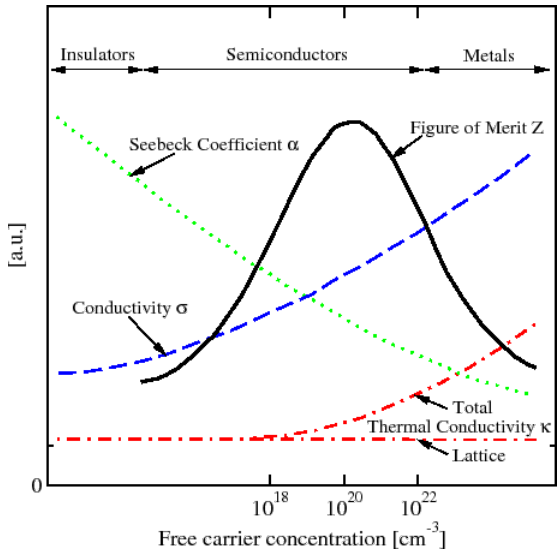

Figure 1.8: Schematic of variation of transport properties as a function of charge carrier concentration adapted from ref.[55]

(Figure-1.9) can be divided into three categories: i) low-temperature TE materials that operate below 500 K, ii) mid-temperature TE materials (between 500 and 900K), and iii) high-temperature TE materials (above 900 K). Bi_2Te_3 and its derivatives from the tetradymite family are studied both as p- and n-type thermoelectric materials, considered as best TE materials for near room-temperature (RT) power generation applications. Bismuth telluride-based TE materials are being used as TEG in many commercialized Peltier coolers and different renowned car companies. PbTe and its derivatives are the best thermoelectric materials for mid-temperature TEGs. But the large-scale production of these materials is limited because of the toxicity and cost-expensiveness of Pb and Te elements. Recent experimental measurements revealed that SnSe can be an outstanding thermoelectric material for the mid-temperature range, both as a p-type [59, 60] and n-type [61, 62] doping. ZT value of 2D n-type single crystal SnSe can reach 3.1.[59] and hence SnSe is being considered as a potential alternative to PbTe. Various oxy-chalcogenides with a layered structure such as BiCuSeO [63, 64] and Bi_2O_2Se [65, 66] are also getting established as high-performance thermoelectric materials in the mid to high-temperature range. In a nutshell, layered 2D materials have been established as potential candidates for TE energy generation over the past decades due to their favorable electrical and phonon transport properties, which can be seen from their significantly large ZT (Figure-1.9).

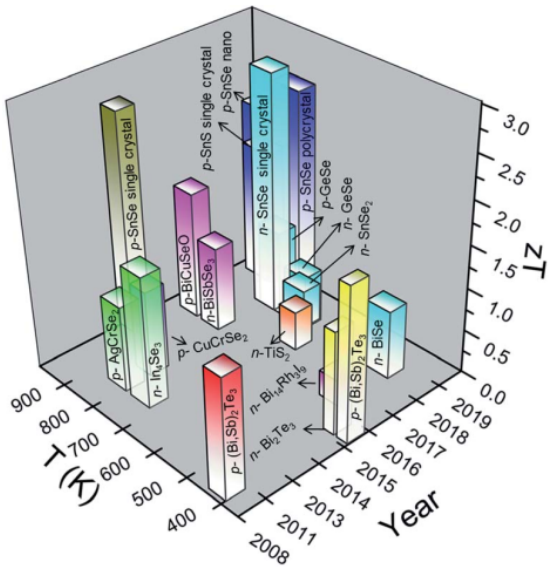

Figure 1.9: Layered 2D materials discovered in past decades showing its figure of merit ZT and optimal working temperature adapted from ref.[67]

1.2.4 Layered two-dimensional material

Research on two-dimensional (2D) materials has come to the forefront when Andre Geim and Konstantine Novoselov isolate graphene from its three-dimensional (3D) layered counterpart graphite by using the scotch tape method in 2004 [68]. In 3D layered materials, individual atomic layers (2D) with strong in-plane chemical bonds are stacked on top of each other in out-of-plane direction via weak couplings such as van-der-Waal interaction, hydrogen bond, and electrostatic interactions. This encompasses a broad category of materials such as graphite, clays, ceramics, oxides, halides, chalcogenides and MAX phases, which leads to the possibility of cleaving these 3D materials layer by layer to obtain their 2D layered counterparts. In the post-graphene era, several layered 2D materials have been predicted and synthesized. This ever-expanding list includes hexagonal boron nitride [69], boron nitride oxide [70], transition metal dichalcogenides [71], holey carbon [72], recently discovered MXene, mono elemental phases like silicene [73], germanene [74], stanene [75], phosphorene [76–78], and borophene [79, 80], comprised of elements from group III to group V, etc.

With the aim of achieving high-performance thermoelectrics, we discuss two kinds of layered 2D materials in the present thesis. In the first category, we study the family of transition metal carbides known as MXene in which atomic layers are formed by multiple elements like TM (M), carbon (X), and passivating elements (T = O, F, OH) providing more compositional tunability in order to get desired ZT. In the second category, we study elemental 2D material composed

of atomic layers formed by only group-VI element Tellurium, known as tellurene which has been reported to have minimum lattice thermal conductivity among other known 2D layered material.

MXene

MXene represents the family of TM carbide, nitride, and carbonitride with chemical formula $M_{n+1}X_n$ where M is 3d/4d TM (such as Sc, Ti, Zr, Hf, V, Nb, Ta, Cr, Mo, Mn), X is C and/or N and n ϵ [81]. Since n ranges from 1 to 3, corresponding MXene sheets comprise 3, 5, or 7 atomic layers for M_2X, M_3X_2, and M_4X_3 respectively. In the MXene structure, the hexagonal layer of X sites is sandwiched between two M layers and the number of $(MX)_n$ -layers are one, two, and three for M_2X, M_3X_2 and M_4X_3 class of MXenes. These materials display many interesting properties, particularly for energy storage both for battery and supercapacitor electrodes [82].

MXene has no van-der-waal bonded layered precursor like most 2D materials. Its 3D precursor called the MAX phase is basically two formula units of MXenes separated by A group element layer (i.e., Group-IIIA and IVA elements such as Al, Si, Ge, Ga, P, As, In) discovered in 1996. MAX phases can be characterized by the combination of different bonding characters; while the M-X bonds are strong directional covalent bonds, M-A bonds are relatively weaker than covalent M-X bonds, M-M bonding being of metallic nature. M-A bonds are thus too strong to be broken by shear/mechanical means. Hence MXene is synthesized from chemical exfoliation of MAX phase (e.g., Ti_3AlC_2) by selective etching of A element using suitable etchent (e.g., hydrofluoric acid) followed by sonication. Titanium carbide (Ti_3C_2) was the first MXene reported at Drexel University [83]. MXenes can also be synthesized from non-MAX-phase precursors.[84, 85] The First MXene of this kind is Mo-based Mo_2CT_x (T=F/O/OH) which was made by etching Ga layers from Mo_2Ga_2C. Despite its similarity to MAX phases, this phase has two A layers (Ga) separating the carbide layers. $Zr_3C_2T_x$ was synthesized by selectively etching aluminum carbide (Al_3C_3) layers, instead of just Al layers, from $Zr_3Al_3C_5$ which is another non-MAX-phase precursor. There are more than 70 MAX phases are synthesized experimentally out of which only 32 MXenes have been exfoliated. In the exfoliation process, MXene surfaces are terminated by a mixture of multiple species (T) depending on the etchent. Recent experiments showed that MXenes with uniform halogen (Cl, Br) and chalcogen (S, Se, Te) terminations could be synthesized using molten inorganic salts as etching materials [86].

Discovery of ordered MAX phases leads to the prediction and synthesis of numerous ordered 2D materials of MXene structure. Out of plane ordered MAX phase (o-MAX), namely Cr_2TiAlC_2 in which a Ti-layer is sandwiched between two outer Cr carbide layers in a M_3AX_2 structure, was discovered in 2014 [87]. In

a later study, the MAX phase with Mo-Al bonds namely Mo_2TiAlC_2 was synthesized [88, 89] wherein TiC_2 -layers are sandwiched between Mo-layers. Using ab initio DFT computations stability of over 20 new, ordered, double-M MXenes, of the form M_2MC_2 and $M_2M_2C_3$, where M (outer layer metal) and M (inner layer metal) can be Ti, V, Nb, Ta, Cr, or Mo, have been predicted [88, 89]. Each of these predicted MMXenes have multiple surface termination groups, such as F, O, or OH. In 2015 Anasori et al. successfully synthesized [88, 89] the ordered double TM 2D MXenes, such as Mo_2TiC_2, $Mo_2Ti_2C_3$, and Cr_2TiC_2. In all cases, the C atoms occupy the octahedral sites between the M-M layers. The first in-plane ordered MAX phase (i-MAX) was discovered in 2017 $(Mo_{2/3}Sc_{1/3})_2AlC$, a 211 MAX phase with M sublattice populated by Mo and Sc in a 2:1 ratio showing an in-plane chemical order [90]. Furthermore, selective etching of Al and Sc produced a novel 2D material with ordered divacancies, $Mo_{1.33}C$ MXene, which displayed superior volumetric capacitance compared to other 2D materials. Unlike oMAX or conventional MAX phase of hexagonal structure (s.g.:$P6_3/mmc$), iMAX phases have base-centered monoclinic structure (s.g.:C2/c).

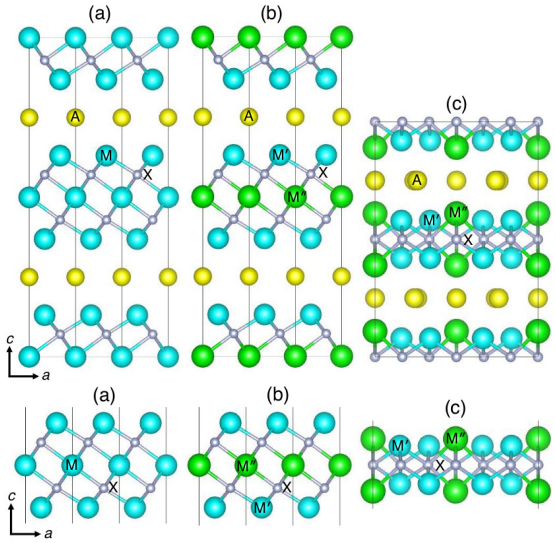

Figure 1.10: Crystal structure of MAX(top) and its MXenes (down) (a) M_3AX_2 , (b) o-M'$_2$M"AX_2, and (c) i-(M'$_{2/3}$M"$_{1/3}$)$_2$AX. The figure is taken from ref.[91]

Electronic properties of MXenes are attractive as they can, in principle, be decided by the choice of their composition M, X, and T. The pristine M_2X (X=C, N) systems are all metallic with the Fermi energy located at the d bands of the transition metals. In most MXenes, the p bands of C/N are below the d bands of the transition metals and these bands are separated by a small band gap. Surface terminating elements play a crucial role in determining the electronic structure as well as magnetic properties of MXene compounds. Sc_2CT_2 (T=F,OH,O), M_2CO_2 (M=Zr, Hf) and $(M_{2/3}M_{1/3})_2CO_2$ (M=Mo,W; M=Sc,Y) become semiconducting

upon surface functionalization [92, 93]. The electronegative termination -F, -OH, and -O receives one and two electrons from the outer transition metal layers respectively, and generates a new band below the Fermi energy, hybridized with the M d orbitals. This reduces the DOS at the Fermi surface or lowers the Fermi surface. Hence, Sc_2CT_2 (T=F, OH, O), M_2CO_2 (M=Zr, Hf) become semiconducting because the Fermi energy is located at the center of the gap between the M d bands and the X p bands after functionalization.

Anasori et.al [89] found that ordered structures are in the ground state for most of the 212 MXenes and for all the 223 MXenes. The calculated density of state of Mo_2TiC_2 MXenes with hydroxyl (-OH), fluorine (-F), and oxygen (-O) termination is found to be similar to that of Mo_3C_2 but very different from Ti_3C_2 MXenes. This suggests that the electronic property of fully ordered double transition metal MXenes will be mainly controlled by the outer transition metal with a small influence from the inner transition metal. Moreover, DFT predictions are validated by synthesizing Mo_2TiC_2, $Mo_2Ti_2C_3$, Cr_2TiC_2, and their electrochemical results. Moreover, DFT calculations showed that replacing the two outer layers of Ti in $Ti_3C_2(OH)_2$ by Mo, to form $Mo_2TiC_2(OH)_2$, while keeping the same surface termination -OH, changed the electronic structure to a semiconductor with a narrow band gap ($\sim$0.05 eV). The same behavior is predicted for $Mo_2Ti_2C_3(OH)_2$. The energy bandgap is found to be tunable in the range of 1.25 to 1.80 eV in $M'_{2(1-x)}M_{2x}CO_2$ (M' and M" are Ti, Zr, and Hf) solid-solution MXenes. Among these MXenes, the $Ti_{2(1-x)}Zr_{2x}CO_2$ alloy with x = 0.2778 is predicted to have the most appropriately aligned band edges for photocatalytic water splitting [94]. The origin of the band gaps in $(M_{2/3}M_{1/3})_2CO_2$ is the splitting of d-orbital bands due to the crystal field around the transition metals surrounded by C and O atoms. The states near the Fermi energy are t_{2g} bands hybridized with C and O p orbitals via dpπ coupling, which split widely, resulting in finite band gaps.

The high value of DFT computed non-spin-polarized density of states at the Fermi level (E_F) suggests magnetic instability. According to Stoner theory [95], the stability of magnetic states is given by $N(0) > 1/I$, where N(0) is the density of states at (E_F) and I is the Stoner parameter. Plugging in I for M site in MXene, several of them are expected to be magnetic. Considering the magnetism of metal atoms, one may expect different possible arrangement of TM spins within the single-unit MXene structure. It can be ferromagnetism (FM) with parallel alignment of all TM spins, or it can be antiferromagnetism (AFM) with certain spin arrangements (A-type, C-type, or G-type). In the case of A-type, the intralayer TM spins are aligned parallelly, while those between the layers are aligned in an antiparallel manner. The reverse is true for C-type AFM with intralayer TM spins aligned antiparallelly and TM spins between layers aligned parallelly. For G-type AFM, the metal spins are aligned antiparallelly in all directions.

Robust half-metallic ferromagnetism supported by high magnetic moments

(up to 9 μB per unit cell) and high Curie temperatures has been reported in Mn_2NT_x with different surface terminations (T = O, OH, and F), as well as in Ti_2NO_2 and Cr_2NO_2, while the intralayer AFM ground state was found in Ti_2NF_2, $Ti_2N(OH)_2$, V_2NF_2, V_2NO_2, $V_2N(OH)_2$, Cr_2NF_2, and $Cr_2N(OH)_2$ [96]. Following the MXenes with single TM, magnetism in ordered phases of MXene also depends on its surface termination. O-MXenes such as $Cr_2MC_2T_2$ (M"= Ti and V, T = F, OH, and O) can be nonmagnetic ($Cr_2TiC_2O_2$), antiferromagnetic ($Cr_2TiC_2F_2$ and $Cr_2TiC_2(OH)_2$), or ferromagnetic ($Cr_2VC_2(OH)_2$, $Cr_2VC_2F_2$, and $Cr_2VC_2O_2$) [97]. Gao et.al performed systematic DFT calculations to investigate the magnetic and electronic properties of 319 i-MXenes with a general chemical formula $(M_{2/3}M'_{1/3})_2X$, focusing particularly on the cases where M' is magnetic where M=Sc, V, Mo, Nb, Ta, Ti, Zr, Hf [98].

Different MXenes have been predicted with varying values of in-plane elastic moduli [99, 100]. According to theoretical investigations by Fu et al., the functionalization by oxygen groups in Ti_3C_2 ($Ti_3C_2O_2$) causes enhancement in strength. This was attributed to the charge transfer from inner Ti-C bonds to the external Ti-O surface bonds, hindering irreversible deformation and a subsequent need for high critical stress for lattice failure [101]. A study carried out by Chakrabarty et al. [102] on Ti_2C highlighted the important role of magnetostructural coupling present in MXene which significantly influence their mechanical properties. They showed that AFM Ti_2C will withstand significantly higher strain as compared with its nonmagnetic counterpart. The same study also explored the effect of substitutional doping of V at M and B at X sites of Ti_2C MXene [102]. The study predicted that B doping at X site [$Ti_2(C_{0.5}B_{0.5})$] significantly improves the elastic properties by reducing the in-plane stiffness and Youngs modulus as well as extending the yield strength for the biaxial and uniaxial strains.

Semiconducting MXenes, Sc_2CF_2, $Sc_2C(OH)_2$, Sc_2CO_2, Ti_2CO_2, Zr_2CO_2, and Hf_2CO_2 are predicted to attain large Seebeck coefficients at low temperatures suggesting MXene as good thermoelectrics [103]. Khazaei et al.[104] predicted the electronic transport properties of more than 35 kinds of different functionalized MXene monolayers and multilayers of the type M_2CT and M_2NT, M=Cr, Ti, Mo, Zr, and Hf, etc and T= O, F, OH. Gandi et al.[105] calculated the lattice thermal conductivity (κ_l) of O passivated Ti-, Zr-, and Hf- based MXenes and found the highest figure of merit for Ti_2CO_2 ($ZT_{max} = 0.45$). The study by Kumar et al.[106] predicted the semiconducting Sc_2CT_2 (T = OH) MXenes with ZT_{max} value of 0.5 at T=900K. Due to its excellent thermal stability in the air, MXene can be classified as high-temperature TE material [107–109]. The discovery[88] of ordered double transition metal provided the further opportunity on expanding on the possible list of MXene compounds with potential TE properties. The presence of two transition metals instead of a single one, as in conventional MXene compounds, offers even better flexibility in tuning properties. Kim et al.[110] reported the measured electronic transport properties of Mo-based double TM

MXene (Mo_2CT_x, $Mo_2TiC_2T_x$, and $Mo_2Ti_2C_3T_x$; T_x: mixed termination of O. F, OH group). Jing et al.[111] predicted the thermoelectric performance of semiconducting Cr_2TiC_2 and $Cr_2TiC_2T_2$ (T= F or OH) MXene and found large Seebeck coefficients of $\sim$ 800, 700 and 600 μVK^{-1}, respectively. The figure of merit of p-type $Cr_2TiC_2(OH)_2$ was predicted to reach as high as 3.0 at 600K.

Motivated by the above, we focus on Mo and Ti-based double transition metal MXenes, namely $Ti_{3-x}Mo_xC_2T_2$ with T = -O/-F/-OH. The Mo concentration is varied over a wide range with x = 0.5, 1, 1.5, 2, 2.5 in order to understand the systematic evolution of properties upon increasing (decreasing) Mo (Ti) concentration. $x = 1$ and 2 of the series correspond to stoichiometric compositions of Ti and Mo in 2:1 and 1:2 ratio, out of which $x = 2$ is the experimentally synthesized $Mo_2TiC_2T_2$ composition.[87]. This study has been discussed in Chapter 6.

Tellurene

After the discovery of graphene, several elemental 2D materials in monolayer form have been predicted and synthesized for almost 20 years, most of which comprise elements from group III to group V. In comparison, only a few studies on 2D materials composed of group VI elements selenium (Se) and tellurium (Te) have been reported.[112, 113] In 2017, 2D nanoflake of Te was successfully fabricated [114, 115], having the ability to surpass several major drawbacks manifested in existing 2D materials, such as the zero band gap of graphene [116], the environmental instability of black phosphorus (BP) [117] and the low current mobility of transition metal dichalcogenides (TMDCs) [118]. It possesses excellent environmental stability, tunable bandgap, nonlinear optical responses, and a high carrier mobility ($\sim 10^3$ $cm^2V^{-1}s^{-1}$) at room temperature. [119–121] These properties are fundamental for practical applications, such as high-performance photodetectors, field-effect transistors (FETs), and modulators. In addition, 2D Te nanoflakes possess unique helical chain structures [114], giving rise to high carrier mobility and strong in-plane anisotropic properties. Structural symmetry breaking and flexible mechanical properties of the 2D Te nanoflakes provide a large in-plane piezoelectric coefficient, which enables it to be a potential material for piezoelectric devices.

The most stable structure of bulk Te is trigonal at ambient pressure having three equivalent Te atoms (Wyckoff position 6c) in the unit cell. Each Te atom is covalently bonded with its two nearest neighbors (bond length = 2.89$\mathring{A}$) forming a helical chiral (either right-handed with space group $P3_121$ or left-handed $P3_221$) chain which runs along the 3 fold screw axis (c-direction) and stacked together along a and b-direction. In the helical chain, each one-third of atoms are straightly above other atoms, so that the projected plane of the chain forms an equilateral triangle.

Tellurene can form a stable monolayer (ML) having three different phases

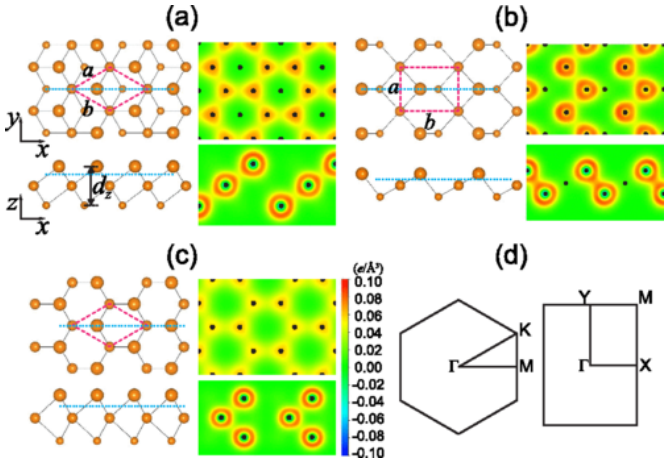

Figure 1.11: Top and side views of the optimized structures of tellurene in different phases: (a) α-Te, (b) β-Te, and (c) γ-Te. The surface Brillouin zones for α (or γ) and β phases are drawn in (d). The dashed lines indicate the unit cell of each structure. The total charge density of each structure is plotted at the horizontal and vertical cross sections indicated by the blue dotted lines. The figure is taken from ref.[114]

caused by the inherent multivalency of Te, namely the most stable 1T-MoS_2 -like α-Te, metastable tetragonal β- Te and 2H-MoS_2 -like γ-Te (figure-1.11). Crystal structure of ML phases of tellurene are explained as follows: β phase tellurene structure has P2/m space group symmetry, i.e., it has a twofold axis along the a-direction with mirror planes perpendicular to this axis. It consists of 2 inequivalent Te atoms in the unit cell i.e., $Te_{1,3}$ of Wyckoff position 4o and Te2 of Wyckoff position 1g with 2 kinds of Te-Te bonds of lengths: Te1-Te2 = Te1-Te4 = 3.03Åand Te2-Te3 = 2.77Å. α phase of tellurene consists of 2 inequivalent Te atoms in the unit cell i.e., $Te_{1,3}$ of Wyckoff position 12k and Te2 of Wyckoff position 2a with all equal kinds of Te-Te bonds of length 3.04Å. It completely loses the original chain structure in the bulk phase but it is similar 1T-MoS_2 structure, which belongs to the $P\bar{3}m1$ space group. The squared buckled phase of C2/m space group symmetry consists of 2 inequivalent Te atoms in the unit cell i.e., Te1 of Wyckoff position 8j and Te2 of Wyckoff position 4i with 3 kinds of Te-Te bond of length: short bond = 2.87Å, medium bond = 3.05Å, long bond = 3.21Å. β phase Te is 30 meV/atom lower than α phase and 60meV/atom lower than buckled square phase. Overall, the β phase is the most stable of all.

α and β- Te is found to be narrow band gap semiconductor but γ-Te is metal. In the absence of a bulk layered counterpart, tellurene should be grown epitaxially on proper substrates. Chen et al. have successfully synthesized ultrathin layers tetragonal β -tellurene on highly oriented pyrolytic graphite (HOPG) by using molecular beam epitaxy.[122] Wang et al. fabricated air-stable and high-

performance field-effect transistors using β tellurene synthesized by substrate-free solution process.[119] Xian et al. predicted new phase of tellurene ML with chair-like square buckled structures showing nontrivial topological properties.[123] Few-layer (FL) tellurene structures and possible phase transition among them are studied by Xiang et al.[123]

The electron configuration of Te is ns^2np^4. The covalent bonds between intra-chain Te atoms are formed between two unpaired p electrons of adjacent atoms and lone pair of p electrons interact between two interchain Te atoms. Thus, the interchain interaction is weaker than the intrachain one in the bulk phase. Spin-orbital coupling (SOC) has a significant influence on the electronic structure of tellurene. The inclusion of SOC transforms the unstrained β-Te from indirect to direct band gap semiconductor at high symmetry Γ point of energy gap 0.98 eV. Such a narrow band gap is beneficial for improved electron transport properties.

Furthermore, the room temperature lattice thermal conductivity of 2D Te was reported to be the lowest among existing 2D materials, e.g. 2.16 and 4.08 $Wm^{-1}K^{-1}$ along arm-chair and zigzag directions of 2D crystal structure of Te [124] compared to 3080-5150 $Wm^{-1}K^{-1}$ for graphene [125] or 101.43 $Wm^{-1}K^{-1}$ and 110.30 $Wm^{-1}K^{-1}$ along arm-chair and zigzag-direction of MoS_2.[126] Such low thermal conductivity is attractive from the perspective of thermoelectric (TE) applications. Following this, calculations were carried out and 2D Te, or tellurene, was found to reach a room temperature ZT value of 0.79 by p-type doping with the dopant concentration of 10^{13} cm^{-2} in square-Te [127], while that in the β structure was found to show a much better performance, can reach to 2.9 [128], especially at high temperature (700K). It will be thus worth exploring how the thermoelectric performance of 2D Te can be further improved. This study has been discussed in Chapter 7.

1.3 Overview of present thesis

In the previous section, we discussed a diverse class of materials with intriguing properties that are technologically important as well as indigenous. Understanding and prediction of such materials need synergy and combined efforts among Nano- and Meso-scale Science, Advanced Instrumentation, Materials synthesis as well as Modelling and Simulation In particular, the present thesis focuses only on modeling and simulation part in two classes of problems. (1) Spin-Crossover and (2) Thermoelectricity.

The present thesis will primarily make use of the power of density functional theory (DFT) based computation in addressing such problems and has been organized into two parts. In the first part, known Fe(II) based SCO complexes are studied focusing on their LIESST properties. After establishing our computational approach, a correlation has been built between the observed low-

temperature relaxation rate and the corresponding metal-ligand covalency of the complexes. We further study several Fe(II) tetrazole-based coordination polymers exhibiting distinct spin transition behavior. We will discuss the spin-dependent elastic and magnetic interactions affecting cooperativity among Fe(II) centers responsible for the spin transition. In the second part, we investigate the thermoelectric properties of known layered 2D materials. We consider double TM carbides known as MXene with alloyed structure and predict new semiconducting compounds under the MXene family that show enhanced thermoelectric properties at high temperatures. Next, we consider elemental 2D materials composed of group-VI element Tellurium known as Tellurene, and show how thermoelectric properties can be improved with the application of biaxial strain which can be imposed on tellurene through van der Waals heterostructing with other known 2D materials.

The contents of the subsequent chapters discussed in the present thesis have been summarized as follows.

Chapter 2 : In this chapter, we discuss the computational methodology employed in our calculations. This contains a background study of the techniques that we use to solve many-electron Hamiltonian for molecules as well as solid-state systems. We will explain both wave-function-based and density-functional-based approaches. We will briefly discuss the density functional theory used to compute ground state properties for both SCO compounds as well as thermoelectric compounds and the time-dependent density functional theory used to compute excited states of SCO complexes. We will further solve Boltzmann transport equations for electrons as well as phonons to estimate the transport properties of thermoelectric materials.

Chapter 3 : LIESST process is investigated computationally in an SCO model system, derived out of $[Fe(abpt)_2(NCS)_2]$ consisting of Fe(II) SCO center coordinated by bidentate as well as monodentate ligands. For this purpose, we use two complementary techniques: (a) time-dependent density functional theory (TDDFT) with the choice of different exchange-correlation functional and (b) multireference approach of complete active space self-consistent field and complete active-space second-order perturbation (CASPT2) theory. We calculate the potential energy curves (PECs) of low-energy states, as well as spin-orbit couplings at crossing points of these PECs. Inputting these pieces of information, and the information related to nuclear degrees of freedom within the Franck-Condon theory, we compute the relaxation rates of possible LIESST mechanisms, as suggested by the two approaches. Our findings conclude that TDDFT is a reasonable approach to estimate the relaxation rates of real complexes, consisting of several tens to several hundreds of atoms, given its computationally inexpensive nature compared with that of the multireference approaches.

Chapter 4 : Our previous study of the LIESST phenomenon on the SCO model system suggests that TDDFT with a suitable choice of exchange-correlation

function is a reasonable approach to estimating the relaxation rates of real complexes. Following that LIESST phenomena in a number of Fe(II) spin crossover complexes, coordinated by monodentate, bidentate and multidentate ligands have been studied, with the goal to uncover the trend in the low-temperature relaxation rate. Out of 21 exchange-correlation functionals of six different kinds, we chose range-separated hybrid functional taking thermal spin transition temperature ($T_{1/2}$ as experimental input capturing the correct electronic HS-LS energy gap for each complex and hence employed to estimate relaxation rate. A nine-order-of-magnitude change in low-temperature relaxation rate is observed among the complexes. The trend is rationalized in terms of the change in metal-ligand covalency, numerically estimated by the crystal orbital Hamiltonian population, thus influencing the back donation or delocalization of the electrons from the low-lying Fe(II)-centered molecular orbital to the empty low-lying ligand-centered π^* antibonding molecular orbitals.

Chapter 5 : In this chapter, we investigate three metal-organic polymers with Fe^{2+} as TM ion and tetrazole-based organic ligands consisting of two, four, and six-carbon(C) linkers respectively. Experimentally, SCO compounds with two and six-C linker show hysteresis of width ($\Delta T_{1/2}$) 29K and 2K respectively with $T_{1/2}$ around 126K. This indicates that the cooperativity among Fe(II) centers must be different for the three polymers. Our motivation is to understand how cooperativity among Fe centers affects while we increase the length of the linkers. Banerjee et al. discussed the microscopic origin of cooperativity in the Fe-triazole system as the interplay of magnetic (J) and spin-dependent elastic interactions (E_v) existing between Fe centers.[51] Our calculations show that E_v for all the compounds are of anti-ferroelastic type and decrease as we move from two to four and six C- linker SCO compounds. J turns out to be anti-ferromagnetic showing a similar trend as that of E_v.

Chapter 6 : In this chapter, employing first-principles electronic structure calculations, we investigate the stability, electronic and magnetic properties of ordered, double transition metal-based, two-dimensional MXene compounds, $Ti_{3-x}Mo_xC_2$ (x = 0.5, 1, 1.5, 2, 2.5). Both unpassivated and compounds passivated with -OH or -O or -F are considered in o-MXene and i-MXene phases. All passivated compounds prefer an o-MXene phase with an antiferromagnetic ground state. Three narrow gap semiconducting compounds are identified, namely, $Ti_2MoC_2F_2$, $TiMo_2C_2F_2$ and $TiMo_2C_2(OH)_2$ for subsequent study of thermoelectric properties within the formalism of Boltzmann transport. Our study highlights the potential of $Ti_2MoC_2F_2$ as thermoelectric material with a ZT value higher than 1 within a large temperature range of 300-800 K upon p-type carrier doping. The ZT value of p-type $Ti_2MoC_2F_2$ is found to reach a high value of 3.1 and efficiency of $\sim$ 27 % at 800 K. To the best of our knowledge, while the double transition metal MXene, Mo_2TiC_2 has been synthesized, Ti_2MoC_2 has not been synthesized. Our exercise should motivate the experimental study of

this yet-to-be-synthesized MXene compound.

Chapter 7 : In this chapter, we investigate the influence of biaxial strain on group VI elemental 2D material of tellurium, which has been discussed for its potential in various applications. Considering realistic estimates of strain that may be imposed on monolayer Te through van der Waals heterostructing with other known 2D materials, we demonstrate that the structural, electrical, and thermal transport properties can get strongly influenced by strain. Importantly, through strain engineering, the thermoelectric performance of elemental 2D Te in p-type doping can be made comparable to that of the known binary or ternary layered compound at room temperature and can outperform the known binary or ternary layered compounds at high to moderate temperature. The ZT of monolayer Te is found to reach a value of 6.07 at 800 K under tensile strain, being larger than 2 for temperatures greater than 400 K. Our study provides a way to tune the thermoelectric properties of 2D Te for future applications.

Chapter 8 : In this chapter, we provide a summary of results obtained from our study of SCO compounds as well as thermoelectric compounds. In addition, the future scope of work has also been discussed here.

References

[1] N. A. Spaldin, "Fundamental materials research and the course of human civilization," *arXiv preprint arXiv:1708.01325*, 2017.

[2] N. R. Council *et al.*, "Materials and man's needs: Materials science and engineering–volume i, the history, scope, and nature of materials science and engineering," 1930.

[3] C. S. Smith, "Materials and the development of civilization and science: Empiricism and esthetic selection led to discovery of many properties on which material science is based.," *Science*, vol. 148, no. 3672, pp. 908–917, 1965.

[4] T. SAHA DASGUPTA, "Understanding and prediction of quantum materials via modelling and computation," *Bulletin of Materials Science*, vol. 44, no. 4, p. 270, 2021.

[5] L. Łukasiak and A. Jakubowski, "History of semiconductors," *Journal of Telecommunications and information technology*, no. 1, pp. 3–9, 2010.

[6] G. E. SMITH, "Jj thomson and the electron: 1897–1899 an introduction," *The chemical educator*, vol. 2, pp. 1–42, 1997.

[7] A. B. Garrett, "The discovery of the transistor: W. shockley, j. bardeen, and w. brattain," *Journal of Chemical Education*, vol. 40, no. 6, p. 302, 1963.

[8] G. E. Moore, "Cramming more components onto integrated circuits," *Proceedings of the IEEE*, vol. 86, no. 1, pp. 82–85, 1998.

[9] I. Tuomi, "The lives and death of moore's law," *First Monday*, 2002.
[10] K. Rupp and S. Selberherr, "The economic limit to moore's law," *IEEE Transactions on Semiconductor Manufacturing*, vol. 24, no. 1, pp. 1–4, 2010.
[11] A. Mann, "Nascent exascale supercomputers offer promise, present challenges," *Proceedings of the National Academy of Sciences*, vol. 117, no. 37, pp. 22623–22625, 2020.
[12] F. Capra, *The science of Leonardo: Inside the mind of the great genius of the Renaissance*. Anchor, 2008.
[13] C. J. Donahue, "Reimagining the materials tetrahedron," *Journal of Chemical Education*, vol. 96, no. 12, pp. 2682–2688, 2019.
[14] J.-F. Létard, P. Guionneau, and L. Goux-Capes, "Towards spin crossover applications," in *Spin Crossover in Transition Metal Compounds III*, 2004.
[15] M. Nihei, H. Tahira, N. Takahashi, Y. Otake, Y. Yamamura, K. Saito, and H. Oshio, "Multiple bistability and tristability with dual spin-state conversions in [fe (dpp) 2][ni (mnt) 2] 2· meno2," *Journal of the American Chemical Society*, vol. 132, no. 10, pp. 3553–3560, 2010.
[16] P. Gütlich, Y. Garcia, and H. A. Goodwin, "Spin crossover phenomena in fe (ii) complexes dedicated to professor fa cotton on occasion of his 70th birthday.," *Chemical Society Reviews*, vol. 29, no. 6, pp. 419–427, 2000.
[17] J. Linares, E. Codjovi, and Y. Garcia, "Pressure and temperature spin crossover sensors with optical detection," 2012.
[18] T. J. Seebeck, *Magnetische polarisation der metalle und erze durch temperatur-differenz*. No. 70, W. Engelmann, 1895.
[19] J. C. A. Peltier, *Nouvelles expériences sur la caloricité des courans électriques*. 1834.
[20] W. Thomson, "4. on a mechanical theory of thermo-electric currents," *Proceedings of the Royal society of Edinburgh*, vol. 3, pp. 91–98, 1857.
[21] L. Tzounis, "Organic thermoelectrics and thermoelectric generators (tegs)," *Advanced thermoelectric materials for energy harvesting applications*, p. 7, 2019.
[22] D. M. Rowe, *Thermoelectrics handbook: macro to nano*. CRC press, 2018.
[23] X. Shi, W. Zhang, L. Chen, and J. Yang, "Filling fraction limit for intrinsic voids in crystals: Doping in skutterudites," *Physical review letters*, vol. 95, no. 18, p. 185503, 2005.
[24] L. E. Bell, "Cooling, heating, generating power, and recovering waste heat with thermoelectric systems," *Science*, vol. 321, no. 5895, pp. 1457–1461, 2008.
[25] G. Mahan and B. Sales, "Thermoelectric materials: New approaches to an old problem.," *Physics Today*, vol. 50, no. 3, pp. 42–47, 1997.
[26] M. A. Halcrow, *Spin-crossover materials: properties and applications*. John Wiley & Sons, 2013.
[27] J. F. Létard, P. Guionneau, and L. Goux-Capes, *Spin Crossover in Transi-*

tion Metal Compounds I-III: Gütlich, P., Goodwinpp, H. Springer: Berlin, Germany, 2004.

[28] T. Saha-Dasgupta and P. M. Oppeneer, "Computational design of magnetic metal-organic complexes and coordination polymers with spin-switchable functionalities," *MRS bulletin*, vol. 39, no. 7, pp. 614–620, 2014.

[29] L. Cambi and L. Szegö, "Über die magnetische susceptibilität der komplexen verbindungen," *Berichte der deutschen chemischen Gesellschaft (A and B Series)*, vol. 64, no. 10, pp. 2591–2598, 1931.

[30] R. C. Stoufer, D. H. Busch, and W. B. Hadley, "Unusual magnetic properties of some six-coördinate cobalt (ii) complexes1electronic isomers," *Journal of the American Chemical Society*, vol. 83, no. 17, pp. 3732–3734, 1961.

[31] K. Madeja and E. König, "Zur frage der bindungsverhältnise in komplexverbindungen des eisen (ii) mit 1, 10-phenanthrolin," *Journal of Inorganic and Nuclear Chemistry*, vol. 25, no. 4, pp. 377–385, 1963.

[32] J. H. Askew and H. J. Shepherd, "Mechanochemical synthesis of cooperative spin crossover materials," *Chemical communications*, vol. 54, no. 2, pp. 180–183, 2018.

[33] S. Decurtins, P. Gütlich, C. Köhler, H. Spiering, and A. Hauser, "Light-induced excited spin state trapping in a transition-metal complex: The hexa-1-propyltetrazole-iron (ii) tetrafluoroborate spin-crossover system," *Chemical physics letters*, vol. 105, no. 1, pp. 1–4, 1984.

[34] A. Hauser, "Intersystem crossing in the [fe (ptz) 6](bf4) 2 spin crossover system (ptz= 1-propyltetrazole)," *The Journal of chemical physics*, vol. 94, no. 4, pp. 2741–2748, 1991.

[35] A. Hauser, "Intersystem crossing in fe (ii) coordination compounds," *Coordination Chemistry Reviews*, vol. 111, pp. 275–290, 1991.

[36] A. Hauser, "Intersystem crossing in iron (ii) coordination compounds: a model process between classical and quantum mechanical behaviour," *Comments on Inorganic Chemistry*, vol. 17, no. 1, pp. 17–40, 1995.

[37] A. Hauser, C. Enachescu, M. L. Daku, A. Vargas, and N. Amstutz, "Low-temperature lifetimes of metastable high-spin states in spin-crossover and in low-spin iron (ii) compounds: The rule and exceptions to the rule," *Coordination Chemistry Reviews*, vol. 250, no. 13-14, pp. 1642–1652, 2006.

[38] E. Buhks, G. Navon, M. Bixon, and J. Jortner, "Spin conversion processes in solutions," *Journal of the American Chemical Society*, vol. 102, no. 9, pp. 2918–2923, 1980.

[39] A. Hauser, A. Vef, and P. Adler, "Intersystem crossing dynamics in fe (ii) coordination compounds," *The Journal of chemical physics*, vol. 95, no. 12, pp. 8710–8717, 1991.

[40] S. Kitagawa, R. Kitaura, and S.-i. Noro, "Functional porous coordination polymers," *Angewandte Chemie International Edition*, vol. 43, no. 18, pp. 2334–2375, 2004.

[41] A. Ozarowski, Y. Shunzhong, B. R. McGarvey, A. Mislankar, and J. E. Drake, "Epr and nmr study of the spin-crossover transition in bis (4, 4'-bi-1, 2, 4-triazole) bis (thiocyanato) iron hydrate and bis (4, 4'-bi-1, 2, 4-triazole) bis (selenocyanato) iron hydrate. x-ray structure determination of fe (4, 4'-bi-1, 2, 4-triazole) 2 (secn) 2. cntdot. h2o," *Inorganic Chemistry*, vol. 30, no. 16, pp. 3167–3174, 1991.

[42] Y. Garcia, N. Adarsh, and A. D. Naik, "Crystal engineering of feii spin crossover coordination polymers derived from triazole or tetrazole ligands," *Chimia*, vol. 67, no. 6, pp. 411–411, 2013.

[43] Y. Garcia, V. Niel, M. C. Munoz, and J. A. Real, "Spin crossover in 1d, 2d and 3d polymeric fe (ii) networks," *Spin Crossover in Transition Metal Compounds I*, pp. 229–257, 2004.

[44] J. Krober, E. Codjovi, O. Kahn, F. Groliere, and C. Jay, "A spin transition system with a thermal hysteresis at room temperature," *Journal of the American Chemical Society*, vol. 115, no. 21, pp. 9810–9811, 1993.

[45] F. Setifi, E. Milin, C. Charles, F. Thetiot, S. Triki, and C. J. Gomez-Garcia, "Spin crossover iron (ii) coordination polymer chains: syntheses, structures, and magnetic characterizations of [fe (aqin) 2 (μ2-m (cn) 4)](m= ni (ii), pt (ii), aqin= quinolin-8-amine)," *Inorganic chemistry*, vol. 53, no. 1, pp. 97–104, 2014.

[46] C. Enachescu, N. Menendez, E. Codjovi, J. Linares, F. Varret, A. Stancu, *et al.*, "Static and light induced hysteresis in spin-crossover compounds: experimental data and application of preisach-type models," *Physica B: Condensed Matter*, vol. 306, no. 1-4, pp. 155–160, 2001.

[47] C. Baldé, W. Bauer, E. Kaps, S. Neville, C. Desplanches, G. Chastanet, B. Weber, and J. F. Létard, "Light-induced excited spin-state properties in 1d iron (ii) chain compounds," *European Journal of Inorganic Chemistry*, vol. 2013, no. 15, pp. 2744–2750, 2013.

[48] S. Schönfeld, C. Lochenie, P. Thoma, and B. Weber, "1d iron (ii) spin crossover coordination polymers with 3, 3'-azopyridine–kinetic trapping effects and spin transition above room temperature," *CrystEngComm*, vol. 17, no. 29, pp. 5389–5395, 2015.

[49] W. Bauer, C. Lochenie, and B. Weber, "Synthesis and characterization of 1d iron (ii) spin crossover coordination polymers with hysteresis," *Dalton Transactions*, vol. 43, no. 5, pp. 1990–1999, 2014.

[50] H. Banerjee, S. Chakraborty, and T. Saha-Dasgupta, "Design and control of cooperativity in spin-crossover in metal–organic complexes: A theoretical overview," *Inorganics*, vol. 5, no. 3, p. 47, 2017.

[51] H. Banerjee, M. Kumar, and T. Saha-Dasgupta, "Cooperativity in spin-crossover transition in metalorganic complexes: Interplay of magnetic and elastic interactions," *Physical Review B*, vol. 90, no. 17, p. 174433, 2014.

[52] J. R. Sootsman, D. Y. Chung, and M. G. Kanatzidis, "New and old concepts

in thermoelectric materials," *Angewandte Chemie International Edition*, vol. 48, no. 46, pp. 8616–8639, 2009.

[53] F. J. DiSalvo, "Thermoelectric cooling and power generation," *Science*, vol. 285, no. 5428, pp. 703–706, 1999.

[54] G. J. Snyder and E. Toberer, "Complex thermoelectric materials. materials for sustainable energy: a collection of peer-reviewed research and review articles from nature publishing group," *World Scientific2011*, pp. 101–110, 2011.

[55] M. Wagner, *Simulation of thermoelectric devices*. PhD thesis, 2007.

[56] L. Hicks and M. Dresselhaus, "Use of quantum-well superlattices to obtain a high figure of merit from nonconventional thermoelectric materials," *MRS Online Proceedings Library (OPL)*, vol. 326, 1993.

[57] L. D. Hicks and M. S. Dresselhaus, "Thermoelectric figure of merit of a one-dimensional conductor," *Physical review B*, vol. 47, no. 24, p. 16631, 1993.

[58] L. Sun, P. Jiang, H. Liu, D. Fan, J. Liang, J. Wei, L. Cheng, J. Zhang, and r. Shi, "Graphdiyne: A two-dimensional thermoelectric material with high figure of merit," *Carbon*, vol. 90, pp. 255–259, 2015.

[59] L.-D. Zhao, S.-H. Lo, Y. Zhang, H. Sun, G. Tan, C. Uher, C. Wolverton, V. P. Dravid, and M. G. Kanatzidis, "Ultralow thermal conductivity and high thermoelectric figure of merit in snse crystals," *nature*, vol. 508, no. 7496, pp. 373–377, 2014.

[60] L.-D. Zhao, G. Tan, S. Hao, J. He, Y. Pei, H. Chi, H. Wang, S. Gong, H. Xu, V. P. Dravid, *et al.*, "Ultrahigh power factor and thermoelectric performance in hole-doped single-crystal snse," *Science*, vol. 351, no. 6269, pp. 141–144, 2016.

[61] C. Chang, M. Wu, D. He, Y. Pei, C.-F. Wu, X. Wu, H. Yu, F. Zhu, K. Wang, Y. Chen, *et al.*, "3d charge and 2d phonon transports leading to high out-of-plane zt in n-type snse crystals," *Science*, vol. 360, no. 6390, pp. 778–783, 2018.

[62] A. T. Duong, V. Q. Nguyen, G. Duvjir, V. T. Duong, S. Kwon, J. Y. Song, J. K. Lee, J. E. Lee, S. Park, T. Min, *et al.*, "Achieving zt= 2.2 with bi-doped n-type snse single crystals," *Nature Communications*, vol. 7, no. 1, p. 13713, 2016.

[63] L.-D. Zhao, J. He, D. Berardan, Y. Lin, J.-F. Li, C.-W. Nan, and N. Dragoe, "Bicuseo oxyselenides: new promising thermoelectric materials," *Energy & Environmental Science*, vol. 7, no. 9, pp. 2900–2924, 2014.

[64] M. Samanta, S. N. Guin, and K. Biswas, "Ultrathin few layer oxychalcogenide bicuseo nanosheets," *Inorganic Chemistry Frontiers*, vol. 4, no. 1, pp. 84–90, 2017.

[65] T. Ghosh, M. Samanta, A. Vasdev, K. Dolui, J. Ghatak, T. Das, G. Sheet, and K. Biswas, "Ultrathin free-standing nanosheets of bi2o2se: room tem-

perature ferroelectricity in self-assembled charged layered heterostructure," *Nano letters*, vol. 19, no. 8, pp. 5703–5709, 2019.

[66] P. Ruleova, C. Drasar, P. Lostak, C.-P. Li, S. Ballikaya, and C. Uher, "Thermoelectric properties of bi2o2se," *Materials Chemistry and Physics*, vol. 119, no. 1-2, pp. 299–302, 2010.

[67] M. Samanta, T. Ghosh, S. Chandra, and K. Biswas, "Layered materials with 2d connectivity for thermoelectric energy conversion," *Journal of Materials Chemistry A*, vol. 8, no. 25, pp. 12226–12261, 2020.

[68] K. S. Novoselov, A. K. Geim, S. V. Morozov, D.-e. Jiang, Y. Zhang, S. V. Dubonos, I. V. Grigorieva, and A. A. Firsov, "Electric field effect in atomically thin carbon films," *science*, vol. 306, no. 5696, pp. 666–669, 2004.

[69] K. S. Novoselov, D. Jiang, F. Schedin, T. Booth, V. Khotkevich, S. Morozov, and A. K. Geim, "Two-dimensional atomic crystals," *Proceedings of the National Academy of Sciences*, vol. 102, no. 30, pp. 10451–10453, 2005.

[70] J. N. Coleman, M. Lotya, A. ONeill, S. D. Bergin, P. J. King, U. Khan, K. Young, A. Gaucher, S. De, R. J. Smith, *et al.*, "Two-dimensional nanosheets produced by liquid exfoliation of layered materials," *Science*, vol. 331, no. 6017, pp. 568–571, 2011.

[71] J. R. Harris and D. Scheffler, "Routine preparation of air-dried negatively stained and unstained specimens on holey carbon support films: a review of applications," *Micron*, vol. 33, no. 5, pp. 461–480, 2002.

[72] J. O. Sofo, A. S. Chaudhari, and G. D. Barber, "Graphane: A two-dimensional hydrocarbon," *Physical Review B*, vol. 75, no. 15, p. 153401, 2007.

[73] P. Vogt, P. De Padova, C. Quaresima, J. Avila, E. Frantzeskakis, M. C. Asensio, A. Resta, B. Ealet, and G. Le Lay, "Silicene: compelling experimental evidence for graphenelike two-dimensional silicon," *Physical review letters*, vol. 108, no. 15, p. 155501, 2012.

[74] M. Dávila, L. Xian, S. Cahangirov, A. Rubio, and G. Le Lay, "Germanene: a novel two-dimensional germanium allotrope akin to graphene and silicene," *New Journal of Physics*, vol. 16, no. 9, p. 095002, 2014.

[75] F.-f. Zhu, W.-j. Chen, Y. Xu, C.-l. Gao, D.-d. Guan, C.-h. Liu, D. Qian, S.-C. Zhang, and J.-f. Jia, "Epitaxial growth of two-dimensional stanene," *Nature materials*, vol. 14, no. 10, pp. 1020–1025, 2015.

[76] L. Li, Y. Yu, G. J. Ye, Q. Ge, X. Ou, H. Wu, D. Feng, X. H. Chen, and Y. Zhang, "Black phosphorus field-effect transistors," *Nature nanotechnology*, vol. 9, no. 5, pp. 372–377, 2014.

[77] F. Xia, H. Wang, and Y. Jia, "Rediscovering black phosphorus as an anisotropic layered material for optoelectronics and electronics," *Nature communications*, vol. 5, no. 1, pp. 1–6, 2014.

[78] Z. Zhu and D. Tománek, "Semiconducting layered blue phosphorus: a computational study," *Physical review letters*, vol. 112, no. 17, p. 176802, 2014.

[79] A. J. Mannix, X.-F. Zhou, B. Kiraly, J. D. Wood, D. Alducin, B. D. Myers, X. Liu, B. L. Fisher, U. Santiago, J. R. Guest, *et al.*, "Synthesis of borophenes: Anisotropic, two-dimensional boron polymorphs," *Science*, vol. 350, no. 6267, pp. 1513–1516, 2015.

[80] B. Feng, J. Zhang, Q. Zhong, W. Li, S. Li, H. Li, P. Cheng, S. Meng, L. Chen, and K. Wu, "Experimental realization of two-dimensional boron sheets," *Nature chemistry*, vol. 8, no. 6, pp. 563–568, 2016.

[81] Y. Gogotsi and B. Anasori, "The rise of mxenes," 2019.

[82] M. Khazaei, A. Mishra, N. S. Venkataramanan, A. K. Singh, and S. Yunoki, "Recent advances in mxenes: From fundamentals to applications," *Current Opinion in Solid State and Materials Science*, vol. 23, no. 3, pp. 164–178, 2019.

[83] M. Naguib, M. Kurtoglu, V. Presser, J. Lu, J. Niu, M. Heon, L. Hultman, Y. Gogotsi, and M. W. Barsoum, "Two-dimensional nanocrystals produced by exfoliation of Ti_3AlC_2," *Advanced materials*, vol. 23, no. 37, pp. 4248–4253, 2011.

[84] U. U. Rahman, M. Humayun, U. Ghani, M. Usman, H. Ullah, A. Khan, N. M. El-Metwaly, and A. Khan, "Mxenes as emerging materials: Synthesis, properties, and applications," *Molecules*, vol. 27, no. 15, p. 4909, 2022.

[85] C. Hu, C.-C. Lai, Q. Tao, J. Lu, J. Halim, L. Sun, J. Zhang, J. Yang, B. Anasori, J. Wang, *et al.*, "Mo 2 ga 2 c: a new ternary nanolaminated carbide," *Chemical Communications*, vol. 51, no. 30, pp. 6560–6563, 2015.

[86] V. Kamysbayev, A. S. Filatov, H. Hu, X. Rui, F. Lagunas, D. Wang, R. F. Klie, and D. V. Talapin, "Covalent surface modifications and superconductivity of two-dimensional metal carbide mxenes," *Science*, vol. 369, no. 6506, pp. 979–983, 2020.

[87] B. Anasori, M. Dahlqvist, J. Halim, E. J. Moon, J. Lu, B. C. Hosler, E. N. Caspi, S. J. May, L. Hultman, P. Eklund, *et al.*, "Experimental and theoretical characterization of ordered max phases Mo_2TiAlC_2 and $Mo_2Ti_2AlC_3$," *Journal of Applied Physics*, vol. 118, no. 9, p. 094304, 2015.

[88] Z. Liu, L. Zheng, L. Sun, Y. Qian, J. Wang, and M. Li, "$(Cr_{2/3}Ti_{1/3})_3AlC_2$ and $(Cr_{5/8}Ti_{3/8})_4AlC_3$: New max-phase compounds in Ti–Cr–Al–C system," *Journal of the American Ceramic Society*, vol. 97, no. 1, pp. 67–69, 2014.

[89] B. Anasori, Y. Xie, M. Beidaghi, J. Lu, B. C. Hosler, L. Hultman, P. R. Kent, Y. Gogotsi, and M. W. Barsoum, "Two-dimensional, ordered, double transition metals carbides (mxenes)," *ACS nano*, vol. 9, no. 10, pp. 9507–9516, 2015.

[90] Q. Tao, M. Dahlqvist, J. Lu, S. Kota, R. Meshkian, J. Halim, J. Palisaitis, L. Hultman, M. W. Barsoum, P. O. Persson, *et al.*, "Two-dimensional $Mo_{1.33}C$ mxene with divacancy ordering prepared from parent 3d laminate with in-plane chemical ordering," *Nature communications*, vol. 8, no. 1,

pp. 1–7, 2017.

[91] P. Gütlich and A. Hauser, "Thermal and light-induced spin crossover in iron (ii) complexes," *Coordination chemistry reviews*, vol. 97, pp. 1–22, 1990.

[92] M. Khazaei, M. Arai, T. Sasaki, C.-Y. Chung, N. S. Venkataramanan, M. Estili, Y. Sakka, and Y. Kawazoe, "Novel electronic and magnetic properties of two-dimensional transition metal carbides and nitrides," *Advanced Functional Materials*, vol. 23, no. 17, pp. 2185–2192, 2013.

[93] M. Khazaei, V. Wang, C. Sevik, A. Ranjbar, M. Arai, and S. Yunoki, "Electronic structures of imax phases and their two-dimensional derivatives: A family of piezoelectric materials," *Physical Review Materials*, vol. 2, no. 7, p. 074002, 2018.

[94] Z. M. Wong, T. L. Tan, S.-W. Yang, and G. Q. Xu, "Enhancing the photocatalytic performance of mxenes via stoichiometry engineering of their electronic and optical properties," *ACS applied materials & interfaces*, vol. 10, no. 46, pp. 39879–39889, 2018.

[95] E. C. Stoner, "Collective electron ferromagnetism ii. energy and specific heat," *Proceedings of the Royal Society of London. Series A. Mathematical and Physical Sciences*, vol. 169, no. 938, pp. 339–371, 1939.

[96] H. Kumar, N. C. Frey, L. Dong, B. Anasori, Y. Gogotsi, and V. B. Shenoy, "Tunable magnetism and transport properties in nitride mxenes," *ACS nano*, vol. 11, no. 8, pp. 7648–7655, 2017.

[97] J. Yang, X. Zhou, X. Luo, S. Zhang, and L. Chen, "Tunable electronic and magnetic properties of cr2m'c2t2 (m'= ti or v; t= o, oh or f)," *Applied Physics Letters*, vol. 109, no. 20, p. 203109, 2016.

[98] Q. Gao and H. Zhang, "Magnetic i-mxenes: a new class of multifunctional two-dimensional materials," *Nanoscale*, vol. 12, no. 10, pp. 5995–6001, 2020.

[99] P. Urbankowski, B. Anasori, T. Makaryan, D. Er, S. Kota, P. L. Walsh, M. Zhao, V. B. Shenoy, M. W. Barsoum, and Y. Gogotsi, "Synthesis of two-dimensional titanium nitride ti 4 n 3 (mxene)," *Nanoscale*, vol. 8, no. 22, pp. 11385–11391, 2016.

[100] M. Kurtoglu, M. Naguib, Y. Gogotsi, and M. W. Barsoum, "First principles study of two-dimensional early transition metal carbides," *Mrs Communications*, vol. 2, pp. 133–137, 2012.

[101] Z. Fu, Q. Zhang, D. Legut, C. Si, T. C. Germann, T. Lookman, S. Du, J. S. Francisco, and R. Zhang, "Stabilization and strengthening effects of functional groups in two-dimensional titanium carbide," *Physical Review B*, vol. 94, no. 10, p. 104103, 2016.

[102] P. Chakraborty, T. Das, D. Nafday, L. Boeri, and T. Saha-Dasgupta, "Manipulating the mechanical properties of ti 2 c mxene: Effect of substitutional doping," *Physical Review B*, vol. 95, no. 18, p. 184106, 2017.

[103] M. Khazaei, M. Arai, T. Sasaki, and C. Chung, "Y., venkataramanan ns, estili m., sakka y., kawazoe y," *Adv. Funct. Mater*, vol. 23, p. 2185, 2013.

[104] M. Khazaei, M. Arai, T. Sasaki, M. Estili, and Y. Sakka, "Two-dimensional molybdenum carbides: potential thermoelectric materials of the mxene family," *Physical Chemistry Chemical Physics*, vol. 16, no. 17, pp. 7841–7849, 2014.

[105] A. N. Gandi, H. N. Alshareef, and U. Schwingenschlögl, "Thermoelectric performance of the mxenes M_2CO_2 (M= Ti, Zr, or Hf)," *Chemistry of Materials*, vol. 28, no. 6, pp. 1647–1652, 2016.

[106] S. Kumar and U. Schwingenschlögl, "Thermoelectric performance of functionalized Sc_2C mxenes," *Physical Review B*, vol. 94, no. 3, p. 035405, 2016.

[107] D. S. Y. Z. B. L. Q. H. A. Z. Zhengyang Li, Libo Wang, "Synthesis and thermal stability of two-dimensional carbide mxene ti3c2," *Materials Science and Engineering B*, vol. 191, pp. 33–40, 2015.

[108] R. Liu and W. Li, "High-thermal-stability and high-thermal-conductivity ti3c2tx mxene/poly(vinyl alcohol) (pva) composites," *ACS Omega*, vol. 3, pp. 2609–2617, 2018.

[109] J. M. W. R. A. M. C. B. T. M. B. Raj Thakur, Armin VahidMohammadi and C. A. Carrero, "Insights into the thermal and chemical stability of multilayered v2ctx mxene," *Nanoscale*, vol. 11, pp. 10716–10726, 2019.

[110] H. Kim, B. Anasori, Y. Gogotsi, and H. N. Alshareef, "Thermoelectric properties of two-dimensional molybdenum-based mxenes," *Chemistry of Materials*, vol. 29, no. 15, pp. 6472–6479, 2017.

[111] Z. Jing, H. Wang, X. Feng, B. Xiao, Y. Ding, K. Wu, and Y. Cheng, "Superior thermoelectric performance of ordered double transition metal mxenes: $Cr_2TiC_2T_2$ (T= -OH or -F)," *The journal of physical chemistry letters*, vol. 10, no. 19, pp. 5721–5728, 2019.

[112] Z. Shi, R. Cao, K. Khan, A. K. Tareen, X. Liu, W. Liang, Y. Zhang, C. Ma, Z. Guo, X. Luo, *et al.*, "Two-dimensional tellurium: progress, challenges, and prospects," *Nano-Micro Letters*, vol. 12, no. 1, pp. 1–34, 2020.

[113] T. Fan, Z. Xie, W. Huang, Z. Li, and H. Zhang, "Two-dimensional non-layered selenium nanoflakes: facile fabrications and applications for self-powered photo-detector," *Nanotechnology*, vol. 30, no. 11, p. 114002, 2019.

[114] Z. Zhu, X. Cai, S. Yi, J. Chen, Y. Dai, C. Niu, Z. Guo, M. Xie, F. Liu, J.-H. Cho, *et al.*, "Multivalency-driven formation of te-based monolayer materials: a combined first-principles and experimental study," *Physical review letters*, vol. 119, no. 10, p. 106101, 2017.

[115] B. Wu, X. Liu, J. Yin, and H. Lee, "Bulk β-te to few layered β-tellurenes: indirect to direct band-gap transitions showing semiconducting property," *Materials Research Express*, vol. 4, no. 9, p. 095902, 2017.

[116] A. C. Neto, F. Guinea, N. M. Peres, K. S. Novoselov, and A. K. Geim, "The electronic properties of graphene," *Reviews of modern physics*, vol. 81, no. 1, p. 109, 2009.

[117] S. Lu, L. Miao, Z. Guo, X. Qi, C. Zhao, H. Zhang, S. Wen, D. Tang, and

D. Fan, "Broadband nonlinear optical response in multi-layer black phosphorus: an emerging infrared and mid-infrared optical material," *Optics express*, vol. 23, no. 9, pp. 11183–11194, 2015.

[118] H. Zhang, S. Lu, J.-l. Zheng, J. Du, S. Wen, D. Tang, and K. Loh, "Molybdenum disulfide (mos 2) as a broadband saturable absorber for ultra-fast photonics," *Optics express*, vol. 22, no. 6, pp. 7249–7260, 2014.

[119] Y. Wang, G. Qiu, R. Wang, S. Huang, Q. Wang, Y. Liu, Y. Du, W. A. Goddard, M. J. Kim, X. Xu, *et al.*, "Field-effect transistors made from solution-grown two-dimensional tellurene," *Nature Electronics*, vol. 1, no. 4, pp. 228–236, 2018.

[120] M. Amani, C. Tan, G. Zhang, C. Zhao, J. Bullock, X. Song, H. Kim, V. R. Shrestha, Y. Gao, K. B. Crozier, *et al.*, "Solution-synthesized high-mobility tellurium nanoflakes for short-wave infrared photodetectors," *ACS nano*, vol. 12, no. 7, pp. 7253–7263, 2018.

[121] T. I. Lee, S. Lee, E. Lee, S. Sohn, Y. Lee, S. Lee, G. Moon, D. Kim, Y. S. Kim, J. M. Myoung, *et al.*, "High-power density piezoelectric energy harvesting using radially strained ultrathin trigonal tellurium nanowire assembly," *Advanced Materials*, vol. 25, no. 21, pp. 2920–2925, 2013.

[122] J. Chen, Y. Dai, Y. Ma, X. Dai, W. Ho, and M. Xie, "Ultrathin β-tellurium layers grown on highly oriented pyrolytic graphite by molecular-beam epitaxy," *Nanoscale*, vol. 9, no. 41, pp. 15945–15948, 2017.

[123] Y. Xiang, S. Gao, R.-G. Xu, W. Wu, and Y. Leng, "Phase transition in two-dimensional tellurene under mechanical strain modulation," *Nano Energy*, vol. 58, pp. 202–210, 2019.

[124] Z. Gao, F. Tao, and J. Ren, "Unusually low thermal conductivity of atomically thin 2D tellurium," *Nanoscale*, vol. 10, no. 27, pp. 12997–13003, 2018.

[125] A. A. Balandin, S. Ghosh, W. Bao, I. Calizo, D. Teweldebrhan, F. Miao, and C. N. Lau, "Superior thermal conductivity of single-layer graphene," *Nano letters*, vol. 8, no. 3, pp. 902–907, 2008.

[126] X. Gu and R. Yang, "Phonon transport in single-layer transition metal dichalcogenides: A first-principles study," *Applied Physics Letters*, vol. 105, no. 13, p. 131903, 2014.

[127] C. Lin, W. Cheng, G. Chai, and H. Zhang, "Thermoelectric properties of two-dimensional selenene and tellurene from group-vi elements," *Physical Chemistry Chemical Physics*, vol. 20, no. 37, pp. 24250–24256, 2018.

[128] D. K. Sang, T. Ding, M. N. Wu, Y. Li, J. Li, F. Liu, Z. Guo, H. Zhang, and H. Xie, "Monolayer β-tellurene: a promising p-type thermoelectric material via first-principles calculations," *Nanoscale*, vol. 11, no. 39, pp. 18116–18123, 2019.

Chapter 2

Methodology

The present thesis deals with the modeling and simulation of two broad classes of materials, a) Spin Crossover (SCO) molecular materials exhibiting light-induced excited spin state trapping (LIESST) phenomena and coordination polymers exhibiting thermally activated spin transition, b) Layered 2D materials like MXene and tellurene exhibiting thermoelectric (TE) properties. In this chapter, we discuss the computational tools used to understand these complex materials and to predict their structure-property relationship. In the following we first provide a brief summary, followed by a detailed background of the methodology in the subsequent sections.

- SCO molecular complexes and coordination polymers
  - Calculation of relaxation rate of LIESST process in molecular materials as described in the previous chapter requires an accurate description of both ground and excited electronic states. Considering a model system we first tested the applicability of both wave function-based approaches such as complete active space self-consistent field (CASSCF) and complete active space second-order perturbation theory (CASPT2) and density functional theory (DFT) based approach of Time-Dependent DFT (TDDFT) to determine the rate constant. Based on this exercise, we next employ the TDDFT-based scheme with a suitable choice of exchange-correlation functional to explain the observed trend in the relaxation rate of the LIESST process for a range of SCO molecular complexes.
  - To explain the thermal spin transition behavior of tetrazole-based coordination polymers, we follow the model Hamiltonian approach proposed by Banerjee et al. We estimate magnetic exchange and spin-dependent elastic exchange interaction among SCO centers of different polymers from DFT calculations, serving as the parameters of the proposed model Hamiltonian.

- Two dimensional (2D) TE materials
  - Transport properties of layered materials are modeled within the framework of semi-classical Boltzmann transport theory under rigid band approximation and relaxation time approximation. Both electronic and lattice transport equations are solved by inputting the electronic and phonon band structure respectively calculated within DFT.

In the following, we present details of each technique along with the underlying methodology.

2.1 Many Body Hamiltonian

The microscopic description of the physical and chemical properties of materials composed of electrons and nuclei is governed by the kinetic energy of these components and the interactions (coulombic) among them. This ensemble of particles may be in the gas phase forming molecules and clusters or in a condensed phase forming crystalline or amorphous, homogeneous or heterogeneous solids and liquids. The most general form of the Hamiltonian of the system of N electrons and P nuclei (neglecting relativistic effect, magnetic field, and quantum electrodynamics for simplicity) is given by,

$$H = -\sum_{I=1}^{P} \frac{\hbar^2}{2M_I}\nabla_I^2 - \sum_{i=1}^{N} \frac{\hbar^2}{2m_i}\nabla_i^2 + \frac{e^2}{2}\sum_{i=1}^{N}\sum_{j\neq i}^{N} \frac{1}{|\mathbf{r_i} - \mathbf{r_j}|}$$
$$-e^2 \sum_{I=1}^{P}\sum_{i=1}^{N} \frac{Z_I}{|\mathbf{R_I} - \mathbf{r_i}|} + \frac{e^2}{2}\sum_{I=1}^{P}\sum_{J\neq I}^{P} \frac{Z_I Z_J}{|\mathbf{R_I} - \mathbf{R_J}|}, \tag{2.1}$$

where, $\mathbf{R} = \{\ \mathbf{R}_I\ \}$, I=1,...P, are P nuclear coordinates, and $\mathbf{r} = \{\ \mathbf{r}_i\ \}$, i=1,N, are a set of N electronic coordinates. Z_I and M_I are the P nuclear charges and masses respectively. m_i are the N electronic masses each of charge e.

The first and second terms of the Hamiltonian are kinetic energy terms of ion (T_n) and electrons (T_e) respectively. The coulomb interactions between electron-electron (V_{ee}), electron-ion (V_{ne}), and ion-ion (V_{nn}) are represented by the last three terms respectively. Therefore to obtain many body eigenstates or wave function $\Psi_i(\mathbf{r}, \mathbf{R})$ one needs to solve the following time independent Schrödinger's Equation:

$$H\Psi_i(\mathbf{r}, \mathbf{R}) = E_i\Psi_i(\mathbf{r}, \mathbf{R}) \tag{2.2}$$

Finding an exact analytical solution for the Eqn. (2.2) is possible only in a few cases like hydrogen atoms because it involves a large number of degrees of freedom

and coulomb interaction of many body natures making the above equation non-separable. Therefore to solve this Hamiltonian for real materials one needs to do approximations at different stages.

The first important approximation in simplifying the many-body problem is *Born-Oppenheimer (BO) Approximation* (1927).[1] As the mass M_I of the nuclei is much greater than the mass m_e of electrons (a ratio of 1836 to 1), nuclei move much slower compared to electrons and electrons can be considered to be moving in the field of nuclei which are apparently frozen with respect to the time scale of electrons. This approximation is also known as Adiabatic approximation, within which electronic and nuclear motion can be decoupled. Thus the electronic part of the Hamiltonian can be written for a fixed nuclei configuration as:

$$H_e = T_e + U_{ee} + V_{ne} + U_{nn} \tag{2.3}$$

where the last term U_{nn} is a constant term arising from ion-ion interaction, known as Madelung energy, and can be obtained classically.

BO approximation reduces the many-body Hamiltonian to many-electron Hamiltonian. Even after this simplification solving the eigenvalue problem for the Hamiltonian given in Eqn. (2.3) is challenging due to the interacting nature of the electrons. If two electrons with the same spin interchange positions, the wave function $\Psi(r_i)$ must change sign. This property is called "exchange" and is a manifestation of the Pauli exclusion principle. Furthermore, each electron is affected by the motion of other electrons which is known as the "correlation" property. *Independent electron approximation* is the next level approximation where electrons are considered as independent particles moving in the mean field created by the other electrons and the nuclei. Basically, it maps the interacting electrons into a system of non-interacting electrons that effectively resemble the original system. This is an appropriate description when the effects of exchange and correlation are not strong enough so that their effect can be treated in an average way.

There are two different approaches to such independent electron approximation. (a) The wave function based approach[2] as implemented in Hartree, [3], Hartree-Fock (HF)[4], configuration-interaction (CI)[5] methods. (b) The density-based approach as implemented in the Kohn-Sham density functional theory (DFT). [6–8] The main disadvantage of the wave function-based method is the heavy computational cost even for a simple system, which increases exponentially with system size for capturing the detailed wave function. On the other hand, DFT is much less expensive but provides a cruder description of electron correlation.

2.2 Wave function-based approach

2.2.1 Hartree Theory

The many-body Hamiltonian for a system of N interacting electrons under BO approximation can be written as,

$$H_e = T_e + V_{ne} + U_{ee} = \sum_{i=1}^{N} h(\mathbf{r}_i) + \frac{1}{2}\sum_{i\neq j}^{N} \frac{e^2}{r_{ij}}, \tag{2.4}$$

writing $|\mathbf{r}_i - \mathbf{r}_j| = r_{ij}$,
where,

$$h(\mathbf{r}) = -\frac{\hbar^2}{2m}\nabla^2 + V_{ne} = \frac{p^2}{2m} + V_{ne}, \tag{2.5}$$

and the many-body eigenvalue problem is written as,

$$H_e\Psi(\mathbf{r}_1\sigma_1, \mathbf{r}_2\sigma_2, ..., \mathbf{r}_N\sigma_N) = E\Psi(\mathbf{r}_1\sigma_1, \mathbf{r}_2\sigma_2, ..., \mathbf{r}_N\sigma_N), \tag{2.6}$$

where $\mathbf{r}_i$ σ_i are the space and spin variables for the i^{th} electron.

According to Hartree's theory proposed in 1928, the ground state wave-function of the N electron system can be expressed as a simple product of N orthonormal one-electron spin orbitals of the form,

$$\Psi(\mathbf{r}_1\sigma_1, \mathbf{r}_2\sigma_2, ..., \mathbf{r}_N\sigma_N) = \psi_1(\mathbf{r}_1\sigma_1)\psi_2(\mathbf{r}_2\sigma_2)...\psi_N(\mathbf{r}_N\sigma_N). \tag{2.7}$$

$\psi_i(\mathbf{r}\sigma)\} = \phi_i(\mathbf{r})\chi_i(\sigma)$ form the complete set of orthonormal spin orbitals, where $\phi_i(\mathbf{r})$ and $\chi_i(\sigma)$ are spatial orbitals and spin functions respectively, and σ could be either spin up α or spin down β. $\mathbf{r}_i$ σ_i are the space and spin variables for the i^{th} electron. Clearly, any given electron is assigned to some given spin-orbital.

The electronic charge density $\rho(\mathbf{r})$ corresponding to the Hartree wave function (2.12) is given by,

$$\rho(\mathbf{r}) = -e\sum_{j}^{occ} \phi_j^*(\mathbf{r})\phi_j(\mathbf{r}), \tag{2.8}$$

where the sum runs over all occupied spin orbitals, entering the ground state Ψ. The Coulomb Potential corresponding to the electronic charge density (2.7) is

$$V_{coul}(\mathbf{r}) = \sum_{j}^{occ} \int \phi_j^*(\mathbf{r}')\frac{e^2}{|\mathbf{r} - \mathbf{r}'|}\phi_j(\mathbf{r}')dr'. \tag{2.9}$$

We note that $V_{Coul}(\mathbf{r})$ is also known as Hartree potential $V_i^H(\mathbf{r})$. The physical significance of $V_i^H(\mathbf{r})$ is the following.

Each electron moves in the effective field corresponding to the Coulomb potential generated by the charge distribution of all the other (N-1) electrons; the effective field for any electron is given by the Hartree Potential. Thus the spin-orbitals entering the product wave function satisfy the Hartree equation.

$$[\frac{\mathbf{p}^2}{2m} + V_{ne} + V_i^H(\mathbf{r})]\psi_i = \epsilon_i\psi_i. \tag{2.10}$$

Here ϵ_i was introduced as a Lagrange multiplier in order to take the variation in wavefunction ψ_i, keeping in mind the orthonormality of wavefunctions. $\sum_i \epsilon_i$ denotes the total energy of the system which includes the electronic energy plus the ion-ion repulsion energy. Now the Hartree function can be determined in a self-consistent method. From a certain initial guess of the functions, $\psi_1, \psi_2, ...\psi_N$ one evaluates the space charge distribution as given in Eqn. (2.8), and the corresponding Hartree Potential as given in Eqn. (2.9). A new set of improved wave functions are then calculated by solving Hartree Eqn. (2.10). The corresponding Hartree Potential is used to again start a new cycle. This iterative process is repeated up to self-consistency of input and output functions and potentials.

2.2.2 Hartree-Fock Theory

In 1930 Slater and V. A. Fock independently pointed out that Hartree's theory does not obey the principle of antisymmetry of the wave function, which should be the case as electrons are fermions.[4] It was subsequently found that Slater determinant, a determinant of one-electron orbitals, first used by Heisenberg and Dirac in 1926, satisfies this antisymmetric property and will thus be appropriate wavefunction to be used rather than the product form of wavefunction used in Hartree theory. Thus taking together the Hartree type wave-functions to form a properly anti-symmetrized wave function for the system, we may write,

$$\Psi^{HF}(\{\mathbf{r}_i\}) = A\{\phi_1(\mathbf{r}_1)\phi_2(\mathbf{r}_2)...\phi_N(\mathbf{r}_N)\}, \tag{2.11}$$

where A is the anti-symmetrization operator,

$$A = \frac{1}{\sqrt{N!}}\sum_{i=1}^{N}(-1)^{p_i}P_i, \tag{2.12}$$

The sum extends over all the $N!$ permutations P_i of the electronic coordinates and $(-1)^{p_i}$ equals +1 or -1 for permutations of even or odd class with respect to the fundamental one. Ψ^{HF} is normalized to one provided the composing orbitals

$$\Psi^{HF}(\{\mathbf{r}_i\}) = \frac{1}{\sqrt{N!}} \begin{vmatrix} \phi_1(\mathbf{r}_1) & \phi_1(\mathbf{r}_2) & \cdots & \phi_1(\mathbf{r}_N) \\ \phi_2(\mathbf{r}_1) & \phi_2(\mathbf{r}_2) & \cdots & \phi_2(\mathbf{r}_N) \\ \cdot & \cdot & & \cdot \\ \cdot & \cdot & & \cdot \\ \cdot & \cdot & & \cdot \\ \phi_N(\mathbf{r}_1) & \phi_N(\mathbf{r}_2) & \cdots & \phi_N(\mathbf{r}_N) \end{vmatrix}$$

are orthonormal. Putting expression (2.12) into (2.11) Ψ^{HF} can be conveniently written in the determinantal form suggested by Slater,

where N is the total number of electrons. This has the required property since interchanging the position of two electrons is equivalent to interchanging the corresponding columns in the determinant, which changes its sign. It also shows that any two electrons with the same spin cannot be in the same spatial position, since the nodes of Ψ^{HF} occur whenever

$$\mathbf{r}_i \equiv \mathbf{r}_j.$$

The total energy with the Hartree-Fock wave function is

$$E^{HF} = \langle \Psi^{HF} | H_e | \Psi^{HF} \rangle,$$

$$E^{HF} = \sum_i^N \langle \phi_i | -\frac{\hbar^2 \nabla^2}{2m} + V_{ne}(\mathbf{r}) | \phi_i \rangle + \frac{e^2}{2} \sum_{i \neq j}^N \langle \phi_i \phi_j | \frac{1}{|\mathbf{r} - \mathbf{r}'|} | \phi_i \phi_j \rangle - \frac{e^2}{2} \sum_{i \neq j}^N \langle \phi_i \phi_j | \frac{1}{|\mathbf{r} - \mathbf{r}'|} | \phi_j \phi_i \rangle, \tag{2.13}$$

and Using variational principle, we obtain the single particle Hartree-Fock equations as follows,

$$[-\frac{\hbar^2 \nabla^2}{2m} + V_{ne}(\mathbf{r}) + V_i^H(\mathbf{r})]\phi_i(\mathbf{r})] - e^2 \sum_{j \neq i}^N \langle \phi_j | \frac{1}{|\mathbf{r} - \mathbf{r}'|} | \phi_i \rangle \phi_j(\mathbf{r}) = \epsilon_i \phi_i(\mathbf{r}). \tag{2.14}$$

The last term is called the exchange term which is not present in the Hartree equation. The exchange term describes the effects of exchange between electrons introduced in the Hartree-Fock wave function by construction.

We define the single-particle and total densities as,

$$\rho_i(\mathbf{r}) = |\phi_i(\mathbf{r})|^2,$$

$$\rho(\mathbf{r}) = \sum_i^N \rho_i(\mathbf{r}),$$

Then the Hartree term can be written as,

$$V_i^H(\mathbf{r}) = \sum_{j\neq i} \int \rho_j(\mathbf{r}') \frac{e^2}{|\mathbf{r}-\mathbf{r}'|} dr' = e^2 \int \frac{\rho(\mathbf{r}') - \rho_i(\mathbf{r}')}{|\mathbf{r}-\mathbf{r}'|} dr', \tag{2.15}$$

Now constructing the single-particle exchange as

$$\rho_i^X(\mathbf{r},\mathbf{r}') = \sum_{j\neq i} \frac{\phi_i(\mathbf{r}')\phi_i^*(\mathbf{r})\phi_j(\mathbf{r})\phi_j^*(\mathbf{r}')}{\phi_i(\mathbf{r})\phi_i^*(\mathbf{r})}, \tag{2.16}$$

single-particle HartreeFock equations take the form as,

$$[-\frac{\hbar^2\nabla^2}{2m} + V_{ne}(\mathbf{r}) + V_i^H(\mathbf{r}) + V_i^X(\mathbf{r})]\phi_i(\mathbf{r}) = \epsilon_i \phi i(\mathbf{r}). \tag{2.17}$$

Thus the exchange potential, in analogy to the Hartree Potential, is given by,

$$V_i^X(\mathbf{r}) = -e^2 \int \frac{\rho_i^X(\mathbf{r},\mathbf{r}')}{|\mathbf{r}-\mathbf{r}'|} dr'. \tag{2.18}$$

The Hartree and exchange potentials together give rise to the electron-electron interaction in the Hartree-Fock approximation with the following potential,

$$V_i^{HF}(\mathbf{r}) = e^2 \int \frac{\rho(\mathbf{r}')}{|\mathbf{r}-\mathbf{r}'|} dr' - e^2 \int \frac{\rho_i^X(\mathbf{r},\mathbf{r}') + \rho_i(\mathbf{r}')}{|\mathbf{r}-\mathbf{r}'|} dr', \tag{2.19}$$

This can be written with the help of Hartree-Fock density,

$$\rho_i^{HF}(\mathbf{r},\mathbf{r}') = \sum_j \frac{\phi_i(\mathbf{r}')\phi_i^*(\mathbf{r})\phi_j(\mathbf{r})\phi_j^*(\mathbf{r}')}{\phi_i(\mathbf{r})\phi_i^*(\mathbf{r})}, \tag{2.20}$$

as the following expression for electron-electron interaction potential,

$$V_i^{HF}(\mathbf{r}) = e^2 \int \frac{\rho(\mathbf{r})'}{|\mathbf{r}-\mathbf{r}'|} dr' - e^2 \int \frac{\rho_i^{HF}(\mathbf{r},\mathbf{r}')}{|\mathbf{r}-\mathbf{r}'|} dr'. \tag{2.21}$$

The first term represents the total Coulombic repulsion common for all states $\phi_i(\mathbf{r})$, while the second term gives the effect of fermionic exchange, and is different for each state $\phi_i(\mathbf{r})$. The flow chart for the algorithm of the Hartree-Fock self-consistent method is shown in Figure 2.1.

2.2.3 Post HF methods

The Hartree-Fock method replaces the explicit electron-electron interaction with an average interaction, called mean-field approximation.[2] The difference between the Hartree Fock energy (E_{HF}) and the exact (correlated) electronic energy at a certain basis is called correlation energy (E_{corr}), given by,

$$E_{corr} = E_{el} - E_{HF} \tag{2.22}$$

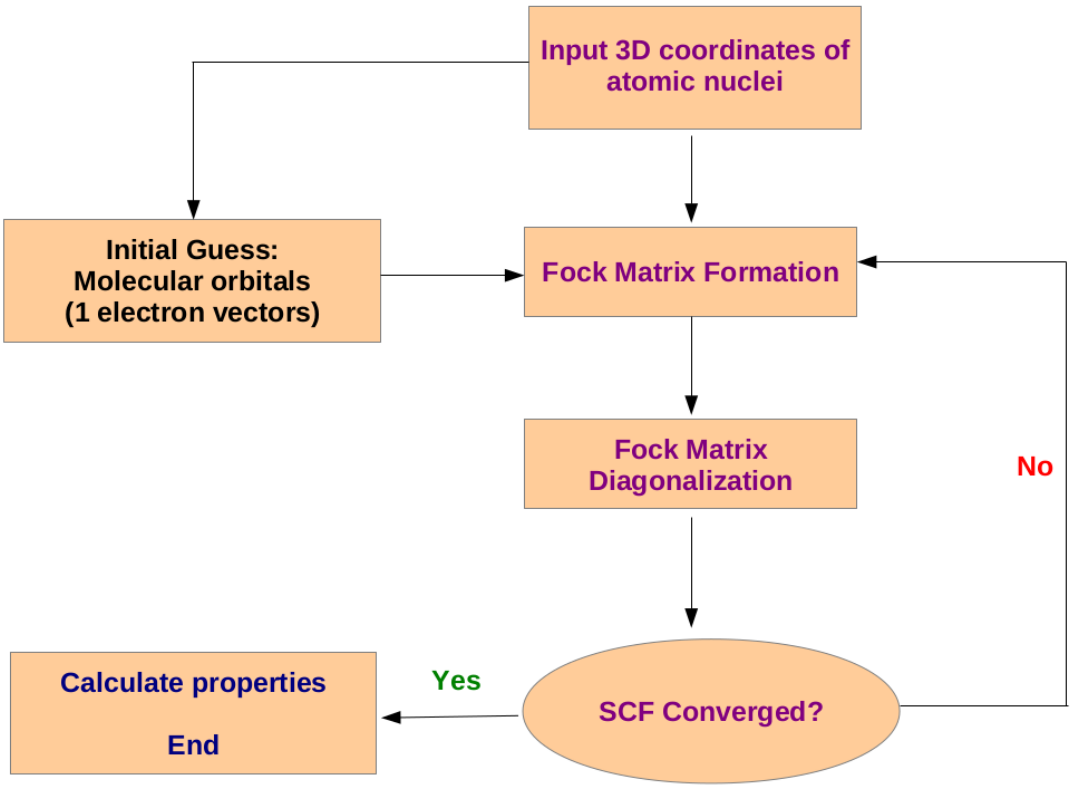

Figure 2.1: Algorithmic flowchart illustrating the Hartree−Fock method.

This correlation energy can be further separated into dynamic and static correlation. Static correlation is the correlation caused by the near degeneracy of orbitals in the valence space (e.g., d-orbitals of TM ions) while all other correlations are dynamic correlations. To retrieve some or all of the missing correlation energy, different post-Hartree-Fock methods have been established.

Configuration interaction

The primary idea of configuration interaction (CI) is to diagonalize the N-electron Hamiltonian in a basis of N electron functions.[2, 5] In other words, we represent the exact wave function as a linear combination of N-electron trial functions and use the linear variational method. The full form of the CI wave function can be given as

$$|\phi\rangle = c_0 |\psi_0\rangle + \sum_{ar} c_a^r |\psi_a^r\rangle + \sum_{\substack{a<b \\ r<s}} c_{ab}^{rs} |\psi_{ab}^{rs}\rangle + \sum_{\substack{a<b<c \\ r<s<t}} c_{abc}^{rst} |\psi_{abc}^{rst}\rangle + \cdots \tag{2.23}$$

where $|\psi_0\rangle$ is the closed-shell restricted Hartree-Fock (HF) determinant. Suppose we have solved HF equations in a finite basis set and obtained a set of $2k$ spin

orbitals $\{\chi_i\}$ and $2k > N$. $\{|\psi_a^r\rangle\}$ are the singly excited determinants which differ from $|\psi_0\rangle$ in having the spin-orbital χ_a replaced by χ_r meaning one electron occupied in χ_a orbital in the HF ground state has been promoted to χ_r, $|\psi_{ab}^{rs}\rangle$ are the doubly excited determinants, etc. Therefore there can be such ${}^{2k}C_N$ excited determinants formed from these spin orbitals but they can not form a complete N electron basis. However, diagonalizing the finite Hamiltonian matrix formed from this set of determinants leads to solutions that are exact within the one-electron subspace spanned by the $2k$ spin orbitals or, equivalently within the N-electron subspace spanned by the ${}^{2k}C_N$ determinants. This procedure is called *full* CI (FCI). But with an increase in system size i.e. no. of electrons and orbitals, it becomes computationally very expensive to calculate FCI energy for a system. To make the calculations computationally affordable, the FCI can be performed in a truncated space, such as the valence space, in Multi-configurational Self-Consistent Field (MCSCF) Theory.

Multi-configurational Self-Consistent Field (MCSCF)

In MCSCF theory,[9] the wave function is written as a linear combination of determinants of configuration state functions (CSFs), whose expansion coefficients are optimized simultaneously with the molecular orbitals (MOs) according to the variation principle. Thus, the MCSCF wave function may be written in the form

$$|\psi_{MCSCF}(\kappa, \mathbf{C}) = e^{-\hat{\kappa}} \sum_i C_i |i\rangle \tag{2.24}$$

where C_i are the configuration expansion coefficients (normalized to unity) and the operator $e^{-\hat{\kappa}}$ carries out the unitary transformations among the spin orbitals in the same way as for Hartree-Fock wave functions. The ground-state MCSCF wave function is obtained by minimizing the energy with respect to variational parameters.

$$E_{MCSCF} = min_{\kappa,\mathbf{C}} \frac{\langle \psi_{MCSCF}(\kappa, \mathbf{C}) | \hat{H} | \psi_{MCSCF}(\kappa, \mathbf{C}) \rangle)}{\langle \psi_{MCSCF}(\kappa, \mathbf{C}) | \psi_{MCSCF}(\kappa, \mathbf{C}) \rangle} \tag{2.25}$$

This model allows for a highly flexible description of the electronic system, where both the one-electron functions (the MOs) and the N-electron function (the configurations) may adapt to the physical situation. The MCSCF wave function is well suited to the systems where degenerate or nearly degenerate configurations are involved and it takes care of the static correlation. Such situations are usually encountered in the description of reaction processes where chemical bonds undergo drastic changes as observed during SCO, but sometimes also in ground-state molecular systems at the equilibrium geometry.

State-averaging MCSCF

State-average MCSCF (SA-MCSCF) methods optimize all states at the same time with respect to the averaged energy (E^{av}_{MCSCF}) of all states using the same set of c_i, and E^{av}_{MCSCF} can be given as

$$E^{av}_{MCSCF} = \sum_{i}^{k} \omega_i E_{MCSCF,i} = \sum_{i}^{k} \omega_i \langle \psi_{MCSCF,i} | \hat{H} | \psi_{MCSCF,i} \rangle. \tag{2.26}$$

where k is the number of states and ω_i is the weight of state i with

$$\sum_{i}^{k} \omega_i = 1 \tag{2.27}$$

The use of ω_i allows for determining the influence a given state has on the shared set of orbitals.

Complete Active Space Self-Consistent Field (CASSCF)

In the complete active space self-consistent field (CASSCF) method[10], the orbitals of the Hartee-Fock calculation are divided into active and inactive orbitals (Fig-2.2). The inactive ones retain their Hartree-Fock occupation value (either 2 or zero) while the active ones are used to generate a set of excited determinants that enter the calculation. This is done by performing a full CI within the subspace of active orbitals while keeping the inactive ones fixed. The chosen active space is commonly denoted as (n_{el}, n_{ψ})-CASSCF, where n_{el} is the number of electrons and n_{ψ} is the number of orbitals taken an active space. As a complete CI expansion is conducted in the active space, the size of the active space has to be limited to a small selection of orbitals. However, these orbitals should be able to describe the behavior of the system. With the use of CASSCF, we obtain a multi-configurational wavefunction that gives a qualitatively correct description of our system. This accounts for large parts of the static correlation but does not include the dynamical correlation. The method of choice to recover the missing correlation is perturbation theory.

Complete Active Space second-order perturbation theory (CASPT2)

CASSCF wavefunctions are subject to a full CI expansion in the chosen active space. Therefore, any electron correlation that occurs inside this active space is accounted for. Any electron-electron interaction that occurs between the inactive space and the active space or in the inactive space alone, is not considered. Perturbation theory can be applied to recover some of this missing correlation. In the specific case of second-order perturbation theory on a CASSCF wavefunction,

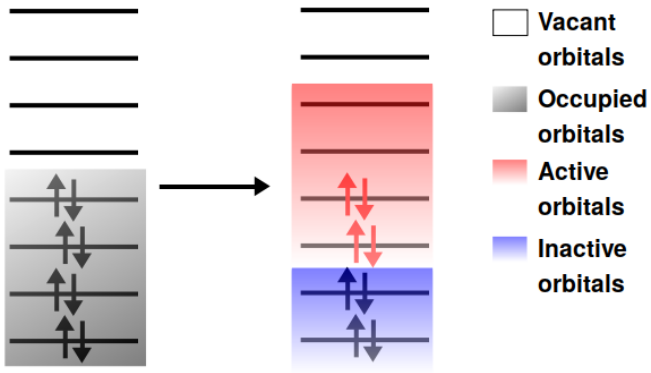

Figure 2.2: Example of (4 electrons, 4 orbitals) active space for CASSCF calculation generated from HF orbitals. HF orbital space has two parts one is vacant and the other is occupied. Occupied space can be divided into two one is active orbitals and other is inactive orbitals. Full CI is performed within active orbital space.

the corresponding method is termed complete active space second-order perturbation (CASPT2) theory.[11] In CASPT2, the Fock operators are projected onto the CASSCF reference space to describe $\widehat{H}_0$. Additionally, a so-called first-order interaction space (FOI) is defined, which includes all states that have non-zero matrix elements with the ground state reference. This FOI is then used to calculate the second-order energy correction according to the equation

$$E^{(2)} = \sum_{i<j}^{\chi_{\text{occ}}} \sum_{a<b}^{\chi_{\text{vir}}} \frac{\left\langle \psi_0 \middle| \widehat{H}' \middle| \psi_{ij}^{ab} \right\rangle \left\langle \psi_{ij}^{ab} \middle| \widehat{H}' \middle| \psi_0 \right\rangle}{E_0^{(0)} - E_{ij}^{ab}} \tag{2.28}$$

where χ_{occ} and χ_{vir} are the number of occupied and virtual orbitals, respectively. ψ_{ij}^{ab} denotes the doubly excited determinant where one electron has been promoted from the occupied spin orbitals χ_i and χ_j to the unoccupied orbitals χ_a and χ_b.E_{ij}^{ab} is the corresponding energy of this determinant. When using CASPT2, care has to be taken as some states in the FOI are almost isoenergetic to the reference state. When calculating the contribution of these so-called intruder states, the denominator is reduced to a very small number. To circumvent this problem, various shifting techniques exist, like the level shift. When using the level shift, a small shift value (l) is added to the denominator of the second-order energy correction:

$$E^{(2)} = \sum_{i<j}^{\chi_{\text{occ}}} \sum_{a<b}^{\chi_{\text{vir}}} \frac{\left\langle \psi_0 \middle| \widehat{H}' \middle| \psi_{ij}^{ab} \right\rangle \left\langle \psi_{ij}^{ab} \middle| \widehat{H}' \middle| \psi_0 \right\rangle}{E_0^{(0)} - E_{ij}^{ab} + l} \tag{2.29}$$

The influence of intruder states diminishes when using a sufficiently large level shift. It has to be kept in mind however that, setting a shift value influences all

contributions to the second-order energy correction on a different footing.

2.3 Density functional based approach

Prior to Hartree's (1928) and Hartree-Fock's (1930) theories, Thomas and Fermi (TF) (1927)[12, 13] proposed the idea of solving many-body problems using a density functional approach. They considered the electron density of non-interacting homogeneous electron gas as a basic variable. The reason is the following, a system with N_e number of electrons has many-body wave-function of $3N_e$ variables, $\Psi(r_1, r_2..., r_{N_e})$, whereas corresponding electron density given by, $\rho(\mathbf{r}) = N \int \Psi^*(\mathbf{r}, \mathbf{r}_2, ..., \mathbf{r}_N)\Psi(\mathbf{r}_1, \mathbf{r}_2, ..., \mathbf{r}_N)d\mathbf{r}_2 d\mathbf{r}_3 ... d\mathbf{r}_N$, has only 3 variables. r_i is the position vector of i-th electron. So dealing with wave function needs huge computational costs while dealing with electron density requires much lower computational costs due to the reduction of variables.

But there are several drawbacks in the TF model. Here the resulting expression for kinetic energy is approximate. Another source of error comes from complete negligence of electronic correlation. It also failed to predict bonding between atoms. In spite of these shortcomings, the TF model paved the way for the development of Density Functional Theory (DFT) to deal with many-electron problems in a more efficient way, making the most convenient choice for electronic structure calculations in condensed matter physics to date.

2.3.1 Reduced Density Matrices

The mathematical formulation of the density functional approach is presented in the following. The ground state electron density is given by

$$\rho(\mathbf{r}_1) = N \int \Psi^*(\mathbf{r}_1, \mathbf{r}_2, ..., \mathbf{r}_N)\Psi(\mathbf{r}_1, \mathbf{r}_2, ..., \mathbf{r}_N)d\mathbf{r}_2 d\mathbf{r}_3 ... d\mathbf{r}_N, \tag{2.30}$$

where $\Psi(\mathbf{r}_1, \mathbf{r}_2, ..., \mathbf{r}_N)$ is a many particle wave-function.

Then single-particle electron-ion interaction can be written as

$$\langle V_{ne} \rangle = \langle \Psi | \sum_i v(\mathbf{r}_i) | \Psi \rangle = \int d\mathbf{r} v(\mathbf{r})\rho(\mathbf{r}), \tag{2.31}$$

In a similar manner, two-electron electron-electron repulsion can be written as,

$$\langle V_{ee} \rangle = \langle \Psi | \frac{1}{2} \sum_{i,j} \frac{1}{\mathbf{r}_{ij}} | \Psi \rangle = \frac{1}{2} \int d\mathbf{r}_1 d\mathbf{r}_2 \frac{\Gamma_2(\mathbf{r}_1, \mathbf{r}_2)}{\mathbf{r}_{12}}, \tag{2.32}$$

where the $\Gamma_2(r_1, r_2)$ is the two-particle density representing joint probability of finding one electron in a volume $\mathrm{d}r_1$ at r_1 and another electron in a volume $\mathrm{d}r_2$

at r_2 and can be expressed as,

$$\Gamma_2(\mathbf{r}_1, \mathbf{r}_2) = N(N-1) \int \Psi^*(\mathbf{r}_1, \mathbf{r}_2, ..., \mathbf{r}_N)\Psi(\mathbf{r}_1, \mathbf{r}_2, ..., \mathbf{r}_N)d\mathbf{r}_3 d\mathbf{r}_4 ... d\mathbf{r}_N, \quad (2.33)$$

one may write the kinetic energy term comprising differential operators as,

$$T = -\langle\Psi|\frac{1}{2}\sum_i \nabla_i^2|\Psi\rangle,$$

$$= -\frac{1}{2}N \int \Psi^*(\mathbf{r}_1, \mathbf{r}_2, ..., \mathbf{r}_N)\nabla_1^2\Psi(\mathbf{r}_1, \mathbf{r}_2, ..., \mathbf{r}_N)d\mathbf{r}_1 d\mathbf{r}_2 ... d\mathbf{r}_N,$$

$$= -\frac{1}{2}N \int [\nabla_1^2\Psi^*(\mathbf{r}_1', \mathbf{r}_2, ..., \mathbf{r}_N)\Psi(\mathbf{r}_1, \mathbf{r}_2, ..., \mathbf{r}_N)]_{\mathbf{r}_1=\mathbf{r}_1'} d\mathbf{r}_1 d\mathbf{r}_2 ... d\mathbf{r}_N,$$

$$= -\frac{1}{2} \int d\mathbf{r}_1 [\nabla_1^2\gamma(\mathbf{r}_1, \mathbf{r}_1')]_{\mathbf{r}_1=\mathbf{r}_1'}, \quad (2.34)$$

where $\gamma(r_1, r_1')$ is first order reduced density matrix given by,

$$\gamma(\mathbf{r}_1, \mathbf{r}_1') = N \int \Psi^*(\mathbf{r}_1', \mathbf{r}_2, ..., \mathbf{r}_N)\Psi(\mathbf{r}_1, \mathbf{r}_2, ..., \mathbf{r}_N)d\mathbf{r}_2 d\mathbf{r}_3 ... d\mathbf{r}_N \quad (2.35)$$

The density matrix formalism can now be used to express the total energy of the system in terms of the above-mentioned Reduced Density Matrices (RDM) as,

$$E[\rho, \gamma, \Gamma_2] = T[\gamma(\mathbf{r}_1, \mathbf{r}_1')] + V_{ne}[\rho(\mathbf{r})] + Vee[\Gamma_2(\mathbf{r}_1, \mathbf{r}_2)], \quad (2.36)$$

and this leads to the possibility of developing a quantum mechanical formalism of many-electron systems in reduced space in terms of RDMs bypassing the wave-function formalism. A pre-requisite of the formalism is the possibility of directly determining the RDMs by minimizing the energy with respect to the RDMs for which the Pauli exclusion principle must be built into the RDMs. Also the existence of an anti-symmetric wave-function Ψ from which the RDMs can be constructed has to be guaranteed. This problem known as the N-representability problem must be solved by imposing necessary and sufficient conditions on $\gamma(\mathbf{r}_1, \mathbf{r}_1')$ and $\Gamma_2(\mathbf{r}_1, \mathbf{r}_2)$ which are yet unknown. The N-representability condition on $\rho(\mathbf{r})$ is given as,

$$\int \rho(\mathbf{r})d\mathbf{r} = N, \rho(\mathbf{r}) \geq 0 \quad (2.37)$$

Thus the single-particle density (simplest reduced quantity) emerges as a promising candidate for the formulation of quantum mechanics in reduced space.

2.3.2 The Hohenberg-Kohn Theorems

The foundation of DFT lies in the theorems proposed by Hohenberg and Kohn in 1964.[6]

H-K theorem I : There is one-to-one correspondence between the ground state density $\rho(r)$ of N_e electron system and external potential $v_{ext}(r)$ acting on it. It means for any system of interacting particles in an external potential $v_{ext}(r)$, the density is uniquely determined.

H-K theorem II: A universal functional for the energy $E[\rho]$ in terms of density $\rho(r)$ can be defined, as valid for any external potential. For any particular external potential, the exact ground state energy of the system is the global minimum value of this functional, and the density that minimizes the functional is the exact ground state density.

Proof of Theorem 1

Let us consider two external potentials $v_1(\mathbf{r})$ and $v_2(\mathbf{r})$ which differ from each other by an additive constant and give the same ground state density $\rho(\mathbf{r})$. As two different external potentials are different they would belong to different Hamiltonians, say, H_1 and H_2 respectively, which have different wave-functions Ψ_1 and Ψ_2. The variational principle tells us that no wavefunction can give rise to the energy that is less than the energy obtained from Ψ_1 for H_1. So

$$E_1 = \langle \Psi_1 | H_1 | \Psi_1 \rangle < \langle \Psi_2 | H_1 | \Psi_2 \rangle, \tag{2.38}$$

We assume here that the ground state is nondegenerate. Since we have identical ground state density for both of the Hamiltonians, Eqn. (2.15) can be rewritten as

$$E_1 < \langle \Psi_2 | H_1 | \Psi_2 \rangle = \langle \Psi_2 | H_2 | \Psi_2 \rangle + \langle \Psi_2 | H_1 - H_2 | \Psi_2 \rangle = E_2 + \int d\mathbf{r} \rho(\mathbf{r}) [v_1(\mathbf{r}) - v_2(\mathbf{r})]. \tag{2.39}$$

Hence

$$E_1 < E_2 + \int d\mathbf{r} \rho(\mathbf{r}) [v_1(\mathbf{r}) - v_2(\mathbf{r})], \tag{2.40}$$

on interchanging the suffices, one has,

$$E_2 < E_2 + \int d\mathbf{r} \rho(\mathbf{r}) [v_2(\mathbf{r}) - v_1(\mathbf{r})]. \tag{2.41}$$

Adding two inequalities Eqn.(2.17) and Eqn.(2.18) we have

$$E_1 + E_2 < E_2 + E_1. \tag{2.42}$$

which is absurd.

So our starting assumption was wrong and a given $\rho(r)$ can correspond to only one external potential $v(r)$. As $v(r)$ corresponding to a $\rho(r)$ is fixed, the Hamiltonian and hence the wave function are also fixed by the density. It proves *Hohenberg-Kohn's first theorem.*

Proof of Theorem 2

Since the wave function is a functional of density, the total energy functional $E_v[\rho]$ for a given external potential $v(\mathbf{r})$ can be written as,

$$E_v[\rho] = F[\rho] + \int \rho(\mathbf{r})v(\mathbf{r})d\mathbf{r},$$

where,

$$H = T_e + U_{ee} + V_{ne},$$

and,

$$F[\rho] = \langle \Psi[\rho]|T_e + U_{ee}|\Psi[\rho]\rangle$$

represents is a universal functional whose exact form is not known and it has no dependency on external potential.

Ground state energy is uniquely determined by the ground state density $\tilde{\rho}$. So,

$$E_v[\tilde{\rho}] = \langle \Psi[\tilde{\rho}]|H|\Psi[\tilde{\rho}]\rangle \tag{2.43}$$

Using variational principle a different density, ρ , gives higher energy ,

$$E_v[\tilde{\rho}] = \langle \Psi[\tilde{\rho}]|H|\Psi[\tilde{\rho}]\rangle < \langle \Psi[\rho]|H|\Psi[\rho]\rangle \tag{2.44}$$

It tells us that if we minimize the total energy *functional* by density $\rho(r)$ we should obtain ground state energy. The density that minimizes the energy is the ground state density. Although the Hohenberg-Kohn theorem is an "exact theory", in principle, for obtaining ground state properties of any system the main disadvantage is we do not know the exact form of the universal functional $F[\rho]$. If we would know the form of $F[\rho]$ we could solve electronic problems exactly.

2.4 Kohn-Sham Formulation

In 1965 Kohn and Sham[7] proposed a formulation that leads to the practical implementation of density functional theory based on the Hohenberg-Kohn theorem. Kohn and Sham proposed the idea of mapping an interacting many-body system into a fictitious non-interacting electron system having the same electron

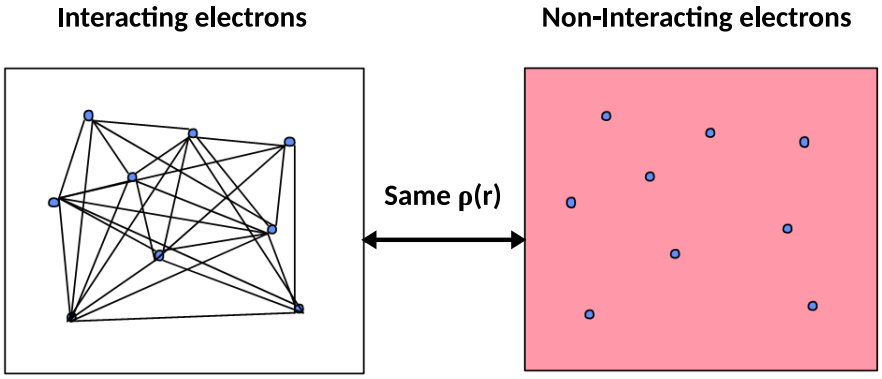

Figure 2.3: Mapping from interacting electron system of density $\rho(r)$ to a non-interacting system of same density using Kohn-Sham approximation. The figure is adapted from [14].

density as in the interacting system (cf. Fig. 2.3). Their formulation lead to a set of self-consistent equations known as Kohn-Sham equations.

For such non-interacting fictitious electrons the universal functional $F[\rho(\mathbf{r})]$ can be written as,

$$F[\rho(\mathbf{r})] = T_0[\rho(\mathbf{r})] + \frac{e^2}{2}\int\int \frac{\rho(\mathbf{r}_1)\rho(\mathbf{r}_2)}{\mathbf{r}_{12}} d\mathbf{r}_1 d\mathbf{r}_2 + E_{xc}[\rho(\mathbf{r})] \tag{2.45}$$

The exact kinetic energy functional of interacting electrons $T[\rho]$ is replaced by the kinetic energy of a system of non-interacting particles $T_0[\rho]$, the second term is the classical electrostatic contribution known as Hartree term E_{coul} and the last term $E_{XC}[\rho] = (V_{ee}[\rho] - E_{coul}[\rho]) + (T[\rho] - T_0[\rho])$, known as exchange-correlation (XC) energy and hence includes all the contribution for many body effect.

Hence one can write the energy functional as,

$$E[\rho] = T_0[\rho(\mathbf{r})] + \int v(\mathbf{r})\rho(\mathbf{r})d\mathbf{r} + \frac{e^2}{2}\int\int \frac{\rho(\mathbf{r}_1)\rho(\mathbf{r}_2)}{\mathbf{r}_{12}} d\mathbf{r}_1 d\mathbf{r}_2 + E_{xc}[\rho(\mathbf{r})] \tag{2.46}$$

Now to obtain the non-interacting K.E. functional $T_0[\rho]$ for a certain $\rho(\mathbf{r})$, one has to consider the solution of the one particle Schrödinger's equations,

$$[-\frac{1}{2}\nabla^2 + \lambda(\mathbf{r})]\psi_i = \epsilon_i\psi_i \tag{2.47}$$

with a suitable choice of $\lambda(\mathbf{r})$ the resulting orbitals produce the density as,

$$\rho(\mathbf{r}) = \sum_{\mathbf{i}} |\psi_{\mathbf{i}}|^{\mathbf{2}}$$

and henceforth evaluating the functional as,

$$T_0[\rho] = \sum_i \epsilon_i - \int d\mathbf{r}\lambda(\mathbf{r})\rho(\mathbf{r}) \tag{2.48}$$

The energy functional for determining equilibrium density then becomes,

$$E[\rho] = \sum_i \epsilon_i - \int d\mathbf{r}\lambda(\mathbf{r})\rho(\mathbf{r}) + \int v(\mathbf{r})\rho(\mathbf{r})d\mathbf{r} + E_{coul}[\rho] + E_{XC}[\rho] \tag{2.49}$$

The functional minimization produces,

$$\lambda(\mathbf{r}) = v(\mathbf{r}) + \frac{\delta E_{coul}[\rho]}{\delta\rho(\mathbf{r})} + \frac{\delta E_{XC}[\rho]}{\delta\rho(\mathbf{r})} \tag{2.50}$$

which clearly shows that if $\lambda(\mathbf{r})$ is chosen by the above expression, the correct density for the system will be obtained from the single particle Schrödinger's equation. Hence one arrives at a set of N-nonlinear integrodifferential equations known as *Kohn-Sham* equations, which are needed to be solved instead of many body Schrödinger's equations, given by,

$$[-\frac{1}{2}\nabla^2 + v_{eff}(\mathbf{r};\rho)]\psi_i = \epsilon_i\psi_i \tag{2.51}$$

where the effective potential can be written as

$$v_{eff}(\mathbf{r}) = v(\mathbf{r}) + \int \frac{\rho(\mathbf{r}')}{|\mathbf{r}-\mathbf{r}'|}d\mathbf{r}' + \frac{\delta E_{XC}}{\delta\rho(\mathbf{r})} = v(\mathbf{r}) + v_{coul}[\rho(\mathbf{r})] + \mathbf{v_{xc}}[\rho(\mathbf{r})] \tag{2.52}$$

The Kohn-sham equations are required to be solved in an iterative manner until self-consistency is reached. The procedure can be summarized as follows: One needs to start with an initial guess ρ_0, which can build up the initial KS equation. After solving the eigenvalue equation, a new density can be obtained and if the new density differs from the previous one by a threshold value then in the next step another new density is evaluated by mixing these two densities. The Hamiltonian for the next iteration will be produced by this density and it will again produce the density for this iteration and so on. The procedure will repeat until the densities of two consecutive steps produce the same solution within a specified error margin. The flowchart is shown in Fig. (2.4).

2.5 Exchange and Correlation

Although DFT is exact in principle, the crux of the matter lies in the fact that exact expressions for the XC energy and potential are yet unknown and these quantities are generally approximated. In practice, the utility of the theory lies in the approximations used for $E_{XC}[\rho]$.

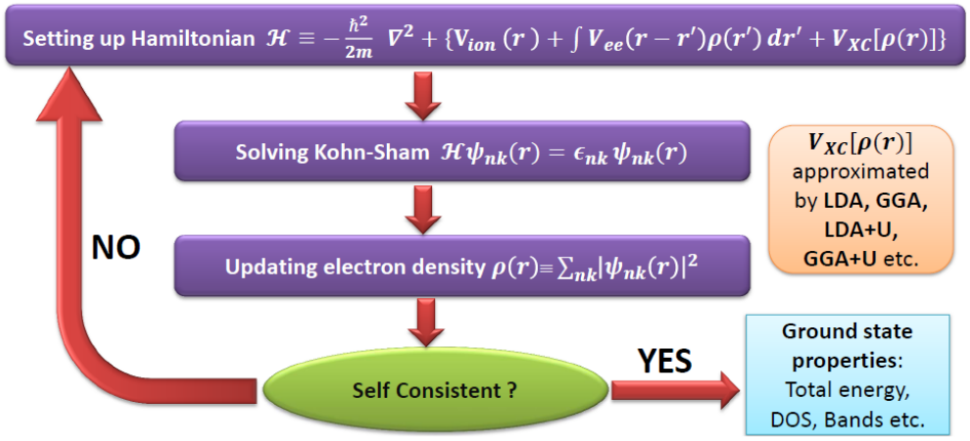

Figure 2.4: Algorithmic flowchart illustrating the iterative procedure to solve the Kohn-sham equations.

2.5.1 Local density approximation (LDA)

LDA is one of the simplest approximations made by Kohn and Sham [7], although its basic idea is rooted in the Thomas-Fermi-Dirac theory. [12, 13] Within this approximation, it is assumed that the exchange-correlation energy has only local dependence on electron density $\rho(\mathbf{r})$. The functional form can be written as

$$E_{XC}^{LDA} = \int \rho(\mathbf{r})\epsilon_{XC}[\rho(\mathbf{r})]d\mathbf{r} \tag{2.53}$$

where $\epsilon_{XC}[\rho(\mathbf{r})]$ corresponds to the exchange and correlation energy density of a homogeneous electron gas with density $\rho(\mathbf{r})$. In practice, within LDA the ϵ_{XC} can be calculated as the individual sum of contributions coming from the exchange and correlation part.

$$\epsilon_{XC}[\rho(\mathbf{r})] = \epsilon_X[\rho(\mathbf{r})] + \epsilon_C[\rho(\mathbf{r})]. \tag{2.54}$$

where the exchange part can be obtained from the Dirac's expression,

$$E_X[\rho(\mathbf{r})] = -C_X \int \rho^{\frac{4}{3}}(\mathbf{r})d\mathbf{r} \tag{2.55}$$

The functional form of the correlation part has been estimated by Ceperley-Alder [15] using numerical quantum Monte Carlo simulation for homogeneous electron gas which has turned out to be exact within numerical accuracy and further different parametrizations have been done by Perdew and Zunger [16], John P. Perdew and Yue Wang correlation (PWC) [17] etc. Though LDA was designed for

systems where the variation of charge density is slow, surprisingly the outcome is quite good even for non-homogeneous systems. [18] Main drawback of this approximation is the overestimation of bond energies and the underestimation of equilibrium bond length in comparison to experimental values.

2.5.2 Generalized gradient approximation (GGA)

In Generalized gradient approximation, the energy functional depends on the spatial variation (gradient) of the density,

$$E_{XC}[\rho] = \int \rho(\mathbf{r})\epsilon_{XC}[\rho(\mathbf{r})]d\mathbf{r} + \int F_{XC}[\rho(\mathbf{r}), \nabla\rho(\mathbf{r})]d\mathbf{r} \tag{2.56}$$

where F_{xc} is known as the enhancement factor which modifies the LDA expression. Conventionally GGA functionals are specified by combining the names for the corresponding exchange and correlation components. In the present thesis, the following exchange and correlation components have been used.

- Exchange
  - B: Beckes functional developed in 1988, which includes the Slater exchange along with corrections involving the gradient of the density [19].
  - O: Handys modification of Beckes exchange functional [20].
  - PBE: The functional by Perdew, Burke and Ernzerhof [21] proposed in 1996.
- Correlation
  - LYP: The correlation functional of Lee, Yang, and Parr, which includes both local and non-local terms [22].
  - P86: Gradient corrected Perdew local functional developed in 1981 [23, 24].

Apart from that there are few GGA functionals that are self-contained and are not combined with any other components such as Handys family of functionals including gradient-corrected correlation (HCTH/407).[20] GGA Functionals that contain empirical parameters whose values have been fitted to reproduce experiments or more accurate calculations are known as Chemists functionals. Examples are BLYP[22], BP86[23, 24], OLYP[25], HCTH[20]. On the other hand, functionals with no empirically determined parameters are known as Physicists functionals. e.g., PBE. Among several GGA functional, PBE functional [21] has

been widely used to calculate the ground state properties.

In comparison to LDA, GGA provides a better description of properties like binding energy, total energy, structural, and magnetic properties of real materials. But it fails to describe the long-range behavior ($1/R^6$) and provides the overestimated result for electric polarization in the polar system.

2.5.3 Beyond GGA functional

The general form of local and semilocal exchange-correlation (XC) energy functional depends on charge density, spin-up, spin-down densities, spin-up, and spin-down kinetic energy densities. In GGA, XC energy, ϵ_{XC} depends on spin densities and their gradients. ϵ_{XC} for beyond GGA functional may include the non-local Hartree Fock exchange term, semi-local correlation term, kinetic energy densities term, etc. which improve the performance of XC functional depending on the characteristic of the system. In Meta-GGA, ϵ_{XC} is a function of the second derivatives of the spin densities and the kinetic energy densities. Hybrid XC energy functionals include a contribution of the nonlocal HF exchange energy. Hybrid meta Functionals are hybrid functionals that contain kinetic energy density, in addition to Hartree-Fock exchange. In range-separated hybrid functionals the electron Coulomb interaction is divided into a short- and a long-range part by a switching function, usually an error function "erf". The double hybrid functional approach substitutes a fraction of the semilocal correlation energy in hybrid functionals with a nonlocal second-order Møller-Plesset (MP2) type correlation energy. In Chapter 4, we judge the performance of above mentioned different functionals by comparing the calculated ΔE^0_{HL} with experimentally determined estimates of ΔE^0_{HL}. The goal is to find a XC functional, that provides optimized performance for Spin-Crossover compounds. In the following sections, we briefly provide an overview of these functionals.

Meta GGA functional

In Meta-GGA functional, E_{XC} is also a function of the second derivatives of the spin densities $\nabla^2\rho_\sigma(r)$ and/or the kinetic energy densities $\tau_\sigma(r)$.

$$\tau_\sigma(r) = \sum_{i\sigma}^{occ.} f_{i\sigma}|\nabla\Psi_{i\sigma}(r)|^2 \tag{2.57}$$

where $f_{i\sigma}$: occupation number and $\Psi_{i\sigma}(r)$: spin-orbital of the i-th σ-type single-particle level of the Kohn-Sham (KS) non-interacting system, and the summation runs over the occupied spin orbitals. A few examples of meta GGA

functionals used in the present thesis are the following, a) TPSS: The exchange functional developed by Tao, Perdew, Staroverov, and Scuseria.[26] b) M06L known Minnesota functional proposed from the Truhlar group.[27] c) PKZB: The correlation functional developed by Perdew, Kurth, Zupan, and Blaha.[28, 29]

Hybrid functional

hybrid exchange energy functionals include a contribution (a_x) of the nonlocal HF exchange energy given by,

$$E_x^{HF}[\rho_\uparrow, \rho_\downarrow] = -\frac{1}{2}\sum_{\sigma=\uparrow,\downarrow}\sum_{i,j}^{occ}\int\int d\mathbf{r}_1 d\mathbf{r}_2 \psi_{i\sigma}^*(\mathbf{r}_1)\psi_{j\sigma}^*(\mathbf{r}_1)\frac{1}{r_{12}}\psi_{i\sigma}^*(\mathbf{r}_2)\psi_{j\sigma}^*(\mathbf{r}_2) \quad (2.58)$$

It explicitly depend on the occupied KS spin orbitals: $E_x^{HF}[\rho_\uparrow, \rho_\downarrow] \equiv E_x^{HF}[(\psi_{i\sigma})_{i\sigma\epsilon occ}]$ and can be written as

$$E_{xc}^{hyb}[\rho_\uparrow, \rho_\downarrow] = a_x E_x^{HF}[\rho_\uparrow, \rho_\downarrow] + (1 - a_x)E_x^{sem}[\rho_\uparrow, \rho_\downarrow] + E_c^{sem}[\rho_\uparrow, \rho_\downarrow] \quad (2.59)$$

where $a_x \epsilon [0, 1]$, and E_x^{sem} and E_c^{sem} are semilocal exchange and correlation functionals. Hybridization with Hartree-Fock (exact) exchange provides a simple scheme for improving the calculations of many molecular properties, such as atomization energies, bond lengths, and vibration frequencies. Several hybrid functionals have been developed. One of the popular hybrid functional is Becke Three-Parameter Hybrid Functionals (B3LYP)[30] which uses the LYP functional for non-local correlation, and VWN functional for local corrrelation. HF percentage (a_x) in B3LYP is 0.2. a_x is reduced to 0.15 in B3LYP*[31]. PBE0 [32, 33] and TPSSh is a hybrid version of GGA functional PBE and TPSS. PBE0 functional uses 25% exact exchange and 75% DFT exchange. X3LYP functional is proposed by Xu and Goddard.[34]

Hybrid meta functional

Hybrid functionals that contain kinetic energy density $\tau_\sigma(\mathbf{r})$, in addition to Hartree-Fock exchange E_X^{HF}. Here semi-local exchange term, $E_x^{sem} = E_x^{sem}[\rho_\uparrow(\mathbf{r}), \rho_\downarrow(\mathbf{r}), \tau_\uparrow(\mathbf{r}), \tau_\downarrow(\mathbf{r})]$. Minnesota functionals M06[35] and M05[36, 37] are examples of hybrid meta functionals having HF percentage (a_x) 0.27 and 0.28 respectively.

Range Separated Hybrid functional

These functionals separate the electron Coulomb interaction into a short- and a long-range part by a switching function, usually an error function "erf".

$$\frac{1}{r_{12}} = \frac{1-[\alpha+\beta erf(\omega r_{12})]}{r_{12}} + \frac{[\alpha+\beta erf(\omega r_{12})]}{r_{12}} \tag{2.60}$$

where first term represents the short range term $v_{ee}^{sr}(r_{12})$ and the second term represents the long range term $v_{ee}^{lr}(r_{12})$. ω denotes the range separation parameter and (α, β) ϵ [0,1] and $0 \leq (\alpha+\beta) \leq 1$. Now we consider two limiting conditions in the following: 1. for $r_{12} << 1/\omega$, $v_{ee}^{sr}(r_{12})$ dominates and $\sim (1-\alpha)/r_{12} \rightarrow 0$ 2. for $r_{12} >> 1/\omega$, $v_{ee}^{lr}(r_{12}) \sim (\alpha+\beta)/r_{12}$.

The splitting of the Coulomb operator allows for a partition of the exchange energy:

$$E_x[\rho_\uparrow, \rho_\downarrow] = E_x^{sr}[\rho_\uparrow, \rho_\downarrow] + E_x^{lr}[\rho_\uparrow, \rho_\downarrow] \tag{2.61}$$

where $E_x^{sr}[\rho_\uparrow, \rho_\downarrow] \sim$ local or semilocal functional and the $E_x^{lr}[\rho_\uparrow, \rho_\downarrow]$ is described by the HF exchange:

$$E_x^{lr}[\rho_\uparrow, \rho_\downarrow] = -\frac{1}{2}\sum_{\sigma=\uparrow,\downarrow}\sum_{i,j}^{occ}\int\int d\mathbf{r}_1 d\mathbf{r}_2 \psi_{i\sigma}^*(\mathbf{r}_1)\psi_{j\sigma}^*(\mathbf{r}_1)v_{ee}^{lr}\psi_{i\sigma}^*(\mathbf{r}_2)\psi_{j\sigma}^*(\mathbf{r}_2) \tag{2.62}$$

Examples of range-separated hybrid functionals are LC-BLYP,[38, 39] CAM-B3LYP.[40] In LC-BLYP scheme: $\alpha = 0$, $\beta = 1$, $\omega = 0.33\ bohr^{-1}$. Here, exchange potential has the correct -1/r_{12} asymptotic behavior. In CAM-B3LYP scheme: $\alpha = 0.19$, $\beta = 0.46$, $\omega = 0.33\ bohr^{-1}$. Here, $\alpha \neq 0$, so that there is a nonvanishing amount "α" of HF exchange at short range. Finally, an RSH XC energy functional is obtained by combining an RSH exchange energy functional with an unmodified semilocal correlation energy functional.

Double Hybrid functional

This approach substitutes in hybrid functionals a fraction (c_x) of the semilocal correlation energy by a nonlocal second-order Møller-Plesset (MP2) type correlation energy. The exchange energy for double hybrid functional is given by,

$$E_{xc}^{dbl-hyb}[\rho_\uparrow, \rho_\downarrow] = a_x E_x^{HF}[\rho_\uparrow, \rho_\downarrow] + (1-a_x)E_x^{sem}[\rho_\uparrow, \rho_\downarrow] + (1-a_c)E_c^{sem}[\rho_\uparrow, \rho_\downarrow] + a_c E_c^{MP2} \tag{2.63}$$

where (a_x , a_c) ϵ [0,1] and $E_c^{MP2}[\rho_\uparrow, \rho_\downarrow] \epsilon [0,1]$, the nonlocal MP2-like contribution, is given in spin-orbital form by

$$E_c^{MP2}[\rho_\uparrow, \rho_\downarrow] = E_c^{MP2}[(\psi_i)_{i\epsilon occ}, (\psi_a)_{a\epsilon virt}] = \frac{1}{4}\sum_{ij\epsilon occ}^{ab\epsilon virt}\frac{[(ia|jb) - (ib|ja)]^2}{\epsilon_i + \epsilon_j - \epsilon_a - \epsilon_b} \tag{2.64}$$

The labels i and j (respectively, a and b) are for the occupied (respectively, virtual) KS spin orbitals ($\psi_k \equiv \psi_{k\sigma}$) of energies ϵ_k (k = i,j, a,b), and $(ia|jb)$ is a two-electron repulsion integral in Mullikan notation.

For the evaluation of $E_c^{MP2}[\rho_\uparrow, \rho_\downarrow]$, the KS spin orbitals are first self-consistently determined using the hybrid XC energy functional defined by the first three terms of the right-hand side of the Eqn. (2.63)., then used for the evaluation of the nonlocal correlation contribution as given by the Eqn. (2.64). Double hybrid functionals used in the thesis are B2-PLYP[41] and mPW2-PLYP[42]. Their exchange and correlation (a_x, a_c) contributions are given by (0.53, 0.27) and (0.55, 0.25) respectively.

2.6 Basis Sets

The choice of the basis set depends on the specification of a given electronic structure problem. In the present thesis, we have used two kinds of basis sets methods, particularly

- For SCO molecular complexes: Gaussian type basis sets as implemented in Gaussian16 package [43]
- For coordination polymers and 2D TE materials: Plane wave based method as implemented in Vienna ab initio simulation package (VASP) [44]

A brief description of each method is provided in the following section.

2.6.1 Gaussian basis set

The concept of molecular orbitals as linear combinations of atomic orbitals (LCAO) suggests a natural set of basis functions: atomic orbital (AO)-type functions centered on each nucleus. One obvious choice is the exact hydrogen AOs, known as Slater-type orbitals (STO)-describing the radial component of the functions. However, the computation of the integrals is greatly simplified by using Gaussian-type orbitals (GTO) for basis functions. But Gaussian functions do not match the shape of an atomic orbital very well. In particular, GTOs are flat rather than steep near the atomic nucleus at $r = 0$, and they fall off more rapidly at large values of r. To tackle this problem, each STO is replaced with a number of Gaussian functions with different values for the exponential parameter. These Gaussian functions form a primitive Gaussian basis set. Linear combinations of the primitive Gaussians are formed to approximate the radial part of an STO. This linear combination is not optimized further in the energy variational calculation but rather is frozen and treated as a single function. The linear combination of primitive Gaussian functions is called a contracted Gaussian function. One of the examples of the Contracted Gaussian-type orbitals (CGTO) basis is the STO-nG basis. This n value represents the number of GTOs used to approximate the Slater Type orbital (STO) for both core and valence orbitals. A CGTO basis

function has the form shown in the following,

$$\psi^{CGTO}_{\zeta,l_x,l_y,l_z}(x,y,z) = N\sum_{i=1}^{n} c_i x^{l_x} y^{l_y} z^{l_z} e^{-\zeta_i r^2} \tag{2.65}$$

where N is a normalization constant, l_x, l_y, l_z determine the type of orbital, coefficients c_i are calculated with the basis set, not obtained variationally, ζ controls the width of the orbital (large ζ gives a tight function, small ζ gives a diffuse function). Figure 2.5 shows the improvement of the fit to Slater 1s function (ζ=1.0) obtained by increasing the number of Gaussian functions.

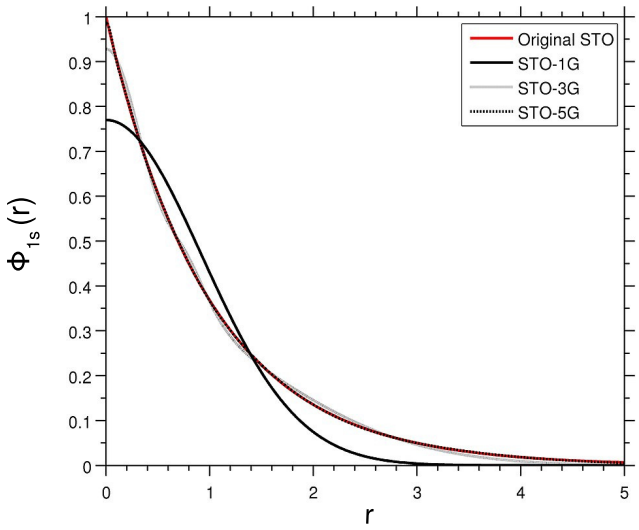

Figure 2.5: Comparison of the quality of least square fit of a 1s Slater function $\zeta = 1.0$ obtained at the STO-1G, STO-2G and STO-5G levels. The figure is adapted from Wikipedia

Minimal basis sets have one function per AO which can be STO, GTO, and CGTO. For example, the H atom has one basis set function i.e., 1s, C atom has five basis functions i.e., $1s$, $2s$, $2p_x$, $2p_y$ and $2p_z$. Minimal basis sets are not sufficient for accurate representation which brings up the need for multiple functions to represent each atomic orbital. The distribution of the electron density of valence electrons is better represented by the sum of two STOs of the same type but different "effective charges". This is known as a double-ζ basis set. These basis sets are associated with the split-valence feature. A split valance (SV) basis uses only one basis function for each core AO and a larger basis for the valance AOs. For example, the double-zeta basis set allows us to treat each orbital separately when we conduct the Hartree-Fock calculation. In the following, 2s atomic orbital

is approximated as a sum of two STOs ϕ_{2s}^{STO}.

$$\phi_i = a_1\phi_{2s}^{STO}(r,\zeta_1) + a_2\phi_{2s}^{STO}(r,\zeta_2) \tag{2.66}$$

The constants a_1 and a_2 determine how much each STO contributes to the final atomic orbital, which will vary depending on the type of atom that the atomic orbit (i.e., hydrogen and lithium orbitals will have different a_1, a_2, ζ_1, and ζ_2 values). Triple zeta (TZ) contains three basis functions per AO. Having different size exponential allows the orbital to change size with perturbations from approaching atoms. In the present thesis, triple zeta valance (TZV) basis sets[45] developed by Ahlrichs and coworkers have been used primarily for molecular calculations as implemented in Gaussian16 package[43].

2.6.2 The plane wave-based method

In the plane wave basis,[46] the Kohn-Sham wave function can be expanded as

$$\Psi_{ks}(\mathbf{r}) = e^{i\mathbf{k}.\mathbf{r}}\sum_G C_G(\mathbf{kr})e^{i\mathbf{G}.\mathbf{r}} \tag{2.67}$$

where $\mathbf{G}$ is the reciprocal lattice vector and $C_{(G)}(\mathbf{kr})$ is the plane wave coefficient with normalization condition $\sum_G |C_G(\mathbf{kr})|^2 = 1$. In reality, computational implementation needs a truncation of the sum up to a finite cut-off. The cut-off is defined in terms of plane wave kinetic energy cut-off as:

$$\hbar\frac{|\mathbf{k}+\mathbf{G}|^2}{2m_e} \leq E_{cut} \tag{2.68}$$

The physical quantities are calculated after checking the convergence in terms of energy cut-off. The main advantages of plane wave basis set are

- The basis set does not depend on the atomic positions and species.
- The forces acting on the atoms known as the Hellman-Feynman forces can easily be calculated and no basis set correction is required.
- It has the advantage of changing real space representation to momentum space representation using Fast Fourier transformation (FFT).

The main disadvantage of the plane wave basis set is that one needs a large number of plane waves to accurately describe the wave functions in the core region as the electrons in this region are tightly bound to the nucleus and the wave functions are highly oscillating due to the orthogonality constraints with the electrons in the valence state.

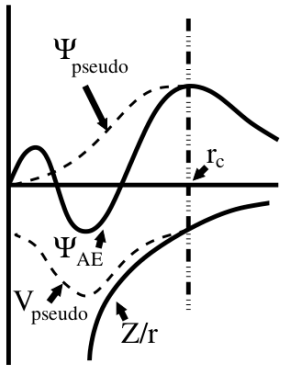

Figure 2.6: Comparison between all-electron (solid line) and pseudo (dashed line) wavefunction and potential. After a cutoff radius r_c, they match with each other. The picture is adapted from Wikipedia.

This difficulty can be overcome through the pseudopotential approximation. The basic idea of pseudopotential can be explained as follows. The actual potential is deep and attractive in the core region. Valence electrons gain kinetic energy due to the rapid oscillation in the core region, which behaves as repulsive potential. The valence wave functions can be considered as smooth nodeless pseudo wavefunction within the core region which is identical to the actual wavefunction outside the core region as shown in Fig. (2.3). Hence far fewer plane waves are required to describe the valence wave functions.

Various methods have been developed to construct more accurate and efficient pseudo-potentials (PS) in the last few decades. Three kinds of pseudopotentials exist which are widely used in electronic structure calculation using plane wave basis.

- **Norm conserving pseudopotential**
- **Ultrasoft pseudopotential**
- **Projector augmented wave (PAW) potential**

In the present thesis, we will be using PAW pseudopotentials for electronic structure calculations discussed in the following.

The Projector-Augmented-Wave (PAW) Formalism

The projector-augmented- wave (PAW) method was developed by P.E. Blöchl in 1994.[47] This method turned out to be a computationally elegant, transferable, and accurate method for electronic structure calculation and facilitates density functional theory calculations to be performed with greater computational efficiency. Later Kresse and Joubert modified this PAW method and

implemented it within the plane wave code of the Vienna Ab-initio Simulation Package(VASP).[44] Here also valence wave functions tend to have rapid oscillations near ion cores due to the requirement that they be orthogonal to core states; this situation is problematic because it requires many Fourier components to describe the wave functions accurately. The PAW approach addresses this issue by transforming these rapidly oscillating wave functions into smooth wave functions (by a linear transformation) which are more computationally convenient. This approach is somewhat reminiscent of a change from the Schrödinger picture to the Heisenberg picture.
In this formalism, the AE wave-function Ψ_n is derived from the PS wave-function $\tilde{\Psi}_n$ by means of a linear transformation:

$$|\Psi_n\rangle = |\tilde{\Psi}_n\rangle + \sum_i (|\phi_i\rangle - |\tilde{\phi}_i\rangle)\langle\tilde{p}_i|\tilde{\Psi}_n\rangle \tag{2.69}$$

The index i is a shorthand for the atomic site at $\mathbf{R}_i$. The all-electron partial waves ϕ_i are the solutions of the radial Schrödinger equation for the isolated atom. The PS partial waves $\tilde{\phi}_i$ are equivalent to the AE partial waves outside a core radius r_c. Of course, these two wave functions match both in value and slope at the boundary r_c^l. The projector function p_i for each PS partial wave localized within the core radius, obeys the relation $\langle\tilde{p}_i|\tilde{\phi}_j\rangle = \delta_{ij}$.
The PAW method is typically combined with the frozen core approximation, in which the core states are assumed to be unaffected by the ions' environment. There are several online repositories of pre-computed atomic PAW data.

2.7 Time Dependent Density Functional Theory (TDDFT)

Ground-state DFT deals with the systems subject to a static external potential, which are governed by the time-independent Schrödinger equation. However, there are many situations of interest that fall outside this category such as an atom or a molecule under the influence of an external electromagnetic field (like a laser field), electron or proton scattering, etc. These systems are correctly described by the time-dependent Schrödinger equation. TDDFT is an extension of ordinary ground-state DFT designed to solve such problems from a density functional perspective. The theoretical foundations of TDDFT were proposed by Runge and Gross[48] in 1984 and proved the time-dependent analogue of HK theorem[6] and developed a KS scheme[7] for the time-dependent case. The technique has now become a standard tool to estimate the excitation and optical absorption spectra of finite systems. how excited states are obtained using TDDFT will be described in the following.

Hohenberg-Kohn-Sham DFT is based on the Rayleigh-Ritz variation principle. In the case of a time-dependent external potential, however, no minimum principle exists. Instead, there is a stationary-action principle. The starting point for studying time-dependent systems is the Schrödinger equation

$$i\frac{\partial\Psi(\vec{r},t)}{\partial t} = \hat{H}\Psi(\vec{r},t) \tag{2.70}$$

where the Hamiltonian

$$\hat{H} = \hat{T} + \hat{V}_{ee} + \hat{v}(\vec{r},t) \tag{2.71}$$

is the same as that of the electronic Hamiltonian used previously except for the fact that now external potential i.e., ion-electron interaction term has a time dependence. Now to have an equivalent theorem for time-dependent systems like the HK theorem (Runge-Gross (RG) theorem), we require, a) The densities of the system evolve from a fixed initial state $\Psi(t_0) = \Psi_0$ (spatial argument are dropped for simplicity). The initial state, Ψ_0, is arbitrary, not necessarily be the ground-state or some other eigenstate of the initial potential $v(\vec{r},t_0) = v_0(\vec{r})$. b) The potentials are required to be Taylor expandable about t_0. This implies that only sudden switching is included in the formalism.

On the other hand, potentials that are switched on adiabatically from $t_0 = -\infty$ are automatically excluded by the Taylor-expandability condition. The RG theorem states that the densities $\rho(\vec{r},t)$ and $\rho'(\vec{r},t)$ evolving from the same initial state Ψ_0 under the influence of two potentials $v(\vec{r},t)$ and $v'(\vec{r},t)$ are always different provided that the potentials differ by more than a purely time-dependent function : $v(\vec{r},t) = v'(\vec{r},t) + C(t)$. Therefore there exists a one-to-one correspondence between the time-dependent external potential, $v(\vec{r},t)$, and the time-dependent electron density, $\rho(\vec{r},t)$, for systems evolving from a fixed initial many-body state. Similar to ordinary DFT, $\rho(\vec{r},t)$ determines the external potential and subsequently helps in obtaining the time-dependent many-body wavefunctions and hence all the time-dependent observables.

Time-Dependent Kohn-Sham Scheme

Time-dependent density can be calculated by considering a fictitious system of non-interacting electrons in which the electrons move in an effective time-dependent potential similar to the ground state DFT approach. This potential is unique by virtue of the RG theorem applied to the KS system. Thus the equation of motion is

$$i\frac{\partial}{\partial t}\phi_i(\vec{r},t) = \left\{-\frac{\nabla^2}{2} + v_{KS}(\vec{r},t)\right\}\phi_i(\vec{r},t) \tag{2.72}$$

The density of the interacting system can be obtained from the time-dependent KS orbitals

$$\rho(\vec{r},t) = \sum_{i}^{occ} |\phi_i(\vec{r},t)|^2 . \tag{2.73}$$

The KS equation above having the form of the one-particle equation, is relatively easier to solve numerically. Like the steady-state DFT, the KS potential, in this case, can be separated in the following way:

$$v_{KS}(\vec{r},t) = v(\vec{r},t) + v_{coul}(\vec{r},t) + v_{xc}[\rho;(\vec{r},t)] \tag{2.74}$$

where the terms have their usual meaning as described earlier. Next, our aim is to discuss the utility of the TDDFT approach to calculate excitation energies will be discussed in the following section.

Excited-States within TDDFT

The formal development of TDDFT as described in the previous section opened the way for a sound treatment of time-dependent properties in DFT. We are particularly interested in the properties involving the linear response of the charge density to an applied field[49] which allow us to study response properties such as dynamic polarizabilities as well as excitation energies and oscillator strengths calculated using the poles and residues of the dynamic polarizability.[49] This provides a formally well-founded treatment of excited states within TDDFT. The starting point is the time-dependent KS equation given by Eqn. (2.72). According to adiabatic local density approximation[50] the exchange-correlation potential in the Eqn. (2.72) is given by

$$v_{xc}[\rho;(\vec{r},t)] = \frac{\delta E_{xc}[\rho;(\vec{r},t)]}{\delta\rho;(\vec{r},t)} \tag{2.75}$$

where $E_{xc}[\rho;(\vec{r},t)]$ is the exchange-correlation energy functional from the TD theory. Now we consider a system initially in its ground electronic state. The linear response to a perturbation $v(t)$ turned on slowly at some time in the distant past is given by

$$\delta\rho(\vec{r},\omega) = \sum_{ij} \phi_i^{\dagger}(\vec{r})\delta P_{ij}(\omega)\phi_i(\vec{r}) \tag{2.76}$$

where $\delta P_{ij}(\omega)$ is the linear response of the KS/HF density matrix in the basis of unperturbed molecular orbitals. By writing the effective TD potential as

$$v^{eff}(t) = v^{appl}(\vec{r},t) + \delta v^{SCF}(\vec{r},t) \tag{2.77}$$

Here the field δv^{SCF} is the last two terms of the Hamiltonian in Eqn. (2.72). The response of the KS density matrix to the perturbation v^{eff} is then given by

the generalized susceptibility for a system of independent particles,

$$\frac{\partial P_{ij}}{\partial v^{eff}_{i'j'}} = \delta_{ii'}\delta_{jj'}\frac{f_j - f_i}{\omega - (\varepsilon_i - \varepsilon_j)} \tag{2.78}$$

Thus

$$\delta P_{ij}(\omega) = \frac{f_j - f_i}{\omega - (\varepsilon_i - \varepsilon_j)}\left[v^{appl}_{ij}(\omega) + \sum_{kl}\mathcal{K}_{ij,kl}\delta P_{kl}(\omega)\right] \tag{2.79}$$

where the coupling matrix $\mathcal{K}$ is the linear response of the self-consistent field to changes in the charge density,

$$\delta v^{SCF}_{ij}(\omega) = \sum_{kl}\mathcal{K}_{ij,kl}\delta P_{kl}(\omega) \tag{2.80}$$

$$\begin{aligned}\mathcal{K}_{ij,kl} =& \frac{\partial P_{ij}}{\partial v^{SCF}_{kl}} = \iint \phi^{\dagger}_i(\vec{r})\phi_j(\vec{r})\frac{1}{|\vec{r} - \vec{r}'|}\phi_k(\vec{r}')\,\phi^{\dagger}_l(\vec{r}')\,d\vec{r}d\vec{r}' \\ &+ \iiint\int \phi^{\dagger}_i(\vec{r})\phi_j(\vec{r})f_{xc}[\rho;(\vec{r},t)]\phi_k(\vec{r}')\,\phi^{\dagger}_l(\vec{r}')\,d\vec{r}d\vec{r}'\end{aligned} \tag{2.81}$$

where

$$f_{xc}[\rho;(\vec{r},t)] = \frac{\delta^2 E_{xc}[\rho;(\vec{r},t)]}{\delta^2[\rho;(\vec{r},t)]} \tag{2.82}$$

is the time-dependent exchange-correlation kernel. Solving Eqn. (2.79) for δP and separating the real imaginary parts one obtains after some algebra[51]

$$\left[\begin{pmatrix}\mathbf{A} & \mathbf{B}\\ \mathbf{B}^{\star} & \mathbf{A}^{\star}\end{pmatrix} - \omega\begin{pmatrix}1 & 0\\ 0 & -1\end{pmatrix}\right]\begin{pmatrix}\delta P\\ \delta P^{\star}\end{pmatrix} = \begin{pmatrix}-\delta v_{appl}\\ -\delta v^{\star}_{appl}\end{pmatrix} \tag{2.83}$$

where the matrices $\mathbf{A}$ and $\mathbf{B}$ are defined as

$$A_{ij,kl} = \delta_{ik}\delta_{jl}\,(\varepsilon_i - \varepsilon_k) + \mathcal{K}_{ij,kl} \tag{2.84}$$

and

$$B_{ij,kl} = \mathcal{K}_{ij,kl} \tag{2.85}$$

In the response theory, excitation energies correspond to the poles of the response function. So at the excitation energies $\omega = \omega_I = E_I - E_0, \delta P$ blows up. In Eqn. (2.83), as δP blows up at the excitation and δv_{appl} is finite, this implies that the matrix multiplying $\delta P, \delta P^{\star}$ should vanish, leading to zero eigenvalues on the left-hand side of Eqn. (2.83). Thus the excitation energies can be determined as solutions to the non-Hermitian eigenvalue problem

$$\begin{bmatrix}\mathbf{A} & \mathbf{B}\\ \mathbf{B} & \mathbf{A}\end{bmatrix}\begin{pmatrix}\mathbf{X}\\ \mathbf{Y}\end{pmatrix} = \omega\begin{bmatrix}1 & 0\\ 0 & -1\end{bmatrix}\begin{pmatrix}\mathbf{X}\\ \mathbf{Y}\end{pmatrix} \tag{2.86}$$

where $X_{ij} = \delta P_{ij}(\omega)$ and $Y_{ij} = \delta P_{ji}(\omega)$. In the lowest order, the excitation energies are obtained with a correction $\mathcal{K}_{ij,ij}$ to the Kohn-Sham transition energies $\omega_{ij} = \varepsilon_j - \varepsilon_i$, which follows from Eqn. (2.105). To date most applications of the time-dependent KS formalism fall into the linear response regime [52]. According to Tamm-Dancoff approximation (TDA)[53], which is usually implemented in many commercial codes for TDDFT calculation, the matrix B can be neglected, so that Eqn. (2.86) Finally is now simplified into an eigenvalue problem.

$$AX = \omega X \tag{2.87}$$

By solving eigenvalues and eigenvectors of matrix A, excitation energies and excitation states are therefore obtained accordingly.

2.8 Boltzmann Transport Theory

To study transport properties in complex materials and devices on experimental length scales, one often needs to consider large systems consisting of many millions or billions of atoms. To simulate such systems accurately and efficiently, two basic ingredients are needed. The first is a realistic description of the structure and electronic properties of the material of interest. This can be achieved by using ab initio electronic structure methods such as DFT.[6, 7] DFT has proven to be highly successful in describing the electronic, optical, and vibrational properties of a large number of materials. The second ingredient is an efficient numerical method for simulating electronic transport. There are several common approaches for simulating electronic transport,[54] including the Boltzmann transport equation, the Landauer-Buttiker formalism, and the Kubo formula. The Boltzmann transport equation is traditionally applied to the semiclassical regime of transport.[46, 55, 56] In this semiclassical picture, Each scattering process can be treated fully quantum mechanically, but between scattering events, the electrons behave as point particles. This semiclassical picture is appropriate in the limit $k_F l_e >> 1$, where l_e is the average distance between scattering events, $k_F = 2\pi/\lambda_F$, and λ_F is the Fermi wavelength of the electrons.

In the present thesis, we adopt the semi-classical Boltzmann transport theory for the quantitative description of thermoelectric effects under constant relaxation time approximation. Within the framework of linear response theory,[46, 57–59] it leads to a series of integrals that form a bridge between the quantum mechanical bandstructure resulting from DFT calculation, and the macroscopic electron transport properties which enable electrical transport properties to be computed from ab-initio calculations.

2.8.1 Boltzmann Transport Theory for electrical transport

Thermoelectric effects are non-equilibrium effects. The statistical description of the thermodynamic system not in the state of equilibrium is characterized by the Boltzmann transport equation (BTE). It is a semi-classical equation, which describes how an electron distribution over a phase space of position $\boldsymbol{r}$ and wave vector $\boldsymbol{k}$ changes with time. The phase-space distribution is defined by using a time-dependent probability density function $f(t, \nu, b, \boldsymbol{k}, \boldsymbol{r})$ such that $f(t, \nu, b, \boldsymbol{k}, \boldsymbol{r}) \times \mathrm{d}^3\boldsymbol{r}\mathrm{d}^3\boldsymbol{k}$ denotes the number of spin ν electrons in the b^{th} band, at time t, in a small phase space volume $\mathrm{d}^3\boldsymbol{r}\mathrm{d}^3\boldsymbol{k}$ about the point $(\boldsymbol{r}, \boldsymbol{k})$ in phase space. BTE for electrons is the equation of motion that describes the time evolution of f throughout the phase space. We assume that f is differentiable with respect to time t, wave vector $\boldsymbol{k}$, and position $\boldsymbol{r}$. The rate of change of f with time $\dot{f}$ is mainly controlled by three distinct processes: free movement or diffusion; interaction with external fields; and scattering,

$$\dot{f} = \dot{f}\Big|_{\text{free}} + \dot{f}\Big|_{\text{fields}} + \dot{f}\Big|_{\text{scatt.}} . \tag{2.88}$$

1. Free movement. If one imagines a single electron existing as a Bloch wave ψ, it will have a certain spatial density $(\psi^*\psi)$. The Bloch wave moves through space with a velocity is given by $\boldsymbol{v}_k = \hbar^{-1}\partial E/\partial \boldsymbol{k}$. Thus, if there is a spatial gradient in $f_{n,k}$, f will change over time as well

$$\dot{f}\Big|_{\text{free}} = -\boldsymbol{v}_{\boldsymbol{k}} \cdot \boldsymbol{\nabla}_{\mathbf{r}} f. \tag{2.89}$$

2. External Field Interactions. The Lorentz force due to external electric ($\mathbf{E}$) and magnetic ($\mathbf{H}$) field accelerate electrons and thereby change the corresponding $\boldsymbol{k}$ vectors according to:

$$\hbar\dot{\boldsymbol{k}} = \boldsymbol{e}\left(\mathbf{E} + \boldsymbol{v}_k \times \mathbf{H}\right). \tag{2.90}$$

   Hence, the occupation of different $\boldsymbol{k}$ points will change over time.

$$\dot{f}\Big|_{fields} = -\frac{e}{\hbar}(\mathbf{E} + \boldsymbol{v}(b, \boldsymbol{k}) \times \mathbf{H}) \cdot \nabla_k f, \tag{2.91}$$

   where $\mathbf{H}$ is the magnetic field strength, c is the speed of light, $\boldsymbol{v}$ is the group velocity of state $(b, \boldsymbol{k})$, and $\mathbf{E}$ is the electric field.

3. Scattering. Real materials have imperfections that scatter electrons. Even in a perfect crystal, electrons still scatter each other or be scattered by phonons. These scattering mechanisms are responsible for equilibrating the

system, and so they cannot be neglected. A scattering event will change the wave vector of an electron from $\boldsymbol{k}$ to $\boldsymbol{k}'$ or vice versa. Thus the scattering term is written as an integral over all wave vectors $\boldsymbol{k}'$ and bands b, with some transition functional $\mathfrak{P}$ which captures the probability of electrons transitioning from the state $(b, \boldsymbol{k})$ to $(b', \boldsymbol{k}')$, or vice versa:

$$\dot{f}(\boldsymbol{r}, b, \boldsymbol{k})\Big|_{\text{scatt.}} = \sum_{b'} \int \mathrm{d}\boldsymbol{k}' \mathfrak{P}_{in}\left(b', \boldsymbol{k}' \to b, \boldsymbol{k}\right) - \mathfrak{P}_{\text{out}}\ \left(b, \boldsymbol{k} \to b', \boldsymbol{k}'\right). \tag{2.92}$$

In principle, this transition function should include all possible scattering mechanisms and is a functional of the external fields and phase-space distribution itself f.

Putting all three processes together yields the Boltzmann Transport Equation for electrons in its most general form:

$$\dot{f}(t, b, \boldsymbol{k}, \boldsymbol{r}) = -\boldsymbol{v} \cdot \boldsymbol{\nabla}_{\boldsymbol{r}} f(t, b, \boldsymbol{k}, \boldsymbol{r}) - \frac{e}{\hbar}(\mathbf{E} + \boldsymbol{v} \times \mathbf{H}) \cdot \boldsymbol{\nabla}_{\boldsymbol{k}} f(t, b, \boldsymbol{k}, \boldsymbol{r}) + \dot{f}\Big|_{\text{scatt.}}. \tag{2.93}$$

Now one of the key components of BTE is the scattering term, and to make the equation tenable steps have to be taken to approximate this term.

Linearizing the Boltzmann Transport Equation

One of the first steps towards simplifying the BTE is to linearize it. At equilibrium $f(t, \nu, b, \boldsymbol{k}, \boldsymbol{r})$ will be the Fermi-Dirac distribution for the local chemical potential $\mu(\boldsymbol{r})$ and temperature $T(\boldsymbol{r})$:

$$f_0(\nu, b, \boldsymbol{k}, \boldsymbol{r}) = \frac{1}{1 + \exp\left[\frac{1}{k_B T}(\varepsilon(\nu, b, \boldsymbol{k}) - \mu(\boldsymbol{r}))\right]} \tag{2.94}$$

Since scattering restores the phase-space distribution f towards equilibrium, the corresponding term must vanish,

$$\dot{f}_0\Big|_{\text{scatt.}} = 0, \tag{2.95}$$

However, if the distribution f is very close to the equilibrium distribution,

$$f(t, \boldsymbol{k}, \boldsymbol{r}) = f_0(\boldsymbol{k}, \boldsymbol{r}) + \delta f(t, \boldsymbol{k}, \boldsymbol{r}), \tag{2.96}$$

For $\delta << 1$, BTE can be rewritten in terms of the equilibrium distribution f_0, and a time-dependent deviation δf. The free movement and external field interaction terms are approximated in terms of f_0 rather than f, whilst only the

lowest-order scattering term is taken. The scattering term is again written as an integral over all possible states $(b', \boldsymbol{k}')$.

If $\delta f(b, \boldsymbol{k})$ is positive, then the state $(b, \boldsymbol{k})$ is more likely to be occupied than it is in equilibrium. Thus electrons are likely to transition out of that wave vector and into a different one, reducing $f(b, \boldsymbol{k})$ in the process.

Similarly, if $\delta f\left(b', \boldsymbol{k}'\right)$ is positive, then electrons are more likely to transition out of $(b', \boldsymbol{k}')$, potentially into $(b, \boldsymbol{k})$.

The transition probability is quantified by a scattering time between the states $(b, \boldsymbol{k})$ and $(b', \boldsymbol{k}')$, weighted by the phase-distribution which captures if the state is occupied or not:

$$\dot{f}(b, \boldsymbol{k})\Big|_{\text{scatt.}} = \sum_{b'} \oint \mathrm{d}\boldsymbol{k}' \left\{\delta f\left(b', \boldsymbol{k}'\right) - \delta f(b, \boldsymbol{k})\right\} \times \tau_{b,k}^{b',k'}. \tag{2.97}$$

Eqn. (2.97) essentially says that the rate of change of $f(b, \boldsymbol{k})$ due to scattering is the sum of scattering rates into $(b, \boldsymbol{k})$, minus the sum of scattering rates out of $(b, \boldsymbol{k})$ to some other state $(b', \boldsymbol{k}')$. According to the principle of microscopic reversibility, scattering time function $\tau_{b,k}^{b',k'}$ must equal $\tau_{b',k'}^{b,k}$. If the scattering mechanism is known, for example, there is a known scattering potential $\mathcal{H}'$, then τ could potentially be calculated using Fermi's Golden Rule.

Adding the scattering term to the rest of the terms gives the full linearized Boltzmann transport equation:

$$\begin{aligned}\delta f(t, \boldsymbol{k}, \boldsymbol{r}) = &-\boldsymbol{v}_{\boldsymbol{k}} \cdot \boldsymbol{\nabla}_{\boldsymbol{r}} f_0(\boldsymbol{k}, \boldsymbol{r}) \\ &-\frac{e}{\hbar}(\mathbf{E} + \boldsymbol{v}_{\boldsymbol{k}} \times \mathbf{H}) \cdot \boldsymbol{\nabla}_{\boldsymbol{k}} f_0(\boldsymbol{k}, \boldsymbol{r}) \\ &+ \sum_{b'} \int \mathrm{d}\boldsymbol{k}' \left\{\delta f\left(b', \boldsymbol{k}'\right) - \delta f(b, \boldsymbol{k})\right\} \times \tau_{b,\boldsymbol{k}}^{b',\boldsymbol{k}'}.\end{aligned} \tag{2.98}$$

For steady-state solutions, the left-hand side vanishes giving:

$$\begin{aligned}\boldsymbol{v}(b, \boldsymbol{k}) \cdot \boldsymbol{\nabla}_{\boldsymbol{r}} f_0(b, \boldsymbol{k}, \boldsymbol{r}) + &\frac{e}{\hbar}\left(\mathbf{E} + \boldsymbol{v}_k \times \mathbf{H}\right) \cdot \boldsymbol{\nabla}_{\boldsymbol{k}} f_0(\boldsymbol{k}, \boldsymbol{r}) = \\ &\sum_{b'} \int \mathrm{d}\boldsymbol{k}' \left\{\delta f\left(b', \boldsymbol{k}'\right) - \delta f(b, \boldsymbol{k})\right\} \times \tau_{b,\boldsymbol{k}}^{b',\boldsymbol{k}'}.\end{aligned} \tag{2.99}$$

Relaxation Time Approximation

Electron scatting time function $\tau_{b,k}^{b',k'}$ can be estimated by calculation of electron-phonon scattering by computing deformation potentials. The Relaxation Time Approximation states that:

1. Scattering events always restore to the local equilibrium value for each state $f_0(b, \boldsymbol{k})$.

2. The scattering time which determines the rate of this restoration is independent of $f(b, \boldsymbol{k})$.

Both of these assumptions are generally appropriate when the phase-space distribution f is only a small perturbation δf from the local equilibrium phase-space distribution f_0, i.e. when using the linearized BTE Equation. Within the Relaxation Time Approximation, the scattering term simplifies to:

$$\dot{f}(b, \boldsymbol{k})\Big|_{\text{scatt.}} = -\frac{1}{\tau(b, \boldsymbol{k})}\delta f. \tag{2.100}$$

so the scattering term tends the phase-space distribution towards local equilibrium, with the timescale given by τ.

Linear Response Theory

BTE results in a series of integrals that can compute transport properties such as the electrical conductivity, and Seebeck coefficient leading to a quantitative description of the TE effect. Within the framework of linear response theory, particle and heat currents (j and j^q) manifest as a linear response to the gradient of the local temperature field ($\boldsymbol{\nabla} T$), the gradient of the chemical potential field ($\boldsymbol{\nabla}\mu$), and the electric field ($\mathbf{E}$) (Kubo Formalism). This gives a tensor equation between the currents $\boldsymbol{j}$ and $\boldsymbol{j}^q$, and the fields $\boldsymbol{\nabla} T$, $\boldsymbol{\nabla}\mu$, and $\mathbf{E}$, with the coefficients $L^{\alpha\beta}$ known as the L-matrices:

$$\begin{pmatrix} \mathbf{j} \\ \mathbf{j}_q \end{pmatrix} = \begin{bmatrix} \mathbf{L}^{11} & \mathbf{L}^{12} \\ \mathbf{L}^{21} & \mathbf{L}^{22} \end{bmatrix} \begin{pmatrix} e\mathbf{E} - \nabla\mu \\ -\nabla T \end{pmatrix}. \tag{2.101}$$

The L-matrices describe how gradients in temperature, chemical potential, and electrical potential fields are related to electron and thermal currents. If a material has a uniform temperature and chemical potential ($\boldsymbol{\nabla}\mu = \boldsymbol{\nabla} T = 0$), and an electric field is applied ($\mathbf{E} \neq 0$), then there will be a resulting electrical current given by

$$\mathbf{j} = \mathbf{L}^{11} e\mathbf{E}. \tag{2.102}$$

Thus the first L-matrix element is related to the electrical conductivity tensor by $e \times \mathbf{L}^{11} = \sigma$. Similarly, for a material with no applied electric or chemical potential field ($\boldsymbol{\nabla}\mu = \mathbf{E} = 0$), the thermal current follows

$$\mathbf{j}^q = -\mathbf{L}^{22}\nabla T. \tag{2.103}$$

Thus $\mathbf{L}^{22}$ is the thermal conductivity of the electrons. The other L-matrices $\mathbf{L}^{12}$ and $\mathbf{L}^{21}$ represent coupling terms between the electric & chemical potential fields, and the temperature field.

The Seebeck Effect: In the Seebeck experiment, no current is allowed to flow ($j = 0$), and a temperature gradient is applied. This leads to the equation:

$$\boldsymbol{j} = \mathbf{L}^{11}(e\mathbf{E} - \boldsymbol{\nabla}\mu) - \mathbf{L}^{12}\boldsymbol{\nabla}T = 0, \tag{2.104}$$

$$\Rightarrow \quad e\mathbf{E} - \boldsymbol{\nabla}\mu = \left[\mathbf{L}^{11}\right]^{-1}\mathbf{L}^{12}\boldsymbol{\nabla}T. \tag{2.105}$$

Eqn. (2.105) describes the Seebeck effect. If a material has an applied $\boldsymbol{\nabla}T$ but no current flows, then there will be a potential difference, the magnitude of which depends on the L-matrices. The Seebeck coefficient, or thermopower, is the linear coefficient relating gradients in the temperature ∇T and voltage ∇V;

$$\boldsymbol{\nabla}V = -\left(\frac{1}{e}\left[\mathbf{L}^{11}\right]^{-1}\mathbf{L}^{12}\right)\boldsymbol{\nabla}T = -\mathbf{S}\boldsymbol{\nabla}T, \tag{2.106}$$

$$\text{with} \quad \mathbf{S} = \frac{1}{e}\left[\mathbf{L}^{11}\right]^{-1}\mathbf{L}^{12}, \tag{2.107}$$

where $\mathbf{S}$ is a $(1,1)$ tensor usually given in microVolts per Kelvin. If the electrical properties of the material are isotropic, then Eqn. (2.105) and (2.107) become scalar equations. Eqn. (2.101) implies $\mathbf{j}_q$ will be non-zero, and a heat current must be maintained to keep the temperature gradient. This intuitively makes sense as otherwise, the material would equilibrate to a uniform temperature.

The Peltier Effect: If an electric current $\mathbf{j}$ is driven through a material that is maintained at a constant temperature then a heat current will be induced. This is the Peltier effect. Substituting $\boldsymbol{\nabla}T = 0$ into Eqn. (2.101) gives a relation for the Peltier coefficient Π:

$$\mathbf{j} = \mathbf{L}^{11}(e\mathbf{E} - \boldsymbol{\nabla}\mu) \neq 0, \tag{2.108}$$

$$e\mathbf{E} - \boldsymbol{\nabla}\mu = \left[\mathbf{L}^{11}\right]^{-1}\mathbf{j}, \tag{2.109}$$

$$\Rightarrow \quad \mathbf{j}_q = \mathbf{L}^{21}\left[\mathbf{L}^{11}\right]^{-1}\mathbf{j}, \tag{2.110}$$

$$\Rightarrow \quad \mathbf{j}_q = \Pi\mathbf{j}, \tag{2.111}$$

$$\text{with} \quad \Pi = \mathbf{L}^{21}\left[\mathbf{L}^{11}\right]^{-1} \tag{2.112}$$

Computing the L-matrices

If the band structure of a material is known, then the L-matrices can be computed by using expressions derived from the Boltzmann transport equation. These expressions are the bridge that connects electron transport properties to the band structure of the material. A brief summary of how these expressions are derived is given here.

The electronic current density j_i at point $\boldsymbol{r}$ in the direction $\hat{i}$ can be written as a sum over all states $(b, \boldsymbol{k})$, weighted by the group velocity v_i and the phase-space distribution f of each state:

$$j_i(\boldsymbol{r}) = e \sum_b \oint \mathrm{d}^3\boldsymbol{k} f(b, \boldsymbol{r}, \boldsymbol{k}) \times v_i(b, \boldsymbol{k}). \tag{2.113}$$

For a periodic crystal, the group velocity $\boldsymbol{v} = \hbar^{-1}\nabla_{\boldsymbol{k}}\varepsilon(b, \boldsymbol{k})$ is the derivative of a function which is periodic in k. As a result, the integral from filled bands must vanish, leading to the expected result that only partially filled bands contribute to the electrical current.

The thermal current density due to electrons j_i^q is given by the flow of electrons, weighted by their energy relative to the chemical potential μ. Electrons with energy ε greater than μ will transfer heat in the same direction they travel, and vice versa.

$$j_i^q(\boldsymbol{r}) = \sum_b \oint \mathrm{d}^3\boldsymbol{k} \left[\varepsilon_b(\boldsymbol{k}) - \mu\right] f(b, \boldsymbol{r}, \boldsymbol{k}) v_i(b, \boldsymbol{k}). \tag{2.114}$$

Within the linearized Boltzmann Transport Equation, the relaxation time approximation, and assuming the scattering time function only depends on the energy of states ($\tau(b, \boldsymbol{k}) = \tau(\varepsilon(b, \boldsymbol{k}))$), the phase-space distribution function f must satisfy:

$$f(b, \boldsymbol{r}, \boldsymbol{k}) = f_0(b, \boldsymbol{r}, \boldsymbol{k}) + \tau(\varepsilon(b, \boldsymbol{k})) \left(-\frac{\partial f}{\partial \varepsilon}\right) \boldsymbol{v}(b, \boldsymbol{k}) \cdot \left[e\boldsymbol{E} - \boldsymbol{\nabla}\mu + \frac{\varepsilon(b, \boldsymbol{k}) - \mu}{T}(-\nabla T)\right]. \tag{2.115}$$

Solving Eqns. (2.113)-(2.115) returns relationships for the L-matrices. To quantify the contribution of each state $(b, \boldsymbol{k})$ to transport properties, we define electron-conductance tensor $\phi(b, \boldsymbol{k})$ as:

$$\phi_{ij}(b, \boldsymbol{k}, \boldsymbol{r}) = \tau(b, \boldsymbol{k}) v_i(b, \boldsymbol{k}) v_j(b, \boldsymbol{k}) \left(-\frac{\partial f}{\partial \varepsilon}\right), \tag{2.116}$$

where $\partial f / \partial \varepsilon$ is the rate of change of the Fermi Dirac distribution for the local temperature $T(\boldsymbol{r})$ and chemical potential $\mu(\boldsymbol{r})$ at energy $\varepsilon(b, \boldsymbol{k})$, v_i is the band group velocity for state $(b, \boldsymbol{k})$ along the direction $\hat{i}$. The τ and $v_i v_j$ terms are

related to the mobility of electrons in a state, while the $-\partial f/\partial\varepsilon$ term quantifies how populated the state $(b, \boldsymbol{k})$ is; quantifying the idea that fully populated, or completely unpopulated states do not contribute towards transport. All the equations for the L-matrices involve the electron-conductance tensor:

$$L_{ij}^{(11)} = e \sum_b \oint \frac{\mathrm{d}^3\boldsymbol{k}}{4\pi^3} \phi_{ij}(b, \boldsymbol{k}, \boldsymbol{r}), \tag{2.117}$$

$$L_{ij}^{(21)} = \frac{T}{e} L_{ij}^{(12)} = \sum_b \oint \frac{\mathrm{d}^3\boldsymbol{k}}{4\pi^3} \phi_{ij}(b, \boldsymbol{k}, \boldsymbol{r})(\varepsilon(b, \boldsymbol{k}) - \mu), \tag{2.118}$$

$$L_{ij}^{(22)} = -\frac{1}{T} \sum_b \oint \frac{\mathrm{d}^3\boldsymbol{k}}{4\pi^3} \phi_{ij}(b, \boldsymbol{k}, \boldsymbol{r})(\varepsilon(b, \boldsymbol{k}) - \mu)^2. \tag{2.119}$$

Following equations quantify the electrical conductivity σ, Seebeck S, and thermal conductivity of electrons tensors κ :

$$\sigma_{ij} = e L_{ij}^{(11)}, \tag{2.120}$$

$$S_{ij} = \sum_\alpha \frac{1}{e} \left(\left[L^{(11)} \right]^{-1} \right)_{i\alpha} L_{\alpha j}^{(12)}, \tag{2.121}$$

$$\kappa_{ij} = L_{ij}^{(12)}. \tag{2.122}$$

Using Eqns. (2.116-2.119), the L-matrices can be evaluated for a given bandstructure, temperature, and chemical potential.

The integrals presented here form a bridge between the quantum mechanical bandstructure, and the macroscopic electron transport properties. They enable electrical transport properties to be computed from ab-initio calculations.

2.8.2 Boltzmann Transport Theory for lattice transport

For the spatially non-uniform phonon distribution, the Boltzmann equation is expressed as,

$$\left(\frac{\partial N}{\partial t}\bigg|_{drift} \right) + \left(\frac{\partial N}{\partial t}\bigg|_{scattering} \right) = 0 \tag{2.123}$$

here, N is the number of phonons in each mode. Generally, one performs the differentiation in the relaxation time approximation expressing the scattering term as $\left(\frac{\partial N}{\partial t}\big|_{\text{scattering}} \right) = -\frac{n}{\tau}$, which leads to,

$$n = -\tau(\mathbf{v}\nabla T)\frac{\partial N_0}{\partial T} \tag{2.124}$$

The Bose-Einstein distribution function is defined here as $N_0 = \frac{1}{e^{\frac{\hbar\omega}{k_B T}-1}}$ and n is the non-equilibrium part of the phonon distribution function, $N = N_0 + n$. ∇T and v is the temperature gradient and phonon group velocity, respectively. The heat flux for a 2D material is obtained from the expression,

$$\mathbf{Q} = \sum_{s,\mathbf{q}} \mathbf{v}(s,\mathbf{q})\hbar\omega(\mathbf{q})n[\mathbf{q},\omega(\mathbf{q})] \tag{2.125}$$

where $n(\omega,\mathbf{q})$ is the number of phonons in the heat flux and $\mathbf{v}\hbar\omega$ is the energy carried by a phonon. Substituting Eqn. (2.124) in Eqn. (2.125), the heat flux can be expressed as,

$$\mathbf{Q} = -\sum_{\beta}(\nabla T)_\beta \sum_{s,\mathbf{q}} \tau v_\beta(s,\mathbf{q})\frac{\partial N_0}{\partial T}\mathbf{v}(s,\mathbf{q})\hbar\omega(\mathbf{q}) \tag{2.126}$$

The macroscopic definition of the lattice thermal conductivity is derived from,

$$\mathbf{Q}_\alpha = -\kappa_{\alpha\beta}(\nabla T)_\beta h L_x L_y \tag{2.127}$$

where $\kappa_{\alpha\beta}$ is the lattice thermal conductivity tensor, L_x is the sample width, L_y is the sample length and h is the sample height. Comparing Eqn. (2.126) and Eqn. (2.127), we obtain the following expression for the lattice thermal conductivity tensor,

$$\kappa_{\alpha\beta} = \frac{1}{hL_xL_y}\sum_{s,\mathbf{q}} \tau(s,\mathbf{q})v_\alpha(s,\mathbf{q})v_\beta(s,\mathbf{q})\frac{\partial N_0(\omega)}{\partial T}\hbar\omega(\mathbf{q}). \tag{2.128}$$

2.8.3 Implementation of Boltzmann Transport Equation

Electron transport coefficients

The linearized version of the BTE under relaxation time approximation (τ) (RTA) is implemented in *BoltzTrap2* code[60]. *BoltzTraP2* calculates transport coefficients based on the rigid-band approximation (RBA), which assumes that changing the temperature or doping a system, does not change the band structure. In the RBA the carrier concentration, for a given T and μ, in a semiconductor can be obtained directly from the density of states (DOS)

$$n(\varepsilon) = \int \sum_b \delta(\varepsilon - \varepsilon_{b,k})\frac{dk}{8\pi^3} \tag{2.129}$$

where the subscript b runs over bands, by calculating the deviation from charge neutrality.

$$c(\mu,T) = N - \int n(\varepsilon)f^{(0)}(\varepsilon;\mu,T)d\varepsilon. \tag{2.130}$$

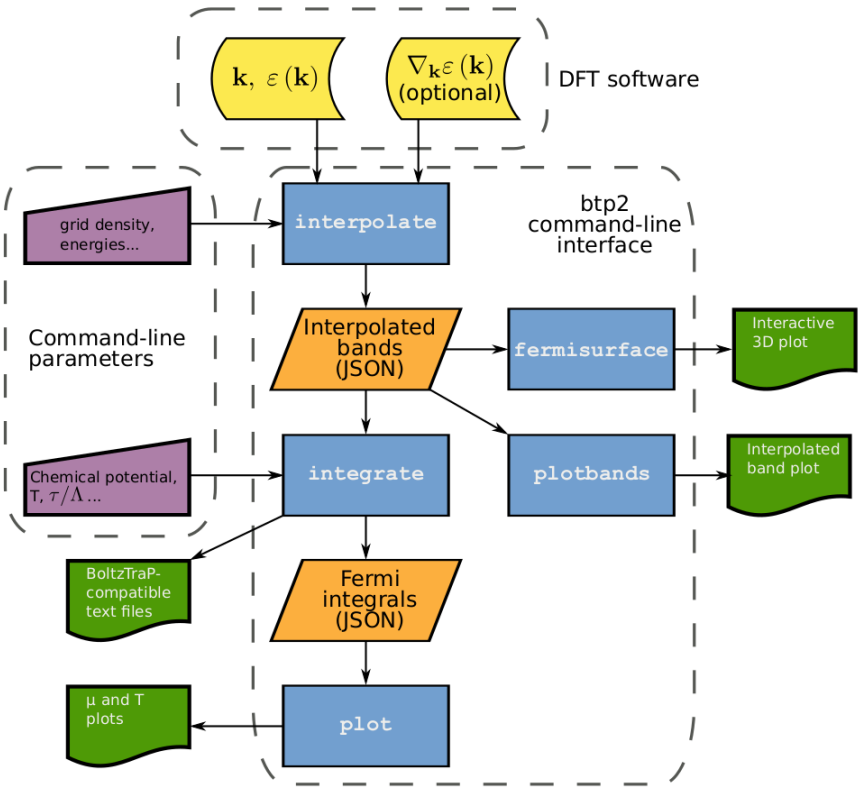

Figure 2.7: Typical *BoltzTraP2* workflow taking the user from the results of a DFT calculation to estimates of the thermoelectric coefficients for the system under study, and other related results, using the btp2 command-line interface. Figure is taken from [60]

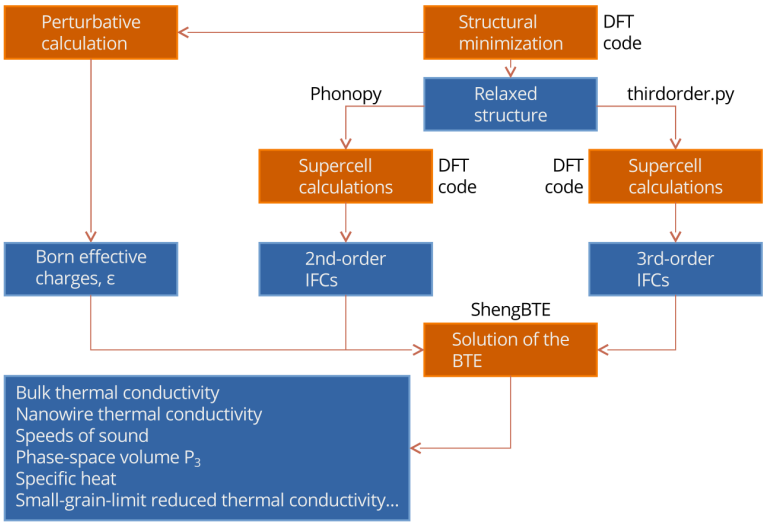

Figure 2.8: Workflow for thermal conductivity calculations using a real-space supercell approach for force constants. Orange boxes represent the steps of the calculations, blue boxes stand for the results of these steps, and computer programs are denoted as black text outside of any box. Figure is taken from [61]

Here N is the nuclear charge and $f^{(0)}$ is the Fermi distribution function. In a semiconductor where charge neutrality would place the Fermi level in the band gap, one can thus imagine how (at $T = 0$) moving μ into the conduction bands would produce a n-type material and moving μ into the valence bands would produce a p-type material.

The main advantage of the *BoltzTraP2* procedure for evaluating the transport coefficients is that it is straightforward to obtain the group velocities from the k-space derivatives of the quasi-particle energies. Under constant RTA (CRTA), the Seebeck coefficient and Hall coefficient become independent of the scattering rate [60]. Therefore, they can be obtained on an absolute scale as a function of doping and temperature in a single scan. The CRTA in combination with the RBA, which makes the group velocities independent of μ and T, also has a computational advantage as it makes the transport distribution function, independent of temperature and doping. The temperature and doping dependence of the transport coefficients $\mathcal{L}^{(\alpha)}$, is solely due to the Fermi distribution function and can be obtained via a scan over a fixed transport distribution function. The CRTA will have limitations. It only delivers σ and κ_e dependent on τ as a parameter. Figure-2.7 shows the flowchart to calculate electron transport properties as followed by *BoltzTrap2* code.

Lattice transport coefficients

To estimate the lattice thermal conductivity, we require second-order harmonic interatomic force constants (IFCs) and third-order anharmonic IFCs. Harmonic IFCs can be obtained from phonon dispersion. Phonon properties are studied within the formulation of density functional perturbation theory (DFPT). To calculate third-order anharmonic IFCs, different sets of displaced supercell configurations are generated using the finite difference method. The number of configurations generated is decided by the following: the number of nearest-neighbor interactions, symmetry of the system, size of the supercell mesh, and size of the unit cell. The third-order anharmonic IFCs are constructed from a set of third-order derivatives of energy, calculated from these configurations using the plane wave method. The phonon lifetimes are calculated from the phonon BTE which are limited by phonon-phonon, isotropic impurity, and boundary scattering. We consider the three-phonon scattering rates to compute κ_l, as implemented in the *ShengBTE* code.[61] Figure-2.8 shows the flowchart to calculate lattice transport properties as followed by *ShengBTE* code. Beyond RTA, lattice thermal conductivity matrix $\kappa_L^{\alpha\beta}$ can be written as,

$$\kappa_L^{\alpha\beta} = \frac{1}{k_B T^2 \Omega N} \sum_s f_0 \left(f_0 + 1\right) \left(\hbar\omega_s\right)^2 v_s^\alpha \tau_s^0 \left(v_s^\beta + \Delta_s^\beta\right) \tag{2.131}$$

$\kappa_L^{\alpha\beta}$ is then diagonalized to obtain the scalar lattice thermal conductivity κ_L in a preferred direction in the xy plane. In Eqn. (2.131) Ω is the volume of the unit cell, N denotes the number of q-points in the Brillouin zone sampling. $f_0 = 1/\left(e^{\hbar\omega_s/k_B T} - 1\right)$ is the Bose-Einstein distribution function, τ_s^0 is the relaxation time for the mode s with phonon frequency ω_s, v_s is the phonon group velocity, and Δ_s denotes the measure of how much associated heat current deviates from the relaxation time approximation. Linearized BTE is solved iteratively using the self-consistent method to obtain phonon transport. The stopping criterion used in the self-consistent method is that the relative change in the thermal conductivity tensor is calculated using Eqn. (2.131) is less than a threshold value of 10^{-5}.

References

[1] M. Born and R. Oppenheimer, "Zur quantentheorie der molekeln," *Annalen der Physik*, vol. 389, no. 20, pp. 457–484, 1927.

[2] A. Szabo and N. S. Ostlund, *Modern quantum chemistry: introduction to advanced electronic structure theory*. Courier Corporation, 2012.

[3] D. R. Hartree, "The wave mechanics of an atom with a non-coulomb central field. part i. theory and methods," in *Mathematical Proceedings of the Cambridge Philosophical Society*, vol. 24, pp. 89–110, Cambridge university press, 1928.

[4] C. C. J. Roothaan, "New developments in molecular orbital theory," *Reviews of modern physics*, vol. 23, no. 2, p. 69, 1951.

[5] C. D. Sherrill, "An introduction to configuration interaction theory," *School of Chemistry and Biochemistry, Georgia Institute of Technology*, 1995.

[6] P. Hohenberg and W. Kohn, "Inhomogeneous electron gas," *Physical review*, vol. 136, no. 3B, p. B864, 1964.

[7] W. Kohn and L. J. Sham, "Self-consistent equations including exchange and correlation effects," *Physical review*, vol. 140, no. 4A, p. A1133, 1965.

[8] W. Kohn, "Nobel lecture: Electronic structure of matterwave functions and density functionals," *Reviews of Modern Physics*, vol. 71, no. 5, p. 1253, 1999.

[9] C. D. Sherrill, "The multiconfigurational self-consistent-field method," *School of Chemistry and Biochemistry Georgia Institute of Technology March*, pp. 1–6, 2004.

[10] B. O. Roos, P. R. Taylor, P. E. Si, *et al.*, "A complete active space scf method (casscf) using a density matrix formulated super-ci approach," *Chemical Physics*, vol. 48, no. 2, pp. 157–173, 1980.

[11] K. Andersson, P.-Å. Malmqvist, and B. O. Roos, "Second-order perturbation theory with a complete active space self-consistent field reference function," *The Journal of chemical physics*, vol. 96, no. 2, pp. 1218–1226, 1992.

[12] L. H. Thomas, "The calculation of atomic fields," in *Mathematical proceedings of the Cambridge philosophical society*, vol. 23, pp. 542–548, Cambridge University Press, 1927.

[13] E. Fermi, "Un metodo statistico per la determinazione di alcune priorieta dellatome," *Rend. Accad. Naz. Lincei*, vol. 6, no. 602-607, p. 32, 1927.

[14] N. Harrison, "An introduction to density functional theory," *Nato Science Series Sub Series III Computer and Systems Sciences*, vol. 187, pp. 45–70, 2003.

[15] D. M. Ceperley and B. J. Alder, "Ground state of the electron gas by a stochastic method," *Physical review letters*, vol. 45, no. 7, p. 566, 1980.

[16] J. P. Perdew and A. Zunger, "Self-interaction correction to density-functional approximations for many-electron systems," *Physical Review B*, vol. 23, no. 10, p. 5048, 1981.

[17] J. P. Perdew and Y. Wang, "Accurate and simple analytic representation of the electron-gas correlation energy," *Physical review B*, vol. 45, no. 23, p. 13244, 1992.

[18] R. O. Jones and O. Gunnarsson, "The density functional formalism, its applications and prospects," *Reviews of Modern Physics*, vol. 61, no. 3, p. 689, 1989.

[19] A. D. Becke, "Density-functional exchange-energy approximation with correct asymptotic behavior," *Physical review A*, vol. 38, no. 6, p. 3098, 1988.

[20] A. D. Boese and N. C. Handy, "A new parametrization of exchange–

correlation generalized gradient approximation functionals," *The Journal of Chemical Physics*, vol. 114, no. 13, pp. 5497–5503, 2001.

[21] J. P. Perdew, K. Burke, and M. Ernzerhof, "Generalized gradient approximation made simple," *Physical review letters*, vol. 77, no. 18, p. 3865, 1996.

[22] C. Y. Lee and W. Parr, "Rg phys. rev. b 1988, 37, 785–789. b) becke, ad," *Phys. Rev. A*, vol. 38, pp. 3098–3100, 1988.

[23] J. P. Perdew, "Density-functional approximation for the correlation energy of the inhomogeneous electron gas," *Physical Review B*, vol. 33, no. 12, p. 8822, 1986.

[24] J. P. Perdew, "Erratum: Density-functional approximation for the correlation energy of the inhomogeneous electron gas," *Physical review B*, vol. 34, no. 10, p. 7406, 1986.

[25] N. C. Handy and A. J. Cohen, "Left-right correlation energy," *Molecular Physics*, vol. 99, no. 5, pp. 403–412, 2001.

[26] J. Tao, J. P. Perdew, V. N. Staroverov, and G. E. Scuseria, "Climbing the density functional ladder: Nonempirical meta–generalized gradient approximation designed for molecules and solids," *Physical Review Letters*, vol. 91, no. 14, p. 146401, 2003.

[27] Y. Zhao and D. G. Truhlar, "A new local density functional for main-group thermochemistry, transition metal bonding, thermochemical kinetics, and noncovalent interactions," *The Journal of chemical physics*, vol. 125, no. 19, p. 194101, 2006.

[28] J. P. Perdew, S. Kurth, A. Zupan, and P. Blaha, "Accurate density functional with correct formal properties: A step beyond the generalized gradient approximation," *Physical review letters*, vol. 82, no. 12, p. 2544, 1999.

[29] J. P. Perdew, S. Kurth, A. Zupan, and P. Blaha, "Accurate density functional with correct formal properties: A step beyond the generalized gradient approximation," *Physical review letters*, vol. 82, no. 12, p. 2544, 1999.

[30] A. D. Becke, "Density-functional thermochemistry. iii. the role of exact exchange," *The Journal of Chemical Physics*, vol. 98, no. 7, pp. 5648–5652, 1993.

[31] M. Reiher, O. Salomon, and B. A. Hess, "Reparameterization of hybrid functionals based on energy differences of states of different multiplicity," *Theoretical Chemistry Accounts*, vol. 107, no. 1, pp. 48–55, 2001.

[32] J. P. Perdew, M. Ernzerhof, and K. Burke, "Rationale for mixing exact exchange with density functional approximations," *The Journal of chemical physics*, vol. 105, no. 22, pp. 9982–9985, 1996.

[33] C. Adamo and V. Barone, "Toward reliable density functional methods without adjustable parameters: The pbe0 model," *The Journal of chemical physics*, vol. 110, no. 13, pp. 6158–6170, 1999.

[34] X. Xu and W. A. Goddard, "The x3lyp extended density functional for accurate descriptions of nonbond interactions, spin states, and thermochemical

properties," *Proceedings of the National Academy of Sciences*, vol. 101, no. 9, pp. 2673–2677, 2004.

[35] Y. Zhao and D. G. Truhlar, "The m06 suite of density functionals for main group thermochemistry, thermochemical kinetics, noncovalent interactions, excited states, and transition elements: two new functionals and systematic testing of four m06-class functionals and 12 other functionals," *Theoretical chemistry accounts*, vol. 120, no. 1, pp. 215–241, 2008.

[36] Y. Zhao, N. E. Schultz, and D. G. Truhlar, "Exchange-correlation functional with broad accuracy for metallic and nonmetallic compounds, kinetics, and noncovalent interactions," *The Journal of chemical physics*, vol. 123, no. 16, p. 161103, 2005.

[37] Y. Zhao, N. E. Schultz, and D. G. Truhlar, "Design of density functionals by combining the method of constraint satisfaction with parametrization for thermochemistry, thermochemical kinetics, and noncovalent interactions," *Journal of chemical theory and computation*, vol. 2, no. 2, pp. 364–382, 2006.

[38] H. Iikura, T. Tsuneda, T. Yanai, and K. Hirao, "A long-range correction scheme for generalized-gradient-approximation exchange functionals," *The Journal of Chemical Physics*, vol. 115, no. 8, pp. 3540–3544, 2001.

[39] Y. Tawada, T. Tsuneda, S. Yanagisawa, T. Yanai, and K. Hirao, "A long-range-corrected time-dependent density functional theory," *The Journal of chemical physics*, vol. 120, no. 18, pp. 8425–8433, 2004.

[40] T. Yanai, D. P. Tew, and N. C. Handy, "A new hybrid exchange–correlation functional using the coulomb-attenuating method (cam-b3lyp)," *Chemical physics letters*, vol. 393, no. 1-3, pp. 51–57, 2004.

[41] S. Grimme, "Semiempirical hybrid density functional with perturbative second-order correlation," *The Journal of chemical physics*, vol. 124, no. 3, p. 034108, 2006.

[42] T. Schwabe and S. Grimme, "Towards chemical accuracy for the thermodynamics of large molecules: new hybrid density functionals including non-local correlation effects," *Physical Chemistry Chemical Physics*, vol. 8, no. 38, pp. 4398–4401, 2006.

[43] M. J. Frisch, G. W. Trucks, H. B. Schlegel, G. E. Scuseria, M. A. Robb, J. R. Cheeseman, G. Scalmani, V. Barone, G. A. Petersson, H. Nakatsuji, X. Li, M. Caricato, A. V. Marenich, J. Bloino, B. G. Janesko, R. Gomperts, B. Mennucci, H. P. Hratchian, J. V. Ortiz, A. F. Izmaylov, J. L. Sonnenberg, D. Williams-Young, F. Ding, F. Lipparini, F. Egidi, J. Goings, B. Peng, A. Petrone, T. Henderson, D. Ranasinghe, V. G. Zakrzewski, J. Gao, N. Rega, G. Zheng, W. Liang, M. Hada, M. Ehara, K. Toyota, R. Fukuda, J. Hasegawa, M. Ishida, T. Nakajima, Y. Honda, O. Kitao, H. Nakai, T. Vreven, K. Throssell, J. A. Montgomery, Jr., J. E. Peralta, F. Ogliaro, M. J. Bearpark, J. J. Heyd, E. N. Brothers, K. N. Kudin, V. N. Staroverov, T. A. Keith, R. Kobayashi, J. Normand, K. Raghavachari, A. P.

Rendell, J. C. Burant, S. S. Iyengar, J. Tomasi, M. Cossi, J. M. Millam, M. Klene, C. Adamo, R. Cammi, J. W. Ochterski, R. L. Martin, K. Morokuma, O. Farkas, J. B. Foresman, and D. J. Fox, "Gaussian16 Revision C.01," 2016. Gaussian Inc. Wallingford CT.

[44] G. Kresse and J. Hafner, "Ab initio molecular dynamics for liquid metals," *Physical review B*, vol. 47, no. 1, p. 558, 1993.

[45] A. Schäfer, C. Huber, and R. Ahlrichs, "Fully optimized contracted gaussian basis sets of triple zeta valence quality for atoms li to kr," *The Journal of Chemical Physics*, vol. 100, no. 8, pp. 5829–5835, 1994.

[46] N. W. Ashcroft and N. D. Mermin, *Solid state physics*. Cengage Learning, 2022.

[47] P. E. Blöchl, "Projector augmented-wave method," *Physical review B*, vol. 50, no. 24, p. 17953, 1994.

[48] E. Runge and E. K. Gross, "Density-functional theory for time-dependent systems," *Physical Review Letters*, vol. 52, no. 12, p. 997, 1984.

[49] M. E. Casida and D. Chong, "Recent advances in density functional methods," *Computational Chemistry: Reviews of Current Trends*, 1995.

[50] A. Zangwill and P. Soven, "Density-functional approach to local-field effects in finite systems: Photoabsorption in the rare gases," *Physical Review A*, vol. 21, no. 5, p. 1561, 1980.

[51] R. E. Stratmann, G. E. Scuseria, and M. J. Frisch, "An efficient implementation of time-dependent density-functional theory for the calculation of excitation energies of large molecules," *The Journal of chemical physics*, vol. 109, no. 19, pp. 8218–8224, 1998.

[52] E. Gross and W. Kohn, "Local density-functional theory of frequency-dependent linear response," *Physical Review Letters*, vol. 57, no. 7, p. 923, 1986.

[53] C. Adamo and D. Jacquemin, "The calculations of excited-state properties with time-dependent density functional theory," *Chemical Society Reviews*, vol. 42, no. 3, pp. 845–856, 2013.

[54] Z. Fan, J. H. Garcia, A. W. Cummings, J. E. Barrios-Vargas, M. Panhans, A. Harju, F. Ortmann, and S. Roche, "Linear scaling quantum transport methodologies," *Physics Reports*, vol. 903, pp. 1–69, 2021.

[55] J. M. Ziman, *Principles of the Theory of Solids*. Cambridge university press, 1972.

[56] J. M. Ziman, *Electrons and phonons: the theory of transport phenomena in solids*. Oxford university press, 2001.

[57] G. D. Mahan, *Many-particle physics*. Springer Science & Business Media, 2000.

[58] J. Luttinger, "Theory of thermal transport coefficients," *Physical Review*, vol. 135, no. 6A, p. A1505, 1964.

[59] F. G. Eich, M. Di Ventra, and G. Vignale, "Density-functional theory of ther-

moelectric phenomena," *Physical review letters*, vol. 112, no. 19, p. 196401, 2014.

[60] G. K. Madsen, J. Carrete, and M. J. Verstraete, "Boltztrap2, a program for interpolating band structures and calculating semi-classical transport coefficients," *Computer Physics Communications*, vol. 231, pp. 140–145, 2018.

[61] W. Li, J. Carrete, N. A. Katcho, and N. Mingo, "Shengbte: A solver of the boltzmann transport equation for phonons," *Computer Physics Communications*, vol. 185, no. 6, pp. 1747–1758, 2014.

Chapter 3

Light Induced Excited Spin State Trapping in Spin Crossover Model System*

3.1 Introduction

Molecular complexes exhibiting Spin-Crossover (SCO) properties find a multitude of applications in various fields ranging from data storage to molecular electronics, to photo-magnetism and non-linear optics.[1–3]

In particular, the photo-magnetic response of SCO complexes, discovered by Decurtins et al. [4] in 1984 by illuminating $[Fe(ptz)_6](BF_4)_2$ sample at low temperature (10K), lead to a reversible spin transition manifesting Light-Induced Excited Spin State Trapping (LIESST), a phenomenon of application potential. According to the relaxation model proposed by Hauser et al.[5], the system is excited with light from the singlet LS ground state to metal-centered (MC) d-d or to metal-to-ligand charge-transfer (MLCT) excited states, which decay to the quintet HS state via intersystem crossings and internal crossing through the participation of triplet states. The relaxation rate from the excited HS state to the ground LS state turns out to be low as the cryogenic temperature is maintained resulting in trapping of the system from several hours to weeks. LIESST effect is of potential technical use as optical switches and magneto-optical storage, but it is limited by the fact that trapping to photo-induced HS state usually happens at rather low temperatures. This calls for the need for a microscopic understanding of the LIESST mechanism which will be beneficial for designing new LIESST materials with tailored properties.

Computational modeling of SCO molecules is a complex problem because of

*This chapter is based on publication : **Shiladitya Karmakar**, Debashree Ghosh, and Tanusri Saha-Dasgupta, *International Journal of Quantum Chemistry*, **120.6**, e26122 (2020).

two reasons, a) the presence of TM ion center with open d sub-shells incorporating strong electron-electron correlation effect and multi-reference character, b) relatively large size of organic ligands incorporating large degrees of freedom to the problem. To understand the LIESST mechanism within the relaxation model, it is essential to capture the electronic structures of ground states as well as excited states of the molecule accurately. Modern quantum chemical methods involving both wave-function and density functional-based approaches have been extensively applied to Fe(II) SCO complexes in order to investigate spin-state transitions during the LIESST process. Wave function-based method is capable of handling the multi-reference nature of the problem but their accuracy crucially depends on the size of the basis set, and the chosen active space,[6] making the use of such ab-initio study limited to small molecules. On the other hand, density functional theory being a single-reference method by its very nature lacks multi-configurational nature but is efficient enough to handle large SCO molecules to connected SCO polymers. Therefore, finding out a suitable computational procedure to understand the LIESST mechanism with sufficient accuracy is thus a challenge.

To investigate the LIESST mechanism, in this chapter we consider a metal-organic complex in the family of $Fe^{II}(L)_n(NCS)_2$, namely $[Fe(abpt)_2(NCS)_2]$ (abpt=4-amino-3,5-bis(pyridin-2-yl)-1,2,4-triazole), which undergoes thermal spin crossover without hysteresis between $\sim$ 202K and 100K with $T_{1/2}$=180K.[7] A LIESST metastable HS structure of the compound was also reported by Meson et al, produced at 30K by continuous irradiation with a 670 nm, 5 mW continuous wave laser on the LS structure of the complex. Motivated by its SCO properties, a hypothetical model for $[Fe(abpt)_2(NCS)_2]$ is constructed in which the long-range structure of the molecule is simplified substantially keeping the short-range structure as well as the asymmetric ligand-field of the real system intact. Typically LS$\rightarrow$HS transition is accompanied by drastic change along a single configuration coordinate: a stretching mode that corresponds to the symmetric elongation of the six FeN bonds (the so-called breathing mode). Hence our model with reduced degrees of freedom enables us to investigate the dynamics of the LIESST process using both complementary quantum chemical tools of time-dependent DFT and multi-configurational wave function-based approach of complete active space self-consistent field (CASSCF). We calculate the potential energy curves (PECs) of low-energy states, as well as spin-orbit couplings at crossing points of these PECs. Inputting these pieces of information, and the information related to nuclear degrees of freedom within the Franck-Condon theory, we compute the relaxation rates of possible LIESST mechanisms. Comparison of the computed rates of the model system with that of the real systems leads us to conclude that TDDFT is a less expensive and reasonable approach to describe LIESST processes. This finding makes the application of TDDFT to real complexes promising, which would involve handling complex structures containing 100 to 200 atoms. Calculation of

relaxation rates of real complexes may provide a microscopic understanding of the relationship between the structure and the relaxation rate.

3.2 Computational details

All the density functional-based calculations are performed using Q-Chem 5.0 package. [8] Constrained optimizations of the quintet and singlet state structures are performed at the DFT level keeping the position of atoms frozen as in real molecule allowing only the hydrogen atoms in the model systems to relax. The exchange-correlation functional within DFT formulation is chosen as Becke's nonlocal three-parameter hybrid functional combined with the Lee-Yang-Parr correlation functional with 20% exchange(B3LYP).[9] The values of a, b and c parameters[10–12] in B3LYP are fixed at default values, $a = 0.2$, $b = 0.72$ and $c = 0.81$. The triple zeta valence basis set, [13] as implemented in Q-chem 5.0, is used for all the atoms. The structures are considered to be optimized when the calculations satisfy the default optimization criterion of Q-Chem software i.e., the maximum component of the gradient is less than 3 $\times 10^{-4}$ a.u. along with energy change less than 10^{-6} in E_h between successive iterations. In order to have a proper assessment of the performance of TDDFT, in addition to B3LYP, two more functionals, namely M06-L[14] and OLYP[15] are tested.

Time-Dependent DFT [16] calculations are carried out to determine the excited states of the quintet, triplet, and singlet spin states with 20 excited states. The intermediate geometries are obtained by linear interpolation between the HS and LS-optimized geometries. In total six such geometries are generated to obtain the potential energy curves (PECs).

The CASSCF [17] as well as CASPT2[18] calculations are performed with a TZV basis set, as in the case of TDDFT, using Molpro 2018 package. [19] Here, we use a [10e,12o] active space comprising 10 electrons occupying 12 orbitals. The active space consists of five iron 3d orbitals, two bonding ligand orbitals of e_g symmetry, and five iron 4d orbitals to describe the so-called double shell effect. For excited state calculation, we employ the state average (SA) method as implemented in the software employing the same choice of active space. The one-electron Breit Pauli Hamiltonian [20] is employed to calculate the spin-orbit coupling for both TDDFT and CASSCF/CASPT2 states.

3.3 Results

3.3.1 Structural details

$[Fe(abpt)_2(NCS)_2]$ is a six-coordinated mononuclear iron (II) based complex, in which Fe(II) is four-coordinated by bidenate ligands, abpt [4-amino-3,5-bis(pyridin-

2-yl)-1,2,4-triazole], and two-coordinated by monodentate ligands, isothiocyanate (NCS) at apical positions, as shown in right panel of Figure 3.1. In bidenate ligand, abpt, two pyridine rings are connected to 3 and 5 positions of a 1,2,4-triazole ring, and an amino group is attached to the 4 position of the triazole ring. It is evident from HS and LS structures reported at 30K,[7] that in the process of spin transition, a significant change of geometry occurs primarily within FeN_6 octahedron. The volume of the octahedron changes from 12.957Å^3 to 10.076 Å^3 as the system transits from HS to LS state. In both the spin state structures, all four C-C bond lengths in the pyridine ring are around 1.39Å, and two C-N bond lengths in the ring are 1.34Å and 1.36Å, respectively. Similarly, the triazole ring hardly changes between the two spin-state structures, with N-N bond length around 1.36Å, four C-N bond lengths of 1.32Å, 1.36Å, 1.37Å, 1.32Å, and bond length connecting N-N with amino group being 1.43Å.

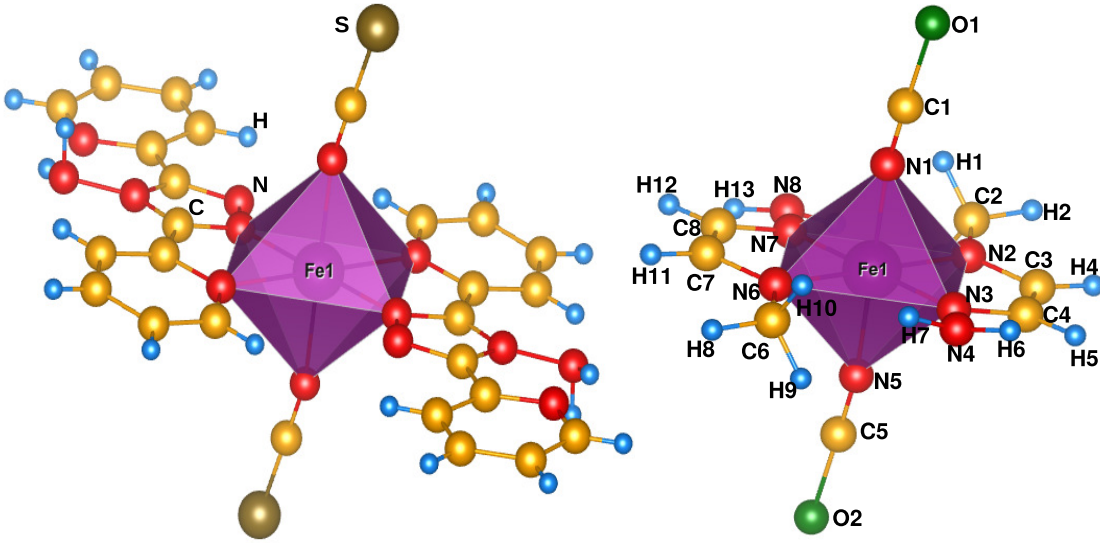

Figure 3.1: Left panel shows the real structure. Central atom Fe is surrounded by six N atoms forming an octahedral structure. The medium-sized golden and red balls represent C and N respectively. The small sky blue balls represent the H atoms while the brown medium-sized balls denote S. Right panel shows the model system built out of the real system keeping the FeN_6 octahedra unchanged. Here S is replaced by O (green medium-sized balls) and the farther away structure is simplified, keeping the asymmetry of the real molecule preserved (see text for details).

As mentioned above, in order to keep the computation tractable, especially for multi-reference calculations, a simplified model system is used in our study. The simplified model system (cf left panel, Figure 3.1) is constructed from the real system keeping the HS and LS geometries of the FeN_6 octahedron unchanged

and making drastic simplification of ligands, though keeping their basic nature unaltered. For example, the bidentate ligand abpt is modified in such a way that it remains bidentate, and the asymmetric nature of the ligand-field as in the real system is preserved. For this, first the amino group is removed along with the nitrogen atom through which it is connected to triazole ring. Similarly one of the pyridine ring is removed along with carbon atom through which it is connected to triazole ring. Instead three hydrogen atoms are attached at their positions so that the valency of the structure is maintained. The other pyridine ring is removed partially where three carbon and three hydrogen atoms in the structure are replaced by three hydrogen atoms. Finally, the sulphur atom of monodentate NCS ligand is replaced by oxygen atom.

In building up the model, the atoms in the nearest shell and next nearest shell of Fe are chosen to be as the real system. This we believe is an improvement on the model used by many groups where they have substituted all the ligands as NCH[21], as we keep not only the same nearest neighbor but also the next nearest neighbor. Furthermore, the heterogeneity of the ligands in the xy plane and along the z-axis is also preserved in our model. In order to judge the goodness of replacement of S by O, we perform B3LYP calculations on the high and low spin structures of O and S substituted species and find that the ΔE_{HL} is 2068 cm^{-1} in S substituted as compared to 1561 cm^{-1} in O substituted species, which indicates that S substitution would have made the low spin state somewhat more stable. However, due to computational challenges in the multireference calculations, we use O substitution, which still retains the heterogeneity of the Fe environment. In the table-3.1, we provide the atomic coordinates of the optimized LS and HS structures, used in the present study, along with their vibrational properties.

Mode type	Bond	Freq.(IR) cm^{-1} (KM/Mole) HS	Freq.(IR) cm^{-1} (KM/Mole) LS
Symm str.	Fe-N1 , Fe-N5	104.62 (17.30)	269.85 (0.11)
Asymm str.	Fe-N1 , Fe-N5	369.14 (507.30)	533.94 (110.47)
Asymm str.	Fe-N3 , Fe-N7	130.35 (0.42)	472.40 (5.52)
Symm str.	Fe-N3 , Fe-N7	435.57 (16.60)	484.91 (9.73)
Bending	Fe-N6-N1	260.44 (61.39)	306.64 (0.02)
Symm str.	N7-C8, N3-C4	1572.46 (0.07)	1629.90 (5.45)
Asymm str.	N7-C8, N3-C4	1577.05 (590.71)	1634.25 (1.67)
Symm str.	N1-C1-O1, N5-C5-O2	2182.20 (0.02)	2224.64 (336.07)
Asymm str.	N1-C1-O1, N5-C5-O2	2168.50 (2722.07)	2212.51 (1644.13)

Table 3.1: Vibrational Analysis of HS and LS structure

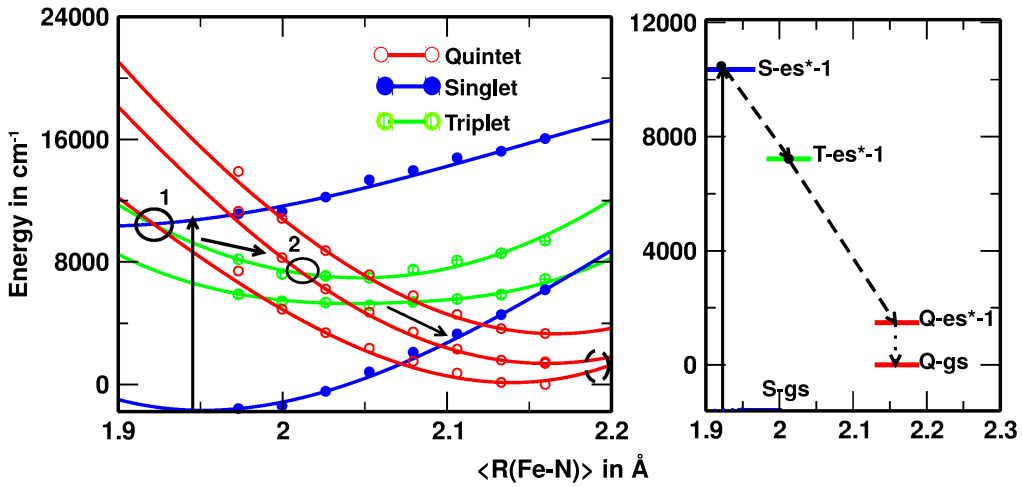

Figure 3.2: Left panel shows PEC's of the low-lying energy states of the SCO model system as function of the mean Fe-N distances resulting from TDDFT calculation. Blue lines with closed circles denote the singlet states, red lines with open circles denote the quintet states and green lines with hashed circles denote the triplet states. We also indicate the LIESST pathway using arrows i.e., S-es*-1→T-es*-1→Q-es*-1→Q-gs. Labels 1 and 2 indicate first and second crossings. Right panel shows the pathways in terms of energy level diagram. Solid line refers to electronic transition, dashed line refers to ISC step and dotted line refers to IC step. Black dots refers to crossing point between the excited states involving ISC.

3.3.2 Potential Energy Curves of Low-energy States, Relaxation Processes

Possible mechanism of LIESST[22, 23] can be described as follows. Fe(II) $3d^6$ system in LS singlet ground state is first photo-excited to an excited singlet state. Then spin transition occurs through a relaxation process involving a number of intersystem crossing (ISC) and internal conversion (IC) steps. Typically, a system relaxes to the intermediate states and finally back to the metastable HS quintet state where it gets trapped at cryogenic temperature (typically T < 50K), before relaxing back to LS ground state. For Fe(II) system low lying triplet and excited quintet states may play the role of intermediate states within the d-d deexcitation scenario. Spin-orbit coupling can mix the ground LS and metastable HS states only via them. [24] The first step to elucidate on the dynamics of the intersystem crossing process of a given metal-organic complex, is the information

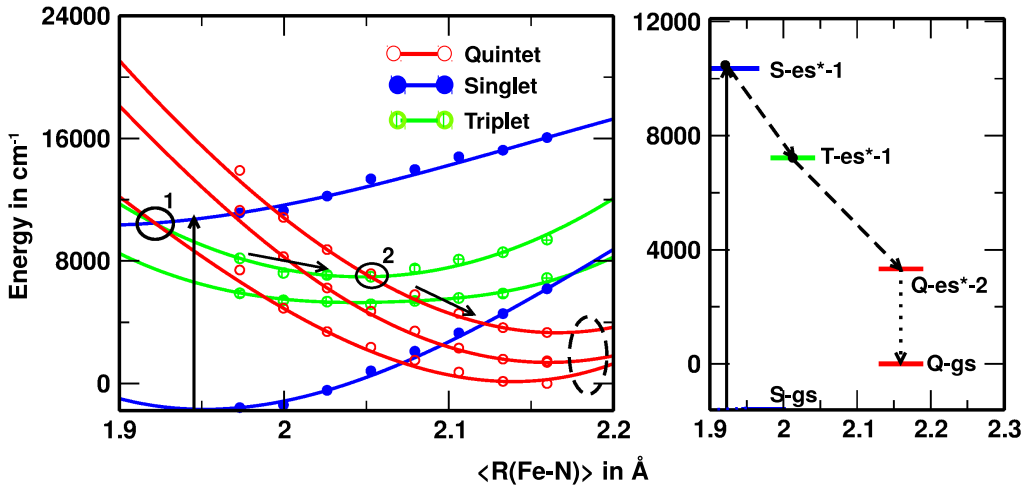

Figure 3.3: Same as Figure 3.2, but shown for the second possible pathway (S-es*-1→T-es*-1→Q-es*-2→Q-gs), as given in TDDFT calculation.

of the potential energy curve (PEC)s of the low-energy states of singlet, triplet and quintet multiplicity, and the crossing between these states. Several possible pathways may be proposed for the LIESST mechanism from the computed PECs. In the following we do so, using both TDDFT and multi-reference approaches of CASSCF and CASPT2.

TDDFT results- We start our discussion on the choice of exchange-correlation functional in DFT. It has been found [25] that the HS-LS splitting depends sensitively on the amount of Hartree-Fock(HF)-like exchange included in the exchange functional. In line with these findings, we also find pure HF theory artificially stabilizes HS relative to LS, leading to splitting energy -10,000 cm^{-1}. On the other hand, pure density functionals with no HF exchange such as local density approximation and various generalized gradient approximations favor the LS state unphysically. [26] B3LYP with 20% mixing of HF exchange is found to be a good choice. B3LYP in our studied system stabilizes the LS state over HS state with ΔE_{HL}=1561 cm^{-1}. Repeating the calculations with choice of other functionals like M06-L and OLYP, also stabilizes the LS state over the HS state for the system under discussion with ΔE_{HL} values of 1756 cm^{-1}, and 621 cm^{-1}, respectively. While the ΔE_{HL} values of the system under discussion, turn to be rather close between B3LYP and M06-L, that of OLYP though smaller in magnitude, still keeps the LS state stabler over the HS state. ΔE_{HL} calculated within DFT is summarized in Table-3.2.

Functional	**B3LYP**	**M06-L**	**OLYP**
ΔE_{HL} in cm^{-1}	1561	1756	621

Table 3.2: Comparison of Ground HS-LS state splitting calculated within DFT

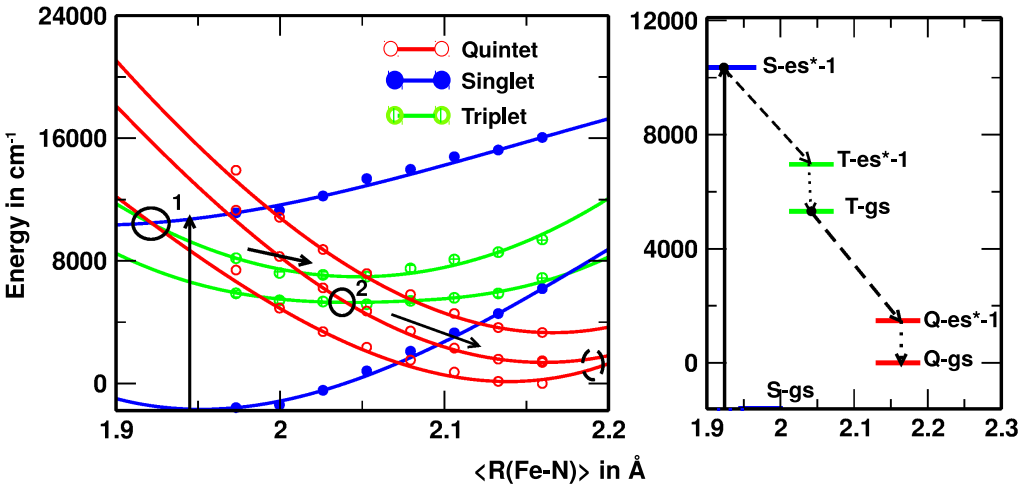

Figure 3.4: Same as Figure 3.2, but shown for the third possible pathway (S-es*-1→T-es*-1→T-gs→Q-es*-1→Q-gs), as given in TDDFT calculation.

The following described results are obtained using B3LYP with 20% mixing of HF exchange. For results obtained with M06-L and OLYP, refer to figure-3.5, 3.6, and 3.7. The PECs for ground state (gs) and a few low-lying excited states (es) of singlet (S), triplet (T), and quintet (Q) multiplicity, as computed in TDDFT(B3YLP) is shown in the left panels of Figures 3.2, 3.3 and 3.4. The excited states are labeled as S-es*-n, T-es*-n, and Q-es*-n, according to increasing energy.

Following the crossing of these TDDFT computed PECs, three possible pathways for LIESST may be proposed, that fulfill the general mechanism of LIESST. These are illustrated in Figures 3.2, 3.3, and 3.4, respectively, both in terms of identification of crossing points, labeled as 1, 2, 3. . ., and energy level diagrams. In all the identified processes, the system first undergoes a spin-conserving transition from the singlet ground state (S-gs) to 1st excited singlet state (S-es*-1). Then it encounters the first intersystem crossing from S-es*-1 to the 1st excited triplet state (T-es*-1). In the first process (cf Figure 3.2), the system further relaxes to the 1st excited quintet (Q-es*-1) state through the second ISC step.

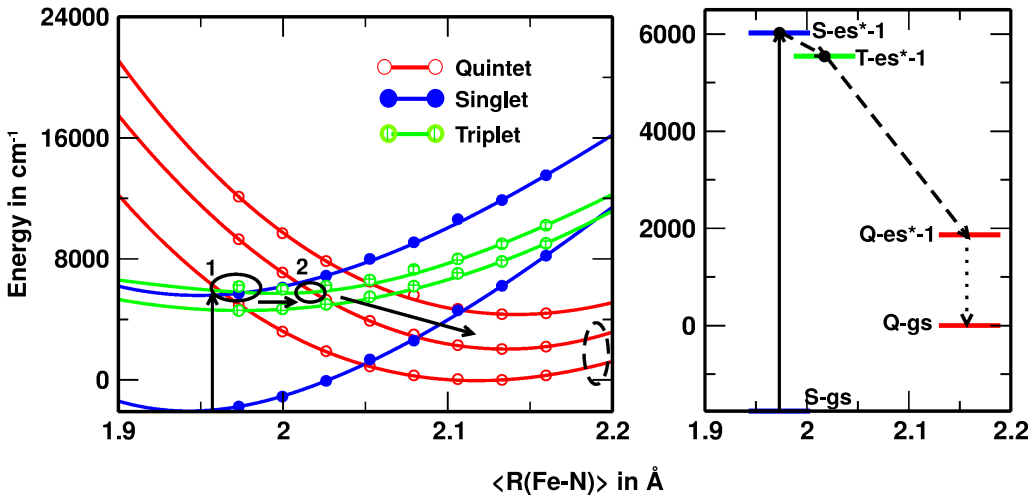

Figure 3.5: Left panel shows PECs of the low-lying energy states of the SCO model system as a function of the mean Fe-N distances resulting from TDDFT calculation with M06-L functional. The right panel shows the pathways in terms of the energy level diagram. The solid line refers to electronic transition, the dashed line refers to the ISC step and the dotted line refers to the IC step. Black dots refer to the crossing point between the excited states involving ISC. LIESST pathways: S-es*-1→T-es*-1→Q-es*-1→Q-gs

The system reaches the Q-gs by an internal conversion step from Q-es*-1 to Q-gs, giving rise to a three-step LIESST mechanism, S-es*-1→T es*-1→Q-es*-1→Q-gs. In the second possible process (cf Figure 3.3), the subsequent relaxation happens to the second excited quintet (Q-es*-2) state through the second ISC step and finally to the Q-gs state by an IC step, giving rise to another possible three-step pathway: S-es*-1→T-es*-1→Q-es*-2→Q-gs. In the third possible process (cf Figure 3.4), the system undergoes an IC from T-es*-1 to triplet ground state (T-gs). Next, it encounters the second ISC step to the first excited quintet state and finally reaches the Q-gs state by the second IC step, giving rise to a four-step pathway: S-es*-1→T-es*-1→T-gs→Q-es*-1→Q-gs.

CASSCF results- In CAS based method, the choice of active space plays a crucial role in the determination of electronic states, especially for SCO compounds. In our chosen (10e,12o) active space, the reference wave function is built by the following procedure: i) six electrons distributed over the five molecular orbitals corresponding to the antibonding combinations of Fe 3d and the ligand valence orbitals are considered. ii) five virtual orbitals with predominant iron d character are included in the active space, in order to describe the double-shell effect, i.e.,

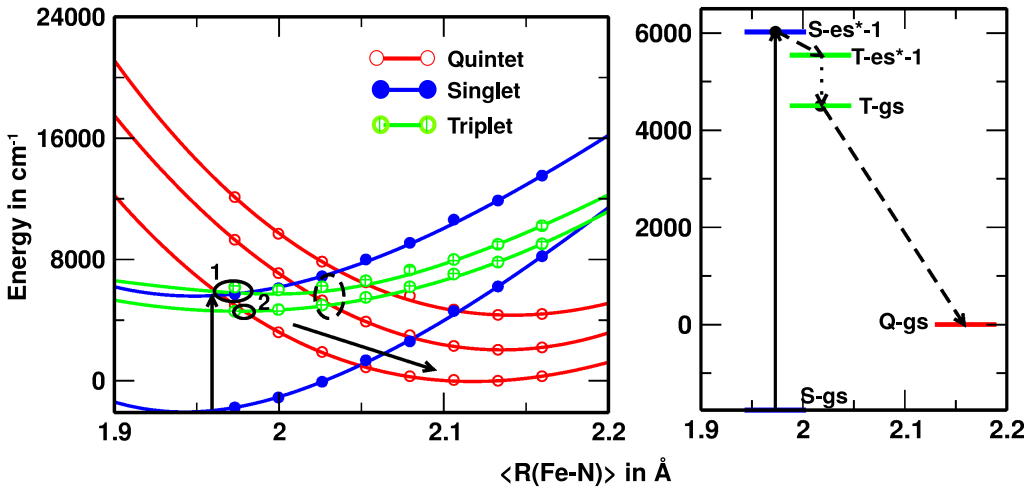

Figure 3.6: Left panel shows PECs of the low-lying energy states of the SCO model system as a function of the mean Fe-N distances resulting from TDDFT calculation with M06-L functional. The right panel shows the pathways in terms of the energy level diagram. The solid line refers to electronic transition, the dashed line refers to the ISC step and the dotted line refers to the IC step. Black dots refer to the crossing point between the excited states involving ISC. LIESST pathways: S-es*-1→T-es*-1→T-gs→Q-gs

radial correlation effects within the iron 3d shell. iii) finally, two bonding orbitals of e_g symmetry with four electrons are included to describe non-dynamic correlation effects associated with covalent metal-ligand interactions. This choice of active space ensures the balanced description of the dynamical correlation associated with the iron 3d electrons and non-dynamical correlation effects associated with the covalent metal-ligand interactions as reported by Pierloot et al. [27] The natural orbitals involved in high spin (10e,12o) CASSCF calculation, are shown in Figure 3.8.

With the above choice, we first calculate ΔE_{HL}, the first step of any SCO calculation. As mentioned above, our CASSCF calculation shows the HS state to be stable compared to the LS state, with the relative stability of ΔE_{HL}=-2040 cm^{-1}. This is in contradiction with the observed SCO properties of the $[Fe(abpt)_2(NCS)_2]$ molecule. Suaud et al. [21] found the same characteristics of the electronic states using the same active space in model $[Fe(NCH)_6]^{2+}$ complex as well as $[Fe(dipyrazol\text{-}pyridine)_2]^{2+}$ complex of the $[Fe(dipyrazolpyridine)_2]^{2+}(BF_4)_2$ compound. This may indicate the bias of the multi-configurational approach towards HS stabilization.

Based on the CASSCF computed PECs for singlet, triplet, and quintet ground

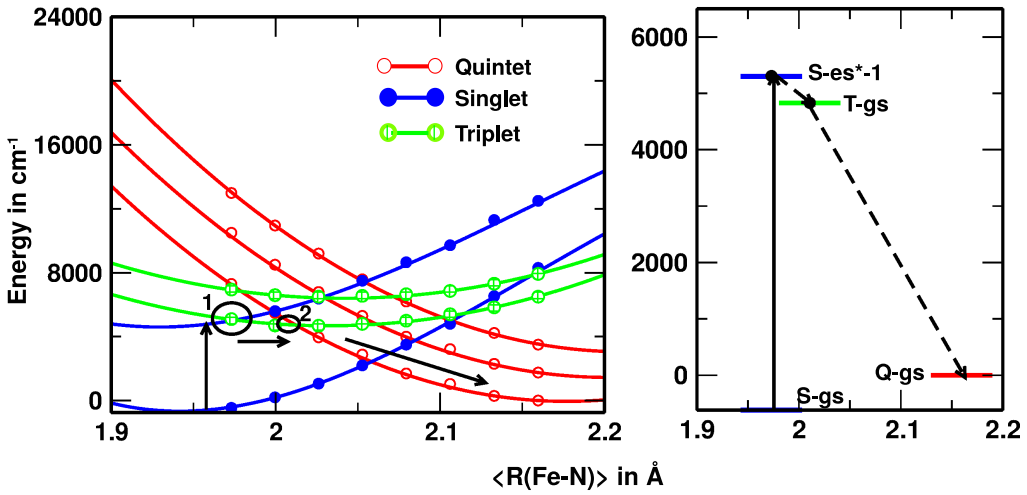

Figure 3.7: Same as Figure-1 but resulting from TDDFT calculation with OLYP functional. LIESST pathways can be indicated as S-es*-1→T-gs→Q-gs

states and a few low-lying excited states, we find two possible pathways for LIESST. In both processes, the system after undergoing the spin-conserving singlet ground state to the first excited singlet state transition, encounters the first intersystem crossing from S-es*-1 to T-es*-4. In the first process (cf Figure 3.9), the system further relaxes to the triplet ground state through an internal conversion step. Next, it undergoes a second ISC from T-gs to the 2nd excited quintet state, from which the system reaches Q-gs by the second IC step, generating the pathway given by: S-es*-1→T-es*-4→T-gs→Q-es*-2→Q-gs. In the second process (cf Figure 3.10), the system undergoes a second ISC from T-es*-4 to the third excited quintet state (Q-es*-3), followed by an IC step to Q-gs. Thus, the second possible pathway for LIESST is: S-es*-1→T-es*-4→Q-es*-3→Q-gs.

CASPT2 results- To ascertain whether the inclusion of dynamical correlation improves the situation, we further calculate ΔE_{HL} within CASPT2 with chosen (10e,12o) active space. We find the inclusion of dynamic correlation does improve the situation, bringing down the bias towards the high spin solution. The ΔE_{HL}, computed within CASPT2, is found to be -1229 cm^{-1}, as opposed to -2040 cm^{-1} in CASSCF.(Table-3.3) This in turn highlights the importance of dynamical correlation in the proper description of the stability of the LS state within the multireference system.

Considering the CASPT2 computed PECs for singlet, triplet, and quintet ground state and few low-lying excited states, two possible pathways are found (see figure-3.11), given by S-es*-1→T-es*-4→T-gs→Q-es*-2→Q-gs, and S-es*-

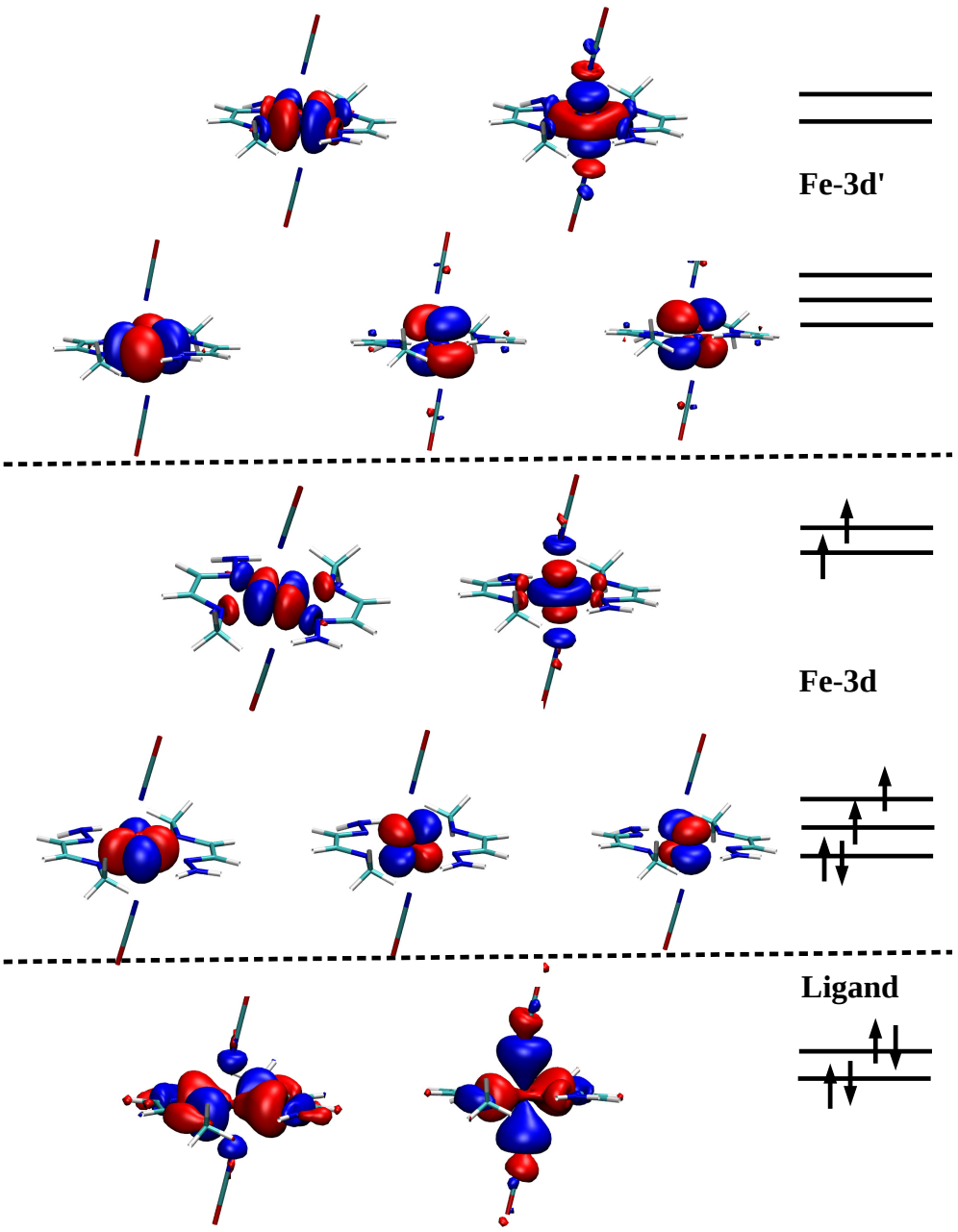

Figure 3.8: The natural orbitals in HS [10e,12o] CASSCF calculation along with their occupations.

1→T-es*-4→Q es*-3→Q-gs, as found for CASSCF.

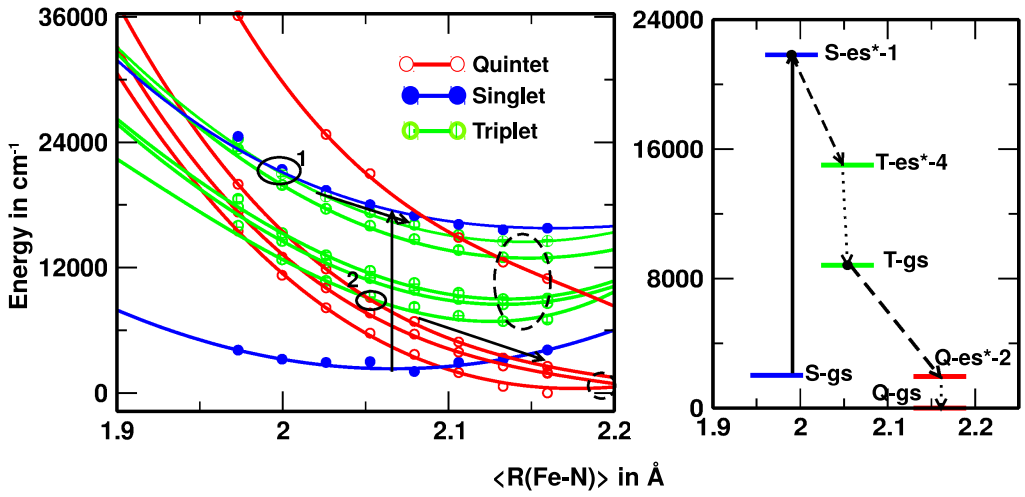

Figure 3.9: Left panel shows PECs of the low-lying energy states of the SCO model system as functions of the mean Fe-N distances resulting from CASSCF calculation. Blue lines with closed circles denote the singlet states, red lines with open circles denote the quintet states, and green lines with hashed circles denote the triplet states. We also indicate the possible LIESST pathway using arrows i.e., S-es*-1→T-es*-4→T-gs→Q-es*-2→Q-gs. Labels 1 and 2 indicate the first and second crossings. The right panel shows the pathway in terms of the energy level diagram. The solid line refers to electronic transition, the dashed line refers to ISC and the dotted line refers to the IC step. Black dots refer to the crossing point between the excited states involving ISC.

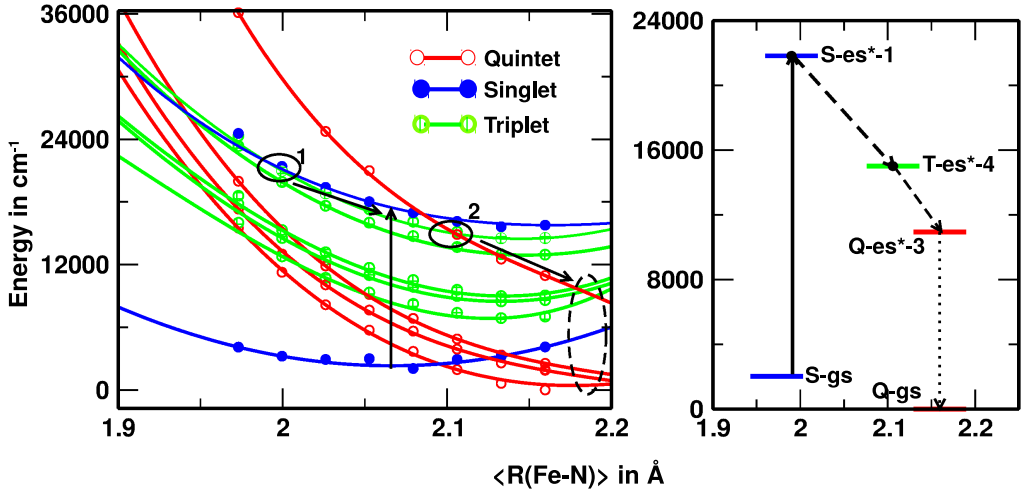

Figure 3.10: Same as in Figure 3.9, but shown for the second possible pathway (S-es*-1→T-es*-4→Q-es*-3→Q-gs), as suggested in CASSCF calculation.

Functional	**CASSCF**	**CASPT2**
ΔE_{HL} in cm^{-1}	-2040	-1229

Table 3.3: Comparison of Ground HS-LS state splitting calculated within CASSCF and CASPT2 theory

3.3.3 Calculated Rate Constants

As discussed in the chapter-1, low-temperature HS→LS relaxation rate involves two components, one is electronic and the other is nuclear. The electronic contribution thus can be computed from knowledge of energy differences $\Delta E_{S(Q),j}$, and SOC matrix elements. Similarly, the nuclear contribution can be computed from the horizontal (for s) and vertical (for p) displacements of the HS and LS ground

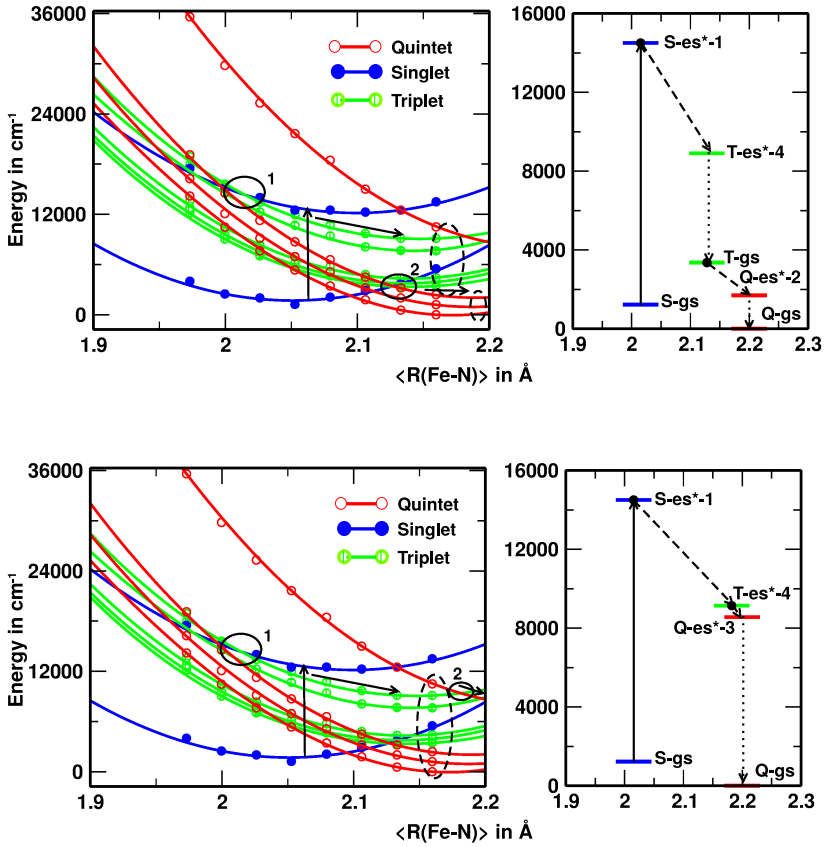

Figure 3.11: Same as Figure-1 but resulting from CASPT2 calculation. LIESST pathways for top panel: S-es*-1→T-es*-4→T-gs→Q-es*-2→Q-gs and for bottom panel: S-es*-1→T-es*-4→Q-es*-3→Q-gs

states relative to each other, vibrational frequencies (ω) and force constant (f) associated with the excited states. As discussed above, TDDFT within B3YLP provides three possible pathways for LIESST of the studied system, while CASSCF and CASPT2 calculation results in two possible pathways. Out of the three TDDFT(B3LYP) suggested pathways, the first and second processes involve two intermediate states coupled by two ISC steps and one IC step, while the third one involves three intermediate states coupled by two ISC steps and two IC steps. Out of the two CASSCF and CASPT2 pathways, the first one involves two intermediate states coupled by two ISC steps and one IC step, and the second one involves three intermediate states coupled by two ISC steps and two IC steps. The choice of M06-L and OLYP functionals in TDDFT, on the other hand, provides two and one possible pathways, involving two ISC steps and one IC step for both processes in M06-L, and two ISC steps in OLYP (see figure-3.5, 3.6, 3.7 for details). The energy difference $\Delta E_{S(Q),j}$ and SOC matrix elements involved in the ISC processes of LIESST mechanism for TDDFT and CASSCF/CASPT2 study are shown in Table 3.4 and Table 3.5, respectively.

Functional	**Process**	ISC states	**SOC** (cm^{-1})	ΔE (cm^{-1})
B3LYP	S-es*-1→T-es*-1→	S-es*-1, T-es*-1	35.72	4113
	Q-es*-1→Q-gs	T-es*-1, Q-es*-1	39.23	5484
	S-es*-1→T-es*-1→	S-es*-1, T-es*-1	35.72	4113
	Q-es*-2→Q-gs	T-es*-1, Q-es*-2	19.31	3629
	S-es*-1→T-es*-1→T-gs→	S-es*-1, T-es*-1	35.72	4113
	Q-es*-1→Q-gs	T-gs, Q-es*-1	28.32	3387
M06-L	S-es*-1→T-es*-1→	S-es*-1, T-es*-1	19.64	455
	Q-es*-1→Q-gs	T-es*-1, Q-es*-1	12.65	4085
	S-es*-1→T-es*-1→	S-es*-1, T-es*-1	19.64	455
	T-gs→Q-gs	T-gs, Q-gs	11.25	4588
OLYP	S-es*-1→T-gs→Q-gs	S-es*-1, T-gs	16.75	415
		T-gs, Q-gs	11.50	4678

Table 3.4: The pathway, involved energy states, SOC matrix element, and involved energy denominators for LIESST as given in TDDFT calculations, with the choice of various functionals.

For the calculation of the nuclear part of the rate constant, we assume that the PECs are harmonic in nature. The corresponding force constants are evaluated by fitting the PECs in a quadratic equation and vibrational frequency ω is determined using the reduced mass of the coordinating atoms (= 14) as suggested by Buhks et al.[24] Using these values, Huang-Rhys factor, s and reduced energy gap, p are calculated for TDDFT and CASSCF electronic states using Eq.(1.4)

and Eq.(1.5), respectively. Finally, the relaxation rate constant is estimated using Eq.(1.1). Table 3.6 shows the comparison of rate constants and their governing parameters resulting from both TDDFT and CASSCF/CASPT2 calculations.

Method	**Process**	ISC states	**SOC** (cm^{-1})	ΔE (cm^{-1})
CASSCF	S-es*-1→T-es*-4→T-gs→	S-es*-1, T-es*-4	76.32	1129
	Q-es*-2→Q-gs	T-gs, Q-es*-2	87.87	4355
	S-es*-1→T-es*-4→	S-es*-1, T-es*-4	76.32	1129
	Q-es*-3→Q-gs	T-es*-4, Q-es*-3	68.95	3549
CASPT2	S-es*-1→T-es*-4→T-gs→	S-es*-1, T-es*-4	112.46	3157
	Q-es*-2→Q-gs	T-gs, Q-es*-2	346.94	944
	S-es*-1→T-es*-4→	S-es*-1, T-es*-4	112.46	3157
	Q-es*-3→Q-gs	T-es*-4, Q-es*-3	86.42	452

Table 3.5: The pathway, involved energy states, SOC matrix element, and involved energy denominators for LIESST as given in CASSCF and CASPT2 calculations.

Considering the different possible pathways, and their associated relaxation rates, the LIESST process will be determined by the fastest process. Thus among the considered low-energy states and the processes, suggested by TDDFT in its B3LYP flavor, the LIESST mechanism will be dominantly contributed by S-es*-1→T-es*-1→Q-es*-1→Q-gs process with a rate of 7.89 $\times$ 10^{-1} sec^{-1}. Use of M06-L functional within TDDFT produces a comparable rate of 9.5 $\times$ 10^{-1} sec^{-1}, while OLYP gives a rate of 3.46 $\times$ 10^{-1} sec^{-1}. Thus, the three functionals tested in this study, provide rates that are consistent with each other, within the accuracy range of various functionals.

Moving to multireference approaches, as suggested by CASSCF, it will be contributed by S-es*-1→T-es*-4→T-gs→Q-es*-2→Q-gs with a rate of 7.57 $\times$ 10^{-5} sec^{-1}. Inclusion of dynamical correlation within CASPT2, the rate corresponding to the process contributed by S-es*-1→T-es*-4→T-gs→Q-es*-2→Q-gs, becomes 1.76 $\times$ 10^{-3} sec^{-1}, which is two orders of magnitude faster than that suggested by CASSCF, and closer to TDDFT estimates.

As mentioned, Hauser et al.[5] measured the relaxation rates for several Fe(II) coordination compounds using time-dependent optical spectroscopy, which showed a large variation over a range of 12 orders of magnitude. From the summarized data, presented in Table I of Ref.[5], a correlation between $T_{1/2}$, reduced energy gap, and the rate is noticed. Following that trend, with $T_{1/2}$ value of 180K of $[Fe(abpt)_2(NCS)_2]$, the p value would have been in the range 3-4, relaxation rate being of the order of 10^{-1} sec^{-1}. The TDDFT calculated value of p of 3 and rates in the range 6-7 $\times$ 10^{-1} sec^{-1} for the model system thus fits this trend,

Method	**Process**	**f**	**s**	**p**	β_{HL} **(cm^{-1})**	k_{HL} **(sec^{-1})**
TDDFT (B3YLP)	**1.** S-es*-1→T-es*-1→ Q-es*-1→Q-gs	3.44	28.83	3	0.5974	7.89 $\times 10^{-1}$
	2. S-es*-1→T-es*-1→ Q-es*-2→Q-gs				0.3578	2.84 $\times 10^{-1}$
	3.S-es*-1→T-es*-1→T-gs→ Q-es*-1→Q-gs				0.5446	6.57 $\times 10^{-1}$
TDDFT (M06-L)	**1.** S-es*-1→T-es*-1→ Q-es*-1→Q-gs	3.49	28.63	3	0.6071	9.5 $\times 10^{-1}$
	2. S-es*-1→T-es*-1→ T-gs→Q-gs				0.5340	7.35 $\times 10^{-1}$
TDDFT (OLYP)	**1.** S-es*-1→T-gs→ Q-gs	2.51	24.34	1	0.5053	3.46 $\times 10^{-1}$
CASSCF	**1.** S-es*-1→T-es*-4→T-gs→ Q-es*-2→Q-gs	7.36	41.20	2	7.48	7.57 $\times 10^{-5}$
	2. S-es*-1→T-es*-4→ Q-es*-3→Q-gs				6.14	5.11 $\times 10^{-5}$
CASPT2	**1.** S-es*-1→T-es*-4→T-gs→ Q-es*-2→Q-gs	6.46	38.98	1	53.69	1.76 $\times 10^{-3}$
	2. S-es*-1→T-es*-4→ Q-es*-3→Q-gs				24.58	0.37 $\times 10^{-3}$

Table 3.6: Force constant(f) $\times 10^5$ in dyne/cm, Huang-Rhys factor(s), reduced energy gap(p), electronic coupling matrix element(β_{HL}), and rate constant(k_{HL}) determined for different suggested pathways by TDDFT with choice of different functional, and multi-reference approaches like CASSCF and CASPT2

.

while CASSCF with its severe caveat of the negative value of ΔE_{HS} gives the rate much slower (10^{-5} sec^{-1}) with a smaller p value of 2. Treatment of dynamical correlation within the CASPT2 framework improves the situation in terms of having a less negative ΔE_{HS}, and a rate that is closer to expected.

3.4 Conclusions and Discussions

To conclude, motivated by the challenging nature of the problem, we computationally investigate the LIESST problem, and compare the results of two complementary techniques of multi configurational wave function-based approach (CASSCF/CASPT2) and density functional-based approach (TDDFT). To make

the computation tractable, we consider a hypothetical model system built from a real complex, showing thermal SCO and LIESST. In building up the model system, the geometry of the SCO core, FeN_6 is kept fixed as in real complex, while the long-range, complex structure of the ligand is simplified considerably, maintaining the asymmetry of the ligand field of the real complex. Comparing the results of TDDFT in its different flavors of choice of functionals and CASSCF within our computational parameter settings, firstly we find CASSCF gives rise to unphysical stabilization of HS state over LS state, contradicting SCO behavior of the studied material, while the DFT with choice of different functionals shows the correct stability. CASPT2 calculations to include the effect of dynamical correlation, make the unphysical stabilization of HS state over LS state much less severe, compared to that in CASSCF, stressing the importance of inclusion of dynamical effect. Continuing nevertheless with the calculation of PECs of the low-energy states, identification of crossing points and resultant LIESST pathways, and the spin-orbit coupling matrix at crossing points, we compute the electronic contributions in the two methods. Incorporating this information along with the evaluation of nuclear contribution within the Franck-Condon model, we arrive at computed values of rate constants of the studied system. Based on the comparison of computed rates with the experimentally found trend[28] we conclude that the rates are captured reasonably by TDDFT.

We end the discussion with possible scopes of improvement. As reflected in the present study, the inclusion of dynamical correlation within the scope of the multi-reference approach is important, to capture the correct ground state stability. Our treatment of dynamical correlation with CASPT2 indicates that to be the right direction, but cannot fix the problem fully. Higher order treatment of complete active space perturbation theory or multi-reference configuration interaction (MRCI) method may be explored in this context. Moreover, the possible participation of ligands in the relaxation process needs to be explored.[29]

References

[1] J. F. Létard, P. Guionneau, and L. Goux-Capes, *Spin Crossover in Transition Metal Compounds I-III: Gütlich, P., Goodwinpp, H.* Springer: Berlin, Germany, 2004.

[2] J. Linares, E. Codjovi, and Y. Garcia, "Pressure and temperature spin crossover sensors with optical detection," *Sensors*, vol. 12, no. 4, pp. 4479–4492, 2012.

[3] S. Cobo, G. Molnár, J. A. Real, and A. Bousseksou, "Multilayer sequential assembly of thin films that display room-temperature spin crossover with hysteresis," *Angewandte Chemie International Edition*, vol. 45, no. 35, pp. 5786–5789, 2006.

[4] S. Decurtins, P. Gütlich, C. Köhler, H. Spiering, and A. Hauser, "Light-induced excited spin state trapping in a transition-metal complex: The hexa-1-propyltetrazole-iron (ii) tetrafluoroborate spin-crossover system," *Chemical physics letters*, vol. 105, no. 1, pp. 1–4, 1984.

[5] A. Hauser, A. Vef, and P. Adler, "Intersystem crossing dynamics in fe (ii) coordination compounds," *The Journal of chemical physics*, vol. 95, no. 12, pp. 8710–8717, 1991.

[6] K. P. Kepp, "Consistent descriptions of metal–ligand bonds and spin-crossover in inorganic chemistry," *Coordination Chemistry Reviews*, vol. 257, no. 1, pp. 196–209, 2013.

[7] H. E. Mason, W. Li, M. A. Carpenter, M. L. Hamilton, J. A. Howard, and H. A. Sparkes, "Structural and spectroscopic characterisation of the spin crossover in [fe (abpt) 2 (ncs) 2] polymorph a," *New Journal of Chemistry*, vol. 40, no. 3, pp. 2466–2478, 2016.

[8] Y. Shao, Z. Gan, E. Epifanovsky, A. T. Gilbert, M. Wormit, J. Kussmann, A. W. Lange, A. Behn, J. Deng, X. Feng, *et al.*, "Advances in molecular quantum chemistry contained in the q-chem 4 program package," *Molecular Physics*, vol. 113, no. 2, pp. 184–215, 2015.

[9] A. D. Becke, "Density-functional thermochemistry. iii. the role of exact exchange," *The Journal of Chemical Physics*, vol. 98, no. 7, pp. 5648–5652, 1993.

[10] S. H. Vosko, L. Wilk, and M. Nusair, "Accurate spin-dependent electron liquid correlation energies for local spin density calculations: a critical analysis," *Canadian Journal of physics*, vol. 58, no. 8, pp. 1200–1211, 1980.

[11] A. D. Becke, "Density-functional exchange-energy approximation with correct asymptotic behavior," *Physical review A*, vol. 38, no. 6, p. 3098, 1988.

[12] C. Lee, W. Yang, and R. G. Parr, "Development of the colle-salvetti correlation-energy formula into a functional of the electron density," *Physical review B*, vol. 37, no. 2, p. 785, 1988.

[13] A. Schäfer, C. Huber, and R. Ahlrichs, "Fully optimized contracted gaussian basis sets of triple zeta valence quality for atoms li to kr," *The Journal of Chemical Physics*, vol. 100, no. 8, pp. 5829–5835, 1994.

[14] Y. Zhao and D. G. Truhlar, "A new local density functional for main-group thermochemistry, transition metal bonding, thermochemical kinetics, and noncovalent interactions," *The Journal of chemical physics*, vol. 125, no. 19, p. 194101, 2006.

[15] N. C. Handy and A. J. Cohen, "Left-right correlation energy," *Molecular Physics*, vol. 99, no. 5, pp. 403–412, 2001.

[16] E. Runge and E. K. Gross, "Density-functional theory for time-dependent systems," *Physical Review Letters*, vol. 52, no. 12, p. 997, 1984.

[17] B. O. Roos, P. R. Taylor, P. E. Si, *et al.*, "A complete active space scf method (casscf) using a density matrix formulated super-ci approach," *Chemical*

Physics, vol. 48, no. 2, pp. 157–173, 1980.

[18] K. Andersson, P.-Å. Malmqvist, and B. O. Roos, "Second-order perturbation theory with a complete active space self-consistent field reference function," *The Journal of chemical physics*, vol. 96, no. 2, pp. 1218–1226, 1992.

[19] H.-J. Werner, P. J. Knowles, G. Knizia, F. R. Manby, M. Schütz, P. Celani, W. Györffy, D. Kats, T. Korona, R. Lindh, A. Mitrushenkov, G. Rauhut, K. R. Shamasundar, T. B. Adler, R. D. Amos, S. J. Bennie, A. Bernhardsson, A. Berning, D. L. Cooper, M. J. O. Deegan, A. J. Dobbyn, F. Eckert, E. Goll, C. Hampel, A. Hesselmann, G. Hetzer, T. Hrenar, G. Jansen, C. Köppl, S. J. R. Lee, Y. Liu, A. W. Lloyd, Q. Ma, R. A. Mata, A. J. May, S. J. McNicholas, W. Meyer, T. F. Miller III, M. E. Mura, A. Nicklass, D. P. O'Neill, P. Palmieri, D. Peng, K. Pflüger, R. Pitzer, M. Reiher, T. Shiozaki, H. Stoll, A. J. Stone, R. Tarroni, T. Thorsteinsson, M. Wang, and M. Welborn, "Molpro, version 2019.2, a package of ab initio programs," 2019.

[20] G. Breit, "Dirac's equation and the spin-spin interactions of two electrons," *Physical Review*, vol. 39, no. 4, p. 616, 1932.

[21] N. Suaud, M.-L. Bonnet, C. Boilleau, P. Labeguerie, and N. Guihéry, "Light-induced excited spin state trapping: ab initio study of the physics at the molecular level," *Journal of the American Chemical Society*, vol. 131, no. 2, pp. 715–722, 2008.

[22] A. Hauser, "Intersystem crossing in iron (ii) coordination compounds: a model process between classical and quantum mechanical behaviour," *Comments on Inorganic Chemistry*, vol. 17, no. 1, pp. 17–40, 1995.

[23] A. Hauser, "Intersystem crossing in fe (ii) coordination compounds," *Coordination Chemistry Reviews*, vol. 111, pp. 275–290, 1991.

[24] E. Buhks, G. Navon, M. Bixon, and J. Jortner, "Spin conversion processes in solutions," *Journal of the American Chemical Society*, vol. 102, no. 9, pp. 2918–2923, 1980.

[25] J. Conradie and A. Ghosh, "Dft calculations on the spin-crossover complex fe (salen)(no): a quest for the best functional," *The Journal of Physical Chemistry B*, vol. 111, no. 44, pp. 12621–12624, 2007.

[26] R. G. Parr and W. Yang, *Density-Functional Theory of Atoms and Molecules*. Oxford University Press, New york, 1989.

[27] K. Pierloot and S. Vancoillie, "Relative energy of the high-(t 2 g 5) and low-(a 1 g 1) spin states of [fe (h 2 o) 6] 2+,[fe (nh 3) 6] 2+, and [fe (bpy) 3] 2+: Caspt2 versus density functional theory," *The Journal of chemical physics*, vol. 125, no. 12, p. 124303, 2006.

[28] A. Hauser, A. Vef, and P. Adler, "Intersystem crossing dynamics in fe (ii) coordination compounds," *The Journal of chemical physics*, vol. 95, no. 12, pp. 8710–8717, 1991.

[29] H. Ando, Y. Nakao, H. Sato, and S. Sakaki, "Theoretical study of low-

spin, high-spin, and intermediate-spin states of [feiii (pap) 2]+(pap= n-2-pyridylmethylidene-2-hydroxyphenylaminato). mechanism of light-induced excited spin state trapping," *The Journal of Physical Chemistry A*, vol. 111, no. 25, pp. 5515–5522, 2007.

Chapter 4

Trend in Light-Induced Excited-State Spin Trapping in Fe(II)-based Spin Crossover Systems*

4.1 Introduction

As discussed, Fe(II) based molecular complexes are well researched for their SCO behavior because of their robust and prompt switching of spin state in response to external stimuli compared to other TM ions. [1–3] In particular, the first-hand understanding of the dynamics of the light-induced excited spin-state trapping (LIESST) process of these complexes can be obtained in terms of the relaxation model based on the Franck-Condon principle as proposed by Hauser et al.[4–6] The model describes the possible relaxation pathway of the optically triggered complex from excited LS state to metastable HS state via intermediate states which may involve several intersystem crossing (ISC) and internal conversion (IC)[4] as elaborated in Chapter 3 where we utilize the Relaxation model to compute low-temperature HS to LS relaxation rate k_{HL} (T→0) on a model system derived out of [Fe(abpt)$_2$ (NCS)$_2$]. k_{HL} (T→0) of the LIESST process is dictated by the particular pathway. A systematic study of HS to LS relaxation rate k_{HL} (T) was done by Hauser et al[7] for several Fe(II) coordination complexes in dilute mixed crystal form in the temperature range 10-270K. From optical spectroscopy measurement, they showed[7] that k_{HL} (T→0) may vary 14 orders of magnitude, from $\sim 10^{-6}$ to $\sim 10^{8}$ s^{-1}, depending on the choice of the organic ligands. A long-lived metastable HS state was found in [Fe(ptz)$_6$](BF$_4$)$_2$ indicated by a small

*This chapter is based on publication : **Shiladitya Karmakar**, Pradip Chakraborty, and Tanusri Saha-Dasgupta, *Physical Chemistry Chemical Physics*, **24.17**, 10201-10209 (2022).

value of rate constant (10^{-6} s^{-1}) leading to slow relaxation.[8] On the other hand, $[Fe(bipy)_6](PF_6)_2$ showed a high value of k_{HL} (T→0) of 10^6 s^{-1}.[9] The exact reason for this large variation in low-temperature relaxation rate is yet to be revealed. In this chapter, a computational study of the LIESST in a number of Fe(II) spin crossover complexes, coordinated by monodentate, bidentate, and multidentate ligands is carried out, with the goal to uncover the trend in the low-temperature relaxation rate.

As concluded in chapter-3, despite its single reference character DFT-based time-dependent density functional theory (TDDFT) with a suitable choice of exchange-correlation functional may produce a reasonable value of k_{HL}, agreeing well with that of actual compound $[Fe(abpt)_2(NCS)_2]$. This makes the situation feasible to apply the TDDFT tools for the microscopic understanding of the large variation of rate constant depending on the choice of ligands of varying degrees of size and complexity. Motivated by these findings in the present chapter, we explore this possibility by considering four different ligands, 1-propyltetrazole (ptz)[10], 2-picolylamine (pic)[11], tris4-[(6-methyl)-2-pyridyl]-3-aza-butenylamine ($(mepy)_3$tren)[12], 2,2'-bipyridine (bipy)[13], as shown in Fig. 4.1. The choice of the specific ligands is primarily based on the relative stability of their charge-transfer and ligand-field electronic states. The geometry of the ligands is expected to exhibit the progressive stabilization of the charge-transfer and ligand-field states from 1-propyltetrazole to 2,2'-bipyridine. The choice is further guided by the availability of the experimental data of the studied Fe(II) complexes.[10–13] Finally, k_{HL} (T→0) of the chosen complexes are estimated and their microscopic origin of large variation in k_{HL} (T→0) is explored.

4.2 Computational Details

The reference geometries $[Fe(ptz)_6]^{2+}$, $[Fe(pic)_3]^{2+}$, $[Fe(mepy)_3(tren)]^{2+}$ and $[Fe(bipy)_3]^{2+}$ used for electronic structure calculation are obtained from the experimental crystal structure provided in Ref.[10–13] respectively. Electronic structure calculations are performed within the framework of density functional theory to obtain ground states and time dependent density functional theory to obtain the low-lying excited states of singlet, triplet and quintet spin symmetries as implemented in the Gaussian16 package.[14] For a LIESST compound ΔE^0_{HL} should be positive and the sign of ΔE^0_{HL} i.e., stability of spin state is found to sensitively depend on the exchange correlation (XC) functional used in DFT calculation. To obtain the optimal XC functional capturing correct ground state for all four LIESST compounds, we use the following six different kinds (in total 21) of XC functional as available in Gaussian16[14] package: 1) GGA (PBE[15], BLYP[16, 17], BP86[18, 19], OLYP[20], HCTCH/407[21]), 2)hybrid GGA (B3LYP[22], B3LYP*[23], X3LYP[24], PBE0[25, 26], B97[27],

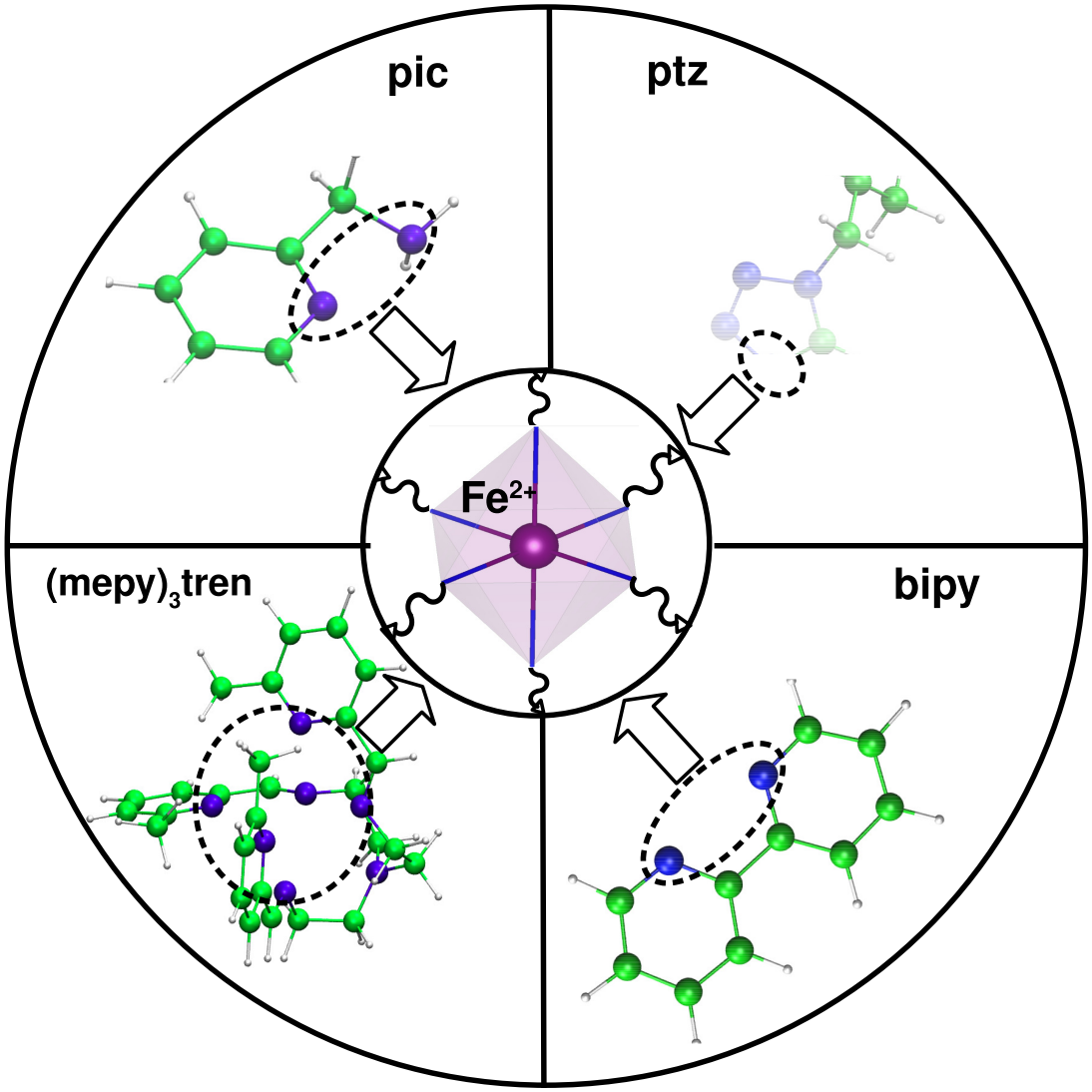

Figure 4.1: Four Fe(II) based metal-organic complexes, considered in the present study. Four organic ligands with different nature of coordination namely bidentate 2-picolylamine (pic), monodentate 1-propyltetrazole (ptz), hexadentate tris4-[(6-methyl)-2-pyridyl]-3-aza-butenylamine ($(mepy)_3$tren) and bidentate 2,2'-bipyridine (bipy) are shown schematically in four different quadrants of the outer annular region. Fe, N, C, and H atoms are shown as big-magenta, medium-blue, medium-green, and small-white balls, respectively. N atoms of each ligand that contribute to Fe(II)-ligand coordination sphere are highlighted by dashed circle. The inner circular region shows the octahedral coordination of Fe(II) ion associated with each complex.

B98[28]), 3) meta GGA (TPSS[29], M06-L[30], PKZB[31, 32]), 4) hybrid meta GGA (TPSSh[33], M05[34, 35], M06[36]), 5) range separated hybrid (CAM-B3LYP[37], LC-BLYP[38, 39]), 6) double hybrid (B2-PLYP[40], mPW2-PLYP[41]). The triple zeta valence basis set (def2-TZVP[42]), Gaussian kind basis set as implemented in [14], is used for all the atoms. The effect of basis set was carefully checked, by repeating calculations with cc-pVTZ[43] and 6-311G[44] basis sets, and best performance was found to be with choice of def2-TZVP. To get the potential energy curves (PEC's), six intermediate geometries are generated in between HS and LS geometries of corresponding compounds by the linear interpolation method. To calculate the spin-orbit coupling matrix element at ISC points, one-electron Breit Pauli Hamiltonian[45] is employed as implemented in pySOC code[46].

To analyze the covalency associated with each Fe-N bond contributed in FeN_6 octahedra for LIESST compounds, we calculate the Crystal Orbital Hamiltonian Population (COHP)[47]. COHP, the density of states weighted by the corresponding Hamiltonian matrix element, provides the energy resolved visualization of chemical bonding. For this purpose, LS geometry of each complex is used and non-spin polarized DFT calculation is carried out using projector augmented-wave pseudopotentials and the Perdew-Burke-Ernzerhof generalized gradient approximation (PBE-GGA)[48] as the exchange correlation functional as implemented in the plane-wave-based Vienna ab initio simulation package (VASP)[49]. The cutoff energy of the plane-wave basis is chosen to be 520 eV. To build the periodic setup, each complex is put inside a simple cubic supercell, so that the vacuum separation between the complex and its neighboring images is maintained at around 12 $\mathring{A}$. Reciprocal space integrations for self consistent field calculations are performed at the Γ point. Projected COHP is calculated by taking the projection into an auxiliary linear combination of atomic orbitals (LCAO) basis using the Lobster code[50]. The consistency of results between Gaussian and plane wave calculations has been checked.

4.3 Results

4.3.1 Exchange correlation and HS-LS energy gap

Thermodynamically, the enthalpy gap between the HS and the LS states of the SCO complex should be of the order of thermally accessible energies, k_BT. It favours the LS state at low temperature and is overcome by entropy difference as temperature increases favouring the HS state leading to entropy driven thermal spin transition. Structure-wise, LS to HS transition is accompanied by considerable elongation of the iron-ligand bond length in HS state (r_{HS}) compared to that of LS state (r_{LS}), consistent with the promotion of two electrons from the octahedrally split non-bonding t_{2g} orbitals to the antibonding e_g orbitals. Typically for

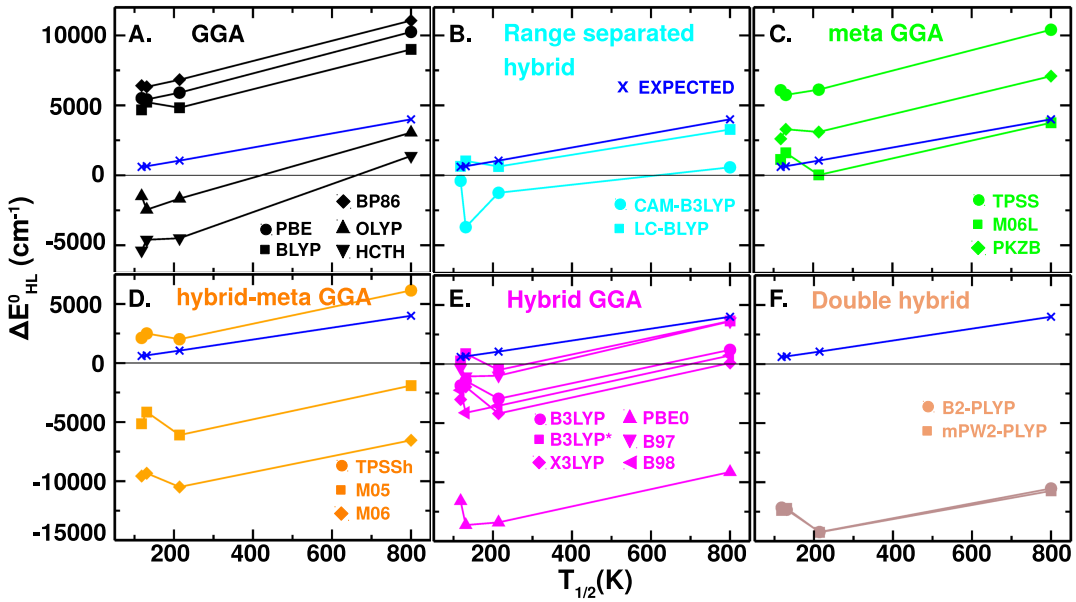

Figure 4.2: Calculated values of ΔE^0_{HL} plotted against $T_{1/2}$ for four different complexes, for a choice of range of XC functionals, belonging to the broad class of GGA (A), range separated GGA (B), meta GGA (C), hybrid-meta GGA (D), hybrid GGA (E), and double hybrid (F). The lines are guide to eye, with each data point representing the specific compound. The ΔE^0_{HL} values estimated from measured $T_{1/2}$ are also shown for comparison, as a blue line with data-points of compounds in asterisk symbols.

Fe^{2+} ions, ΔR_{HL} = r_{HS} - r_{LS} is found to lie in the range of 0.16-0.22$\mathring{A}$. Hence, the two parameters, ΔE_{HS-LS} and ΔR_{HL} signifying the vertical and horizontal displacement of ground state potential energy curve, respectively, play key roles in determining the low temperature HS to LS relaxation rate.

In the following we discuss the estimation of the electronic energy difference between HS and LS states of the SCO compound i.e., $\Delta E^0_{HL} = E_{HS} - E_{LS}$. This quantity can be approximately set equal to standard enthalpy difference ΔH^0_{HL} and roughly estimated by the following relation $\Delta E^0_{HL} \approx \Delta H^0_{HL} = \Delta S^0_{HL} T_{1/2}$ where $T_{1/2}$ is the thermal spin transition temperature and ΔS^0_{HL} is the entropy difference. Although ΔS^0_{HL} is dependent on SCO complex, but it is found to vary within a small range ($\sim 5 cm^{-1}K^{-1}$)[4]. So given the experimental value of $T_{1/2}$ of SCO complexes, it is possible to have an experimental estimate of ΔE^0_{HL}. ΔE^0_{HL} values estimated from experimentally reported $T_{1/2}$ together with k_{HL} (T$\rightarrow$0), for the four complexes under study are listed in Table 4.1.

Since the numerical value of ΔE^0_{HL} is small, its calculation is extremely sensitive to a bias towards a particular spin multiplicity. Hartree Fock (HF) method systematically favours higher spin multiplicities since the correlation between electrons with the same spin projection (Fermi correlation) is taken into account by exchange interaction. For example, the four unpaired 3d electrons in a Fe(II) HS complex avoid each other to a large extent due to the orthogonality of the 3d orbitals. On the other hand, in the LS complex, three lower energy 3d orbitals are doubly occupied. Due to the monodeterminantal form of the wavefunction, the spin-up and spin-down electrons occupying the same 3d orbital cannot avoid each other to the same extent. As a result, in the LS case, the Coulomb repulsion between the electrons is too large. Within the wavefunction based theory, the accuracy of the results beyond HF can be systematically improved by resorting to methods by improving the treatment of the static and dynamic correlation effects, for example through complete active space self-consistent field (CASSCF)[51] or computationally more expensive CASPT2[52]. Our previous model study[53] discussed in the chapter-3 showed even the use of CASSCF could not remedy the issue of HF namely ΔE^0_{HL} turned out to be negative. ΔE^0_{HL} , calculated within CASPT2, turned to be also negative but was found to have a significantly reduced value compared to CASSCF. This undoubtedly hints towards the importance of inclusion of the dynamical effect, which possibly requires even improved treatment of the dynamical correlation beyond CASPT2, through high-level coupled-cluster (CC) methods[54–56]. However, such methods are significantly limited by system size. For example, the CCSD and CCSDT methods have canonical scaling of $O(N^6)$ and $O(N^8)$, respectively, thus making them unsuitable for studying the trend involving simple to complex ligands of varying sizes. In contrast, the application of DFT is not restricted to small system sizes, due to its single reference nature.

In DFT approach, on the other hand, the results are strongly dependent on the

Compound	**Reference**	$T_{1/2}$**(K)**	Δ $\mathbf{E}^0_{HL}$ (cm^{-1})	$\mathbf{k}_{HL}$ (T $\rightarrow$ 0) (s^{-1})
$[Fe(ptz)_6](BF_4)_2$	Ref[8]	T$\uparrow$ = 128K T$\downarrow$ = 134K	655	3×10^{-5}
$[Fe(pic)_3]Cl_2$.MeOH	Ref[8]	T1 = 122K T2 = 114K	590	5×10^{-4}
$[Fe(mepy)_3(tren)](PF_6)_2$	Ref[12]	214K	1070	7.2×10^{-2}
$[Fe(bipy)_3](PF_6)_2$	Ref[9]	800K LS	4000	10^4 - 10^8

Table 4.1: Estimated value of ΔE^0_{HL} from $T_{1/2}$, and reported value of k_{HL} in literature.[8, 9, 12]

exchange-correlation (XC) functional used. ΔE^0_{HL} is thus computed for a range of 21 different exchange correlation functionals of varying degrees of sophistication of the functional, belonging to the broad class of GGA (PBE, BLYP, BP86, OLYP, HCTCH/407), hybrid GGA (B3LYP, B3LYP*, X3LYP, PBE0, B97, B98), meta GGA (TPSS, M06-L, PKZB), hybrid meta GGA (TPSSh, M05, M06), range separated hybrid (CAM-B3LYP, LC-BLYP), double hybrid (B2-PLYP, mPW2-PLYP). A brief review of the mentioned functionals are given in the chapter-2. We judge the performance of different functionals by comparing the calculated ΔE^0_{HL} with experimentally determined estimates of ΔE^0_{HL}. The goal is to find a choice of XC functional, that provides optimized performance for all four compounds. The results are summarized in Fig 4.2.

As found, double hybrid functionals strongly underestimate ΔE^0_{HL} and fail to provide the correct sign for all compounds. Among the range separated hybrid functional, CAM-B3LYP underestimates the ΔE^0_{HL} and fails to provide the right sign except for bipy compound. Within hybrid meta functionals, M05, M06 underestimate ΔE^0_{HL} and fail to provide the correct sign. TPSSh tends to give the correct sign, but overestimates ΔE^0_{HL}. Most of the Hybrid Functionals underestimate ΔE^0_{HL} and often fail to produce right sign. Within GGA, PBE, BLYP, BP86 overestimates ΔE^0_{HL}, though tend to produce the right sign. HCTH and OLYP on the other hand, underestimate ΔE^0_{HL}. The best performance is found to be that of range separated hybrid functional of LC-BYLP, followed by meta GGA functional of M06L. The deviation from the expected values in LC-BLYP was found to be within 1-2 kcal/mol for all four compounds (1.09 for ptz, -1.22 for mepy-tren, 0.10 for pic and -2.1 for bipy). In the remaining part of the study, the calculations are carried out with the choice of LC-BYLP XC and choice of def2-TZVP basis set.

Complex	**Process**	ISC states	**SOC** (cm^{-1})	ΔE (cm^{-1})	β_{HL} ($\mathbf{cm^{-1}}$)
$[Fe(ptz)_6]^{2+}$	S-es*-1→T-es*-4	S-es*-1, T-es*-4	107	5640	2.07
	→T-gs→Q-gs	T-gs, Q-gs	91	4730	
$[Fe(pic)_3]^{2+}$	S-es*-1→T-es*-3	S-es*-1, T-es*-3	110	2822	4.99
	→T-gs→Q-gs	T-gs, Q-gs	78	4382	

Table 4.2: The calculated pathway, involved energy states, SOC matrix element, and involved energy denominators for LIESST of ptz and pic complexes.

4.3.2 LIESST mechanism and Calculated Rate Constant

The mechanism of LIESST is complex and its description strongly depends on the nature of the chosen ligand. A possible scenario is d-d excitation-deexcitation scenario, which holds when the d manifold is widely separated from the metal-ligand charge-transfer (MLCT) manifold. The d manifold for ptz complexes has been shown to be widely separated from the charge-transfer manifold[57]. Although there is no report focusing exclusively on the ultrafast dynamics of the pic-complex, we envision that since the nature of the complex is very similar to ptz-complex, pic-complex would show similar excited state energetics and LIESST mechanism.[58] Thus, d-d excitation-deexcitation scenario is a valid scenario for the two out of four complexes under discussion namely ptz and pic complexes.

However, the LIESST mechanism is expected to be different and much more complicated for [(6-mepy)$_3$tren] and bipy complexes where the charge-transfer states are low-lying and would hide the d-d transition of the LS species. The ultrafast dynamics for [(6-mepy)$_3$tren] and its low-spin analog [(py)$_3$tren] were probed and explained in detail by McCusker and coworkers that show a rather complicated relaxation pathway upon excitation into the charge-transfer states [59–61]. For bipy, the excited state dynamics and the role of ligand-field states are complicated and debatable. As covered in the landmark work by Aubock and Chergui [62] and Bressler et al. [63] as well as in [64], the photoexcitation and relaxation process in the bipy complex possibly is a complicated pathway involving both MLCT and d states. Although the photoexcitation from the ground LS state to the excited d manifolds is not possible for [(6-mepy)$_3$tren] and bipy complexes, the role and involvement of the intermediate d states during LIESST via excited states relaxation are, however, found to be non-negligible [65, 66]

Keeping the above complex scenario in mind, in the following we thus focus on only ptz and pic complexes, for which d-d excitation-deexcitation scenario is a valid scenario, without the complexity of MLCT states.

Within the d-d excitation-deexcitation scenario, the possible pathway of LIESST involves photoexcitation of the LS singlet ground state to excited singlet state,

followed by relaxation process to intermediate states and finally to metastable HS quintet ground state, being trapped at cryogenic temperature (typically T < 50 K), before relaxing back to the LS ground state. Low lying triplet and excited quintet states may play the role of intermediate states. The first step to elucidate on the dynamics of the LIESST process of a given metal-organic complex is the information of the potential energy curves (PECs). In particular, we compute the PECs of the low-energy states, namely the ground state (gs) and a few low-lying excited states (es) of singlet (S), triplet (T), and quintet (Q) multiplicity, as a function of variation of the coordination sphere radius, ⟨R(Fe-N)⟩, parametrizing the continuous geometry change from LS to HS, and calculate the crossing points on a 1-dimensional PEC. While this is a simplistic approach, this is a pragmatic approach given the complexity and diversity of the actual complexes. A more involved and sophisticated approach considering explicit nuclear quantum dynamics [67] has been applied in context [68–80] of model system. It will be a computational challenge to apply such approach to realistic systems.

While there can be many possible pathways, the rate determining pathway is the one which gives the fastest relaxation rate. In case of both ptz and pic, the fastest LIESST process turns out to be a three step process as described below. The system first encounters a spin-conserving transition from singlet ground state (S-gs) to first-excited singlet state (S-es*-1). Then, it undergoes first ISC from S-es*-1 to the excited triplet state (T-es*), followed by IC to T-gs. Next, it encounters the second ISC step to the quintet ground state (Q-gs).

As discussed in the chapter-1, low temperature HS→LS relaxation rate involves two components, one is electronic and other is nuclear. The calculated value of β_{HL} of the ptz and pic complexes, along with the associated information are listed in Table 4.2. For calculation of the nuclear contribution, the corresponding force constants are evaluated by fitting the PEC's in a quadratic equation, assuming the harmonic nature of PEC. The vibrational frequency ω is determined by using the reduced mass of the coordinating atoms as suggested by Buhks et al.[81] Using these values, Huang-Rhys factor, the s and the reduced energy gap, p, and thus the Franck-Condon factor, $F_p(T \to 0)$ are calculated for the four complexes. The results are given in Table 4.3. Finally, the relaxation rate constant for ptz and pic complexes is estimated using Eq.(1.1). The computed values of k_{HL} (T→0) (sec^{-1}) turn out to be 4.37×10^{-5} and 7.2×10^{-4} for ptz and pic complexes. In spite of rather simplistic approach, the computed values are found to be in excellent agreement with experimental estimates of 3×10^{-5} and 5×10^{-4} for ptz and pic complexes respectively, demonstrating the effectiveness of the adopted computational framework.

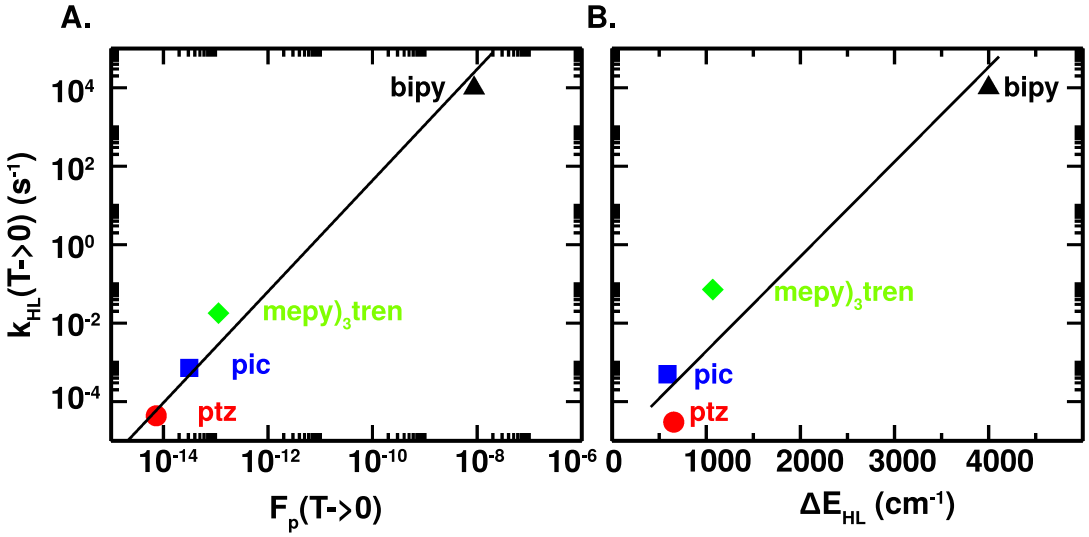

Figure 4.3: The nuclear contribution, measured through Franck-Condon factor (left) and the electronic contribution, measured through HS-LS energy gap (right), plotted against the measured relaxation rate for the four complexes.

4.3.3 Chemical origin of Trend in Relaxation Rate

In order to understand the microscopic origin of the trend observed in relaxation rate, we first examine the trend in the nuclear and electronic contribution, by plotting the Franck-Condon factor and the HS-LS energy gap, against the relaxation rate of the four complexes (cf Fig. 4.3). As found, the relaxation rate shows an almost linear dependency on both the quantities. Examining Table 4.3, we find that the dominant contribution in the trend of nuclear part is due to Huang-Rhys factor, *s*, related to force constant and thereby on the stiffness of the metal-ligand bond. Similarly, for the electronic component, the energy gap values, are strongly dependent on the ligand field effect.

In order to characterize the trend in the nature of metal-ligand covalency, which consequently affects the bond stiffness and the ligand field, we calculate the crystal orbital Hamiltonian populations (COHPs). The crystal orbital Hamiltonian population, COHP, which is the density of states weighted by the corresponding Hamiltonian matrix element, is a tool that permits energy-resolved analysis of pairwise interactions between atoms. It is indicative of the strength and nature of a bonding (negative COHP) or antibonding (positive COHP) interaction. The integrated value of COHP (ICOHP) until Fermi energy provides information of the net covalency between the metal and ligand. The inset of Fig. 4.4 shows the calculated COHP in a Fe-N bond for four different complexes.

The ICOHP obtained by integrating COHP until Fermi energy, set at zero in the inset plot, plotted against the relaxation rate is shown in the main panel of

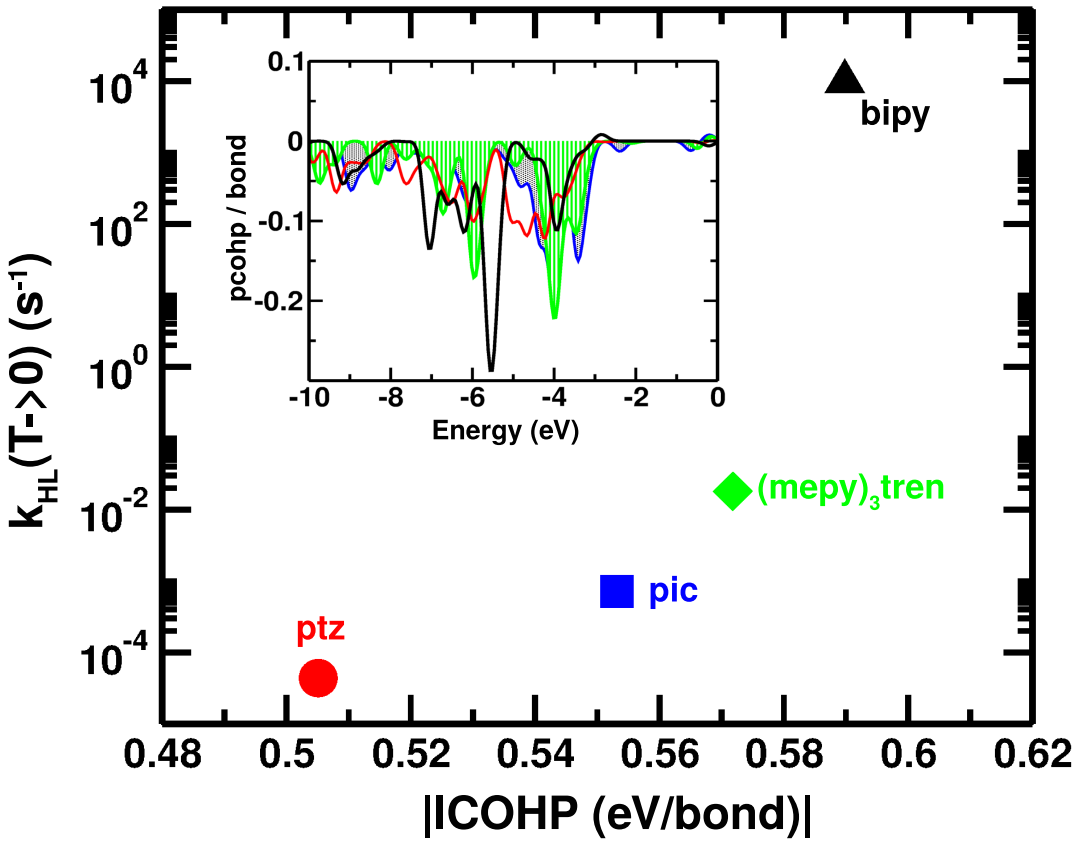

Figure 4.4: The calculated values of modulus of ICOHP for four complexes, plotted against the relaxation rate. The inset shows the Fe-N COHP for the four complexes. The color convention followed; red (ptz), blue (pic), green (mepy-tren) and black (bipy). For ease of visualization of COHP, the mepy and pic data are shown as shaded area.

Fig. 4.4. We find a clear correlation between the relaxation rate and ICOHP, the measure of metal-ligand covalency.

	$[Fe(ptz)_6]^{2+}$	$[Fe(pic)_3]^{2+}$	$[Fe(mepy)_3(tren)]^{2+}$	$[Fe(bipy)_3]^{2+}$
ΔR_{HL} (Å)	0.1916	0.1834	0.1770	0.1734
ΔQ_{HL} (Å)	0.4693	0.4492	0.4336	0.4247
s	36.15	34.24	33.31	30.21
F_p (T $\rightarrow$ 0)	7×10^{-15}	3×10^{-14}	1×10^{-13}	9×10^{-9}

Table 4.3: The HS-LS structural parameters, calculated Huang-Rhys factor, and Franck-Condon factor for four complexes.

The observed increasing degree of the metal-ligand covalency occurs via the possibility of back donation or delocalization of the electrons from the suitable low-lying Fe(II)-centered molecular orbital to the empty low-lying ligand-centered π^* antibonding molecular orbitals. For instance, in the case of 1-propyltetrazole, the excessive electron density in the tetrazole ring inhibits the possibility of back donation, thus pushing the π^* antibonding molecular orbitals towards higher energy, thereby increasing the relative energies of the charge transfer and ligand-field states towards UV and bluish-green region of the electromagnetic spectrum respectively. In turn, it decreases the density of electronic states, the zero-point energy difference (ΔE^0_{HL}), spin transition temperature ($T_{1/2}$), and the corresponding value of the tunneling rate constant k_{HL} (T$\rightarrow$0) in Fe(II)-1-propyltetrazole complex to a large extent.[8] In comparison, the situation is better in the case of 2-picolylamine due to the higher degree of stabilization of the ligand-centered π^* antibonding molecular orbitals, effectively resulting in the somewhat better stabilization of the charge-transfer and ligand-field states and a slight increase in the density of electronic states. However, in contrast to 1-propyltetrazole, the relative magnitude of the ΔE^0_{HL} and $T_{1/2}$ is marginally smaller. Evidently, all these factors collectively contribute to the increase in k_{HL} (T$\rightarrow$0) value observed in Fe(II)-2-picolylamine complex.[8] In contrast, for Fe(II) complexes of tris 4-[(6-methyl)-2- pyridyl]-3-aza- butenylamine and 2,2'-bipyridine, the large degree of metal-ligand covalency favors the electronic stabilization of the charge-transfer and ligand-field states towards the red region of the electromagnetic spectrum strongly, thereby increasing the density of electronic states significantly, in particular for 2,2'-bipyridine. As a result, notably, it increases the $T_{1/2}$ by increasing the magnitude of ΔE^0_{HL} and eventually becomes a pure low-spin compound with the ligand 2,2'-bipyridine. The corresponding value of k_{HL} (T$\rightarrow$0) increases a couple of orders of magnitude in Fe(II)-4-[(6-methyl)-2- pyridyl]-3-aza- butenylamine complex[12] and by several orders of magnitude in Fe(II)- 2,2'-bipyridine

complex.[9]

4.4 Conclusion

The work by Hauser et al.[7], determining the relaxation rates for several Fe(II) coordination complexes, reported a large variation of 14 orders of magnitude, depending of the choice of ligands. It is an intriguing issue to understand what causes this large variation. However, a microscopic understanding of the systematics of this significant variation demands handling ligands of different sizes and complexities, restricting the available theoretical tools. In a previous study,[53] it was demonstrated by comparing the calculated rate constant of a model system with a real system that TDDFT may provide a cheap, yet not an unreasonable, approach to describe LIESST processes. In particular, for describing LIESST in complex structures containing 100 to 200 atoms, TDDFT may be a possible tool. Motivated by this finding, in this work we apply DFT scheme to analyze the low temperature relaxation rates of four Fe(II) SCO complexes with 1-propyltetrazole (ptz), 2-picolylamine (pic), tris4-[(6-methyl)-2-pyridyl]-3-aza-butenylamine ((mepy)$_3$tren), and 2,2'-bipyridine (bipy) ligands. By carefully examining 21 different XC functionals of the GGA, meta-GGA, hybrid, range separated hybrid, hybrid-meta GGA and double-hybrid types, a consistent description of ΔE^0_{HL} of the four compounds is established by comparing with experimental estimates drawn from knowledge of $T_{1/2}$ and ΔS^0_{HL}. Following this, the rate constants for for ptz and pic complexes are computed within the d-d excitation-deexcitation scenario of Franck-Condon theory from the knowledge of the potential energy curves of low-energy states, spin-orbit couplings at crossing points of these PECs, and the force constant. We refrain from applying such an approach to mepy and bipy complexes due to additional complexities involving MLCT states. The calculated rate constants of ptz and pic complexes are found to be in excellent agreement with measured values. It is noteworthy that the measured relaxation rates from the four complexes vary over a range of nine orders of magnitude with $\sim 4 \times 10^{-5}$ for ptz to $\sim 10^4$ for bipy. Both the HS-LS energy gap and nuclear contribution of rate constant are found to contribute to this trend being coupled to metal-ligand bond stiffness and the ligand field effect. The metal-ligand covalency, quantified through integrated value of crystal orbital Hamiltonian population, reveals correspondence with the low temperature rate constant. This in turn establishes the progressive stabilization of the charge-transfer and ligand-field states from 1-propyltetrazole to 2,2'-bipyridine utilizing an increasing degree of covalency. Our study underlines the relationship between the geometry of the ligands and the relaxation rate. The microscopic understanding, thus provided, may be useful in rational designing of the ligands, with desired LIESST properties.

References

[1] S. Brooker and J. A. Kitchen, "Nano-magnetic materials: spin crossover compounds vs. single molecule magnets vs. single chain magnets," *Dalton Transactions*, no. 36, pp. 7331–7340, 2009.

[2] S.-i. Ohkoshi, K. Imoto, Y. Tsunobuchi, S. Takano, and H. Tokoro, "Light-induced spin-crossover magnet," *Nature chemistry*, vol. 3, no. 7, p. 564, 2011.

[3] G. J. Halder, C. J. Kepert, B. Moubaraki, K. S. Murray, and J. D. Cashion, "Guest-dependent spin crossover in a nanoporous molecular framework material," *Science*, vol. 298, no. 5599, pp. 1762–1765, 2002.

[4] A. Hauser, C. Enachescu, M. L. Daku, A. Vargas, and N. Amstutz, "Low-temperature lifetimes of metastable high-spin states in spin-crossover and in low-spin iron (ii) compounds: The rule and exceptions to the rule," *Coordination Chemistry Reviews*, vol. 250, no. 13-14, pp. 1642–1652, 2006.

[5] A. Hauser, "Intersystem crossing in iron (ii) coordination compounds: a model process between classical and quantum mechanical behaviour," *Comments on Inorganic Chemistry*, vol. 17, no. 1, pp. 17–40, 1995.

[6] A. Hauser, "Intersystem crossing in fe (ii) coordination compounds," *Coordination Chemistry Reviews*, vol. 111, pp. 275–290, 1991.

[7] A. Hauser, A. Vef, and P. Adler, "Intersystem crossing dynamics in fe (ii) coordination compounds," *The Journal of chemical physics*, vol. 95, no. 12, pp. 8710–8717, 1991.

[8] A. Hauser, "Light-induced spin crossover and the high-spin to low-spin relaxation," *Spin crossover in transition metal compounds II*, pp. 155–198, 2004.

[9] L. M. Lawson Daku, A. Vargas, A. Hauser, A. Fouqueau, and M. E. Casida, "Assessment of density functionals for the high-spin/low-spin energy difference in the low-spin iron (ii) tris (2, 2'-bipyridine) complex," *ChemPhysChem*, vol. 6, no. 7, pp. 1393–1410, 2005.

[10] J. Kusz, H. Spiering, and P. Gütlich, "The deformation tensor of the spin transition in the mixed crystal [fe0. 46zn0. 54 (ptz) 6](bf4) 2," *Journal of applied crystallography*, vol. 37, no. 4, pp. 589–595, 2004.

[11] D. Chernyshov, M. Hostettler, K. W. Törnroos, and H.-B. Bürgi, "Ordering phenomena and phase transitions in a spin-crossover compound-uncovering the nature of the intermediate phase of [fe (2-pic) 3] cl2. etoh," *Angewandte Chemie International Edition*, vol. 42, no. 32, pp. 3825–3830, 2003.

[12] P. Chakraborty, A. Tissot, L. Peterhans, L. Guénée, C. Besnard, P. Pattison, and A. Hauser, "Determination of the molecular structure of the short-lived light-induced high-spin state in the spin-crossover compound [fe (6-mepy) 3 tren](pf 6) 2," *Physical Review B*, vol. 87, no. 21, p. 214306, 2013.

[13] L.-Q. Fan and J.-H. Wu, "Crystal structure of tris (2, 2-bipyridine) iron (ii) catena-bis ((tris-μ-iodo)-plumbate (ii)),[fe (c10h8n2) 3][pbi3] 2," *Zeitschrift*

für Kristallographie-New Crystal Structures, vol. 223, no. 1, pp. 72–74, 2008.

[14] M. J. Frisch, G. W. Trucks, H. B. Schlegel, G. E. Scuseria, M. A. Robb, J. R. Cheeseman, G. Scalmani, V. Barone, G. A. Petersson, H. Nakatsuji, X. Li, M. Caricato, A. V. Marenich, J. Bloino, B. G. Janesko, R. Gomperts, B. Mennucci, H. P. Hratchian, J. V. Ortiz, A. F. Izmaylov, J. L. Sonnenberg, D. Williams-Young, F. Ding, F. Lipparini, F. Egidi, J. Goings, B. Peng, A. Petrone, T. Henderson, D. Ranasinghe, V. G. Zakrzewski, J. Gao, N. Rega, G. Zheng, W. Liang, M. Hada, M. Ehara, K. Toyota, R. Fukuda, J. Hasegawa, M. Ishida, T. Nakajima, Y. Honda, O. Kitao, H. Nakai, T. Vreven, K. Throssell, J. A. Montgomery, Jr., J. E. Peralta, F. Ogliaro, M. J. Bearpark, J. J. Heyd, E. N. Brothers, K. N. Kudin, V. N. Staroverov, T. A. Keith, R. Kobayashi, J. Normand, K. Raghavachari, A. P. Rendell, J. C. Burant, S. S. Iyengar, J. Tomasi, M. Cossi, J. M. Millam, M. Klene, C. Adamo, R. Cammi, J. W. Ochterski, R. L. Martin, K. Morokuma, O. Farkas, J. B. Foresman, and D. J. Fox, "Gaussian16 Revision C.01," 2016. Gaussian Inc. Wallingford CT.

[15] J. P. Perdew, K. Burke, and M. Ernzerhof, "Generalized gradient approximation made simple," *Physical review letters*, vol. 77, no. 18, p. 3865, 1996.

[16] A. D. Becke, "Density-functional exchange-energy approximation with correct asymptotic behavior," *Physical review A*, vol. 38, no. 6, p. 3098, 1988.

[17] C. Y. Lee and W. Parr, "Rg phys. rev. b 1988, 37, 785–789. b) becke, ad," *Phys. Rev. A*, vol. 38, pp. 3098–3100, 1988.

[18] J. P. Perdew, "Density-functional approximation for the correlation energy of the inhomogeneous electron gas," *Physical Review B*, vol. 33, no. 12, p. 8822, 1986.

[19] J. P. Perdew, "Erratum: Density-functional approximation for the correlation energy of the inhomogeneous electron gas," *Physical review B*, vol. 34, no. 10, p. 7406, 1986.

[20] N. C. Handy and A. J. Cohen, "Left-right correlation energy," *Molecular Physics*, vol. 99, no. 5, pp. 403–412, 2001.

[21] A. D. Boese and N. C. Handy, "A new parametrization of exchange–correlation generalized gradient approximation functionals," *The Journal of Chemical Physics*, vol. 114, no. 13, pp. 5497–5503, 2001.

[22] A. D. Becke, "Density-functional thermochemistry. iii. the role of exact exchange," *The Journal of Chemical Physics*, vol. 98, no. 7, pp. 5648–5652, 1993.

[23] M. Reiher, O. Salomon, and B. A. Hess, "Reparameterization of hybrid functionals based on energy differences of states of different multiplicity," *Theoretical Chemistry Accounts*, vol. 107, no. 1, pp. 48–55, 2001.

[24] X. Xu and W. A. Goddard, "The x3lyp extended density functional for accurate descriptions of nonbond interactions, spin states, and thermochemical properties," *Proceedings of the National Academy of Sciences*, vol. 101, no. 9,

pp. 2673–2677, 2004.

[25] J. P. Perdew, M. Ernzerhof, and K. Burke, "Rationale for mixing exact exchange with density functional approximations," *The Journal of chemical physics*, vol. 105, no. 22, pp. 9982–9985, 1996.

[26] C. Adamo and V. Barone, "Toward reliable density functional methods without adjustable parameters: The pbe0 model," *The Journal of chemical physics*, vol. 110, no. 13, pp. 6158–6170, 1999.

[27] A. D. Becke, "Density-functional thermochemistry. v. systematic optimization of exchange-correlation functionals," *The Journal of chemical physics*, vol. 107, no. 20, pp. 8554–8560, 1997.

[28] H. L. Schmider and A. D. Becke, "Optimized density functionals from the extended g2 test set," *The Journal of chemical physics*, vol. 108, no. 23, pp. 9624–9631, 1998.

[29] J. Tao, J. P. Perdew, V. N. Staroverov, and G. E. Scuseria, "Climbing the density functional ladder: Nonempirical meta–generalized gradient approximation designed for molecules and solids," *Physical Review Letters*, vol. 91, no. 14, p. 146401, 2003.

[30] Y. Zhao and D. G. Truhlar, "A new local density functional for main-group thermochemistry, transition metal bonding, thermochemical kinetics, and noncovalent interactions," *The Journal of chemical physics*, vol. 125, no. 19, p. 194101, 2006.

[31] J. P. Perdew, S. Kurth, A. Zupan, and P. Blaha, "Accurate density functional with correct formal properties: A step beyond the generalized gradient approximation," *Physical review letters*, vol. 82, no. 12, p. 2544, 1999.

[32] J. P. Perdew, S. Kurth, A. Zupan, and P. Blaha, "Accurate density functional with correct formal properties: A step beyond the generalized gradient approximation," *Physical review letters*, vol. 82, no. 12, p. 2544, 1999.

[33] V. N. Staroverov, G. E. Scuseria, J. Tao, and J. P. Perdew, "Comparative assessment of a new nonempirical density functional: Molecules and hydrogen-bonded complexes," *The Journal of chemical physics*, vol. 119, no. 23, pp. 12129–12137, 2003.

[34] Y. Zhao, N. E. Schultz, and D. G. Truhlar, "Exchange-correlation functional with broad accuracy for metallic and nonmetallic compounds, kinetics, and noncovalent interactions," *The Journal of chemical physics*, vol. 123, no. 16, p. 161103, 2005.

[35] Y. Zhao, N. E. Schultz, and D. G. Truhlar, "Design of density functionals by combining the method of constraint satisfaction with parametrization for thermochemistry, thermochemical kinetics, and noncovalent interactions," *Journal of chemical theory and computation*, vol. 2, no. 2, pp. 364–382, 2006.

[36] Y. Zhao and D. G. Truhlar, "The m06 suite of density functionals for main group thermochemistry, thermochemical kinetics, noncovalent interactions, excited states, and transition elements: two new functionals and systematic

testing of four m06-class functionals and 12 other functionals," *Theoretical chemistry accounts*, vol. 120, no. 1, pp. 215–241, 2008.

[37] T. Yanai, D. P. Tew, and N. C. Handy, "A new hybrid exchange–correlation functional using the coulomb-attenuating method (cam-b3lyp)," *Chemical physics letters*, vol. 393, no. 1-3, pp. 51–57, 2004.

[38] H. Iikura, T. Tsuneda, T. Yanai, and K. Hirao, "A long-range correction scheme for generalized-gradient-approximation exchange functionals," *The Journal of Chemical Physics*, vol. 115, no. 8, pp. 3540–3544, 2001.

[39] Y. Tawada, T. Tsuneda, S. Yanagisawa, T. Yanai, and K. Hirao, "A long-range-corrected time-dependent density functional theory," *The Journal of chemical physics*, vol. 120, no. 18, pp. 8425–8433, 2004.

[40] S. Grimme, "Semiempirical hybrid density functional with perturbative second-order correlation," *The Journal of chemical physics*, vol. 124, no. 3, p. 034108, 2006.

[41] T. Schwabe and S. Grimme, "Towards chemical accuracy for the thermodynamics of large molecules: new hybrid density functionals including non-local correlation effects," *Physical Chemistry Chemical Physics*, vol. 8, no. 38, pp. 4398–4401, 2006.

[42] A. Schäfer, C. Huber, and R. Ahlrichs, "Fully optimized contracted gaussian basis sets of triple zeta valence quality for atoms li to kr," *The Journal of Chemical Physics*, vol. 100, no. 8, pp. 5829–5835, 1994.

[43] R. A. Kendall, T. H. Dunning Jr, and R. J. Harrison, "Electron affinities of the first-row atoms revisited. systematic basis sets and wave functions," *The Journal of chemical physics*, vol. 96, no. 9, pp. 6796–6806, 1992.

[44] R. Krishnan, J. S. Binkley, R. Seeger, and J. A. Pople, "Self-consistent molecular orbital methods. xx. a basis set for correlated wave functions," *The Journal of chemical physics*, vol. 72, no. 1, pp. 650–654, 1980.

[45] G. Breit, "Dirac's equation and the spin-spin interactions of two electrons," *Physical Review*, vol. 39, no. 4, p. 616, 1932.

[46] X. Gao, S. Bai, D. Fazzi, T. Niehaus, M. Barbatti, and W. Thiel, "Evaluation of spin-orbit couplings with linear-response time-dependent density functional methods," *Journal of chemical theory and computation*, vol. 13, no. 2, pp. 515–524, 2017.

[47] R. Dronskowski and P. E. Bloechl, "Crystal orbital hamilton populations (cohp): energy-resolved visualization of chemical bonding in solids based on density-functional calculations," *The Journal of Physical Chemistry*, vol. 97, no. 33, pp. 8617–8624, 1993.

[48] J. P. Perdew, K. Burke, and M. Ernzerhof, "Generalized gradient approximation made simple," *Physical review letters*, vol. 77, no. 18, p. 3865, 1996.

[49] G. Kresse and J. Hafner, "Ab initio molecular dynamics for liquid metals," *Physical review B*, vol. 47, no. 1, p. 558, 1993.

[50] S. Maintz, V. L. Deringer, A. L. Tchougréeff, and R. Dronskowski, "Lobster:

A tool to extract chemical bonding from plane-wave based dft," 2016.

[51] B. O. Roos, P. R. Taylor, P. E. Si, *et al.*, "A complete active space scf method (casscf) using a density matrix formulated super-ci approach," *Chemical Physics*, vol. 48, no. 2, pp. 157–173, 1980.

[52] K. Andersson, P.-Å. Malmqvist, and B. O. Roos, "Second-order perturbation theory with a complete active space self-consistent field reference function," *The Journal of chemical physics*, vol. 96, no. 2, pp. 1218–1226, 1992.

[53] S. Karmakar, D. Ghosh, and T. Saha-Dasgupta, "Light-induced excited spin-state trapping in spin crossover model system," *International Journal of Quantum Chemistry*, vol. 120, no. 6, p. e26122, 2020.

[54] R. J. Bartlett and M. Musiał, "Coupled-cluster theory in quantum chemistry," *Reviews of Modern Physics*, vol. 79, no. 1, p. 291, 2007.

[55] A. I. Krylov, "Equation-of-motion coupled-cluster methods for open-shell and electronically excited species: The hitchhiker's guide to fock space," *Annu. Rev. Phys. Chem.*, vol. 59, pp. 433–462, 2008.

[56] K. Kowalski and M. Valiev, "Extensive regularization of the coupled cluster methods based on the generating functional formalism: Application to gas-phase benchmarks and to the sn 2 reaction of chcl 3 and oh- in water," *The Journal of chemical physics*, vol. 131, no. 23, p. 234107, 2009.

[57] A. Marino, P. Chakraborty, M. Servol, M. Lorenc, E. Collet, and A. Hauser, "The role of ligand-field states in the ultrafast photophysical cycle of the prototypical iron (ii) spin-crossover compound [fe (ptz) 6](bf4) 2," *Angewandte Chemie International Edition*, vol. 53, no. 15, pp. 3863–3867, 2014.

[58] P. Adler, A. Hauser, A. Vef, H. Spiering, and P. Gütlich, "Dynamics of spin state conversion processes in the solid state," *Hyperfine Interactions*, vol. 47, no. 1, pp. 343–356, 1989.

[59] J. E. Monat and J. K. McCusker, "Femtosecond excited-state dynamics of an iron (ii) polypyridyl solar cell sensitizer model," *Journal of the American Chemical Society*, vol. 122, no. 17, pp. 4092–4097, 2000.

[60] M. Khalil, M. A. Marcus, A. L. Smeigh, J. K. McCusker, H. H. Chong, and R. W. Schoenlein, "Picosecond x-ray absorption spectroscopy of a photoinduced iron (ii) spin crossover reaction in solution," *The Journal of Physical Chemistry A*, vol. 110, no. 1, pp. 38–44, 2006.

[61] A. L. Smeigh, M. Creelman, R. A. Mathies, and J. K. McCusker, "Femtosecond time-resolved optical and raman spectroscopy of photoinduced spin crossover: Temporal resolution of low-to-high spin optical switching," *Journal of the American Chemical Society*, vol. 130, no. 43, pp. 14105–14107, 2008.

[62] G. Auböck and M. Chergui, "Sub-50-fs photoinduced spin crossover in [fe (bpy) 3] 2+," *Nature chemistry*, vol. 7, no. 8, pp. 629–633, 2015.

[63] W. Zhang, R. Alonso-Mori, U. Bergmann, C. Bressler, M. Chollet, A. Galler, W. Gawelda, R. G. Hadt, R. W. Hartsock, T. Kroll, *et al.*, "Tracking excited-

state charge and spin dynamics in iron coordination complexes," *Nature*, vol. 509, no. 7500, pp. 345–348, 2014.

[64] C. de Graaf and C. Sousa, "Study of the light-induced spin crossover process of the [feii (bpy) 3] 2+ complex," *Chemistry–A European Journal*, vol. 16, no. 15, pp. 4550–4556, 2010.

[65] E. A. Juban, A. L. Smeigh, J. E. Monat, and J. K. McCusker, "Ultrafast dynamics of ligand-field excited states," *Coordination chemistry reviews*, vol. 250, no. 13-14, pp. 1783–1791, 2006.

[66] W. Zhang, R. Alonso-Mori, U. Bergmann, C. Bressler, M. Chollet, A. Galler, W. Gawelda, R. G. Hadt, R. W. Hartsock, T. Kroll, *et al.*, "Tracking excited-state charge and spin dynamics in iron coordination complexes," *Nature*, vol. 509, no. 7500, pp. 345–348, 2014.

[67] M. Pápai, "Photoinduced low-spin to high-spin mechanism of an octahedral fe (ii) complex revealed by synergistic spin-vibronic dynamics," *Inorganic chemistry*, vol. 60, no. 18, pp. 13950–13954, 2021.

[68] C. Sousa, M. Llunell, A. Domingo, and C. de Graaf, "Theoretical evidence for the direct 3 mlct-hs deactivation in the light-induced spin crossover of fe (ii)–polypyridyl complexes," *Physical Chemistry Chemical Physics*, vol. 20, no. 4, pp. 2351–2355, 2018.

[69] C. Sousa, C. de Graaf, A. Rudavskyi, and R. Broer, "Theoretical study of the light-induced spin crossover mechanism in [fe (mtz) 6] 2+ and [fe (phen) 3] 2+," *The Journal of Physical Chemistry A*, vol. 121, no. 51, pp. 9720–9727, 2017.

[70] G. Vanko, A. Bordage, M. Pápai, K. Haldrup, P. Glatzel, A. M. March, G. Doumy, A. Britz, A. Galler, T. Assefa, *et al.*, "Detailed characterization of a nanosecond-lived excited state: X-ray and theoretical investigation of the quintet state in photoexcited [fe (terpy) 2] 2+," *The Journal of Physical Chemistry C*, vol. 119, no. 11, pp. 5888–5902, 2015.

[71] T. J. Penfold, E. Gindensperger, C. Daniel, and C. M. Marian, "Spin-vibronic mechanism for intersystem crossing," *Chemical reviews*, vol. 118, no. 15, pp. 6975–7025, 2018.

[72] C. Sousa, C. de Graaf, A. Rudavskyi, R. Broer, J. Tatchen, M. Etinski, and C. M. Marian, "Ultrafast deactivation mechanism of the excited singlet in the light-induced spin crossover of [fe (2, 2'-bipyridine) 3] 2+," *Chemistry–A European Journal*, vol. 19, no. 51, pp. 17541–17551, 2013.

[73] G. Capano, T. Penfold, M. Chergui, and I. Tavernelli, "Photophysics of a copper phenanthroline elucidated by trajectory and wavepacket-based quantum dynamics: a synergetic approach," *Physical Chemistry Chemical Physics*, vol. 19, no. 30, pp. 19590–19600, 2017.

[74] S. Gómez, M. Heindl, A. Szabadi, and L. González, "From surface hopping to quantum dynamics and back. finding essential electronic and nuclear degrees of freedom and optimal surface hopping parameters," *The Journal of*

Physical Chemistry A, vol. 123, no. 38, pp. 8321–8332, 2019.

[75] M. Pápai, "Toward simulation of fe (ii) low-spin to high-spin photoswitching by synergistic spin-vibronic dynamics," *Journal of chemical theory and computation*, vol. 18, no. 3, pp. 1329–1339, 2022.

[76] M. Kondo and K. Yoshizawa, "A theoretical study of spin–orbit coupling in an fe (ii) spin-crossover complex. mechanism of the liesst effect," *Chemical physics letters*, vol. 372, no. 3-4, pp. 519–523, 2003.

[77] Y. Shiota, D. Sato, G. Juhász, and K. Yoshizawa, "Theoretical study of thermal spin transition between the singlet state and the quintet state in the [fe (2-picolylamine) 3] 2+ spin crossover system," *The Journal of Physical Chemistry A*, vol. 114, no. 18, pp. 5862–5869, 2010.

[78] M. Papai, G. Vanko, C. De Graaf, and T. Rozgonyi, "Theoretical investigation of the electronic structure of fe (ii) complexes at spin-state transitions," *Journal of chemical theory and computation*, vol. 9, no. 1, pp. 509–519, 2013.

[79] C. Sousa, A. Domingo, and C. de Graaf, "Effect of second-order spin–orbit coupling on the interaction between spin states in spin-crossover systems," *Chemistry–A European Journal*, vol. 24, no. 20, pp. 5146–5152, 2018.

[80] M. Alías-Rodríguez, M. Huix-Rotllant, and C. de Graaf, "Quantum dynamics simulations of the thermal and light-induced high-spin to low-spin relaxation in fe (bpy) 3 and fe (mtz) 6," *Faraday Discussions*, 2022.

[81] E. Buhks, G. Navon, M. Bixon, and J. Jortner, "Spin conversion processes in solutions," *Journal of the American Chemical Society*, vol. 102, no. 9, pp. 2918–2923, 1980.

Chapter 5

Trend in cooperativity in spin-crossover of metal-organic polymers*

5.1 Introduction

Thermal hysteresis which confers memory effect in Spin Crossover (SCO) materials is a manifestation of cooperativity among active SCO sites within the crystal lattice.[1] As discussed in chapters 3 and 4, the fundamental origin of SCO is molecular, and the low spin (LS) to high spin (HS) conversion in an SCO complex is accompanied by a drastic change in the metal-to-ligand average bond distance. When the intermolecular interactions in the lattice become appreciable, the change in molecular size can be transmitted from one site to another. This induces a cooperative effect leading to first-order phase transitions and hysteresis effects may be observed.[2, 3] Consequently, magnetic, optical, and structural properties change significantly enabling bistable character in the compound, which could be useful for designing memory-based electronic devices.[4, 5] To achieve cooperativity coordination polymeric compounds are better choices compared to molecular crystals with isolated molecular units as discussed in Chapter 1.

While undoubtedly cooperativity is an important attribute of SCO polymers for practical applications, it is crucial to understand, control, and design the cooperativity. Several theoretical studies have been reported in the literature to provide a microscopic understanding in this regard. The most prevailing concept was that cooperativity arises solely due to the long-range elastic interaction arising due to interaction between local lattice distortions at each molecular unit.[6]

*This chapter is based on "Trend in cooperativity in spin-crossover of metal-organic polymers" **Shiladitya Karmakar**, Pradip Chakraborty and Tanusri Saha-Dasgupta, (In preparation).

The importance of magnetic superexchange interaction, mediated through the organic ligands connecting the metal centers, has been pointed out in a density functional theory (DFT) based study[7] which estimated the strength of magnetic exchange interaction in a Fe-triazole compound, and found it to be of the same order of magnitude as that of elastic exchange, estimated in similar compounds. Banerjee et al first studied the interplay of the two possible driving mechanisms of cooperativity, namely elasticity, and magnetism, employing Monte Carlo simulation in the context of a general model Hamiltonian.[8]

Over the past few decades, azole-based ligands connecting $Fe(II)N_6$ chromophores have drawn significant attention as bridging ligands in SCO polymeric compounds.[1] In such compounds, a single N-donor ligand is involved in the synthetic procedure which avoids the formation of mixed ligand species, hence high yields are usually obtained. In addition, the choice of such relatively small heterocyclic ligands favors almost regular O_h symmetry around the low-spin Fe(II) ion. Polymeric $[Fe(4\text{-R-}1,2,4\text{-triazole})_3](anion)_2$ systems (R=amino, alkyl, hydroxyalkyl) are extensively studied as it provides desired SCO properties for device application i.e., pronounced thermochromism, transition temperatures near room temperature, and large thermal hysteresis. This compound precipitates as a fine, polymeric powder, and single crystals cannot be grown because the polymer is insoluble in water and organic solvents.[1] Banerjee et al used a simplified computer-designed crystal structure of the Fe-triazole compound in the ab-initio Density functional theory (DFT) based study. Extracting the material-specific inputs from DFT, and plugging in the model Hamiltonian, they explained the microscopic origin of cooperativity discussing the equal importance of elastic and magnetic exchange interaction.[8] Interest in tetrazole-based ligand family arises since $[Fe(btzp)_3](ClO_4)_2$ (btzp = 1,2-di(tetrazole-2-yl)propane) and $[Fe(btze)_3](BF_4)_2$ (btze = 1,2-di(tetrazole-2-yl)ethane) represent the first structurally characterised Fe(II) linear chain compounds exhibiting spin crossover. Both compounds crystallize in the trigonal space group $P\bar{3}c1$, and this space group remains unchanged upon the Fe(II) SCO. A gradual incomplete spin transition was observed with a thermal spin transition temperature ($T_{1/2}$) of 148 K and 140 K, respectively.[1]

Further investigations on coordination properties of 1,ω-di(tetrazole-2-yl) alkanes ligands revealed that bis-(tetrazole-2-yl)alkanes can form iron(II) complexes containing a $[Fe(\text{tetrazole-2-yl})_2(A)_2]$-type core (A: ligand connected to apical position to Fe(II)). Particularly, 1,2-di(tetrazole-2-yl)ethane (ebtz)[9] and 1,6-di(tetrazole-2-yl)hexane (hbtz)[10] as bridging ligands reacting with Fe(II) perchlorate give rise to 1D and 2D coordination networks, in which axial positions are occupied by ethyl cyanide (C_2H_5CN) and acetonitrile (CH_3CN) molecules respectively. These tetrazole-based bridging ligands are differed by the number of carbon atoms present in the alkyl linker between two tetrazole rings (two carbon atoms in ebtz and six carbon atoms in hbtz ligands). Both $[Fe(ebtz)_2(C_2H_5CN)_2$

$](ClO_4)_2$ and $[Fe(hbtz)_2(CH_3CN)_2\ ](ClO_4)_2$ show abrupt spin transition accompanied by hysteresis of width ($\Delta T_{1/2}$) 29K and 2K respectively with $T_{1/2}$ around 126K indicating that the cooperativity among Fe(II) centers must be different for the polymers. Clearly, the presence of a direct linkage between SCO centers is not a sufficient condition for the occurrence of the cooperative spin transition. Intersite interactions can be greatly influenced by the size and flexibility of the ligand structure or the elasticity of the whole coordination network which may decide the degree of cooperativity in SCO materials.

In the present Chapter, we aim to understand how cooperativity among Fe(II) centers builds upon increasing the length of the alkyl linkers that connects two tetrazole rings. The HS and LS crystal structures for Fe-ebtz with two-C linker connectivity and Fe-hbtz with six-C linker connectivity compounds are available. To understand the systematic trend in cooperativity with varying linkers, one needs to add to this list an intermediate-C linker connectivity tetrazole-based Fe(II) compound. The available crystal structure for $[Fe(pbtz)_3](ClO_4)_2$, (pbtz = 1,3-di(tetrazol-2-yl)propane)[11] having three carbon atoms in the alkyl linker forms a 3D coordination network in absence of the axially coordinated ligand, making it different from the other two discussed compounds with [Fe(tetrazole-2-yl)$_2$(A)$_2$] core. Moreover, it undergoes incomplete HS$\rightarrow$LS transition with shortening of the Fe-N bond lengths at $0.15\mathring{A}$ whereas for complete SCO to occur in the tetrazole-based complexes found to be ranging from 0.16 to 0.20 $\mathring{A}$. Tetrazole-based ligands having five carbon atoms in the alkyl linker have not been reported to the best of our knowledge. Hence to maintain the uniformity in the structural motif, we choose the experimentally reported triclinic $[Cu(bbtz)_2(MeOH)_2](ClO_4)_2$ (bbtz=1,4-di(1,2,3,4-tetrazol-2-yl)butane) structure[12] with similar core to that of other two compounds but four carbon atoms present in the alkyl linker. We generate the corresponding Fe counterpart theoretically by spin-polarized structural relaxation starting from the Cu compound and replacing Cu with Fe. This provides us with the opportunity to study the systematic evolution of cooperativity as one moves from two-C linker to four-C linker to six-C linker connectivity ligand within the Fe(II) tetrazole family. To probe the evolution in cooperativity, we estimate the Fe-Fe magnetic exchange interaction (J) and spin-state dependent elastic interaction (E_v) for all three compounds from ab-initio DFT calculation. Following this, the interplay of these two parameters in associated hysteresis has been discussed in the light of the results of Monte Carlo simulation obtained by Banerjee et al. [8]

5.2 Theoretical Models on Cooperativity: Background Study

Most of the theoretical studies on SCO in extended polymeric systems were based on the prevailing idea that the interaction between different SCO centers stems from phononic excitations due to coupling between local lattice distortions at each molecular unit, setting up a long-range elastic wave. Two different model Hamiltonian approaches were followed to deal with elastic interactions between SCO centers to calculate thermodynamic quantities like HS fraction. HS fraction is defined by the ratio $\frac{n_{HS}}{N}$, where N is the total number of lattice sites and n_{HS} is the number of the sites in the HS state. The first category of approaches [13, 14] considers Ising-like Hamiltonians describing the elastic interaction between spin states, LS or HS, that interact via the nearest neighbor coupling.

The study by Boukheddaden et al.[13] considered a one-dimensional (1D) spin-phonon model, which is expected to simulate the SCO behavior of linear polymeric compounds. The model consisted of the assembly of a two-level system with elastic interaction between them. The HS state, represented by pseudo-spin $\sigma = 1$ was assumed to be n_H fold degenerate, while the LS state represented by σ = -1 was assumed to be n_L fold degenerate. The elastic interaction linking the sites i and $i + 1$ was denoted by $e_{i,i+1}$. The volume of the molecule changes upon the spin state transition, and hence the elastic interactions between two successive SCO sites were assumed to depend on their spin states (Figure-5.1) in the following manner, $e_{i,i+1} = e--$ for $\sigma_i = \sigma_{i+1}$ = -1, $e_{i,i+1} = e++$ for $\sigma_i = \sigma_{i+1}$ = +1, and $e_{i,i+1} = e+-$ for σ_i = -σ_{i+1}. The constructed model was solved in the framework of classical statistical mechanics using the transfer matrix technique. The effective interaction turned out to be ferroelastic for $e+- > \sqrt{e++ \times e--}$ and of antiferroelastic nature for $e+- < \sqrt{e++ \times e--}$. These situations is found to have a direct influence on the cooperativity. Ferroelastic interaction favors cooperativity with sharp spin state transition while the antiferroelastic interaction makes the transition gradual. This hinted at the fact that the first-order phase transition along with hysteresis might take place in higher dimensions in the presence of ferroelastic interaction. Following that interchain interaction terms were introduced keeping mind in that the interchain steric and electrostatic interactions could arise due to the presence of non-coordinated molecules or counter anions. The mean-field treatment of interchain interactions was found to reproduce the desired first-order nature of HS→LS transition together with hysteresis for ferroelastic intrachain interactions.

In the second category of calculations,[6] the free energy of SCO systems has been calculated based on an anisotropic sphere model describing the volume and shape changes of the lattice at the transition. The above-described approaches completely disregard the importance of the long-range magnetic interaction that

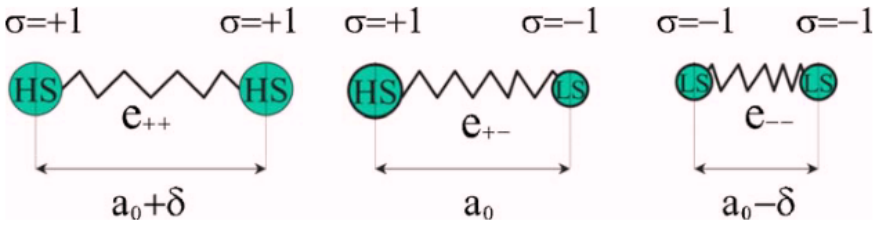

Figure 5.1: A schematic view of the three pseudo spin configurations of two neighboring atoms in the chain. The elastic constant of the spring linking two atoms depends on their spin states. e_{++}, e_{--}, and e_{+-} respectively, associated with the HS-HS, HS-LS, and LS-LS states. The figure is adapted from [13]

may build up between transition metal centers via superexchange interaction mediated through the organic linkers connecting the metal centers. To address this issue, the collective properties of SCO chains were investigated taking into account both elastic interaction and Ising-like magnetic interaction, and the ground state phase diagram was mapped out.[15] This calculation though ignored the spin-phonon coupling, considering the elastic interactions to be spin-independent, and thus were unable to distinguish between Ferro and antiferroelastic situations.

Banerjee et al.[8] have studied extensively the microscopic mechanism giving rise to cooperativity in spin crossover considering both the effect of magnetic super-exchange interaction and elastic interactions together with spin-phonon coupling in a coupled 1D chain model. A model Hamiltonian was set up on the basis of pseudo-spins, corresponding to the elastic part of the interaction, and the actual spin quantum number, describing the magnetic superexchange interaction. The system consisted of connected chains of spin-crossover ions, as shown in Figure-5.2. The SCO ions in a chain were assumed to be connected by intrachain elastic interactions that depend on their spin states given by $E_v(\sigma_{i,k}, \sigma_{i,k+1}) = \frac{e_{k,k+1}}{2} q_i^2$ where q_i being a small displacement. The spin dependence of $e_{k,k+1}$ was considered to be the same as in the model by Boukheddaden et al.[13] Magnetism was accounted for by actual spin S, where $m_{i,k} = S_{i,k}$ with $m_{i,k} = 0$ for $s_{i,k}$ = -1 (LS state) and $m_{i,k}$ = -2, ..., 2 for $s_{i,k} = 1$, corresponding to the HS state S = 2. Thus the constructed model Hamiltonian was given by

$$\begin{aligned} H = \quad & -\sum_k E_v(\sigma_{i,k}, \sigma_{i,k+1})\sigma_{i,k}\sigma_{i,k+1} + \Delta \sum_{i,k} \sigma_{i,k} \\ & -\sum_{i,k} [V_\perp \sigma_{i,k}\sigma_{i+1,k} + V_\parallel(\sigma_{i,k} + \sigma_{i+1,k})] \\ & + J \sum_k m_{i,k} m_{i,k+1} \end{aligned}$$

where Δ denoted the difference in energy between the HS and the LS states,

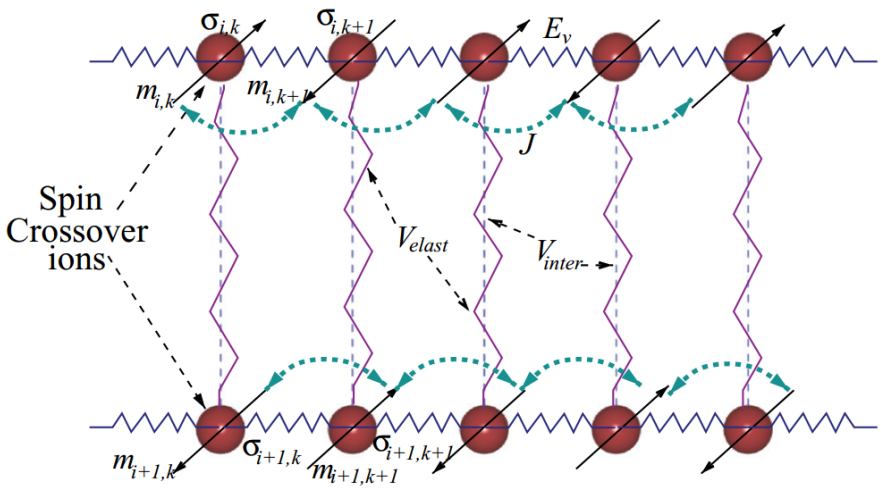

Figure 5.2: Schematic diagram showing the different site labels of the interconnected chains and the various intra- and interchain interactions. The figure is adapted from [8]

$V_\perp$ and $V_\parallel$ represented the interchain interactions arising out of electrostatic and steric interactions, respectively, as discussed earlier. The interchain interactions, though expected to be weaker compared to intrachain interactions, are crucial for the description of cooperativity in SCO as a strict 1D system cannot support phase transition. The third term of the Hamiltonian describes the magnetic exchange, which involves Ising-like antiferromagnetic superexchange interaction J acting between two Fe(II) ions with spin S = 2. The constructed Hamiltonian was solved using a Monte Carlo simulation based on a standard Metropolis algorithm.

5.3 Study of Present Compounds

5.3.1 Ab-initio calculation details

Ab initio calculation is carried out within the framework of density functional theory supplemented by Hubbard U (DFT + U) approach employing projector augmented-wave pseudopotentials and Perdew-Burke-Ernzerhof generalized gradient approximation (PBE-GGA)[16] as exchange-correlation functional as implemented in the plane-wave based Vienna ab initio simulation package (VASP)[17]. The choice of U in our calculation is guided by the study done by Banerjee et al.[8] where they took U = 4.0 eV and J = 0.8 eV for Fe-triazole compound and The variation within $3 \leq U \leq 6$ eV was found to keep the qualitative result the same. The cutoff energy of the plane-wave basis is chosen to be 500 eV, sufficient to achieve convergence in self-consistent field (SCF) calculations. HS and LS structures of $[Fe(bbtz)_2(MeOH)_2]$ $(ClO_4)_2$ compound are generated through

structural optimization taking the spin of Fe(II) fixed, for HS: S=2 and LS: S=0. Since LS structure is expected to have a more rigid lattice compared to HS, we follow a two-step route for optimization i.e., optimization with respect to unit cell volume is followed by that of ionic position. The relaxation of Fe-bbtz compound and model structures for elastic exchange calculation is done using a convergence threshold of 10^{-5} eV for the total energy and 0.01 eV/$\mathring{A}$ for maximum force/atom employing Monkhorst-Pack mesh[18]. For magnetic and elastic exchange calculation, k-mesh of size 2×2×2, 4×4×2, and 2×2×2 (Fe-hbtz) have been used for SCF calculation using respective supercell structures with increased energy convergence threshold of 10^{-8} eV.

5.3.2 Crystal Structure details

In the following, we discuss the details of the crystal structure of the coordination polymeric compounds used in this Chapter for understanding the underlying mechanism of cooperativity associated with corresponding spin transitions. Table-5.1 summarize the crystal structure details of three compounds.

$[Fe(ebtz)_2(C_2H_5CN)_2](ClO_4)_2$

$Fe(ebtz)_2(C_2H_5CN)_2](ClO_4)_2$ compound[9] crystallizes in the monoclinic $P21/n$ space group which remains unchanged over temperature. The coordination environment of iron(II) consists of four tetrazole rings forming the basal plane of the octahedron, and two axially coordinated propionitrile molecules (Figure-5.3). As evident from Figure-5.4, two ebtz molecules connect Fe(II) ions, and such linkage is propagated along a direction leading to the formation of a 1D network. Polymeric units, gathered in the (010) plane, are tethered through C-H—N weak intermolecular interactions into 2D supramolecular layers visible in the stacking pattern. Consecutive supramolecular layers are separated by perchlorate anions participating in the formation of numerous C-H—O intermolecular contacts.

At 250 K, the average bond length of the FeN_6 octahedra is 2.171$\mathring{A}$ and the corresponding N-Fe-N angles are 92.3^o. After the temperature lowering from 250 to 110K the Fe-N distances and the average N-Fe-N angles remain the same. Also after fast cooling (2K/min) from 110 to 100K Fe-N bond lengths retain HS characteristics. At 80K, the average bond length of the FeN_6 octahedra becomes 1.965 $\mathring{A}$ indicating the presence of the LS Fe(II) ions in the sample. Clearly, HS→LS spin transition is accompanied by the shortening of the Fe-N(tetrazole) bond lengths at 0.21 $\mathring{A}$. Now increasing the temperature from 80 to 120K does not affect the LS FeN_6 octahedral geometry. The increase of temperature from 120 to 160K is accompanied by the LS→HS transition, and Fe-N bond lengths become comparable to the ones found for HS geometry.

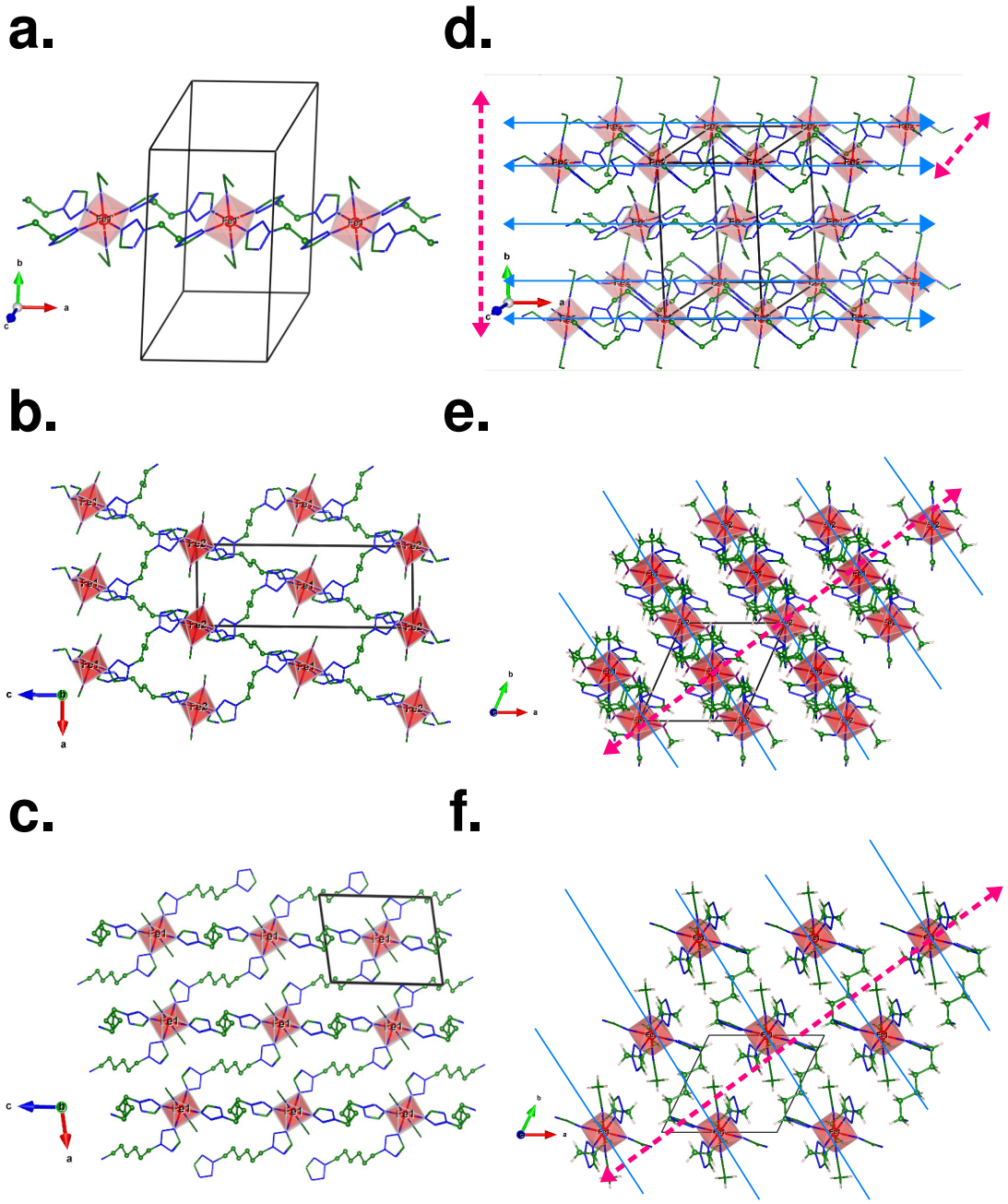

Figure 5.3: Different networks formed by Fe(II) centres connected by tetrazole based ligands shown for **a.** Fe-ebtz, **b.** Fe-bbtz and **c.** Fe-hbtz compounds. $(ClO_4)^-$ are ommited for clarity. The small green balls represent the C atoms situated at the linker of tetrazole-based ligands. The black solid line represents the unit cell for each compound. **d-f.** shows the stacking pattern of corresponding compounds. Double-headed blue arrows in **d.** indicate the direction of the 1D network along a-direction. Blue lines in **e-f.** indicate the planes of the 2D network. Red dashed double-headed arrows indicate the stacking arrangements of different networks.

$[Fe(hbtz)_2(CH_3CN)_2](ClO_4)_2$

$Fe(hbtz)_2(CH_3CN)_2](ClO_4)_2$ compound[10] crystallize in the $P\bar{1}$ space group and do not undergo a crystallographic phase transition. Similar to the Fe-ebtz compound, the coordination environment of Fe(II) consists of four tetrazole rings forming the basal plane of the octahedron, and two axially coordinated acetonitrile molecules (Figure-5.3). The first coordination sphere consists of two crystallographically inequivalent hbtz molecules that differ from each other in their conformations. Both conformers bridge Fe(II) ions in different directions. a) Alkyl spacer of hbtz molecules linking Fe(II) ions in the $[1\bar{1}1]$ direction adopts an *extended zigzag conformation*. The tetrazole rings are transoidal oriented, and the distance between Fe(II) ions in the $[1\bar{1}1]$ bridging direction equals $12.928\mathring{A}$. b) In another hbtz molecule, transoidal oriented tetrazole rings are tethered by a hexyl spacer adopting an *S-shaped conformation*. The S-shaped ligand molecule links Fe(II) ions arranged in the [001] direction separating them at a distance of $11.736\mathring{A}$. As a result, cross-linking of the Fe(II) ions gathered in a common plane leads to the formation of a 2D layer with a grid-like pattern.

At 293K, the average bond length of the FeN_6 octahedra is 2.172 $\mathring{A}$. The geometry of the FeN_6 chromophore shows the HS characteristic and remains unchanged during cooling to 200K. Lowering of temperature below 150K involves more abrupt alterations of the crystal structure parameters. At 125K, the Fe-N distances manifest approximately equal amounts of HS and LS Fe(II) in the sample. After cooling to 100K, the average bond length of the FeN_6 octahedra becomes 2.006 $\mathring{A}$ corresponding to LS characteristics. Here Fe-N(tetrazole) bond length is shortened by 0.17 $\mathring{A}$ during HS$\rightarrow$LS spin transition induced by temperature lowering from 293 to 100K.

$[Fe(bbtz)_2(MeOH)_2](ClO_4)_2$

HS and LS structures of $[Fe(bbtz)_2(MeOH)_2](ClO_4)_2$ compound are computer generated. Structural optimization causes the structure to acquire the lowest symmetry P1. Here we assume that spin transition is not accompanied by crystallographic phase transition. The unit cell volume for the HS structure ($1493.3\mathring{A}^3$) turns out to be larger than the LS one ($1478.8\mathring{A}^3$) which validates our expectation that the LS structure must have a more rigid lattice compared to that of HS. Similar to the other two compounds, the coordination environment of Fe(II) consists of four tetrazole rings forming the basal plane of the octahedron, and two axially coordinated methanol (MeOH) molecules (Figure-5.3). Basal planes are formed by nitrogen atoms coming from tetrazole moieties and axial positions are occupied by oxygen atoms from methanol molecules. The calculated average bond length of the FeN_4O_2 octahedra is found to be 2.190 $\mathring{A}$ in HS and 2.001 $\mathring{A}$ in LS state. Thus, Fe-N(tetrazole) bond length is expected to be shortened by

Compound	No.of C in alkyl Linkers	Fe-Fe connectivity	Stacking pattern
Fe-ebtz	2	Two ebtz ligands connect Fe(II) ions forming 1D network along [100]	Fe chains tethered via C-H—N bonds in (010) plane forming supra-molecular layer that stack along [001]
Fe-bbtz	4	Four bbtz ligands connect Fe(II) ions along $[1\bar{1}1]$ and $[1\bar{1}\bar{1}]$ forming 2D network in $(\bar{1}\bar{1}0)$ plane	2D network stack along perpendicular to $(\bar{1}\bar{1}0)$ plane
Fe-hbtz	6	Four hbtz ligands connect Fe(II) ions along $[1\bar{1}1]$ (*zigzag conformation*) and [001] (*S-shaped conformation*) forming 2D network in $(\bar{1}\bar{1}0)$ plane	2D network stack along perpendicular to $(\bar{1}\bar{1}0)$ plane

Table 5.1: Comparison of the crystal structure of two-C linker connectivity Fe-ebtz, four-C linker connectivity Fe-bbtz, and six-C linker connectivity Fe-hbtz compound. Fe(II)-Fe(II) connectivity and stacking pattern present in the polymer is discussed.

$0.19\mathring{A}$ when HS→LS spin transition will be realized. Unlike hbtz ligand, bbtz molecules have the same conformations within the coordination sphere. Fe(II) ions bridged by bbtz molecules propagate along $[1\bar{1}1]$ and $[1\bar{1}\bar{1}]$ directions leading to 2D polymeric network similar to Fe-hbtz compound.

5.3.3 Ab-initio derived parameters for cooperativity

As discussed above spin-state dependent elastic interaction (E_v) and magnetic exchange interaction (J) are the crucial parameters in driving cooperativity. In the following section, we calculate these material-specific parameters for three

polymeric compounds.

Magnetic exchange interactions

To estimate magnetic exchange, we consider a spin-Hamiltonian $H = JS_iS_{i+1}$ where J denotes the exchange interaction between nearest neighbors Fe(II) spins S_i. Figure-5.4 shows the supercell of each compound used for J calculation marking the superexchange path between nearest neighbor Fe(II) ions.

For J calculation of Fe-ebtz compound, we extend the unit cell along chain [100] direction to build a 2×1×1 supercell. Distance between two intrachain Fe(II) distance is 8.388$\mathring{A}$. Now we compute the total energies taking ferromagnetic and antiferromagnetic spin orientations for two Fe(II) intrachain nearest neighbor ions. They are given by E_{FM} = 8J and E_{AFM} = -8J. Now, $E_{FM} - E_{AFM}$ for Fe-ebtz compound, = 28.8 meV, and therefore J turns out 1.8 meV (20.9 K). Fe-hbtz compound consists of one Fe(II) ion inside the unitcell. For J calculation, we extend the unit cell in all three lattice vector directions to build a 2×2×2 supercell. Supercell is so chosen that all interactions along alkyl linkers can be taken care of. Distance between Fe(II) ions along zigzag conformation linker is 12.928$\mathring{A}$ whereas along S-shaped conformation linker is 11.736$\mathring{A}$. Taking four Fe(II) nearest neighbor ions, total energy corresponding to ferromagnetic and antiferromagnetic spin orientations is given by, E_{FM} = 16J and E_{AFM} = -16J. Now, $E_{FM} - E_{AFM}$ for Fe-hbtz compound, = 17.28 meV and therefore J turns out 0.54 meV (6.3K). For Fe-bbtz compound, calculation is done on the unitcell which consists of two Fe(II) ions connected along both possible linker direction, one of the ion being corner shared. The distance between Fe(II) ions is 11.605$\mathring{A}$. Similar to Fe-hbtz, $E_{FM} - E_{AFM}$ for Fe-bbtz compound, = 24.32 meV and therefore J turns out 0.76 meV (8.82K). Table-5.2 summarizes our results regarding the magnetic exchange calculation. Positive values of magnetic exchange interaction for all three polymeric compounds indicate that it is antiferromagnetic in nature.

Magnetic exchange for Fe-ebtz compound (20.9K) is found to be comparable with that of Fe-triazole compound (18K) computed by Banerjee et al. We also notice that the value of J decreases as the length of the alkyl linker increase in the polymeric structure. This suggests that the magnetic superexchange interaction mediated through the organic ligands will become weaker as the distance between Fe(II) increases.

Spin dependent elastic interactions

We estimate the spin-state-dependent elastic interactions by taking the following steps. For that three model structures for each polymeric compound are constructed having two regular FeN_6 octahedrons inside unitcell with the following spin configuration: a) HS-HS, b) LS-LS, and c) HS-LS. For HS-HS and LS-LS

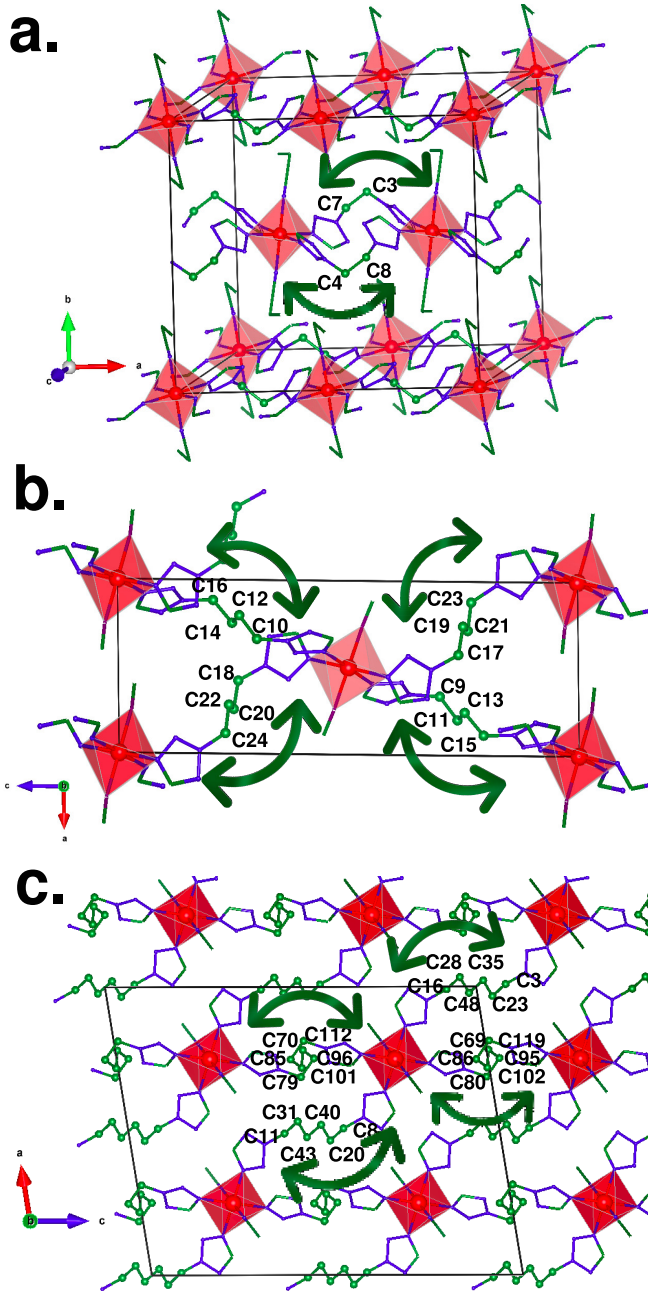

Figure 5.4: Supercell of each compound used for J calculation is shown. Possible superexchange paths between neighboring Fe(II) ions are also marked and C atoms of the alkyl linker of corresponding compounds involving the path are labeled.

Compound (Cell dimension)	No. of n.n. Fe-Fe (d_{Fe-Fe} (Å))	Superexchange path between n.n. Fe-Fe	E(FM-AFM) (meV)	J (K)
Fe-ebtz (2×1×1)	2 (8.39)	1. trz-C4-C8-trz 2. trz-C7-C3-trz	28.80 (Anti-ferro)	20.90
Fe-bbtz (1×1×1)	4 (11.61)	1. trz-C10-C12-C14-C16-trz 2. trz-C18-C22-C20-C24-trz 3. trz-C17-C19-C21-C23-trz 4. trz-C9-C11-C13-C15-trz	24.32 (Anti-ferro)	8.82
Fe-hbtz (2×2×2)	4 (12.33)	1. trz-C80-C95-C119-C102-C86-C89-trz 2. trz-C70-C85-C101-C112-C98-C79-trz 3. trz-C16-C28-C48-C35-C23-C3-trz 4. trz-C8-C20-C40-C43-C31-C11-trz	17.28 (Anti-ferro)	6.30

Table 5.2: Calculation of magnetic exchange parameter (J) for three polymeric compounds. Dimension of supercells, no. of Fe(II) nearest neighbor (n.n.) used for J calculation is mentioned. Possible superexchange paths between n.n. Fe(II)s for different polymeric networks, marked in figure-5.4, are also mentioned, where "trz" denote the tetrazole ring attached to FeN_6 octahedron.

model structure we use the supercell used for J calculation with HS and LS geometry respectively. To construct model HS-LS model structure, first, we took the LS-LS model structure and replaced one of the LS FeN_6 octahedrons with an HS one. Then we adjust the unit cell volume equal to the average of the HS-HS and LS-LS model structure. Finally, we carried out an ionic relaxation (selective dynamics) freezing the coordinates of atoms involving FeN_6 octahedra to obtain the HS-LS structure.

To determine E_v, total energies (E) of all three model configurations of undeformed and deformed structures are computed varying the average Fe-N bond length within the harmonic limit [-0.03, 0.03 $\mathring{A}$]. Slope of ΔE vs Δ <Fe-N> curve for HS-HS, LS-LS and HS-LS configuration gives e_{++}, e_{--} and e_{+-} respectively. (Figure-5.5) Now we calculate E_v using the following formula, $E_v(\sigma_{i,k}, \sigma_{i,k+1}) = 0.5 * e_{k,k+1} * (q_i)^2$. Setting q=0.005Å, E_v for different polymeric compounds are

listed in Table-5.3.

Compound	model	e ($eV/\mathring{A}^2$)	E_v (K)	$\sqrt{e_{++} \times e_{--}}$ ($eV/\mathring{A}^2$)
Fe-ebtz	HS-HS	439.73	64	
	LS-LS	517.58	75	477
	HS-LS	459.30	66	(anti-ferroelastic)
Fe-bbtz	HS-HS	290.45	41	
	LS-LS	305.08	44	298
	HS-LS	292.34	42	(anti-ferroelastic)
Fe-hbtz	HS-HS	234.43	33.6	
	LS-LS	246.08	36	240
	HS-LS	237.44	34.8	(anti-ferroelastic)

Table 5.3: Spin-dependent elastic interaction of three polymeric compounds and corresponding elastic interaction type

From Table-5.3, we find that $e_{++} < e_{--}$ for all three polymeric compounds confirming that the LS crystal lattice is more rigid than the HS one. Effective elastic interaction decreases as the size of the alkyl linker increase in the polymeric structure. This can be witnessed from the decrease in the slope of ΔE vs Δ <Fe-N> curve as we move from Fe-ebtz, Fe-bbtz, and Fe-hbtz compounds. Moreover, spin-dependent elastic interaction (E_v) for all three polymeric compounds turns out to be antiferro type in nature signaling the fact that associated cooperativity in these compounds will be decided by the long-range magnetic interaction.

5.4 Discussion on Hysteresis

Spin transition in Fe-ebtz and Fe-hbtz compounds is confirmed by the temperature-dependent magnetic susceptibility measurements carried out over the range of 5-300K.[9, 10] In the following we will first discuss the spin transition behavior of Fe-ebtz and Fe-hbtz compounds.

a) For Fe-ebtz compound, Upon cooling (scan rate = 0.1 K/min), $\chi_M T$ remains almost constant in the temperature range 300-117K. Further lowering of temperature involves the abrupt drop in the $T_{1/2}$ value with $T^{\downarrow}_{1/2} = 112$ K. In the temperature range from 116K to 108K 80% of the HS→LS transition occurs. At 103K SCO is practically nished, indicating complete HS→LS transition. After reaching 5K, a measurement in the heating mode was performed. 80% of the LS→HS transition ($T^{\uparrow}_{1/2} = 141$ K) occurs in the range from 137K to 145K. This opens up a hysteresis loop of width $\Delta T_{1/2} = 29$K. Cooling at the rate of 1K/min

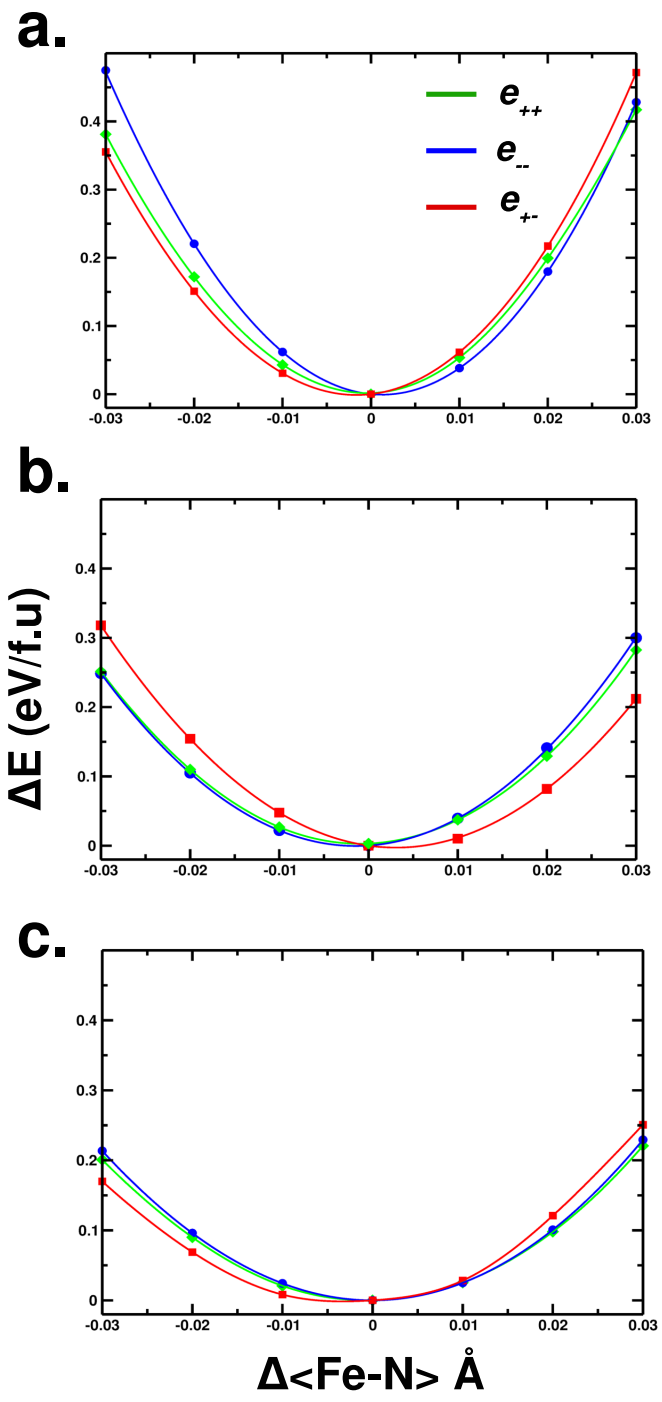

Figure 5.5: The variation of total energy as a function of variation of Fe-N bond length about the equilibrium value, for three different configurations: LS-LS (circles), LS-HS (squares), and HS-HS (diamonds) of **a.** Fe-ebtz, **b.** Fe-bbtz and **c.** Fe-hbtz compound. Solid lines are fit to data points.

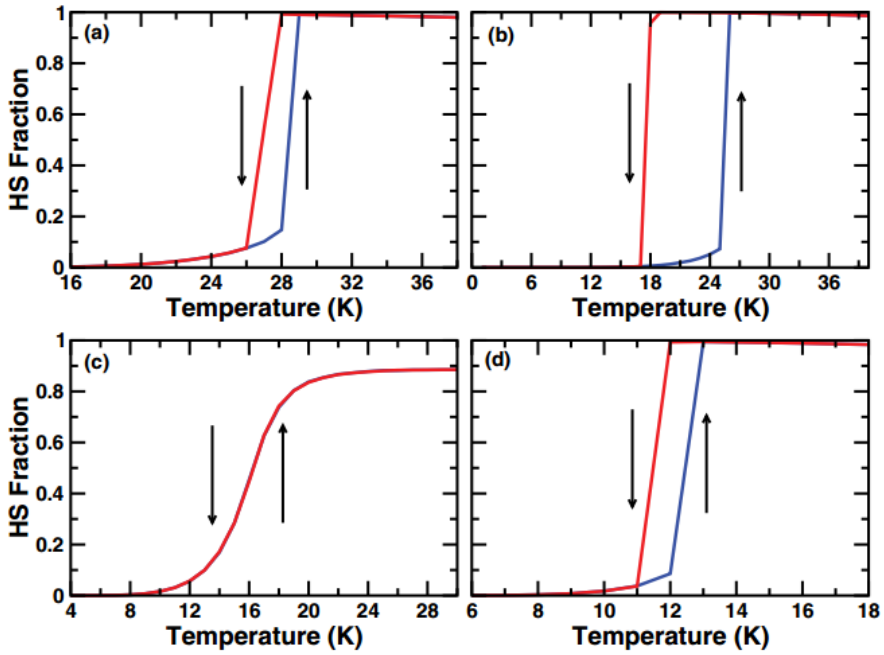

Figure 5.6: Results of Monte Carlo simulation. High spin fraction plotted as a function of increasing temperature (heating cycle) and decreasing temperature (cooling cycle), for (a) ferroelastic intrachain coupling with magnetic coupling set to zero, (b) ferroelastic intrachain coupling with finite, nonzero magnetic coupling, (c) antiferroelastic intrachain coupling with magnetic coupling set to zero, and (d) antiferroelastic intrachain coupling with finite, nonzero magnetic coupling. The figure is adapted from [8]

reveals a shift of $T_{1/2}^{\downarrow} \sim 102$K to lower temperature values whereas the course of the $\chi_M T$ in the heating mode remained independent of the scan rate.

b) For Fe-hbtz compound, variation of $\chi_M T$ with temperature leads to the following observations. $\chi_M T$ (χ_M: molar susceptibility, T: temperature) value at 300K shows HS characteristic of Fe(II) ion. In the temperature range of 300-200K the $\chi_M T$ value slightly increases. Further lowering of the temperature involves a gradual lowering of the $\chi_M T$. In the range of 150-120K the $\chi_M T$ value decreases more abruptly ($T_{1/2}^{\downarrow} = 128$ K). Below 120 K the $\chi_M T$ decreases gradually reaching 75K which confirms the HS→LS transition. In the warming mode, the course of the $\chi_M T$(T) dependency is almost same as it was observed in the cooling cycle.

Fe-ebtz with two-C linker connectivity and Fe-hbtz with six-C linker connectivity compound shows abrupt thermal spin transition accompanied by hysteresis of width 29K and 2K respectively, indicating that the cooperativity among Fe(II) ions is greatly affected upon increasing the length of the alkyl linker. To study the systematic evolution, we follow the route proposed by Banerjee et al.[8] based on the model Hamiltonian approach which involves the estimation of material-specific parameters i.e., Fe-Fe magnetic exchange interaction (J) and spin-state dependent elastic interaction (E_v) for all three SCO compounds, discussed in the previous section. According to the study by Banerjee et al.[8], depending on the nature of E_v i.e., spin-phonon coupling, the magnetic superexchange was found to contribute to the development of cooperativity in a quantitative or qualitative manner as summarized in Figure-5.6. In the case of ferroelastic interaction, the superexchange interaction was found to enhance the hysteresis effect, set up by the elastic interaction. This is evident from the top panel of Figure-5.6 (a, b). In the case of the antiferro nature of elastic interaction, the magnetic exchange interaction was found to play a decisive role in driving the hysteresis in the system, putting the elastic coupling in a back seat. As is seen from the bottom panel of Figure-5.6 (c, d), in the presence of Antiferroelastic interaction alone, the system did not show any hysteresis. Only when the magnetic superexchange interaction J was introduced, a hysteresis loop was observed in the HS fraction. It was thus concluded that the magnetic superexchange interaction is of prime importance in driving cooperativity in the system if the intrachain elastic interaction is of antiferro type.

Our calculations show that the elastic exchange E_v for all the compounds is of an anti-ferroelastic type. Given the fact that E_v is of antiferro origin, the hysteresis loop may open up in the spin transition curve only upon the introduction of magnetic exchange J as evident from the bottom panel of Figure-5.6(c, d). The width of the hysteresis loop is found to be $\sim$ 1K for the choice of J = 2K as evident from Figure-5.6(d). Banerjee et al.[8] reported J = 18K for Fe-triazole polymer which shows spin transition accompanied by hysteresis of width $\Delta T_{1/2}$ = 20K. Hysteresis width ($\Delta T_{1/2}$) turned out to be the same order of magnitude as that of the magnetic interaction J existing among the Fe(II) center of the

polymers. With this knowledge, a correlation can be built between J and $\Delta T_{1/2}$ for our studied polymers. In our case, J turns out to be anti-ferromagnetic for all compounds. J decreases as we move from Fe-ebtz (20.9K) to Fe-bbtz (8.82K) and Fe-hbtz (6.30K) compound. The decrease of the J value with the increasing length of the ligand confirms the experimental observation of a decrease in $\Delta T_{1/2}$ from Fe-ebtz (29K) to Fe-hbtz (2K) compound. Clearly, cooperativity among Fe(II) center, dictated by the value of $\Delta T_{1/2}$, decreases as the length of the bridging ligands increase. J value for Fe-bbtz compound lies intermediate between Fe-ebtz and Fe-hbtz compound suggesting the computed Fe-bbtz structure must show spin transition accompanied by hysteresis of $\Delta T_{1/2} \sim 9$K which is yet to be validated from the experiment.

5.5 Summary

Following the route proposed by Banerjee et al., [8], we aim to provide an understanding of the microscopic origin of cooperativity associated with the several Fe tetrazole-based SCO polymers in this Chapter. The key question we address here is that how the cooperativity among Fe(II) centers builds upon while the size of the bridging ligands changes. To maintain the uniformity in the structural motif, we choose three Fe(II)-tetrazole-based polymeric compounds namely, a) $[Fe(ebtz)_2(C_2H_5CN)_2](ClO_4)_2$, b) $[Fe(bbtz)_2(MeOH)_2](ClO_4)_2$, and c) $[Fe(bbtz)_2(MeOH)_2](ClO_4)_2$ in which bridging ligands are differed by the number of carbon atoms present in the alkyl linkers joining two tetrazole rings leading to the formation of 1D and 2D coordination networks. HS and LS crystal structure of a) and c) was available whereas b) is generated theoretically by spin-polarized structural relaxation starting from the Cu compound and replacing Cu with Fe. To probe the evolution in cooperativity, we estimate the Fe-Fe magnetic exchange interaction (J) and spin-state dependent elastic interaction (E_v) for all three compounds from ab-initio DFT calculation. Depending on the nature of E_v i.e., spin-phonon coupling, the magnetic superexchange was found to contribute to the development of cooperativity in a quantitative or qualitative manner.[8] Our calculations show that the elastic exchange E_v for all the compounds is of an anti-ferroelastic type. Given the fact that E_v is of antiferro origin, the hysteresis loop may open up in the spin transition curve only upon the introduction of magnetic exchange J. The decrease of the J value with the increasing length of the ligand confirms the experimental observation of a decrease in $\Delta T_{1/2}$ from Fe-ebtz to Fe-hbtz compound. Hence, cooperativity among Fe(II) center decreases as the length of the bridging ligands increase. Moreover, the J value for the yet-to-be synthesized Fe-bbtz compound suggests that it must show spin transition accompanied by hysteresis of $\Delta T_{1/2} \sim 9$K.

References

[1] J. F. Létard, P. Guionneau, and L. Goux-Capes, *Spin Crossover in Transition Metal Compounds I-III: Gütlich, P., Goodwinpp, H.* Springer: Berlin, Germany, 2004.

[2] O. Kahn, "Spin-crossover molecular materials," *Current Opinion in Solid State and Materials Science*, vol. 1, no. 4, pp. 547–554, 1996.

[3] T. Saha-Dasgupta and P. M. Oppeneer, "Computational design of magnetic metal-organic complexes and coordination polymers with spin-switchable functionalities," *MRS bulletin*, vol. 39, no. 7, pp. 614–620, 2014.

[4] J. Linares, E. Codjovi, and Y. Garcia, "Pressure and temperature spin crossover sensors with optical detection," *Sensors*, vol. 12, no. 4, pp. 4479–4492, 2012.

[5] S. Cobo, G. Molnár, J. A. Real, and A. Bousseksou, "Multilayer sequential assembly of thin films that display room-temperature spin crossover with hysteresis," *Angewandte Chemie International Edition*, vol. 45, no. 35, pp. 5786–5789, 2006.

[6] H. Spiering, K. Boukheddaden, J. Linares, and F. Varret, "Total free energy of a spin-crossover molecular system," *Physical Review B*, vol. 70, no. 18, p. 184106, 2004.

[7] H. O. Jeschke, L. A. Salguero, B. Rahaman, C. Buchsbaum, V. Pashchenko, M. U. Schmidt, T. Saha-Dasgupta, and R. Valentí, "Microscopic modeling of a spin crossover transition," *New Journal of Physics*, vol. 9, no. 12, p. 448, 2007.

[8] H. Banerjee, M. Kumar, and T. Saha-Dasgupta, "Cooperativity in spin-crossover transition in metalorganic complexes: Interplay of magnetic and elastic interactions," *Physical Review B*, vol. 90, no. 17, p. 174433, 2014.

[9] A. Białonska and R. Bronisz, "Role of fe–n–c geometry flip-flop in bistability in fe (tetrazol-2-yl) 4 (c2h5cn) 2-type core based coordination network," *Inorganic Chemistry*, vol. 51, no. 23, pp. 12630–12637, 2012.

[10] A. Białonska and R. Bronisz, "High spin and spin-crossover two-dimensional coordination polymers containing feii (tetrazol-2-yl) 4 (solv) 2 (solv= ethanol, acetonitrile) cores linked by flexible/elastic spacers," *Inorganic chemistry*, vol. 49, no. 10, pp. 4534–4542, 2010.

[11] R. Bronisz, "Tetrazol-2-yl as a donor group for incorporation of a spin-crossover function based on fe (ii) ions into a coordination network," *Inorganic chemistry*, vol. 46, no. 16, pp. 6733–6739, 2007.

[12] R. Bronisz, "1, 4-di (1, 2, 3, 4-tetrazol-2-yl) butane as a precursor of new 2d and 3d coordination polymers of cu (ii)," *Inorganica chimica acta*, vol. 357, no. 2, pp. 396–404, 2004.

[13] K. Boukheddaden, S. Miyashita, and M. Nishino, "Elastic interaction among transition metals in one-dimensional spin-crossover solids," *Physical Review*

B, vol. 75, no. 9, p. 094112, 2007.

[14] K. Boukheddaden, J. Linares, R. Tanasa, and C. Chong, "Theoretical investigations on an axial next nearest neighbour ising-like model for spin crossover solids: one-and two-step spin transitions," *Journal of Physics: Condensed Matter*, vol. 19, no. 10, p. 106201, 2007.

[15] C. Timm, "Collective effects in spin-crossover chains with exchange interaction," *Physical Review B*, vol. 73, no. 1, p. 014423, 2006.

[16] J. P. Perdew, K. Burke, and M. Ernzerhof, "Generalized gradient approximation made simple," *Physical review letters*, vol. 77, no. 18, p. 3865, 1996.

[17] G. Kresse and J. Hafner, "Ab initio molecular dynamics for liquid metals," *Physical review B*, vol. 47, no. 1, p. 558, 1993.

[18] H. J. Monkhorst and J. D. Pack, "Special points for brillouin-zone integrations," *Physical review B*, vol. 13, no. 12, p. 5188, 1976.

Chapter 6

First-principles Prediction of Enhanced Thermoelectric Properties of Double Transition Metal MXenes: $Ti_{3-x}Mo_xC_2T_2$ (x =0.5, 1, 1.5, 2, 2.5, T = -OH/-O/-F)*

6.1 Introduction and Motivation

MXene, the family of transition-metal (TM) carbides, nitrides and carbonitrides having general formula $M_{n+1}X_nT_x$ (n = 1-3) have drawn the attention of scientific community due to its unique electronic properties ranging from metallic to semiconducting, depending on the nature of M, X and T.[1, 2] MXene has been studied as a high-temperature thermoelectric (TE) materials due to its excellent thermal stability in air [3–5]. TE properties of MXenes with single TM have been studied extensively using the Boltzmann transport theory and first-principles electronic structure calculations. Khazaei et al.[6] predicted the electronic transport properties of more than 35 kinds of different functionalized MXene monolayers and multilayers of the type M_2CT and M_2NT, M=Cr, Ti, Mo, Zr, and Hf etc and T= O, F, OH. Gandi et al.[7] calculated the lattice thermal conductivity (κ_l) of O passivated Ti-, Zr-, and Hf- based MXenes and found the highest figure of merit for Ti_2CO_2 (ZT_{max} = 0.45). The study by Kumar et al.[8] predicted the semiconducting Sc_2CT_2 (T = OH) MXenes with ZT_{max} value of 0.5 at T=900K.

*This chapter is based on publication : **Shiladitya Karmakar** and Tanusri Saha-Dasgupta, *Physical Review Materials*, **4.12**, 124007 (2020).

The discovery[9] of ordered double transition metal 2D carbides in 2014 and subsequent successful synthesis[10] of ordered double transition metal 2D MXenes such as Mo_2TiC_2, $Mo_2Ti_2C_3$, and Cr_2TiC_2 in 2015 provided further opportunity on expanding on the possible list of MXene compounds with potential TE properties. Presence of two transition metals instead of a single one, as in conventional MXene compounds, offer even better flexibility in tuning of properties. Kim et al.[11] reported the measured electronic transport properties of Mo-based double TM MXene (Mo_2CT_x, $Mo_2TiC_2T_x$, and $Mo_2Ti_2C_3T_x$; T_x : mixed termination of O. F, OH group). Jing et al.[12] predicted the thermoelectric performance of semiconducting Cr_2TiC_2 and $Cr_2TiC_2T_2$ (T= F or OH) MXene and found large Seebeck coefficients of $\sim$ 800, 700 and 600 μVK^{-1}, respectively. Figure of merit of p-type $Cr_2TiC_2(OH)_2$ was predicted to reach as high as 3.0 at 600K.

Motivated by the above, in the present chapter we focus on Mo and Ti based double transition metal MXenes, namely $Ti_{3-x}Mo_xC_2T_2$ with T = -O/-F/-OH. The Mo concentration is varied over a wide range with x = 0.5, 1, 1.5, 2, 2.5 in order to understand the systematic evolution of properties upon increasing (decreasing) Mo (Ti) concentration. x = 1 and 2 of the series correspond to stoichiometric compositions of Ti and Mo in 2:1 and 1:2 ratio, out of which x = 2 is the experimentally synthesized $Mo_2TiC_2T_2$ composition.[13] As described in the chapter-1, MXenes with ordered double TM can exist in two different forms,[14, 15] a) O-MXene: out-of-plane ordering of $M^{'}$ and $M^{''}$-rich layers. For stoichiometric compounds, this results in layers containing $M^{'}$ or $M^{''}$ TMs only, as observed in Mo_2TiC_2, $Mo_2Ti_2C_3$, Cr_2TiC_2.[10, 13], and b) I-MXene: in-plane ordering of $M^{'}$ and $M^{''}$ TMs, which is repeated in out-of-plane direction, such as $(Mo_{2/3}Sc_{1/3})_2C$.[16].

In this chapter employing first-principles calculations, we study the relative structural stability of O-MXene and I-MXene phases, which uncovers the role of magnetism and passivation on the nature of chemical ordering exhibited by the compounds. Following the understanding of the structure, electrical and magnetic properties of the five Ti-Mo based double transition metal carbide MXenes, we thus investigate the lattice and electron transport properties of the compounds exhibiting semiconducting properties. The thermoelectric properties are studied based on Boltzmann theory under relaxation time approximation. The goodness of the calculations is validated by computing the electronic transport coefficients for $TiMo_2C_2O_2$, $TiMo_2C_2F_2$ and $TiMo_2C_2(OH)_2$ as well as mixed passivated compounds, and comparing with the experimental data of $TiMo_2C_2T_x$.[11]

6.2 Computational Details

The first-principles electronic structure calculations are performed within the framework of density functional theory (DFT) using projector augmented wave

(PAW) pseudo-potentials as implemented in the plane wave based Vienna Ab-initio Simulation Package (VASP).[17] The exchange-correlation functional is chosen to be that of the generalized gradient approximation (GGA) as implemented in the Perdew-Burke-Ernzerhof (PBE-GGA) formalism.[18] The cut-off energy of plane-wave basis is chosen to be 520 eV, which is found to be sufficient for achieving necessary convergence in self-consistent energy. To take into account the correlation effects beyond GGA in *d* orbitals of TM atoms, simulations are performed using a spin-dependent GGA with supplemented Hubbard U (GGA+U).[19] The U values for the *d* orbitals of Ti and Mo atoms are set to 4 eV as used by Anasori et al[14] for Mo_2TiC2 and $Mo_2Ti_2C_3$ MXenes, and a value also widely applied for Ti and Mo oxides.[20, 21] For the semiconducting compounds, the obtained band gaps have been further checked by repeating the calculations with HSE06 (Heyd-Scuseria-Ernzerhof) functional.[22] The HSE06 bandgap values are found to be in good agreement with GGA+U values, differing at most by 0.02-0.03 eV, justifying the goodness of our calculation scheme.

Alloy	**O-phase**		**I-phase**	
	outer layers	middle layer	outer layers	middle layer
$Ti_{0.5}Mo_{2.5}C_2$	36Mo	18Mo + 18 Ti	30Mo + 6 Ti	30Mo + 6Ti
$TiMo_2C_2$	36Mo	36Ti	24Mo + 12 Ti	24Mo + 12 Ti
$Ti_{1.5}Mo_{1.5}C_2$	12Mo + 24 Ti	30Mo + 6Ti	18Mo + 18Ti	18Mo + 18Ti
Ti_2MoC_2	36Ti	36Mo	24Ti +12 Mo	24Ti + 12 Mo
$Ti_{2.5}Mo_{0.5}C_2$	36Ti	18Ti + 18 Mo	30Ti + 6Mo	30Ti + 6Mo

Table 6.1: Number of Mo and Ti atoms in TM layers of $Ti_{3-x}Mo_xC_2$ MXenes within 6 × 6 × 1 supercell.

To create the studied MXene compounds, we first exfoliate Mo_2TiC_2 MXene from its corresponding MAX phase Mo_2TiAlC_2 with hexagonal space group $P6_3/mmc$. In order to consider $Ti_{3-x}Mo_xC_2$ 2D alloy structures of varying compositions, x =0.5, 1, 1.5, 2, 2.5, 6×6×1 supercell of the optimized Mo_2TiC_2 structure is considered. To enable calculation of 2D structures within periodic set-up, a vacuum space of $\sim 18\mathring{A}$ is considered between the periodic images, minimizing the artificial interaction between 2D images. Structural relaxation of the constructed structures is achieved with respect to lattice constant and internal atomic coordinates using convergence threshold of 10^{-5} eV for total energy and 10^{-3} eV/$\mathring{A}$ for maximum force/atom. For Brillouin zone sampling 10×10×2

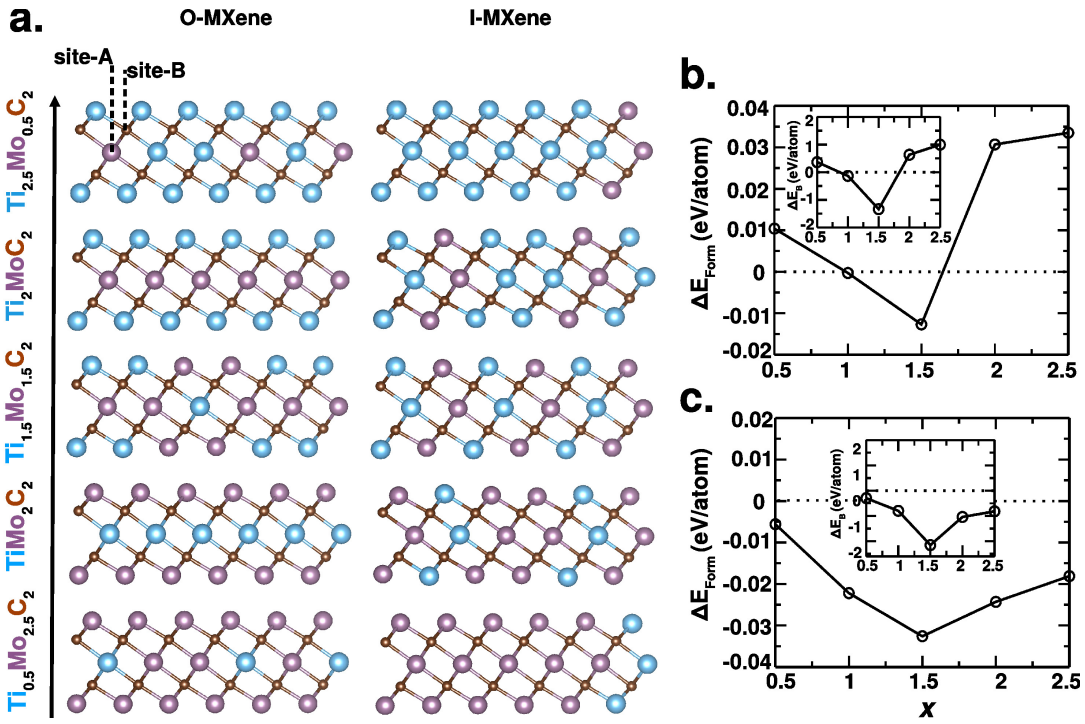

Figure 6.1: **a.** The $Ti_{3-x}Mo_xC_2$ MXenes in O- and I-phase, viewed along b axis with c-axis oriented vertically. The probable hollow sites that may host the passivating atoms are marked. **b.** The difference in formation energy of the I- and O-phases plotted as a function of Mo concentration x, as obtained in non-spin-polarized calculations. The inset shows the difference in bond energy (see text) of the I- and O-phases plotted as a function of Mo concentration x. **c.** Same as **b.** but results obtained in spin-polarized calculations.

Monkhorst-pack mesh[23] is employed. The experimentally synthesized Mo_2TiC_2 compound forms O-MXene structure with the Mo atoms sandwiching the middle Ti-C layer. Following this input, we consider two different possible ordered structures of $Ti_{3-x}Mo_xC_2$, in O-MXene and I-MXene form. For the former, the Mo(Ti)-rich outer layers sandwich Mo(Ti)-poor layers, while for the later, the Mo and Ti atoms form an ordered layer, which repeat between outer and middle layer. Fig.6.1**a.** shows the $Ti_{3-x}Mo_xC_2$ compounds in O-MXene and I-MXene structures, upon varying concentration of Mo(Ti). The number of Mo and Ti atoms in the outer and middle layers in O- and I-MXene structures are listed in Table 6.1.

When F, OH, or O atoms are adsorbed on top of TM surface, they usually move to hollow sites during the structural relaxation calculations. There are two types of hollow sites on MXene surfaces (cf Fig.6.1**a.**): site-A - the sites having no C atom available below them, and site-B - the sites having C atoms below

them. In our optimized structures, -O, -F, OH groups are found to occupy site-A, sitting above the TM atoms of middle layer. Anasori et al. predicted[13] the same configuration for passivated Mo_2TiAlC_2 and $Mo_2Ti_2AlC_3$. Stable structures for each passivation (-O,-F,-OH) and each concentration is determined, using convergence threshold of 10^{-5} eV for total energy and 10^{-3} eV/ for maximum force/atom. To investigate the influence of magnetism, calculations are carried out for non-magnetic (NM) as well as magnetic, ferromagnetic (FM) and five antiferromagnetic (AFM) configurations.

Electronic transport properties, namely electron conductivity (σ/τ), Seebeck coefficient (S), and electronic thermal conductivity (κ_e/τ) are determined within the framework of Boltzmann theory under rigid band and constant relaxation time (τ) approximation as implemented in BoltzTrap2 code.[24] Relaxation time approximation is a widely used approximation in a number of studies to solve the Boltzmann equation, which basically transforms the integro-differential quation to numerically simpler differential equation. The applicability of relaxation time approxiation has been demonstrated in good comparison between calculated mobility and experimental one in bulk semiconductors,[25–27] as well as in 2D materials.[28] For MoS_2, the comparison of Monte Carlo transport simulations instead of the relaxation time was found to be provide very similar results, supporting the use of the computationally much easier and more efficient relaxation time approximation.[29] Based on the above, in the present case we have calculated the temperature and carrier-concentration dependent relaxation time using calculated deformation potential and used it in solving the Boltzmann equation for electronic transport. To determine the electron relaxation time we use the model[30] as implemented in BoltzTrap code,[31] where

$$\tau(E,T) = \tau_0(\frac{E - E_{VBM/CBM}}{k_B T})^{r-1/2}(\frac{T_0}{T})^l \tag{6.1}$$

Here, $E_{VBM/(CBM)}$ is the valence band maximum (conduction band minimum) for the p-type (n-type) conduction. τ_0 is the reference lifetime, specified at some reference temperature T_0, k_B is the Boltzmann constant. The reference lifetime is calculated as

$$\tau_0 = (\frac{\pi}{\sqrt{m_x m_y}})(\frac{\hbar}{2\pi})(\frac{\hbar^2}{|\langle f|H'|i\rangle|^2}) \tag{6.2}$$

m_x, m_y are the principle directional effective masses, $\langle f|H'|i\rangle$ is the matrix element of the perturbation Hamiltonian between the initial state $|i\rangle$ and the final state $|f\rangle$. m_x and m_y are determined by fitting band along $\Gamma \rightarrow$M and M$\rightarrow$K k path respectively at valence band maximum for electrons and conduction band minimum for holes. The matrix element is given by the deformation potential of the material. The material and carrier-type dependent deformation potentials are calculated by following the change of valence band maximum (conduction band minimum) for the p-type (n-type) conduction as a function of applied strain.[32]

The exponent of energy r and the exponent of the temperature dependence, l are known as the scattering parameters. The scattering parameters are chosen to be $r = \frac{3}{2}$ and $l = 0$, typical values for the deformation potential scattering by alloys of 2D material.[33]

Phonon calculations are carried out within the formulation of density functional perturbation theory (DFPT) as implemented in VASP using a 2×2×1 supercell on a 8×8×2 k mesh of the Brillouin zone (BZ) of the hexagonal cell. The dynamical matrices are computed using PHONOPY code[34] and the phonon band structures, obtained by Fourier interpolation of the real-space force constants, are plotted along the high-symmetry k points of the BZ. To estimate the lattice thermal conductivity tensor(κ_l), one needs a) 2nd order harmonic interatomic force constants (IFCs) and b) 3rd order anharmonic IFCs. 2nd order IFCs are calculated from the phonon dispersion using PHONOPY code. To calculate the 3rd-order IFCs we use thirdorder.py python script. First we generate different configurations with displaced atoms taking up to 4^{th} near neighbour interaction, after checking the convergence in terms of number of near neighbours. The atomic displacement cut off is set to 0.31, 0.29 and 0.33 nm for $Mo_2TiC_2F_2$, $Ti_2MoC_2F_2$ and $Mo_2TiC_2(OH)_2$, respectively. Total number of configurations generated for $Mo_2TiC_2F_2$, $Ti_2MoC_2F_2$ and $Mo_2TiC_2(OH)_2$ are 960, 924 and 3492 respectively. 3rd order IFCs are evaluated using the same supercell size and k-mesh size as that of 2nd order IFC calculation. Finally κ_l is determined by solving phonon Boltzmann transport equation as implemented in ShengBTE code[35] using 8×8×1 k mesh. The convergence in terms of k mesh has been checked.

6.3 Results and Discussions

6.3.1 Formation energy and Stability analysis

To evaluate the stability of the alloyed structures, we first compute the formation energy for the unpassivated compounds $Ti_{3-x}Mo_xC_2$ in ordered O- and I-phases expressed as

$$\begin{aligned} E_{form}(Ti_{3-x}Mo_xC_2) &= E(Ti_{3-x}Mo_xC_2) - (3-x)E(Ti) \\ &\quad -xE(Mo) - 2E(C) \end{aligned}$$

where, $E(Ti_{3-x}Mo_xC_2)$ is the total energy of the MXene. $E(Mo)$, $E(Ti)$, and $E(C)$ are the chemical potential of Mo, Ti and C atoms, respectively, determined from the total energy of the corresponding solid state structures, HCP Ti, BCC Mo and graphite. Formation energies are calculated for non-magnetic as well as magnetic states, in order to explore the influence of magnetism on chemical ordering.

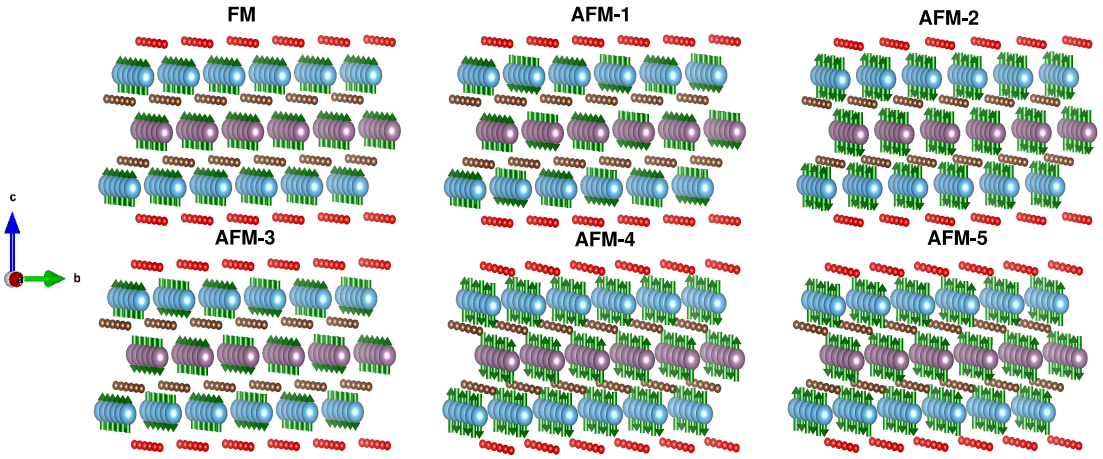

Figure 6.2: The FM and five different AFM spin arrangements in passivated $Ti_{3-x}Mo_xC_2$ MXenes, with passivated atoms shown as small balls, and magnetic TM atoms shown as large balls.

First of all, we find E_{form} is negative for all the structures indicating their stability. Relative stability between the I-phase and O-phase for particular concentration x is expressed as,

$$\Delta E_{form}(x) = E_{form}(I - mxene) - E_{form}(O - mxene) \tag{6.3}$$

Fig.6.1**b.** and Fig.6.1**c.** show the variation of $\Delta E_F(x)$ with concentration of Mo (x) for non-spin-polarized and spin-polarized calculations, respectively. We notice that while in non-spin-polarized calculation, upon increasing Mo concentration the relative stability shows change from O-MXene to I-MXene and again to O-MXene, the I-MXene phase is always favored in spin-polarized calculation, indicating a profound role of magnetism on chemical ordering. Magnetic state is found to be energetically lowered compared to non-magnetic state for all the concentrations, with magnetic moment of 1-2 μ_B on Mo atoms, 0.6-0.2 μ_B on Ti atoms, and small moment on C atoms (< 0.1 μ_B) due to covalency.

In order to understand the trend in formation energy, we further calculated the bond energy, expressed as the sum of energy of individual bonds,

$$\begin{aligned} E_b &= \sum n_{Mo-Mo}\epsilon_{Mo-Mo} + n_{Ti-Ti}\epsilon_{Ti-Ti} \\ &+ n_{Ti-Mo}\epsilon_{Ti-Mo} + n_{Mo-C}\epsilon_{Mo-C} + n_{Ti-C}\epsilon_{Ti-C} \end{aligned}$$

where ϵ_{Mo-Mo}, ϵ_{Ti-Ti}, ϵ_{Mo-Ti}, ϵ_{Mo-C} and ϵ_{Ti-Mo} are energy of the Mo-Mo, Ti-Ti, Mo-TI, Mo-C, Ti-C individual bonds, n's being the corresponding number of such bonds in a structure for a particular x value. ϵ_{Mo-Mo}, ϵ_{Ti-Ti}, ϵ_{Mo-Ti}, ϵ_{Mo-C} and ϵ_{Ti-Mo} show 165 -3 % increase in bond strength between the non-spin-polarized to spin-polarized calculation, explaining the stability of magnetic state

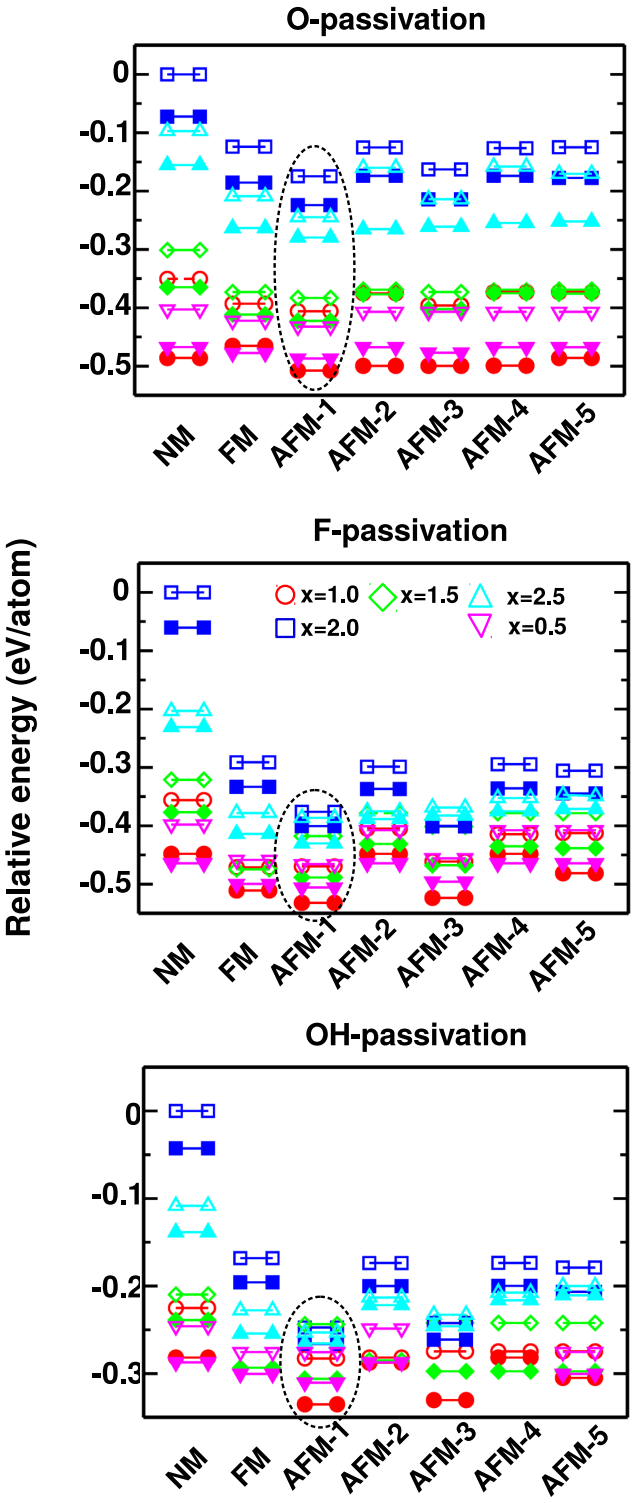

Figure 6.3: The energetic of different magnetic configurations of different spin arrangements of passivated $Ti_{3-x}Mo_xC_2$ MXenes, together with non magnetic case. The energies for O-MXenes and I-MXenes are shown with solid and open symbols, respectively. The lowest energy magnetic configuration (AFM-1) is encircled.

over the non-magnetic state. The largest increase (165 %) is observed for Mo-Mo bond energy followed by Mo-Ti bond energy (92%), due to strong magnetism of Mo atoms, and smallest decrease (3%) is found to for Ti-C bond energy. As expected the number of Mo-Mo bonds increases monotonically upon increase of Mo concentration, while the number of Ti-Ti bonds show a monotonic decrease for both I-MXene and O-MXene phases. For both I- and O-MXene, the number of Mo-Ti bonds show a non monotonic dependency with x, being maximum for $x = 1.5$. The number of Mo(Ti)-C bonds show a monotonic increase(decrease) with x for I-MXene, while that in O-MXene is found to be non-monotonic. This makes the bond energy of I-MXene magnetic phase energetically stable compared to magnetic O-MXene for all x, but the interplay makes stability of nonmagnetic I-MXene over nonmagnetic O-MXene non-monotonic in x, as shown in insets of Fig.6.1**b.** and Fig.6.1**c.**.

The stability changes remarkably when passivated compounds $Ti_{3-x}Mo_xC_2T_2$ (T = -O/-F/-OH), which is the situation in reality, are considered. Considering several possible collinear magnetic structures, ferromagnetic and five different antiferromagnetic structures (cf Fig.6.2), AFM-1: ferro along a and c and antiferro along b, AFM-2: ferro along b and c and antiferro along a, AFM-3: antiferro along b and c and ferro along a, AFM-4: antiferro along a and c and ferro along b, AFM-5: antiferro along all directions, and the nonmagnetic structure, the relative stability of O-MXene and I-MXene is computed for the passivated compounds. The obtained results are summarized in Fig.6.3. The passivation is found to favour O-MXene configuration for all x with stabilization of AFM-1 magnetic state.

Among the studied compounds, $Mo_2TiC_2T_x$ has been experimentally synthesized,[10] and the stability of unpassivated Mo_2TiC_2 and Ti_2MoC_2 has been theoretically studied[10] by considering the energetics of O-MXene phase with Mo/Ti only outer layers, sandwiched between Ti/Mo only layers, with respect to different mixed Ti-Mo layer configurations. This theoretical study[10] concluded that Mo is strongly preferred in the outer layer for Mo_2TiC_2 and only marginally for Ti_2MoC_2. This observation agrees with our result obtained on the basis of non-magnetic calculations. Our results taking into account the effect of magnetism by considering different possible magnetic structures, as well as passivation, however, provides a more complete understanding of the stability, which are found to be significantly influence the nature of stability, as elaborated above.

To further ascertain the thermodynamic stability of the studied $Ti_{3-x}Mo_xC_2$ compounds, we calculated the convex hull. The results are shown in the following section. It proves the thermal stability of the compounds of importance, Ti_2MoC_2 and $TiMo_2C_2$.

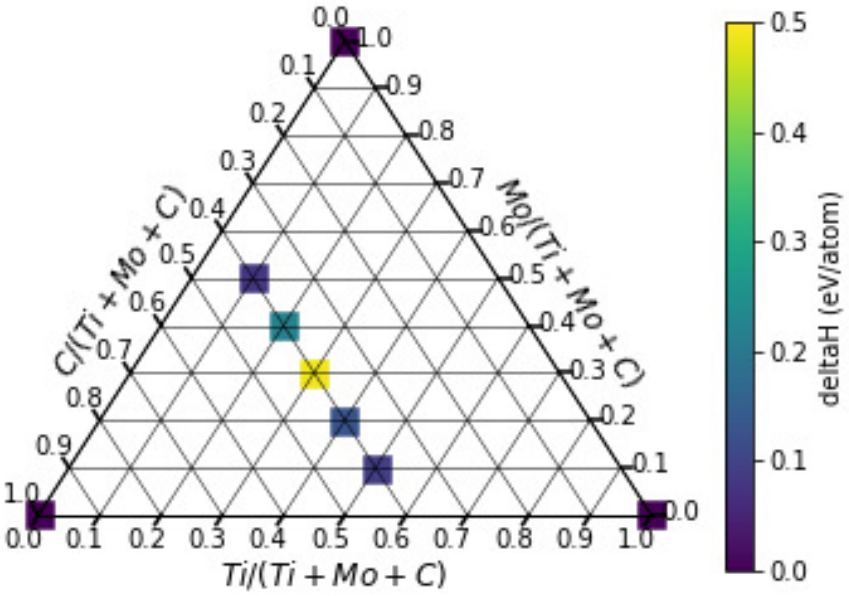

Figure 6.4: Ternary composition-formation enthalpy phase diagram of the $Ti_xMo_yC_z$ compounds. Each structure is colored by the distance from the convex hull in eV/atom, see the color bar legend on the right.

Convex Hull

The construction of the ternary convex hull requires the knowledge of the stable phases of pure elemental compounds at the corners and stable binary compounds on the boundaries of the convex hull. Therefore, the following phases labeled by space group symmetry were used,[36] HCP Ti, BCC Mo and graphite, $Fm\bar{3}m$ TiC, $Fd\bar{3}m$ Ti_2C, $Im\bar{3}m$ (Ti,Mo), $P\bar{6}m2$ MoC. The resultant ternary composition-formation enthalpy phase diagram of the $Ti_xMo_yC_z$ compounds is depicted in Fig. 6.4, which shows the convex hull construction for the $Ti_xMo_yC_z$ ternary compounds. Structures with lower (negative) formation enthalpy are closer to the convex hull and therefore colored by more darker color.

6.3.2 Electronic structure

We find that all unpassivated structures of studied alloyed MXenes show metallic behaviour (not shown), with hybridized C $2s$ and TM d states positioned around 12-10 eV below Fermi level (E_F), hybridized C $2p$ and TM d states situated from 7 to 3 eV below E_F, and nonbonding TM d states around E_F giving to finite density of states (DOS) at E_F. The electronegative termination -F, -OH, and -O receives one and two electrons from the outer TM layers respectively and gives rise to new bands below the Fermi energy, hybridized with the TM d states. This

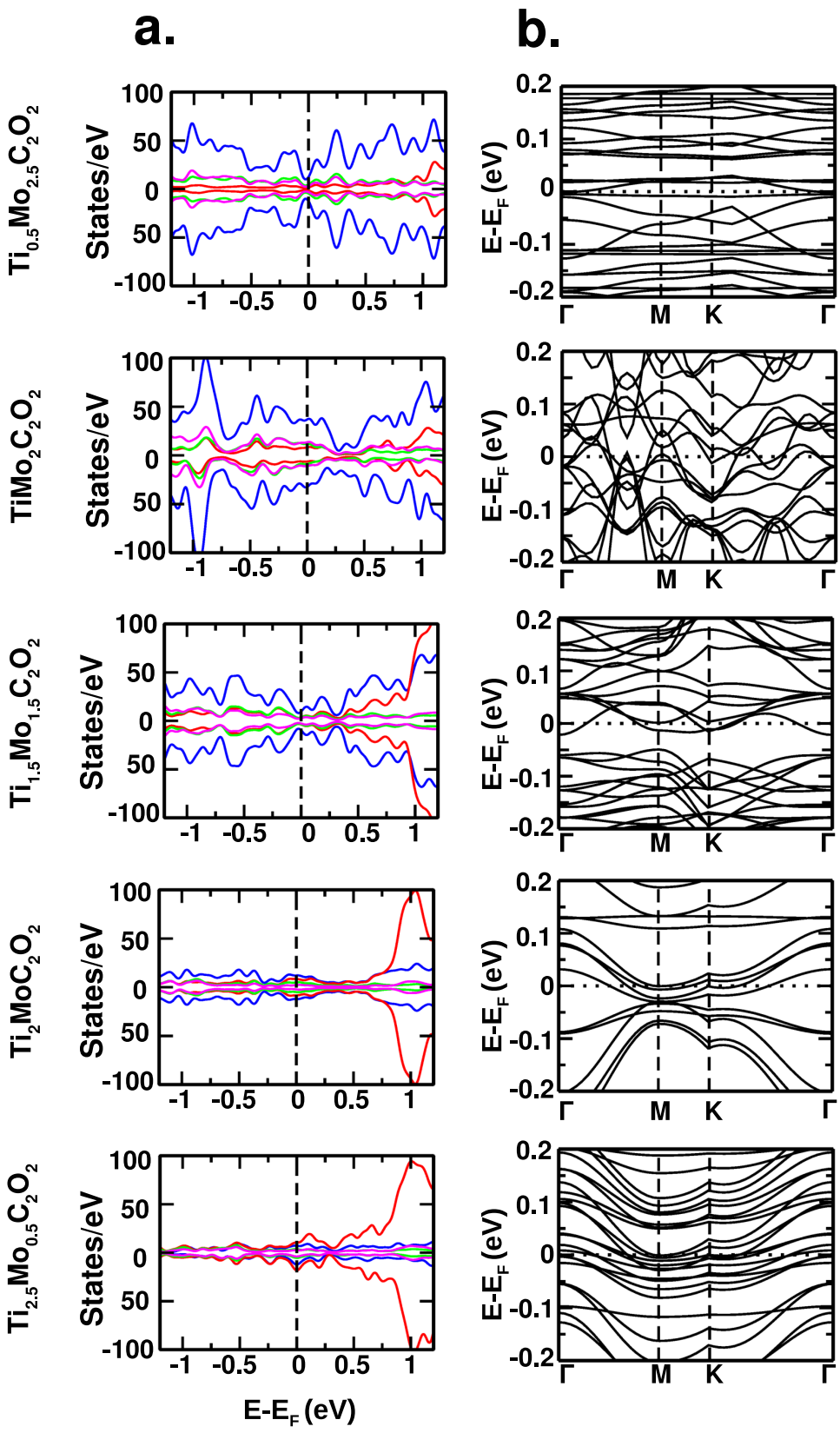

Figure 6.5: **a.** The density of states in O-passivated $Ti_{3-x}Mo_xC_2$ MXenes, projected to Ti d (red), Mo d (blue), C p (green) and O p (magenta) states. The zero of the energy is fixed at Fermi energy (E_F). **b.** The corresponding band structure plotted along the high symmetry points of the BZ, Γ-M(1/2,0,0)-K(2/3,1/3,0)-Γ.

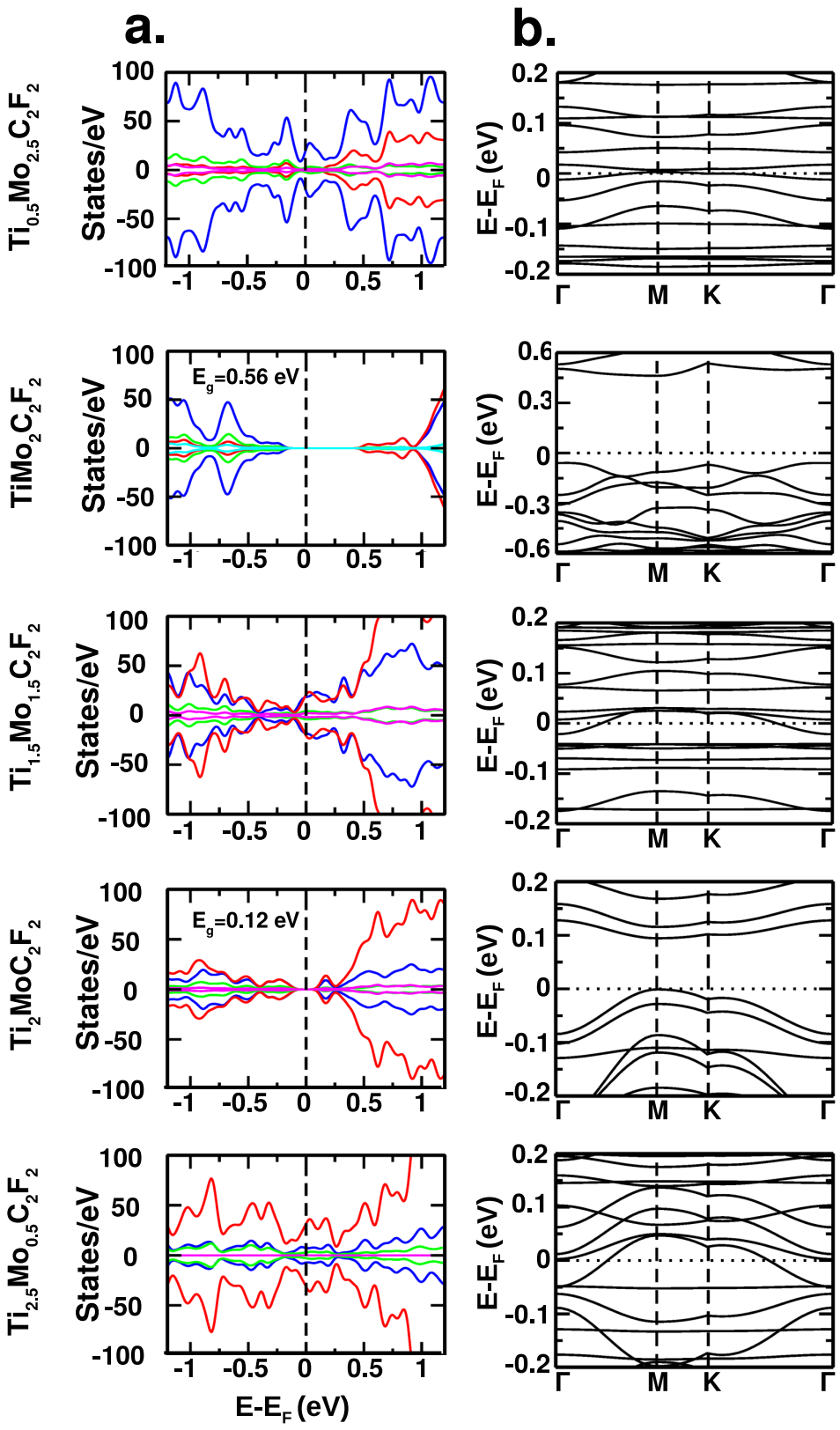

Figure 6.6: **a.** The density of states in F-passivated $Ti_{3-x}Mo_xC_2$ MXenes, projected to Ti d (red), Mo d (blue), C p (green) and F p (magenta) states. The zero of the energy is fixed at Fermi energy (E_F). The band gaps for semiconducting $TiMo_2C_2F_2$ and $Ti_2MoC_2F_2$ are marked. **b.** The corresponding band structure plotted along the high symmetry points of the BZ, Γ-M(1/2,0,0)-K(2/3,1/3,0)-Γ.

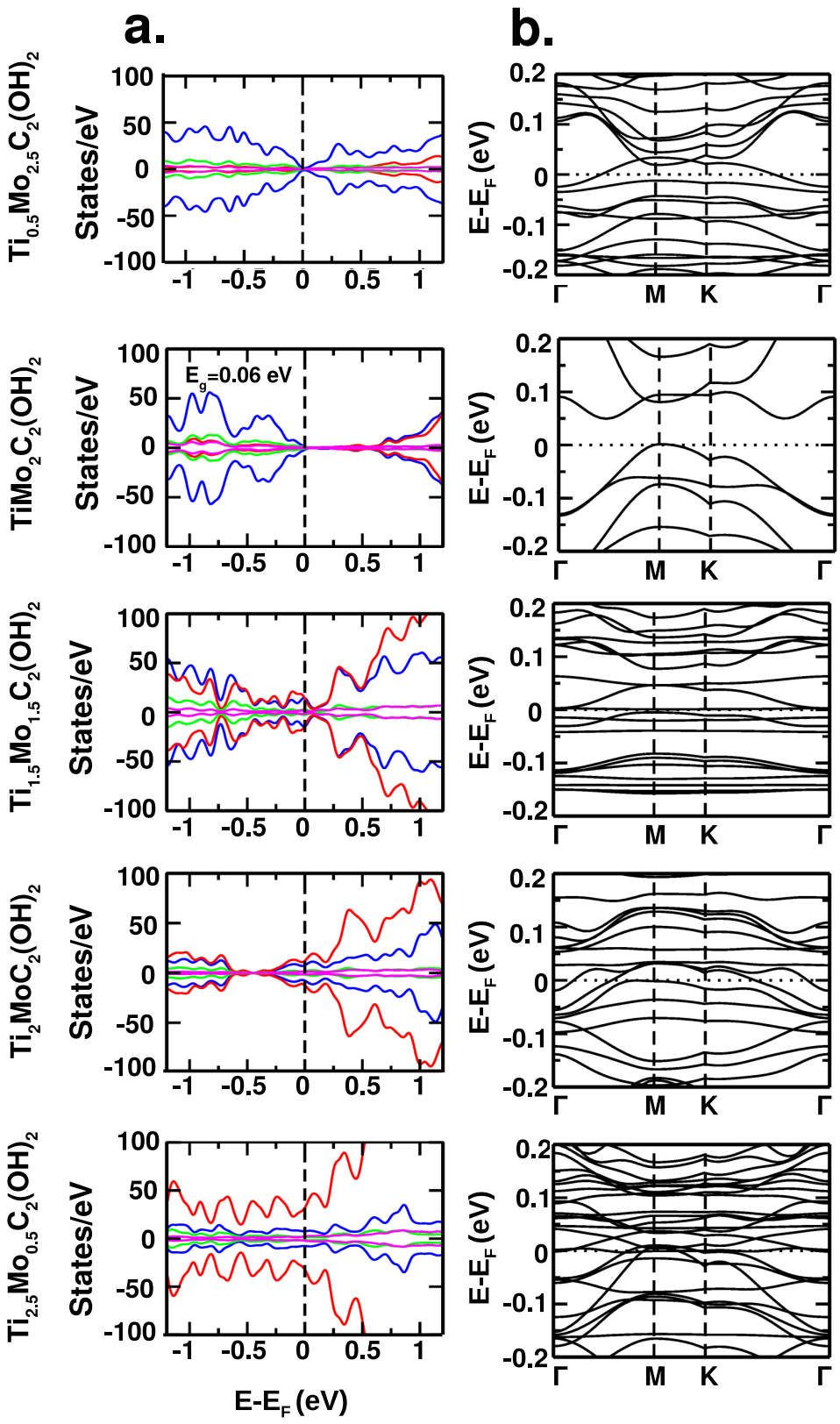

Figure 6.7: **a.** The density of states in OH-passivated $Ti_{3-x}Mo_xC_2$ MXenes, projected to Ti d (red), Mo d (blue), C p (green) and OH (magenta) states. The zero of the energy is fixed at Fermi energy (E_F). The band gap for semiconducting $TiMo_2C_2(OH)_2$ is marked. **b.** The corresponding band structure plotted along the high symmetry points of the BZ, Γ-M(1/2,0,0)-K(2/3,1/3,0)-Γ.

reduces the DOS at the Fermi surface and can open up a band gap resulting in non-metallic MXenes, depending on the strength of covalency and ionicity of the bonds between transition metal and the attached chemical groups. The computed DOS projected to Mo d states, Ti d states, C p states, and T (T = -O/-F/-OH) states along with band structures in AFM-1 magnetic structure in O-phase for all x values are shown in Figs 6.5, 6.6 and 6.7, for T = -O, -F, and -OH, respectively. The states close of E_F are strongly contributed by transition metal d states as found for unpassivated structures. The d levels of transition metal gets split by the ligand field of the bonded carbon atoms and the passivating atoms, making the passivated structures either metallic or semiconducting with small band gaps.

All O-passivated $Ti_{3-x}Mo_xC_2O_2$ compounds are found to be metallic, though low DOS values at E_F are observed in all cases except for $TiMo_2C_2O_2$. Band gap engineering through straining may be explored for these low DOS value compounds. Fluorination is found to be effective in opening band gaps in $TiMo_2C_2F_2$ and $Ti_2MoC_2F_2$ with band gap values 0.56 eV and 0.12 eV, respectively. Upon passivation with OH, a small gap of 0.06 eV is found to open for $TiMo_2C_2(OH)_2$ and a low DOS situation is achieved for $Ti_{0.5}Mo_{2.5}C_2(OH)_2$. The electronic structure thus show a strong dependency on the choice of passivating ions, and may drive metal to semiconductor transition, a feature which is often seen in transition metal-based compounds with octahedral or trigonal symmetries.[37, 38]

The band structures show non trivial changes upon change of x as well as change of passivation. The magnetic moments on Mo, Ti, C and T atoms for non-metallic MXenes are listed in Table 6.2. We find magnetic moments of both Mo and Ti atoms show a strong variation with x values. Mo atoms are strongly magnetic with a large moment of $\approx 2.4\ \mu_B$ for Mo-rich compounds and a reduced moment of $\approx 1.8\ \mu_B$ for Mo-poor compounds, while Ti moments show a large variation from essentially non magnetic in Mo-rich compounds to magnetic with a moment of about $0.9\ \mu_B$ for Mo-poor compounds. The induced moments on C, O and F atoms are tiny (0.04-0.01 μ_B) while that on H atoms are even smaller (not listed).

6.3.3 Electrical transport coefficients

In the next step, we examine the electrical transport properties such as temperature and carrier concentration dependent scaled electron conductivity (σ/τ), Seebeck coefficient (S) and power factor (PF/τ) on the basis of Boltzmann theory under relaxation time (τ) approximation taking first-principles band structure as input. Electronic relaxation time is a constant in the calculation which needs to be estimated. The temperature and carrier density-dependent relaxation time is estimated using the model described by following.

Atom	$TiMo_2C_2F_2$	$TiMo_2C_2(OH)_2$	$Ti_2MoC_2F_2$
Mo	2.44, 2.37	2.43, -2.41	1.77, -1.77
	2.44, -2.37	2.43, 2.41	1.77, -1.77
Ti	0.00, 0.00	0.00, 0.00	0.92, -0.92,
			0.88, -0.88
C	-0.02, 0.04	-0.02, 0.03	0.02, -0.02,
			0.03, -0.03
O / F	0.03, -0.01	0.03, -0.01	0.01, -0.01,
			0.01, -0.01

Table 6.2: Magnetic moments in μ_B on Mo, Ti, C, T atoms for non-metallic passivated $Ti_{3-x}Mo_xC_2T_2$ MXenes.

$$\tau(E,T) = \tau_0(\frac{E - E_{VBM/CBM}}{k_B T})^{r-1/2}(\frac{T_0}{T})^l \tag{6.4}$$

The effective masses, deformation potentials and E_{VBM}/E_{CBM} employed in the calculation for relaxation time are tabulated in Table 6.3 for representative compounds. The computed relaxation time for $T = 300$ K and 800 K and carrier concentration of 10^{19} cm^{-3} are also listed in Table 6.3. The relaxation times, as presented in Fig.6.8 for representative compounds, show a strong dependency on temperature as well as the value and nature (p-type or n-type) of carrier concentration. The calculations reported in the following are carried out with these computed relaxation times.

Among the studied compounds, only electrical transport properties of passivated $TiMo_2C_2$ MXene has been measured which may serve as a reference.[11] In that work[11] the temperature variation of electron conductivity, Seebeck coefficient and power factor were measured and n-type Seebeck coefficient was observed. To compare with the experimental measurement, we compute the variation of these transport coefficients with temperature for $TiMo_2C_2T_2$ with n-type charge carrier. In absence of precise information of the nature of passivation in the measured sample, we consider uniform passivation by -O, -F, -OH, as well as mixed passivation of OOH and OF. The results are presented in Fig.6.9, and the values at 800 K are listed in Table 6.4, in comparison to experimental values. The best agreement between computed and measured values is obtained for $TiMo_2C_2(OH)_2$, validating our methodology.

In the next step we compute the temperature-dependent electrical transport properties of three semiconducting compounds, $Ti_2MoC_2F_2$, $TiMo_2C_2F_2$ and $TiMo_2C_2(OH)_2$ for both p-type and n-type dopants, with a carrier concentration of $10^{19}cm^{-3}$. The results are shown in Fig.6.10. Following the expression, ZT can be maximized when the power factor is maximized and the thermal conductivity is

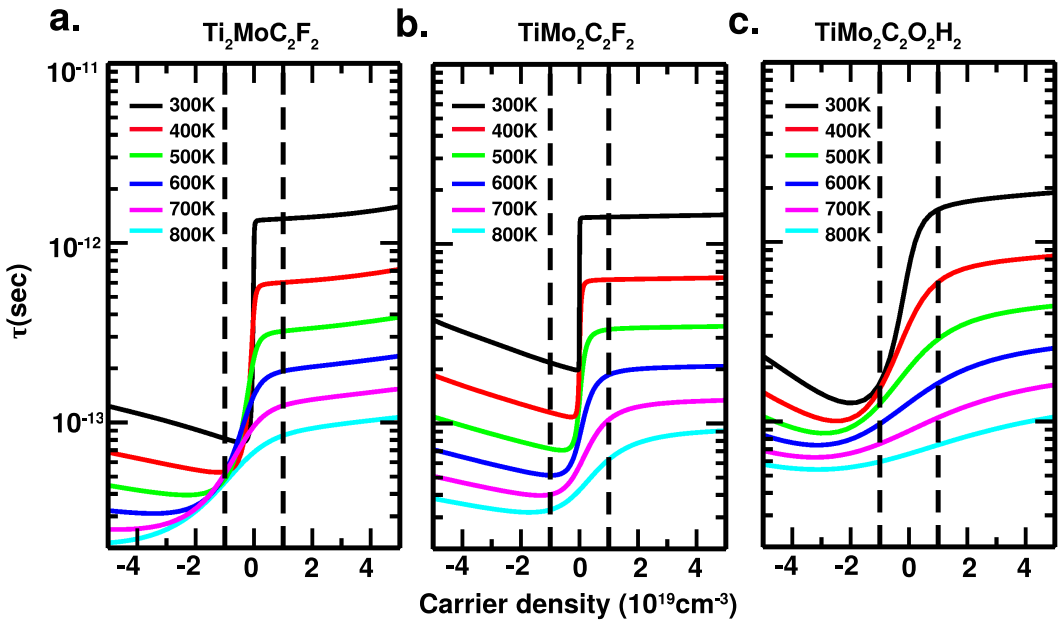

Figure 6.8: **a.** The calculated electronic relaxation time shown for representative cases of $Ti_2MoC_2F_2$, $TiMo_2C_2F_2$ and $TiMo_2C_2(OH)_2$ MXenes, plotted as a function of carrier density for different temperatures. The n-doped and p-doped carrier density $10^{19}cm^{-3}$ are marked.

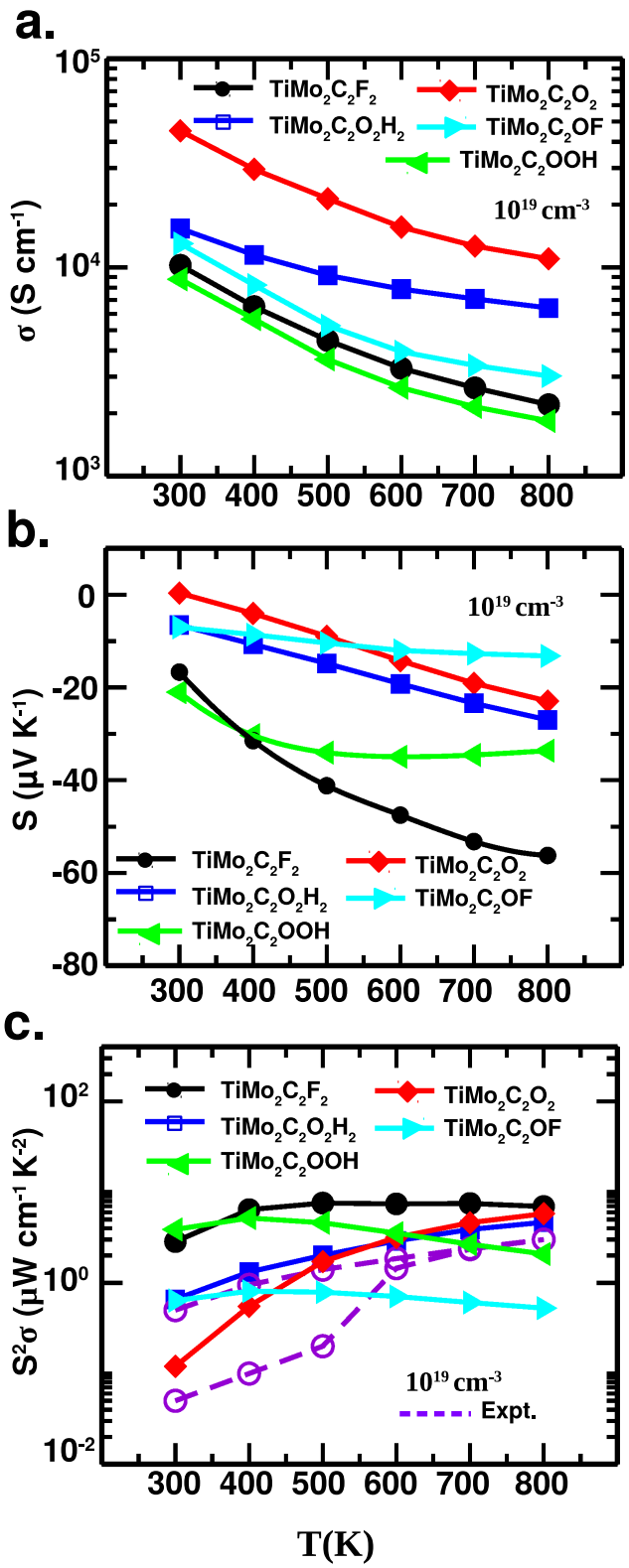

Figure 6.9: Electrical transport properties of n-type passivated $TiMo_2C_2$, considering uniform passivation by O_2, F_2, $(OH)_2$, as well as mixed passivation by OF and OOH. Shown are results for temperature dependent conductivity (**a.**), Seebeck coefficient (**b.**) and power factor (**c.**). The experimentally measured power factor is shown for comparison.

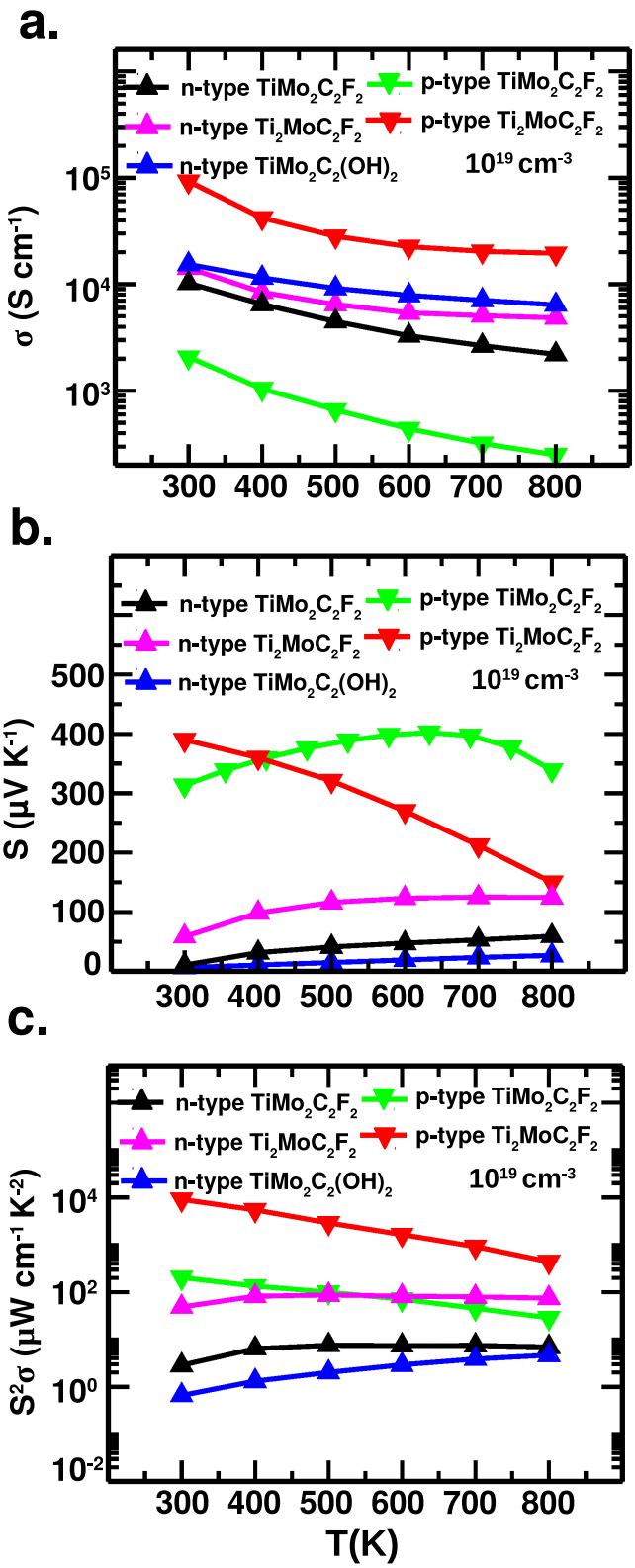

Figure 6.10: Electrical transport properties of -O or -F or -OH passivated semiconducting Ti_2MoC_2 and $TiMo_2C_2$. Shown are the results for temperature-dependent conductivity (**a.**), absolute value of Seebeck coefficient (**b.**) and power factor (**c.**).

	Direction /τ (sec)	electron eff. mass	hole eff. mass	E_{VBM} /E_{CBM}
$TiMo_2C_2F_2$	$\Gamma \rightarrow M$	2.817	1.106	0.127
	$M \rightarrow K$	1.524	2.715	0.267
	E_d (eV)	6.90	0.56	
	τ (300K)	2.19×10^{-13}	1.41×10^{-12}	
	τ(800K)	3.29×10^{-14}	6.43×10^{-14}	
$TiMo_2C_2(OH)_2$	$\Gamma \rightarrow M$	2.215	1.594	0.0118
	$M \rightarrow K$	1.438	2.047	0.0589
	E_d (eV)	5.28	0.90	
	τ (300K)	1.58×10^{-13}		
	τ (800K)	5.91×10^{-14}		
$Ti_2MoC_2F_2$	$\Gamma \rightarrow M$	2.680	1.814	0.0701
	$M \rightarrow K$	1.234	2.986	0.506
	E_d (eV)	5.16	0.48	
	τ (300K)	8.06×10^{-14}	1.37×10^{-12}	
	τ (800K)	4.63×10^{-14}	8.41×10^{-14}	

Table 6.3: Effective masses, relaxation times and deformation potential (E_d) of non-metallic compounds at $10^{19}cm^{-3}$ carrier concentration.

minimized. There exist different possible means to minimize the thermal conductivity by engineering enhanced phonon scatterings by the introduction of edges, interfaces, grain boundaries etc.[39] However, maximizing $S^2\sigma$ is non-trivial. Both S and σ are strongly coupled to the electronic structure of the system and may behave inversely. Therefore a balance between the Seebeck coefficient and the electrical conductivity at a particular p- or n-type carrier concentration is needed to maximize the power factor.

As found from Fig.6.10**a.** variation of σ with temperature is more or less similar between different compounds. The conductivity of p-type $TiMo_2C_2F_2$ is found to be lower than n-type counterpart, though the conductivity for p-type $Ti_2MoC_2F_2$ exceeds its n-type counterpart and attains maximum conductivity among all. Among the n-type compounds, the conductivity of $TiMo_2C_2(OH)_2$ is found to be largest.

Seebeck coefficient is a measure of induced TE voltage in response to unit temperature gradient across the material. S can be used to determine the type of majority charge carrier of the material. Negative S value corresponds to electron and positive corresponds to hole for a semiconductor. For n-type compounds, as seen in Fig.6.10**b.**, we find that the absolute value of S increases with temperature in all the cases. Among the n-type doped compounds, S is found to be largest for n-type $Ti_2MoC_2F_2$, followed by n-type $TiMo_2C_2F_2$, and n-type $TiMo_2C_2(OH)_2$.

This observation may be rationalized by the effect of band gap on enhancement of S as explained in Ref.[40]. Large Seebeck coefficient of 300-400 μVK^{-1} is observed for p-type compounds, though that of $Ti_2MoC_2F_2$ also shows strong temperature dependence, the temperature dependence being inverse to that observed for conductivity (cf Fig.6.10**a.**).

We notice that for both n-type and p-type compounds PF value increases with temperature. Maximum power factor is observed for p-type $Ti_2MoC_2F_2$ mxene, being about two order of magnitude larger compared to that of p-type $TiMo_2C_2F_2$. As mentioned above, for p-type $Ti_2MoC_2F_2$, the Seebeck coefficient show a decrease with temperature, which gets delicately balanced by the corresponding in conductivity, thereby maximizing the power factor. For n-type $Ti_2MoC_2F_2$ also, the power factor is found to be two order of magnitude larger than that of $TiMo_2C_2F_2$. These strongly suggest effectiveness of Ti_2MoC_2 as a promising thermoelectric material over synthesized $TiMo_2C_2$ MXene.

	σ (S cm^{-1})	S (μVK^{-1})	PF ($\mu Wcm^{-1}K^{-2}$)
$TiMo_2C_2O_2$	11000	-24	4.80
$TiMo_2C_2F_2$	2200	-60	7.85
$TiMo_2C_2(OH)_2$	5800	-28	4.24
$TiMo_2C_2OOH$	1840	-33	2.08
$TiMo_2C_2OF$	3021	-13.3	0.53
$TiMo_2C_2T_x$ (expt)	1380	-47	3.09

Table 6.4: Comparison of electrical transport coefficients of n-type doped, passivated $TiMo_2C_2$ at 800 K.

6.3.4 Dynamical stability

Fig.6.11 shows the phonon dispersion plotted along the high-symmetry points of the hexagonal brillouin zone for non metallic O-MXenes in AFM-1 configuration. We notice that phonon frequencies are real and positive indicating dynamical stability of the structures. Three lowest-energy phonon modes are the acoustic modes corresponding to long-wavelength vibrations, classified as ZA, TA and LA respectively and rest are optical modes (O). ZA mode, also known as flexural mode, governs the out-of-plane transverse vibration and shows the quadratic dispersion close to Γ point under zero strain condition, which is a characteristic feature of 2D materials. Other two acoustic branches TA and LA govern the in-plane transverse and longitudinal vibration respectively and show linear behaviour near Γ point. Unlike $Ti_2MoC_2F_2$, no frequency gap is observed between LA and optical modes for $TiMo_2C_2F_2$, $TiMo_2C_2(OH)_2$, leading to finite hybridization between LA and optical modes. From partial phonon DOS, we notice that

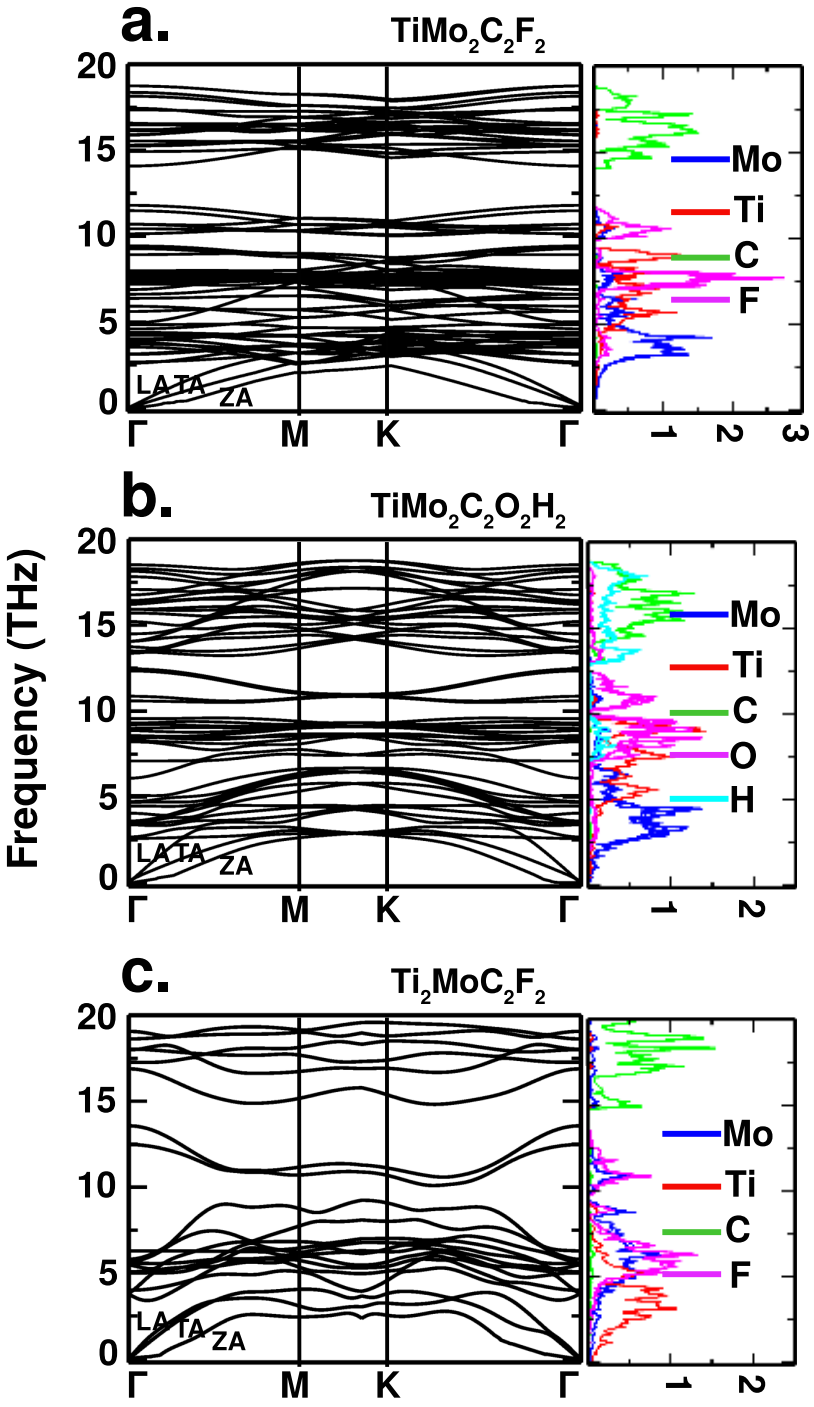

Figure 6.11: The phonon dispersion (left) and phonon density of states (right) shown for $TiMo_2C_2F_2$ (**a.**), $TiMo_2C_2(OH)_2$ (**b.**) and $Ti_2MoC_2F_2$ (**c.**). In phonon dispersion, the branches corresponding to acoustic branches, namely LA, TA and ZA are marked.

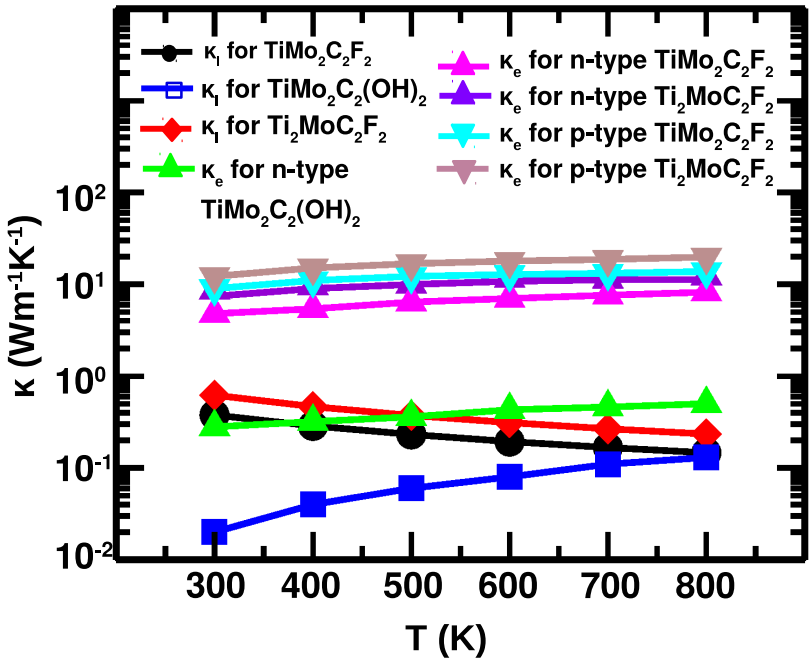

Figure 6.12: The temperature dependent electronic and lattice thermal conductivity.

around acoustic frequency region phonon density exists only for TM ion and density of states for acoustic modes is greater in $Ti_2MoC_2F_2$ mxene compared to the other two.

Knowledge of phonon dispersion also allows us to incorporate the entropy effect[13] in the stability analysis. Following this, we estimate the free energy difference between I-Phase and O-Phase, which confirms the stability of O-phases over I-phases for passivated compounds in AFM-1 magnetic phase at finite temperature. The stability of the O-phase over I-phase is found to increase with increase of temperature. In particular, the O-phase for $Ti_2MoC_2F_2$ is found to be stable over I-Phase by 9 meV/f.u. at 300K and 20 meV/f.u at 800K. For $TiMo_2C_2F_2$, the corresponding stability of O-phase over I-phase is found to be 16 meV/f.u. at 300 K and 45 meV/f.u. at 800 K.

6.3.5 Lattice transport coefficient: Lattice thermal conductivity

Phonon dispersion plays a vital role in investigation of the lattice thermal conductivity. Our calculation has been carried out considering intrinsic scattering events that involved three phonons. The Taylor series expansion of the potential

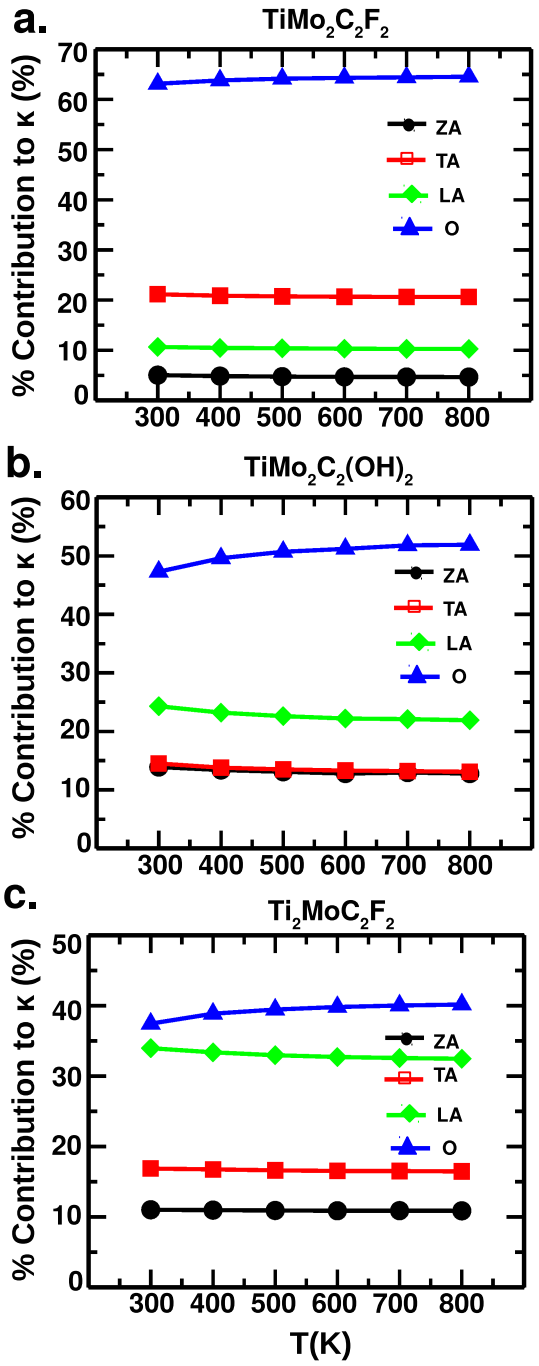

Figure 6.13: Normalized lattice thermal conductivities as a function of temperature for different phonon branches.

energy in terms of displacement is infinite, so scattering events involving more then three phonons are possible. The importance of four-phonon scattering has been discussed.[41, 42] As with three-phonon processes, the four phonons must satisfy constraints related to their wave vectors and energies. Calculation of the scattering rate requires the fourth-order (i.e., quartic) force constants. The BTE can be solved under the relaxation time approximation. The main challenge associated with including four-phonon scattering events is their sheer number. While there have been reports of calculation of thermal conductivity including four phonon scattering[43] they are primarily based on model potential like Tersoff potential, which is quite outside the scope of present work.

The calculated electronic and lattice thermal conductivities for non-metallic O-mxene as a function of temperature are shown in Fig.6.12. For all cases, we notice that electronic thermal conductivity is almost an order larger compared to lattice thermal conductivity. This indicates that the heat is mainly transported through charge carrier. A similar trend has been observed for $Cr_2TiC_2(OH)_2$.[12] κ_e for $TiMo_2C_2(OH)_2$ is found to be quite smaller compared to that of $Ti_2MoC_2F_2$ and $TiMo_2C_2F_2$. Highest thermal conductivity is observed for $Ti_2MoC_2F_2$ followed by $TiMo_2C_2X_2$ (X= OH and F). At 800K, κ_l of $TiMo_2C_2F_2$ and $TiMo_2C_2(OH)_2$ are found to be 0.20 and 0.15 $Wm^{-1}K^{-1}$, respectively while that of $Ti_2MoC_2F_2$ is found to be 0.30 $Wm^{-1}K^{-1}$, as compared to $\sim$ 6.5 $Wm^{-1}K^{-1}$ reported for $Cr_2TiC_2(OH)_2$.[12]

To study the contribution of acoustic and optical phonon modes to κ_l separately, we compute mode decomposed κ_l (normalized by the total κ_l) as a function of temperature, shown in Fig.6.13. The lattice thermal conductivity in the functionalized MXenes is found to be predominated contributed by the optical phonon modes, except for $Ti_2MoC_2F_2$. The contribution from optical modes to the total value is found to increase with temperature whereas that of acoustic modes (ZA+LA+TA) is found to be remain more or less constant throughout the temperature range, with the exception of $Ti_2MoC_2F_2$. For F passivated $TiMo_2C_2$ mxene, total weight of optical mode is 65% whereas for OH passivation it is slightly greater than 50% at T = 800K. Among the acoustic modes, ZA and TA contributes equally but less than LA mode ($\sim$20%) for OH passivation, whereas for F passivation, contribution of TA mode ($\sim$25%) is greater than the ZA and LA mode. Distinctly, for F passivated Ti_2MoC_2 mxene, weight of optical mode and LA mode are 40% and 32% respectively indicating simultaneous contribution of acoustic and optical mode to κ_l.

We note that the thermal conductivity for different materials , which differ in termination and/or composition of (Ti,Mo) are different and deviates from more commonly observed 1/T behavior.[44] The large deviation from the 1/T law appears to stem from the optic phonon branch, whose contribution to total thermal conductivity increases with the temperature increase and eventually dominates the phonon transport by overwhelming the acoustic phonon branches.

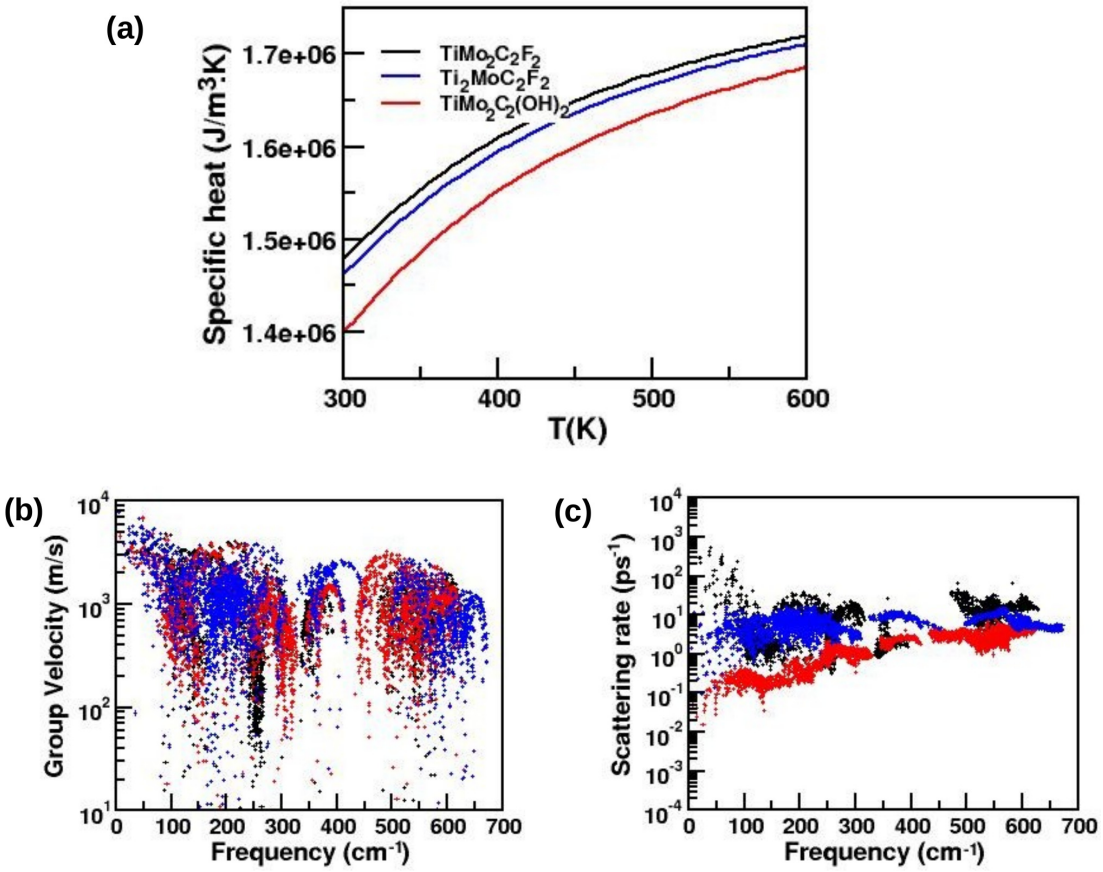

Figure 6.14: Calculated (a) volumetric specific heat, (b) group velocity, and (c) scattering rate of $Ti_2MoC_2F_2$, $TiMo_2C_2F_2$ and $TiMo_2C_2(OH)_2$.

Such surface termination dependent, thermal conductivity with varying nature of temperature dependence has been observed in $Ti_3C_2T_z$ MXenes,[45] as well as in $Cr_2TiC_2T_2$ (T = -OH or -F).[12] The material variation has been argued to stem from interplay of varying degree of specific heat, group velocity and scattering rate.

To better understand how different composition and surface termination result in such a large variation in the thermal conductivity of $Ti_{3-x}Mo_xC_2T_2$ MXenes, we calculated three effective parameters that predominantly contribute to the thermal conductivity, namely specific heat, group velocity, and scattering rate of phonon modes. The results are shown in the following section.

Specific heat, Group Velocity and Scattering Rate

To provide microscopic understanding of the differential lattice thermal conductivity of the three compounds, $Ti_2MoC_2F_2$, $TiMo_2C_2F_2$ and $TiMo_2C_2(OH)_2$, three

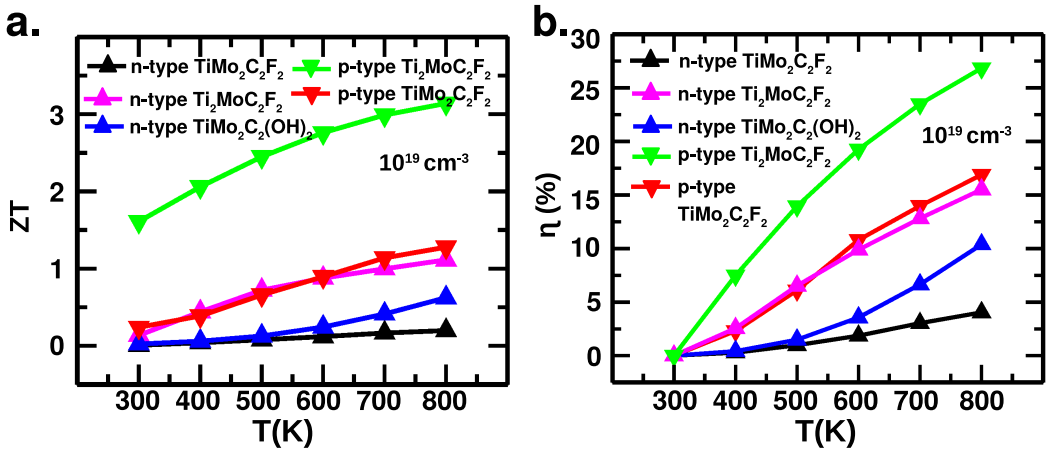

Figure 6.15: Thermoelectric figure of merit (ZT) and TE conversion efficiency for passivated $Ti_2MoC_2T_2$ and $TiMo_2C_2T_2$ (T = -F, -O and -OH): **a.** ZT between 300 and 800 K and **b.** TE conversion efficiency in the same temperature range.

deciding parameters, volumetric specific heat, group velocity, and phonon scattering rate were calculated. The results are summarized in Fig. 6.14. The calculated volumetric specific heat of all three compounds within the temperature range of 300-600 K, show that while specific heat of $Ti_2MoC_2F_2$ and $Mo_2TiC_2F_2$ are comparable, it is appreciably larger compared to that of $TiMo_2C_2(OH)_2$. The group velocity of phonons, which is the spatial derivative of frequency with respect to wavevector, indicate that the average group velocity is largest for $Ti_2MoC_2F_2$. Furthermore, we obtained three-phonon scattering rates of q-points for three compounds. The scattering rate is found to highest for $TiMo_2C_2F_2$. Thus, based on our results, since the specific heat of $Ti_2MoC_2F_2$ and $TiMo_2C_2F_2$ are in the same range, lower conductivity of $TiMo_2C_2F_2$ compared to $Ti_2MoC_2F_2$ is attributed to its lower average group velocity of phonons and higher scattering rates compared to $Ti_2MoC_2F_2$. On the other hand, the higher thermal conductivity of $Ti_2MoC_2F_2$ compared to $TiMo_2C_2(OH)_2$ may be attributed to its higher specific heat and dominant contributions of both optic and acoustic modes in $Ti_2MoC_2F_2$.

6.3.6 Figure of merit and TE efficiency

Temperature dependence of two thermoelectric figure of merit, namely ZT and efficiency are shown in Fig.6.15. We notice that among the three compounds, $Ti_2MoC_2F_2$ has the highest ZT followed by $TiMo_2C_2(OH)_2$ and $TiMo_2C_2F_2$. In particular, for p-type $Ti_2MoC_2F_2$ at carrier concentration of 10^{19}cm^{-3}, ZT remains above 2, for temperatures above 400 K. The ZT value of p-type $Ti_2MoC_2F_2$ is found to be 1.5 at T = 300 K and reaches a ZT value of 3.1 at T= 800 K.

The superior performance of $Ti_2MoC_2F_2$ stems from higher power factor compared to $TiMo_2C_2$ compounds, which supersedes the higher thermal conductivity of $Ti_2MoC_2F_2$ compared to $TiMo_2C_2$ compounds. The ZT values of some of the compounds in this study, in comparison of those of single TM and double TM MXenes are listed in Table 6.5.

Compound (T)	charge carrier	ZT_{max}	Ref.
$Sc_2C_2O_2$ (900K)	p-type	0.35	Ref.[8]
$Sc_2C_2F_2$ (900K)	n-type	0.45	Ref.[8]
$Sc_2C_2(OH)_2$ (900K)	p-type	0.5	Ref.[8]
Cr_2TiC_2 (600K)	n-type	0.75	Ref.[12]
$Cr_2TiC_2F_2$ (600K)	p-type	1.5	Ref.[12]
$Cr_2TiC_2(OH)_2$ (600K)	p-type	3.0	Ref.[12]
$TiMo_2C_2F_2$ (800K)	n-type	0.20	present work
$TiMo_2C_2F_2$ (800K)	p-type	1.28	present work
$TiMo_2C_2(OH)_2$ (800K)	n-type	0.62	present work
$Ti_2MoC_2F_2$ (800K)	n-type	1.20	present work
$Ti_2MoC_2F_2$ (800K)	p-type	3.14	present work

Table 6.5: ZT_{max} for different MXene compounds at different temperatures.

Finally, TE performance of MXenes can be evaluated by computing their TE conversion efficiencies, related to Carnot efficiency and ZT value as follows

$$\eta = \frac{T_h - T_c}{T_h} \frac{\sqrt{1+ZT}-1}{\sqrt{1+ZT}+T_c/T_h} \tag{6.5}$$

where T_h and T_c are the hot and cold end of the TE devices, respectively and Carnot efficiency is given by $\frac{T_h - T_c}{T_h}$. We take T_c = 300 K and T_h to range from 300 to 800 K. Temperature dependence of TE efficiency of non-metallic O-MXenes are shown in Fig.6.15**b.**. We notice that, maximum efficiency for p-type $Ti_2MoC_2F_2$ is ∼27%, stressing on possible applicability of this material as efficient thermoelectric.

6.4 Conclusion

Motivated by the experimental synthesis of ordered double transition metal MXene compounds, we study the magnetic, electronic structure and transport properties of Ti-Mo based compounds employing first-principles density functional theory and Boltzmann transport formalism. For this purpose, we consider five ordered alloyed structures $Ti_{3-x}Mo_xC_2$ with x = 0.5, 1, 1.5, 2, 2.5 in two possible

ordered forms, I-MXene and O-MXene. First we take the unpassivated structures and study the relative stability between I- and O-phases. This uncovers the role of magnetism on chemical ordering. To capture the realistic situation, we next consider the Ti-Mo MXenes, passivated by -O or -F or -OH, which is found to stabilize the O-phases. Passivated Ti-Mo MXenes show an antiferromagnetic AFM-1 ground state with ferro ordering of TM's along a-axis, antiferro ordering of TM's along b-axis and ferro ordering of TM's along c-axis. Among all the studied MXenes, $Ti_2MoC_2F_2$, $TiMo_2C_2F_2$, and $TiMo_2C_2(OH)_2$ are found to be semiconducting, opening up the possible use of these compounds as thermoelectric materials. In order to validate our scheme of transport calculation, we first investigate the electrical transport properties of passivated n-type $TiMo_2C_2$, for which experimental results are available.[11] Since the precise nature of passivation in experimental study is not known, we consider uniform as well as mixed passivation by -O or -F or -OH. The calculated results are found to show good agreement with experimental data for choice of passivation with O and OH. Calculated electrical transport properties on systems on interest, $Ti_2MoC_2F_2$, $TiMo_2C_2F_2$, and $TiMo_2C_2(OH)_2$, show superior electrical transport properties of Ti_2MoC_2 compared to $TiMo_2C_2$ with a power-factor of 10^4 μWcm^{-1}K^{-2} at 300 K for a p-type carrier density of 10^{19}cm^{-3}. This leads to an exceptional thermoelectric figure of merit of ZT of 1.5 at 300 K and 3.1 at 800 K, the latter with a 27 % efficiency, thereby reaching the close to the desired target.

Our theoretical prediction should motivate study of passivated Ti_2MoC_2 compounds, exploring their usage as potential thermoelectric materials. While $TiMo_2C_2$ Mxene has been experimentally synthesized[10], to the best of our knowledge, the 2:1 composition of the double transition metal Ti-Mo series, Ti_2MoC_2 has not yet been synthesized. Our computational exercise shows that Ti_2MoC_2 is both thermodynamically and dynamically stable. Further more passivated Ti_2MoC_2 with two Ti-C layers sandwiching the middle Mo-C layer, the so-called O-phase, should be thermodynamically and dynamically stable over the in-plane ordered phase, and should remain stable in O-phase even at high temperature. This should encourage synthesize of Ti_2MoC_2 Mxene, the sister compound of synthesized double transition metal Mxene, $TiMo_2C_2$.

Several stragegies may be followed for p-type doping of Ti_2MoC_2 Mxene, as followed for monolayer and few layer transition metal dichalcogenides (TMDCs) which include substitutional doping during growth,[46] back gate or top liquid gate[47], gas molecule adsorption[48] etc. Creation of vertical heterostructures between Mxene and TMDCs have been established as an effective means for p-type doping.[49]

References

[1] M. Naguib, M. Kurtoglu, V. Presser, J. Lu, J. Niu, M. Heon, L. Hultman, Y. Gogotsi, and M. W. Barsoum, "Two-dimensional nanocrystals produced by exfoliation of Ti_3AlC_2," *Advanced materials*, vol. 23, no. 37, pp. 4248–4253, 2011.

[2] M. Naguib, O. Mashtalir, J. Carle, V. Presser, J. Lu, L. Hultman, Y. Gogotsi, and M. W. Barsoum, "Two-dimensional transition metal carbides," *ACS nano*, vol. 6, no. 2, pp. 1322–1331, 2012.

[3] D. S. Y. Z. B. L. Q. H. A. Z. Zhengyang Li, Libo Wang, "Synthesis and thermal stability of two-dimensional carbide mxene ti3c2," *Materials Science and Engineering B*, vol. 191, pp. 33–40, 2015.

[4] R. Liu and W. Li, "High-thermal-stability and high-thermal-conductivity ti3c2tx mxene/poly(vinyl alcohol) (pva) composites," *ACS Omega*, vol. 3, pp. 2609–2617, 2018.

[5] J. M. W. R. A. M. C. B. T. M. B. Raj Thakur, Armin VahidMohammadi and C. A. Carrero, "Insights into the thermal and chemical stability of multilayered v2ctx mxene," *Nanoscale*, vol. 11, pp. 10716–10726, 2019.

[6] M. Khazaei, M. Arai, T. Sasaki, M. Estili, and Y. Sakka, "Two-dimensional molybdenum carbides: potential thermoelectric materials of the mxene family," *Physical Chemistry Chemical Physics*, vol. 16, no. 17, pp. 7841–7849, 2014.

[7] A. N. Gandi, H. N. Alshareef, and U. Schwingenschlögl, "Thermoelectric performance of the mxenes M_2CO_2 (M= Ti, Zr, or Hf)," *Chemistry of Materials*, vol. 28, no. 6, pp. 1647–1652, 2016.

[8] S. Kumar and U. Schwingenschlögl, "Thermoelectric performance of functionalized Sc_2C mxenes," *Physical Review B*, vol. 94, no. 3, p. 035405, 2016.

[9] Z. Liu, L. Zheng, L. Sun, Y. Qian, J. Wang, and M. Li, "$(Cr_{2/3}Ti_{1/3})_3AlC_2$ and $(Cr_{5/8}Ti_{3/8})_4AlC_3$: New max-phase compounds in Ti–Cr–Al–C system," *Journal of the American Ceramic Society*, vol. 97, no. 1, pp. 67–69, 2014.

[10] B. Anasori, Y. Xie, M. Beidaghi, J. Lu, B. C. Hosler, L. Hultman, P. R. Kent, Y. Gogotsi, and M. W. Barsoum, "Two-dimensional, ordered, double transition metals carbides (mxenes)," *ACS nano*, vol. 9, no. 10, pp. 9507–9516, 2015.

[11] H. Kim, B. Anasori, Y. Gogotsi, and H. N. Alshareef, "Thermoelectric properties of two-dimensional molybdenum-based mxenes," *Chemistry of Materials*, vol. 29, no. 15, pp. 6472–6479, 2017.

[12] Z. Jing, H. Wang, X. Feng, B. Xiao, Y. Ding, K. Wu, and Y. Cheng, "Superior thermoelectric performance of ordered double transition metal mxenes: $Cr_2TiC_2T_2$ (T= -OH or -F)," *The journal of physical chemistry letters*, vol. 10, no. 19, pp. 5721–5728, 2019.

[13] B. Anasori, M. Dahlqvist, J. Halim, E. J. Moon, J. Lu, B. C. Hosler, E. N.

Caspi, S. J. May, L. Hultman, P. Eklund, *et al.*, "Experimental and theoretical characterization of ordered max phases Mo_2TiAlC_2 and $Mo_2Ti_2AlC_3$," *Journal of Applied Physics*, vol. 118, no. 9, p. 094304, 2015.

[14] B. Anasori, C. Shi, E. J. Moon, Y. Xie, C. A. Voigt, P. R. Kent, S. J. May, S. J. Billinge, M. W. Barsoum, and Y. Gogotsi, "Control of electronic properties of 2d carbides (mxenes) by manipulating their transition metal layers," *Nanoscale Horizons*, vol. 1, no. 3, pp. 227–234, 2016.

[15] Z. M. Wong, T. L. Tan, S.-W. Yang, and G. Q. Xu, "Enhancing the photocatalytic performance of mxenes via stoichiometry engineering of their electronic and optical properties," *ACS applied materials & interfaces*, vol. 10, no. 46, pp. 39879–39889, 2018.

[16] Q. Tao, M. Dahlqvist, J. Lu, S. Kota, R. Meshkian, J. Halim, J. Palisaitis, L. Hultman, M. W. Barsoum, P. O. Persson, *et al.*, "Two-dimensional $Mo_{1.33}C$ mxene with divacancy ordering prepared from parent 3d laminate with in-plane chemical ordering," *Nature communications*, vol. 8, no. 1, pp. 1–7, 2017.

[17] G. Kresse and J. Hafner, "Ab initio molecular dynamics for liquid metals," *Physical review B*, vol. 47, no. 1, p. 558, 1993.

[18] J. P. Perdew, K. Burke, and M. Ernzerhof, "Generalized gradient approximation made simple," *Physical review letters*, vol. 77, no. 18, p. 3865, 1996.

[19] V. I. Anisimov, I. Solovyev, M. Korotin, M. Czyżyk, and G. Sawatzky, "Density-functional theory and nio photoemission spectra," *Physical Review B*, vol. 48, no. 23, p. 16929, 1993.

[20] M. Nolan, S. D. Elliott, J. S. Mulley, R. A. Bennett, M. Basham, and P. Mulheran, "Electronic structure of point defects in controlled self-doping of the TiO_2 (110) surface: Combined photoemission spectroscopy and density functional theory study," *Physical Review B*, vol. 77, no. 23, p. 235424, 2008.

[21] G. Hautier, S. P. Ong, A. Jain, C. J. Moore, and G. Ceder, "Accuracy of density functional theory in predicting formation energies of ternary oxides from binary oxides and its implication on phase stability," *Physical Review B*, vol. 85, no. 15, p. 155208, 2012.

[22] M. E. Jochen Heyd, Gustavo E. Scuseria, "Hybrid functionals based on a screened coulomb potential," *J. Chem. Phys*, vol. 118, p. 8207, 2003.

[23] H. J. Monkhorst and J. D. Pack, "Special points for brillouin-zone integrations," *Physical review B*, vol. 13, no. 12, p. 5188, 1976.

[24] G. K. Madsen, J. Carrete, and M. J. Verstraete, "Boltztrap2, a program for interpolating band structures and calculating semi-classical transport coefficients," *Computer Physics Communications*, vol. 231, pp. 140–145, 2018.

[25] D. O. R. et al *Appl. Phys. Lett*, vol. 94, p. 212103, 2009.

[26] D. O. R. et al *Phys. Rev. Lett*, vol. 109, p. 166604, 2012.

[27] J. P. et al *Appl. Phys. Lett*, vol. 89, p. 122111, 2006.

[28] S. M. Ransell D'Souza, "Thermoelectric transport in graphene/h-

bn/graphene heterostructures: A computational study," *Physica E*, vol. 81, pp. 96–101, 2016.

[29] K. K. et al *Phys. Rev. B*, vol. 85, p. 115317, 2012.

[30] M. Zahedifar and P. Kratzer, "Band structure and thermoelectric properties of half-heusler semiconductors from many-body perturbation theory," *Physical Review B*, vol. 97, no. 3, p. 035204, 2018.

[31] G. K. Madsen and D. J. Singh, "Boltztrap. a code for calculating band-structure dependent quantities," *Computer Physics Communications*, vol. 175, no. 1, pp. 67–71, 2006.

[32] Z. Huang, W. Zhang, and W. Zhang, "Computational search for two-dimensional MX_2 semiconductors with possible high electron mobility at room temperature," *Materials*, vol. 9, no. 9, p. 716, 2016.

[33] R. DSouza, S. Mukherjee, and S. Ahmad, "Strain induced large enhancement of thermoelectric figure-of-merit (ZT$\sim$ 2) in transition metal dichalcogenide monolayers ZrX_2 (X= S, Se, Te)," *Journal of Applied Physics*, vol. 126, no. 21, p. 214302, 2019.

[34] A. Togo and I. Tanaka, "First principles phonon calculations in materials science," *Scripta Materialia*, vol. 108, pp. 1–5, 2015.

[35] W. Li, J. Carrete, N. A. Katcho, and N. Mingo, "ShengBTE: a solver of the Boltzmann transport equation for phonons," *Comp. Phys. Commun.*, vol. 185, p. 17471758, 2014.

[36] R. S. D. Bandyopadhyay, B. Haldar and N. Chakraborti, "The ti-mo-c (titanium-molybdenum-carbon) system," *Journal of Phase Equilibria*, vol. 20, pp. 332–336, 1999.

[37] L. Mattheiss, "Band structures of transition-metal-dichalcogenide layer compounds," *Physical Review B*, vol. 8, no. 8, p. 3719, 1973.

[38] W. Sun, Y. Xie, and P. R. Kent, "Double transition metal mxenes with wide band gaps and novel magnetic properties," *Nanoscale*, vol. 10, no. 25, pp. 11962–11968, 2018.

[39] L. Hicks and M. S. Dresselhaus, "Effect of quantum-well structures on the thermoelectric figure of merit," *Physical Review B*, vol. 47, no. 19, p. 12727, 1993.

[40] J. R. Sootsman, D. Y. Chung, and M. G. Kanatzidis, "New and old concepts in thermoelectric materials," *Angewandte Chemie International Edition*, vol. 48, no. 46, pp. 8616–8639, 2009.

[41] "Stronger role of four-phonon scattering than three-phonon scattering in thermal conductivity of iii-v semiconductors at room temperature," *Phys. Rev. B*, vol. 100, p. 245203, 2019.

[42] "Observation of strong higher-order lattice anharmonicity in raman and infrared spectra," *Phys. Rev. B*, vol. 101, p. 161202(R), 2020.

[43] T. Feng and X. Ruan *Physical Review B*, vol. 97, p. 045202, 2018.

[44] G. Qin, Q.-B. Yan, Z. Qin, S.-Y. Yue, M. Hu, and G. Su, "Anisotropic

intrinsic lattice thermal conductivity of phosphorene from first principles," *Physical Chemistry Chemical Physics*, vol. 17, no. 7, pp. 4854–4858, 2015.

[45] Z. H. A. S.-K. Hamed Gholivand, Shadi Fuladi and F. Khalili-Aragh, "Effect of surface termination on the lattice thermal conductivity of monolayer ti3c2tz mxenes," *J. Appl. Phys*, vol. 126, p. 065101, 2019.

[46] C. H. J. H.-Z. N. Zehua Hu, Zhangting Wu and W. Chen, "Two-dimensional transition metal dichalcogenides: interface and defect engineering," *Chem. Soc. Rev.*, vol. 47, p. 3100, 2018.

[47] Y. W. C. Cong, J. Shang and T. Yu *Adv. Opt. Mater.*, vol. 6, p. 1700767, 2016.

[48] Y. G. Y. C.-L. Z. L. L. W. Z. G. E. W. Z. G. G. S. A. M. J. K. W. Y. C. Q. Z. Wang, Z. Dong and A. T. S. Wee *Nat. Commun.*, vol. 7, p. 11283, 2016.

[49] H. X. Y. Liu and W. A. Goddard *J. Am. Chem. Soc.*, vol. 138, p. 1585315856, 2016.

Chapter 7

High-performance Thermoelectric Properties of Strained Two-Dimensional Tellurium*

7.1 Introduction and Motivation

In Chapter 6, we discuss the thermoelectric properties of Mo-Ti based double transition metal MXene compound with complex alloyed structure showing promising figure of merit for practical application. In the present chapter, we will consider elemental two-dimensional (2D) materials in monolayer form that are attractive due to their simplicity and indigenous properties. After the isolation of graphene from graphite in 2004, there are several such materials are experimentally synthesized and predicted computationally. Here we will focus on recently discovered elemental 2D material composed of group-VI element Tellurium (Te), known as Tellurene. The room temperature lattice thermal conductivity of 2D Te was reported to be the lowest among existing 2D materials, e.g. 2.16 and 4.08 $Wm^{-1}K^{-1}$ along arm-chair and zigzag directions of 2D crystal structure of Te [1] compared to 3080-5150 $Wm^{-1}K^{-1}$ for graphene [2] or 101.43 $Wm^{-1}K^{-1}$ and 110.30 $Wm^{-1}K^{-1}$ along arm-chair and zigzag-direction of MoS_2.[3] Such low thermal conductivity is attractive from perspective of thermoelectric (TE) applications. Furthermore, 2D nanoflake of Te was reported to possess excellent environmental stability [4–6] compared to other existing 2D materials. Following this, calculations were carried out and 2D Te, or tellurene was found to reach a room temperature ZT value of 0.79 by p-type doping with the dopant concentra-

*This chapter is based on publication : **Shiladitya Karmakar** and Tanusri Saha-Dasgupta, *Physical Review Materials*, **5.12**, 124006 (2021).

tion of 10^{13}cm^{-2} in square-Te [7], while that in β structure it was found to show a much better performance, especially at high temperature.[8] It will be thus worth to explore how the thermoelectric performance of 2D Te can be further improved.

With the development of 2D materials, 2D van der Waals heterojunctions formed by putting one 2D material on another 2D material have been an active field of research to explore improved functionalities and potential applications. Although the van der Waals interlayer coupling in 2D van der Waals heterojunctions is weak, creation of van der Waals heterostructures may introduce compressive or tensile strain, thus modifying the properties of the 2D materials. In particular, strain engineering has been proved to be a effective tool to enhance ZT of layered 2D materials.[9, 10] In this chapter, we attempt to do so by considering the strained structures of 2D Te. As shown in Fig 7.1, the calculated minimized strain arising due to lattice mismatch between 2D Te and other possible 2D materials like graphene, MoS_2, $MoSe_2$, WS_2, WSe_2 varies within about -1.5% to about 1.2%. We have thus considered 2D Te under 0.5%-1% tensile strain and 1.5-2% compressive strain. Our calculation show that under tensile strain, the unstrained, centrosymmetric β-phase of 2D Te spontaneously transform to non-centrosymmetric $\alpha\prime$ phase with helical chain like structure at tensile strain equal to or exceeding 0.5%, while structural symmetry remains unaltered under compressive strain.

Considering realistic estimates of strain that may be imposed to monolayer Te through van der Waals heterostructing with other known 2D materials, we demonstrate that the structural, electrical, and thermal transport properties can get strongly influenced by strain. Importantly, through strain engineering, the thermoelectric performance of elemental 2D Te in p-type doping can be made comparable to that of the known binary or ternary layered compound at room temperature, and can outperform the known binary or ternary layered compounds at high to moderate temperature. Our study provides a way to tune the thermoelectric properties of 2D Te for future applications. Having said that there are several points of caution in this suggestion. It should be emphasized that unless the ML of tellurene can be used selectively in TE measurement, the TE properties of the bottom layer will also contribute. Depending on the device geometry, the bottom layer may also undergo some amount of strain. Also other than geometrical effect namely strain, there can be chemical effects like charge transfer between component MLs which may influence the transport properties and thereby the TE properties of the heterojunctions. Our predictions thus need to be validted in experimental setups.

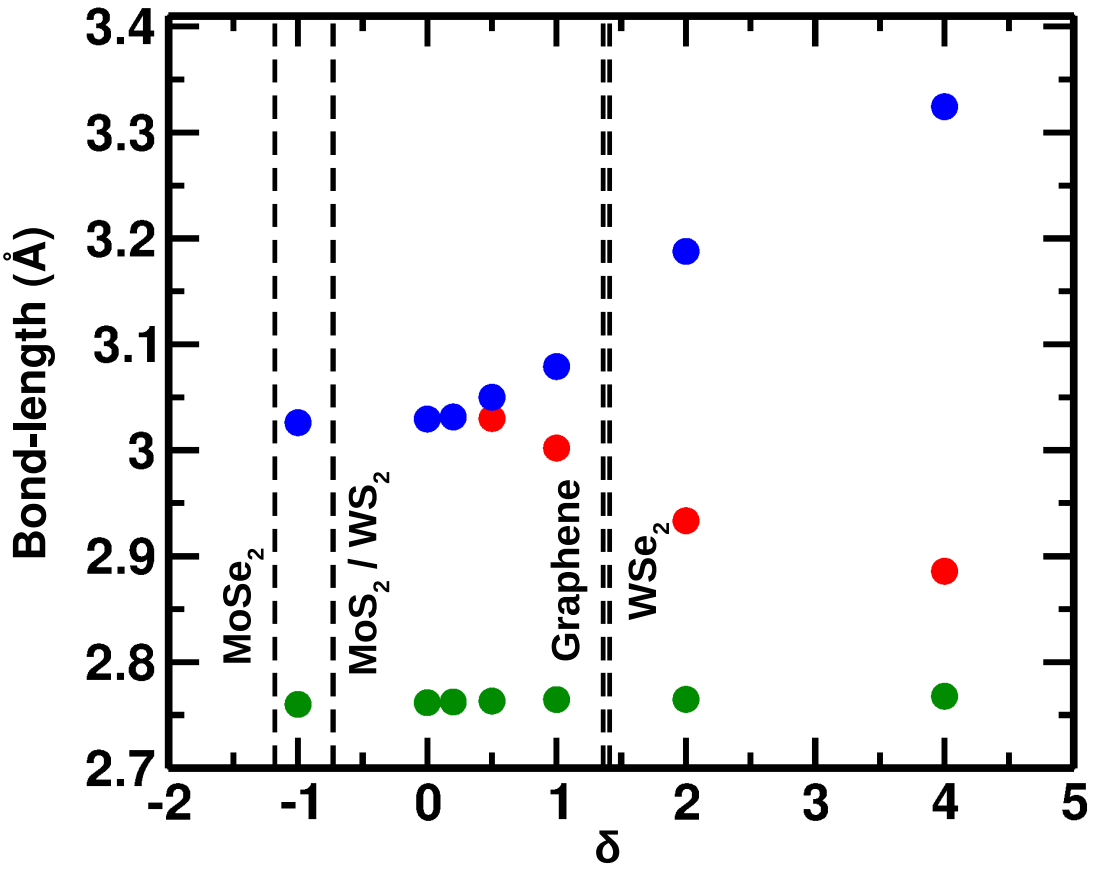

Figure 7.1: The variation of three Te-Te bond lengths of monolayer Te, marked by red, blue and green colored closed circle, as a function of compressive and tensile biaxial strain, measured by δ. The strain imposed in heterojunctions with known 2D materials, like $MoSe_2$, MoS_2, WS_2, WSe_2, graphene are marked by dashed lines.

7.2 Computational details

Ab-initio electronic structure calculations are carried out within the framework of density functional theory (DFT) using projector augmented-wave pseudopotentials and Perdew-Burke-Ernzerhof generalized gradient approximation (PBE-GGA) [11] as exchange correlation functional as implemented in the plane-wave based Vienna ab initio simulation package (VASP).[12] The cutoff energy of the plane-wave basis is chosen to be 520 eV which is found to be sufficient to achieve convergence in self-consistent field (SCF) calculations. In order to minimize artificial interaction between a monolayer and its images along the out-of-plane direction within the periodic set-up of calculation, a vacuum space of $\sim 22\mathring{A}$ is used. To find the optimum k-mesh for brillouin zone sampling, we perform convergence test for k-mesh with each monolayer phases of tellurene. Relaxation of tellurene structures is done with respect to internal atomic coordinates and unit cell volume using a convergence threshold of 10^{-5} eV for total energy and 10^{-3} eV/$\mathring{A}$ for maximum force/atom employing 14×14×1 Monkhorst-Pack mesh.[13] Converged k-mesh of 20×14×1 is used for SCF calculation with increased energy convergence threshold of 10^{-7} eV. In this work, which involves group-VIA element tellurium, we consider spin-orbit coupling (SOC) effects to compute band structures and subsequent thermoelectric calculations.

Electron transport properties along two orthogonal principle axis in the monolayer, along the zig-zag x and arm-chair y-directions are determined by solving semi empirical electron Boltzmann transport equations (BTEs) applied to the DFT derived band electrons under rigid band and constant relaxation time approximation (CRTA) as implemented in the BoltzTrap2 code.[14] Phonon properties are studied within the formulation of density functional perturbation theory (DFPT) as implemented in VASP. First we examine supercell and k-mesh convergence in order to validate our subsequent calculations. We find that supercell of size 4×4×1 and k-mesh of size 4×4×1 for all structures are sufficient to avoid soft phonon modes. The second order harmonic force constants and dynamical matrices are computed and the phonon band structures as obtained by Fourier interpolation of the real-space force constants using PHONOPY [15] code, are plotted along the high-symmetry k points of the BZ. To estimate lattice thermal conductivity (κ_l), we require second order harmonic interatomic force constants (IFCs) and third order anharmonic IFCs. Harmonic IFCs can be obtained from phonon dispersion as mentioned earlier. To calculate third order anharmonic IFCs, we generate different configurations having displaced atoms using finite difference method as implemented in thirdorder.py python script. [16] The number of configurations generated is decided by the following: number of nearest neighbour interactions, symmetry of the system, size of the supercell mesh, and size of the unit cell. Supercell of size 4×4×1 is used for all of our calculations. The atomic displacement cut off varies from unstrained to different strained struc-

tures: Hence, to construct the displaced configurations we consider up to 14th nearest neighbour interactions for unstrained structure case, and up to 9, 9, 20 and 14th nearest neighbour interactions for strain values, δ= -2, -1.5, 0.5 and 1 respectively. Total number of generated configurations are: 456, 456, 554, 1260, 660 for strain values, δ= -2, -1.5, 0, 0.5 and 1 respectively.

7.3 Results

7.3.1 Crystal Structure

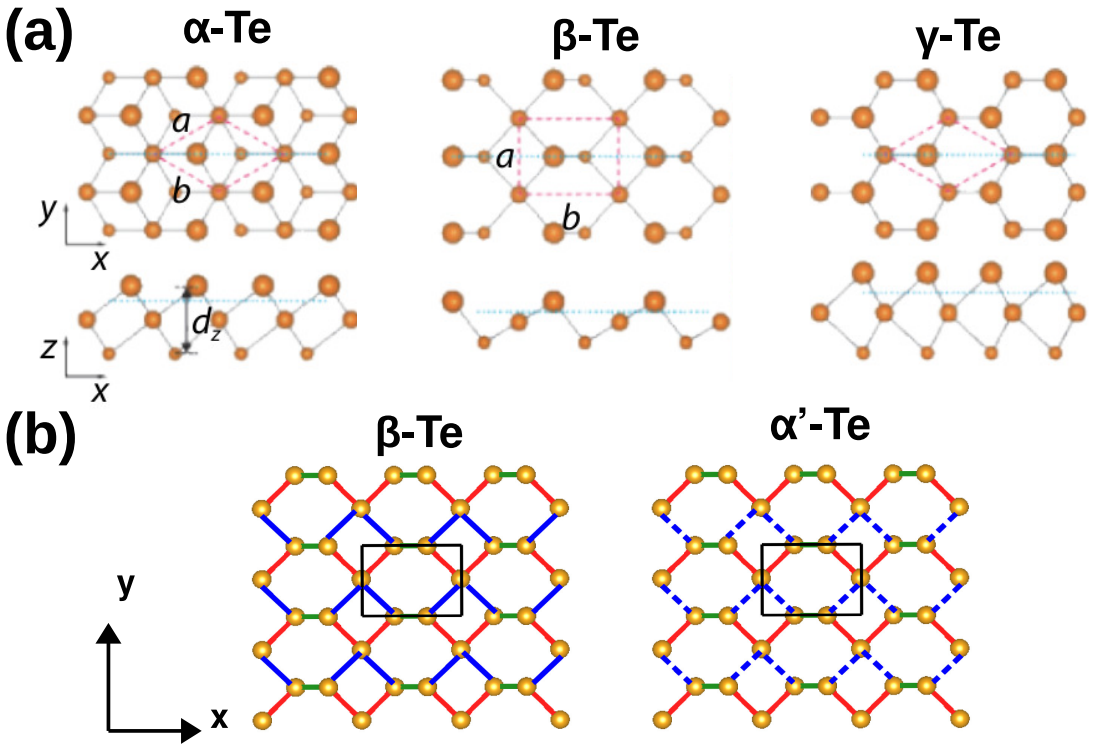

Figure 7.2: (a) Top and side views of the optimized structures of tellurene in different phases: α-Te, β-Te, and γ-Te. The figure is taken from ref.[17] (b) A structural transition from β to $\alpha\prime$ phase is signaled in terms of splitting of Te-Te bond lengths, colored by red and blue.

The most stable structure of bulk Te is trigonal at ambient pressure having three equivalent Te atoms at wyckoff position 6c of the unit cell. Each Te atom is covalently bonded with its two nearest neighbors forming helical chirals, either right handed in space group $P3_121$ or left handed in space group $P3_221$, which run along the three-fold screw axis (c-axis) and are stacked together along a and b-direction.

Upon reduction in dimensionality to monolayer (ML) limit, three different structures of Te were proposed by Zhu et al [17], 1T-MoS_2-like α-Te, orthorhombic β-Te and 2H-MoS_2-like γ-Te. According to the nomenclature followed by Zhu et al [17], α- and γ phases show a three- and sixfold coordination structure, respectively, the β phase exhibits a mixture of three- and fourfold coordination structures, as Te can possess multiple bonding configurations (cf Fig. 7.2(a)). A different nomenclature has been followed by Xiang et al [18] in which naming of different phases of tellurene are proposed based on their space group and their relationship with the bulk Te. Following this, α-Te (hexagonal, P-3m1 space group) named by Zhu et al.[17] is the ML γ Te. In the following discussion, we have used the nomenclature by Xiang et al.[18] However to avoid confusion with nomenclature by Zhu et al [17], we name the "non-centrosymmetric β" with P2 space group symmetry as $\alpha\prime$ phase ML.

At unstrained condition, β phase is found to be 30 meV/atom lower than γ phase, while ML $\alpha\prime$ phase is found to be not stable at unstrained condition. This observation is contrary to that reported in [17] in which γ phase was found to be most stable, but in accordance with the study by Qiao et al.[19] No soft phonon modes were observed for monolayer β-Te, and a cohesive energy of 2.567 eV/atom indicated that the kinetics of single-layer β-Te is relatively more stable.[20] We find that relative stability of ML tellurene phases crucially depends on the choice of exchange correlation functional. For example PBE-GGA stabilizes the β-Te over γ-Te by 30 meV/atom whereas inclusion of Grimme's van-der-Waal interaction as used by Zhu et al. stabilize γ-Te by 50 meV/atom.

Starting from the unstrained β structure, we apply both compressive strain and tensile strain. In order to estimate the strain exerted on ML Te in the heterostructure geometry, we build suitable supercell of the component structures to minimize their lattice mismatch ($\sim$ <2%). For stacking 2D materials, one on top of another, putting 1×1 cell of one material on 1×1 cell of another generally creates large lattice mismatch between the two, thereby large strain imparted to each other for a common inplane lattice constant. On the other hand, the lattice mismatch can be greatly reduced by placing m × m supercell of one material on n × n supercell of another, the choice of m and n being decided by condition that lattice mismatch to be minimized. Under this condition, only a small strain requires to be imparted to top layer to adjust to the lattice constant of the bottom layer. In the above we assume the bottom layer to be held fixed. We use graphene, MoS_2, $MoSe_2$, WS_2 and WSe_2 as substrate having good environmental stability. In particular, we use the Latticematch method based on rotation matrix as implemented in LatticeMatch code.[21, 22] Since the symmetry of β Te is orthorhombic while the other 2D substrates are of hexagonal symmetry, we rotate the substrate cell up to certain angle in order to match the lattice facing to that of β Te. The strain induced on 2D Te due to lattice mismatch in van der Waals structure is computed as,

$$\delta(\%) = \sqrt{\frac{S_{other} - S_{Te}}{S_{Te}}} \times 100 \tag{7.1}$$

where S_{Te} denotes the surface area of supercell of β-Te and S_{other} denotes that of other 2D materials. This method has been applied not only to full heterostructures [23, 24], but also to monolayers, as often considered for the graphene-MoS_2 heterostructure or transition-metal dichalcogenide/transition-metal dichalcogenide heterostructures [25, 26]. We notice that substrate MoS_2, $MoSe_2$ and WS_2 cause negative strain whereas graphene and WSe_2 cause positive strain in the β-Te structures. This leads to compression of β-Te ML for van der Waals heterostructure with MoS_2, $MoSe_2$ and WS_2, and expansion for graphene and WSe_2. Depending on value of δ, we construct β-Te under different tensile and compressive biaxial strains. The variation of lattice parameter of Te ML due to strain can be expressed as follows:

$$a_i(\delta) = (1 + \frac{\delta}{100})a_i^{eq}, i = a, b \tag{7.2}$$

a_i^{eq} represents the unstrained lattice constant of β-Te along a and b direction. We choose $\delta = 0.5\%$, 1% for tensile strain and $\delta = 1.5\%$ and 2% for compressive strain. Table 7.1, summarizes the lattice constants of the supercells of the components, the angle of rotation, θ, the surface areas of the components and the strain. Relaxing the condition of the bottom layer to be fixed, results into straining of the bottom layer of opposite sign as 2D Te, and slight modification of the strain imparted on Te, as shown in Table 7.1.

As mentioned above ML $\alpha\prime$ phase is not stable at unstrained condition. This situation does not alter under compressive strain, but does change under tensile strain.

2D Te in β structure consists of two inequivalent Te atoms in the unit cell, Te_1=Te_3 at wyckoff position 4o, and Te_2 at wyckoff position 1g resulting in two types of Te-Te bonds, long bond, marked by red and blue in Fig 7.2(b), and short bond, marked by green in Fig 7.2(b). In contrast, the $\alpha\prime$ phase there are three inequivalent Te atoms with inequivalence of Te_1 and Te_3, giving rise to three types of Te-Te bonds, with unequal lengths of red, blue and green bonds, as shown in Fig 7.1 and Fig 7.2(b). In moving from $\alpha\prime$ to β structure, one of the three inequivalent Te atoms in $\alpha\prime$ structure slightly shifts towards their closest neighbouring helical chains resulting loss of chain like feature of $\alpha\prime$ structure, as evident from Fig. 7.2(b). Upon application of compressive strain, the optimization starting from $\alpha\prime$ structure is found to relax back to the centrosymmetric β-phase. However under tensile strain, centrosymmetric β-phase is found to spontaneously transform to non-centrosymmetric $\alpha\prime$ phase for $\delta \geq 0.5$, as evident in terms of splitting of red and blue bond lengths (cf Fig 7.1).

vdwh	β-Te			Other 2D					
	a	b	S_{Te}	a	b	θ	S_{other}	$\delta(\%)$	$\delta\prime(\%)$
Te/ graphene	17.1	8.5	144.9	17.3	8.6	90	147.6	1.36	1.57 (-0.28)
Te/ MoS_2	21.9	11.4	250.2	22.3	11.5	106.1	248.9	-0.73	-0.43 (0.11)
Te/ $MoSe_2$	16.9	11.4	193.3	16.6	11.5	90	190.6	-1.18	-1.26 (0.13)
Te/ WS_2	21.9	11.4	250.2	22.3	11.5	106.1	248.9	-0.73	-0.45 (0.08)
Te/ WSe_2	17.1	8.5	144.7	17.3	8.6	90	147.5	1.41	1.62 (-0.38)

Table 7.1: Calculated strain (δ) due to lattice mismatch in van der Waals heterostructures (vdwh) of 2D-Te and other 2D materials, obtained assuming the bottom layer to be fixed. Calculated strain on Te ($\delta^{'}$) assuming both Te and bottom layer to relax is also shown. The strain on bottom layer is shown in parenthesis.

The splitting of red and blue bonds under tensile strain removes the mirror plane symmetry of ML β phase and brings back one dimensional helical chain nature in the structure leading to formation of non-centrosymmetric ML $\alpha\prime$ phase. Thus the ML tellurene put on top on MoS_2, $MoSe_2$ and WS_2 will stabilize in β phase, and that put on top on graphene and WSe_2 is expected to stabilize in $\alpha\prime$ phase. Table 7.2, summarizes the optimized lattice parameters for different strain values which confirms the conservation of orthorhombic symmetry of beta phase Te upon straining. Hence, second ranked tensor properties should be anisotropic along the in plane directions of ML, as found in the following.

δ	**a**	**b**	α
-2.0	4.14	5.58	90^o
-1.5	4.16	5.61	90^o
0	4.23	5.69	90^o
+0.5	4.25	5.72	90^o
+1.0	4.27	5.75	90^o

Table 7.2: Lattice parameters of biaxially strained β tellurene structures

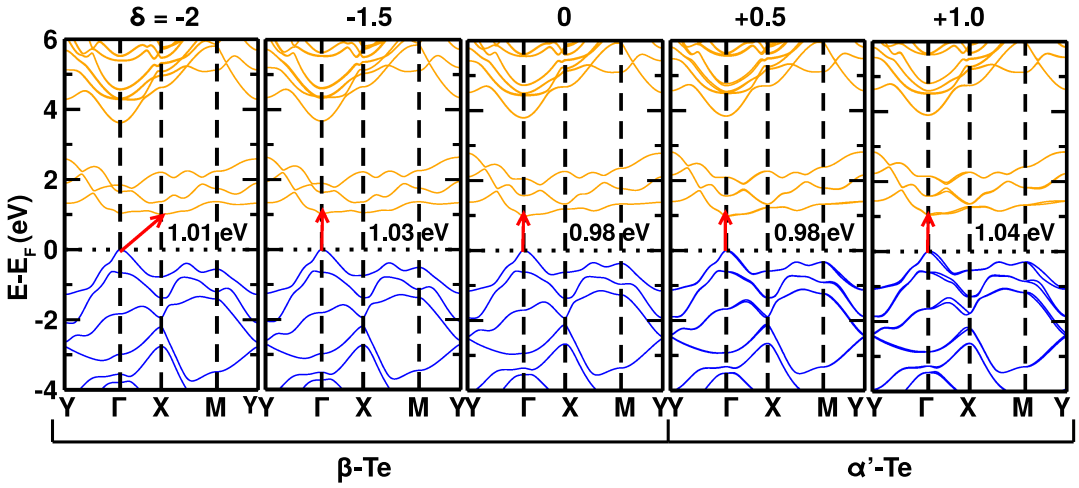

Figure 7.3: The variation of electronic band structure of 2D Te under different biaxial strain. A structural transition from β to $\alpha\prime$ phase is seen under tensile strain. The zero of the energy is set at Fermi level (E_F). Marked are the direct and indirect band gaps.

7.3.2 Electronic Structure

The electron configuration of Te is $5s^2 5p^4$. While the covalent bonds between intrachain Te atoms is formed by two unpaired p-electrons of adjacent atoms, the lone pair of p-electrons contribute in interaction between two interchain Te atoms. Thus, the interchain interaction is weaker than the intrachain one. The calculated band structure of unstrained and strained ML tellurene, plotted along the high symmetry **k** points of the 2D BZ, is shown in Fig. 7.3. As expected, it is found that SOC has a significant influence on the electronic structure of tellurene. Inclusion of SOC transforms the unstrained β-Te from indirect to direct band gap semiconductor at high symmetry Γ point with energy gap 0.98 eV. Biaxial strain with δ value ranging from -2% to +1% has very little effect on energy band gap with gap value around 1 eV. The direct gap nature of the semiconducting band structure persists under tensile strain, although degeneracy of the bands along certain symmetry directions get lifted due to breaking of centrosymmetry in $\alpha\prime$-Te structure. Under compressive strain exceeding 1.5 %, the band gap changes from direct to indirect with conduction band minima (CVM) shifting from Γ to high symmetry X point.

7.3.3 Electron conductivity

Under CRTA, the electrical conductivity σ depends on electron relaxation time, τ as a parameter and electrical BTE provides scaled electron conductivity (σ/τ) as

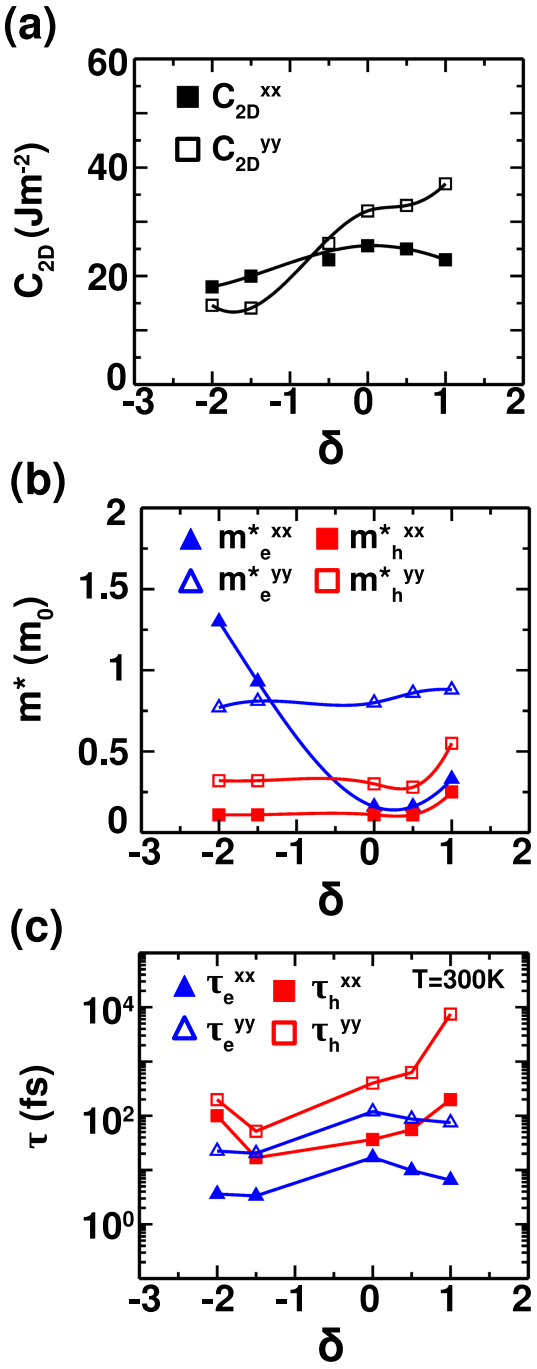

Figure 7.4: (a) Effective elastic modulus along the zig-zag (x) and arm-chair (y) directions plotted as a function of strain. (b) The effective mass for electron and hole along the zig-zag (x) and arm-chair (y) directions plotted as a function of strain. (c) The relaxation time for electron and hole along the zig-zag (x) and arm-chair (y) directions plotted as a function of strain.

output. Thus knowledge of τ, which refers to time interval between two successive collisions of charge carriers during conduction, is required for determination of σ. Moreover the 3D expression for σ (Eq. 2) involves the unit cell volume (Ω) of the 2D material. Hence calculated σ depends on the length of the unit cell used in the calculations along the z direction, and so should be normalized by multiplying by Lz/d, where Lz is the length of the unit cell along the z direction and d is the thickness of 2D material, but the d value is not well defined.[27] In this connection, several strategies are proposed by different researchers. In most calculations the interlayer distances (t_1) of the corresponding 3D materials is used.[28–30] Researchers have also used the buckling distance i.e., the out of plane direction distance between the topmost and bottommost atoms in the 2D structure (t_2) as the thickness.[31] Others have used the summation of the buckling distance and the van der Waals (vdW) radii of the outer-most surface atoms (t_3).[1, 32, 33] While the third choice (t_3) usually yields values close to the inter-layer distance (t_1), the second choice has an obvious flaw - the graphene thickness would be zero since it is of single atom layer. It should however be understood that no matter which definition is used, the normalization constant is a number, and as long as specified and used uniformly between unstrained and strained structures, should provide the right trend.

As mentioned, the most stable structure of bulk Te has trigonal space group symmetry in ambient condition which is quite different from that of β-tellurene ML. β-tellurene has orthorhombic space group ($a \neq b$) symmetry and thus no stable bulk counterpart. Hence we cannot use the first definition. However, most of the previous applications of definition are to 2D materials with minimal in-plane anisotropy, which is very different from our studied case. ML β-Te has a large inplane anisotropy. This should be reflected in the normalization procedure in order to consider the anisotropic character of transport properties of ML β-Te. Keeping this in mind, and difficulties associated with defining the out-of-plane thickness, we have chosen the in plane length of the unit cell in a (=4.23$\mathring{A}$) or b (=5.69$\mathring{A}$) direction instead of out-of-plane distance for normalization of transport properties along x or y direction, respectively. This leads to two distinct normalization constant along x or y transport direction equal to 5.20 and 3.87 respectively. Thus, σ along specific transport direction have been normalized by multiplying respective normalization constant.

τ along particular transport direction is proportional to corresponding carrier mobility (μ_{2D}). We consider electron-phonon scattering to estimate mobility as well as carrier relaxation time with the help of deformation potential theory. Here, we assume that charge carrier mobility is inversely proportional to their effective mass provided there is no change in the time scale for quasi particle scattering, *i.e.* relaxation time τ. The transport mobility can be expressed within deformation potential theory as follows, [34–36]

$$\mu_{2D} = \frac{e\tau}{m^*} = \frac{e\hbar^3 C_{2D}}{K_B T m^* m_a (E_1{}^i)^2} \tag{7.3}$$

where, $\hbar$ is the reduced planks constant, K_B is the Boltzmanns constant, T is absolute temperature. m^* (m^{*x} or m^{*y}) is the effective mass in transport direction along x and y respectively. m_a is defined as $\sqrt{m^{*x} m^{*y}}$. $E_1{}^i$ is the deformation potential of the VBM for hole or the conduction band minimum (CBM) for electron along transport direction, defined by $E_1{}^i = (\Delta E_i)/(\Delta l/l_0)$. ΔE_i represents the energy change of VBM and CBM with reference to vacuum energy and $\Delta l/l_0$ is uniaxial strain. C_{2D}, effective elastic modulus due to longitudinal strain along propagation direction (x or y) of acoustic wave, is defined by, $\frac{2(E-E_0)}{S_0} = C_{2D}(\Delta l/l_0)^2$, where E and E_0 are the total energies of the strained and equilibrium configuration respectively. S_0 is the equilibrium surface area, l and l_0 represent deformed and undeformed lattice parameters. Scattering rate increases with temperature leading to lowering of mobility as well as relaxation time captured by its T^{-1} behaviour.

The directional effective mass tensor can be expressed as,

$$m^* = \frac{h^2}{4\pi^2}\left(\frac{\partial^2 E}{\partial k^2}\right)^{-1} \tag{7.4}$$

i.e. the curvature of a band at a particular k-point.

Fig. 7.4(a) shows the variation of C_{2D} as a function of strain which essentially measures the ability of a material to withstand longitudinal strain caused by propagation of longitudinal acoustic wave along transport directions, x and y. For unstrained β-Te, C_{2D}^{xx} and C_{2D}^{yy} are found to be 25.6 Jm^{-2} and 32 Jm^{-2}, respectively, bearing the signature of anisotropy. Under tensile strain, the magnitude of C_{2D} as well as asymmetry between x and y-direction increases due to the structural transition from more 2D-like β to helical chain more 1D like $\alpha\prime$ phase. C_{2D}^{xx} (C_{2D}^{yy}) changes slightly to 23 (37) from 25.6 (32) J-m^{-2} as δ increase from 0 to 1. On the contrary upon compressive strain both the magnitude of C_{2D} as well as asymmetry between x and y direction decreases. We notice that a crossover of C_{2D}^{xx} and C_{2D}^{yy} occurs around δ = -0.5.

For unstrained β-Te, the deformation potential for electron along x and y direction are found to be, $E_1^x = 7.1$ and $E_1^y = 3$ and that of for hole are found to be $E_1^x = 6.8$ and $E_1^y = 2.3$. For electrons, the E_1 do not show significant changes upon straining whereas for holes, E_1 decreases with tensile strain. E_1^x (E_1^y) for holes decreases to 2.1 (0.4) from 6.8 (2.3) eV as δ increase from 0 to 1.

The effect of biaxial strain on effective masses of hole and electrons are shown in Fig. 7.4(b). Under compressive strain, electron effective mass along x direction m_e^{*xx} changes significantly, shows a jump at maximum value around -2%. This is also evident from band structures of -2% strained β Te structure, in which CBM

shifts from Γ to X point resulting direct to indirect band gap transition. Under tensile strain, m_h^{*xx} (m_h^{*yy}) inreases to 0.25 (0.55) from 0.11 (0.3) m_e as δ increase from 0 to 1.

Using the knowledge of C_{2D}, m^* and deformation potential, the carrier mobility and hence the relaxation time is calculated, as shown in Fig. 7.4(c) for T = 300 K. For unstrained β-Te, maximum relaxation time is observed for hole transport along y or arm-chair direction with value 400 fs whereas corresponding value for electron is found to be 125 fs at T = 300K. Under compressive strain, overall relaxation time is found to decrease whereas tensile strain is found to cause increase of it. Maximum value of τ is noticed for hole transport along y-direction for both compressive and tensile strains. At δ=-1.5, τ_h^{yy} = 32 fs which increase to 158 fs for δ=-2 at T = 300K reflecting corresponding change in mobility value (μ_{2D}^{yy}) from 170 to 820 $cm^2V^{-1}s^{-2}$. Tensile strain causes τ for hole along y-direction to dominate over x-direction by large difference. At δ=+1, τ_h^{yy} attains 7500 fs whereas τ_h^{xx} = 200 fs. This increase of τ_h upon tensile strain along both transport directions is due to the combined effect of m^*, C_{2D} and E_1. Now as δ goes from 0 to 1, m_h^{*xx} (m_h^{*yy}) increases by 127% (83%) and C_{2D}^{xx} (C_{2D}^{yy}) changes slightly to -10% (15%). But τ is inversely proportional to square of E_1. So even slight decrease in E_1 can increase the τ significantly. The corresponding percentage change of E_1^x and E_1^y is -69% and -83% respectively. This drives the factor of 5 increase of τ_h^{xx} and order of magnitude increase of τ_h^{yy}.

Fig. 7.5(a) shows the variation of electrical conductivity, σ at room temperature (300 K) as a function of strain in 2D Te structures calculated for carrier concentration of $10^{13}cm^{-2}$. The optimum PF for unstrained Te in β phase was shown to be achieved for carrier concentration of $10^{13}cm^{-2}$.[8] We have considered the carrier concentration of $10^{13}cm^{-2}$ for both n- and p- type carrier for electrical transport calculation of unstrained and strained structures. σ is found to decrease with temperature for all cases since scattering of charge carriers with phonons increases with temperature. Following the nature of carrier mobility and relaxation time, the major contribution to σ is found to be from holes. For unstrained case, maximum σ is obtained for hole transport along y-direction (σ_h^{yy}) with the value of 1.45×10^6 Sm^{-1} which is significantly larger compared to that of electron, σ_e^{yy} = 7.74×10^5 Sm^{-1}. Under tensile strain, σ increases for both electron and hole. At δ=+1.0, σ_h^{yy} is found to be 2.86×10^7 Sm^{-1} which is more than order of magnitude larger than that of unstrained case. On the other hand, under compressive strain, σ is found to show only marginal changes from the unstrained value, even a decrease for δ = -2.0.

The variation of Seebeck coefficient, evaluated at 300 K, with strain value, which represents induced TE voltage in response to a unit temperature gradient across the material is shown in Fig. 7.5(b). Since the band gap does not show much variation upon straining, there is not much variation observed for Seebeck coefficient upon straining, with values around 100-200 μVK^{-1}. These values are

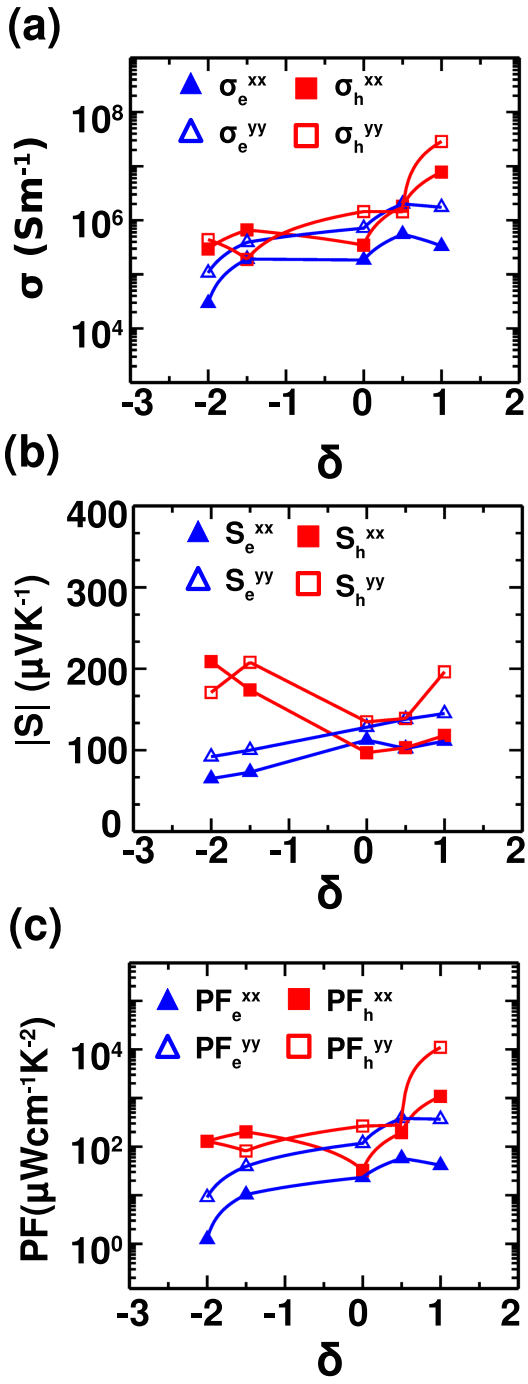

Figure 7.5: The electrical conductivity (a), Seeback coefficient (b) and power factor (c) at 300 K for electron and hole carriers along the zig-zag (x) and arm-chair (y) directions plotted as a function of strain.

comparable to the well-known TE materials such as Bi_2Te_3 and PbTe (∼250 μVK^{-1} at 350K, ∼250 μVK^{-1} at 500K respectively).[37, 38]

The corresponding PF determined from computed S and σ is shown in Fig. 7.5(c). For unstrained case, maximum PF is obtained for $PF_h^{yy} = 2.64\times10^2$ $\mu Wcm^{-1}K^{-2}$ followed by $PF_e^{yy} = 1.17\times10^2$ $\mu Wcm^{-1}K^{-2}$ at $T = 300K$ which agrees well that obtained by Sang et al.[8] Under tensile strain, PF shows a large enhancement with $PF_h^{yy} = 1.1\times10^4$ $\mu Wcm^{-1}K^{-2}$ for $\delta = 1.0$, which is about two order of magnitude larger than that of unstrained case. PF of electron transport along y direction is also quite appreciable for $\delta = 1.0$, with $PF_e^{yy} = 3.67\times10^2$ $\mu Wcm^{-1}K^{-2}$. This large enhancement of PF is primarily due to the large increase of σ on application of biaxial tensile strain with strain having only a moderate effect on S. On the other hand, under compressive strain, the PF shows only marginal change compared to unstrained, following the same trend as electrical conductivity.

7.3.4 Phonon dispersion

Phonon dispersion is important to understand the dynamical stability of a material. Fig. 7.6 shows the phonon band structure of unstrained as well as strained 2D Te with representative strain values of δ= -2 and +1, plotted along the high symmetry k points of the monoclinic space group. As is seen, phonon dispersion do not contain imaginary frequencies suggesting the strained structures are dynamically stable. As there are three atoms in the unit cell, there are total nine phonon modes, out of which three are acoustic modes and rest six are optical modes. Three acoustic modes with increasing frequency can be classified as ZA, TA and LA mode, as marked in the figure. The ZA mode, also known as the flexural mode, governs the out-of-plane transverse vibration of the 2D structure and must show the quadratic dispersion close to Γ point for the unstrained structure. Other two acoustic branches TA and LA govern the in-plane transverse and longitudinal vibration, respectively, and show linear behavior near the Γ point. We found at unstrained condition, for q values close to Γ point, ZA mode shows linear dependence with q. This artifact has been evident in many recent ab-initio calculation for 2D systems like MoS_2, WS_2, WSe_2 etc [39][40][41] and can affect the phonon transport significantly [42]. Accurate description of ZA mode in long wavelength limit has been obtained in both ab-initio and empirical calculations by enforcing the translational and rotational invariance condition related to crystal structure of the 2D system [42]. Translational invariance can be imposed using PHONOPY [15]. To employ the rotational invariance (huang condition)[43] upon the 2nd order IFC, we use the hiPhive [44] software package. After imposing both invariance conditions, the expected quadratic behavior of ZA mode near Γ point is observed at unstrained condition. We notice an unique feature of the dispersions, an asymmetric optical phonon branch overlapping with acoustic modes in

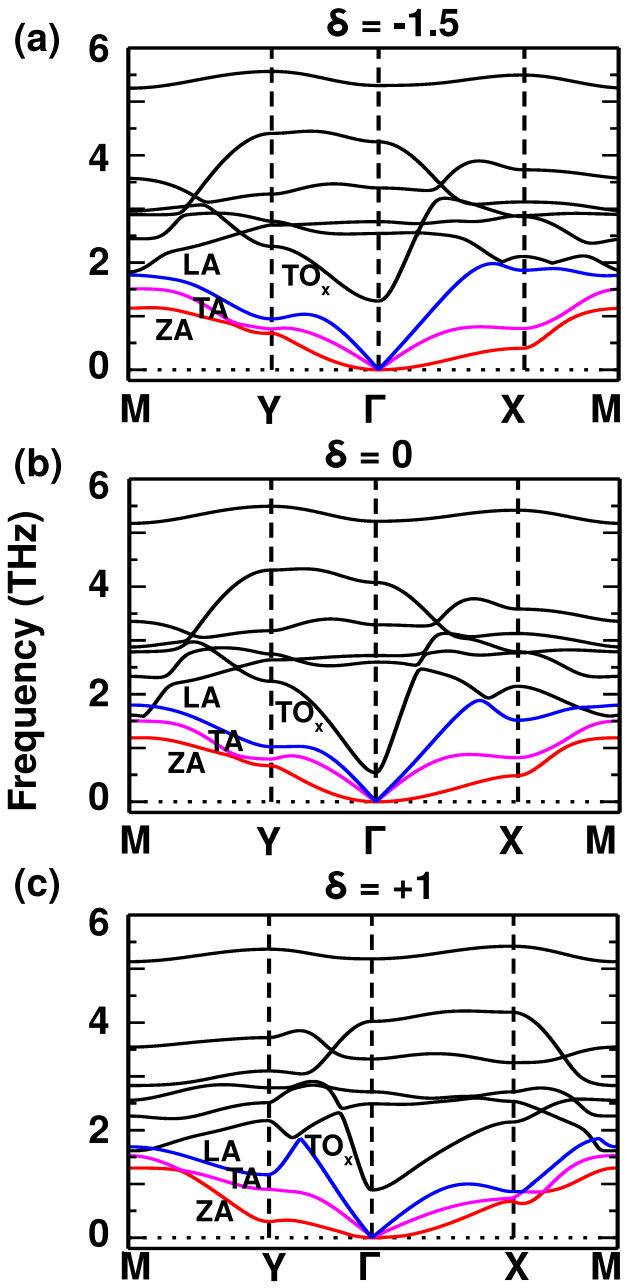

Figure 7.6: Phonon dispersion of 2D Te for representative strain values of δ= -1.5 (a), 0. (b) and +1.0 (c). Marked are the three acoustic modes and the low frequency transverse optic mode, TO_x.

low frequency regime. The corresponding optical mode vibrates along x direction. We label it as TO_x mode.

7.3.5 Thermal conductivity

Thermal conductivity (κ) measures the intrinsic ability of a material to conduct or transfer heat. Heat can be transported by both lattice and charge carrier giving rise to two components of κ namely electron thermal conductivity (κ_e) and lattice thermal conductivity (κ_l). We calculate κ_e/τ from electron BTE which is governed by electronic structure of material and compute κ_e using value of τ. On the other hand, κ_l is determined by solving lattice BTE using the information of 2nd order harmonic IFC and 3rd order anharmonic IFC's related to the lattice structure of material. The 3D expression for κ_l (Eq. 2.131) involves Ω similar to that of σ. Likewise κ_l is normalized.

As seen in Fig 7.7, for unstrained structures, κ_e is order of magnitude higher than κ_l, implying that heat is primarily transported through charge carriers. Maximum κ_e is noticed for electrons κ_{ee}^{yy}, with comparable values of κ_{ee}^{xx}, κ_{eh}^{xx} and κ_{eh}^{yy} (21.8 $\mathrm{Wm^{-1}K^{-1}}$, 6.9, 7.7, 8.6 $\mathrm{Wm^{-1}K^{-1}}$ respectively at $T = 300$K). We observe that the 3D lattice thermal conductivity depends sensitively on the quadracity of the out-of-plane ZA mode around Γ point. In absence of huang invariance condition, κ_l turns out to be order of magnitude smaller than κ_e with values $\kappa_l^{xx} = 1.29$ and $\kappa_l^{yy} = 0.43$ $\mathrm{Wm^{-1}K^{-1}}$ at $T = 300$K which matches well with that of obtained using uncorrected ZA mode [45]. After incorporating huang invariance, κ_l^{xx} and κ_l^{yy} becomes 3.96 and 1.99 $\mathrm{Wm^{-1}K^{-1}}$ at $T = 300$K respectively. These values are in good agreement with the values $\kappa_l^{xx} = 4.08$ and $\kappa_l^{yy} = 2.16$ $\mathrm{Wm^{-1}K^{-1}}$ reported in [1] where 2nd order IFCs are corrected using continuum approach for long-wavelength acoustic phonons as proposed in [46]. Thus implementation of huang invariance condition improves the underestimation of κ_l rectifying for the inaccuracies in ZA mode.

Under tensile strain, due to additional asymmetry in the structure in the $\alpha\prime$-phase, large variation is observed between transport along x and y-directions, both for charge and lattice components. Interestingly while the heat transport by the holes show more than an order of magnitude enhancement compared to that in unstrained structure, the lattice component shows order of magnitude decrease. This leads to κ_e more than two order of magnitude higher than κ_l causing ZT to be solely controlled by κ_e and little perturbed by changes in κ_l. For compressive strain, with added inversion symmetry in the structure in the β phase, variation among charge and lattice components of thermal conductivity becomes less. This allows both κ_e and κ_l to have non-negligible contribution in ZT. Imposition of huang invariance causes slight increase of κ_l compared to unstrained structure, with values $\kappa_l^{xx} = 4.40$ and $\kappa_l^{yy} = 2.06$ $\mathrm{Wm^{-1}K^{-1}}$. This follows the general trend that compressive strain increases lattice thermal conductivity.

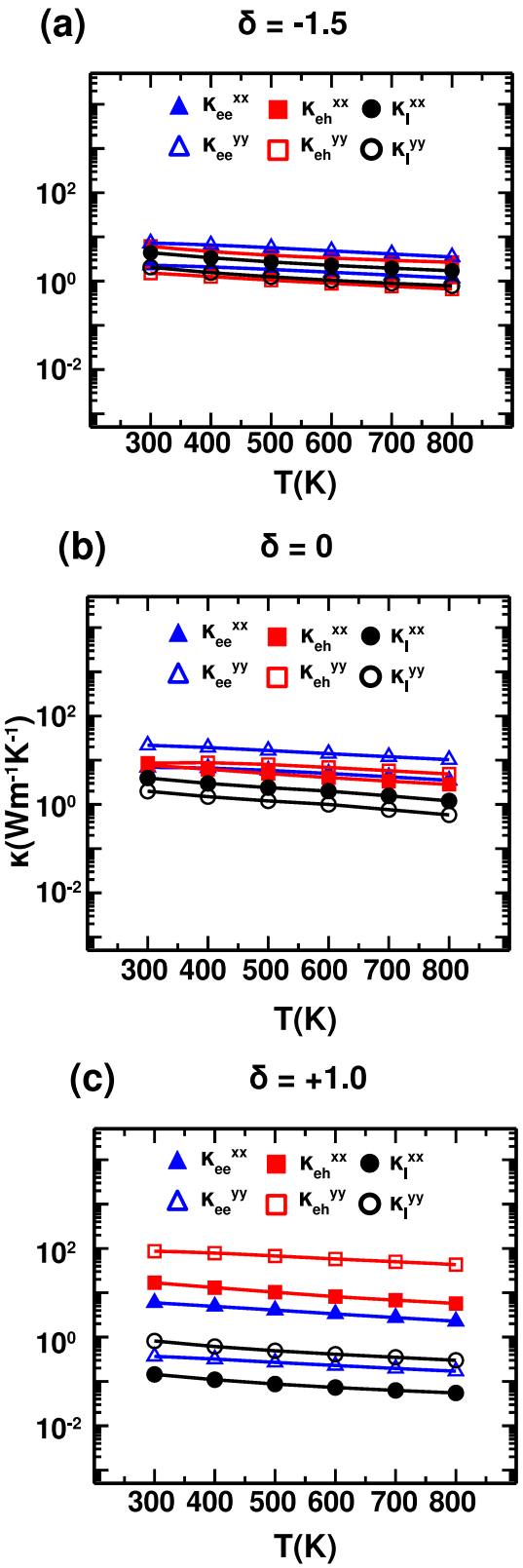

Figure 7.7: The temperature variation of electronic, κ_e and lattice thermal conductivity κ_l along the zig-zag (xx) and arm-chair (yy) directions for representative strain values of δ= -1.5 (a), 0. (b) and +1.0 (c).

It is interesting to find that κ_l in both unstrained and strained structures of 2D Te in both transport directions follow T^{-1} behavior. This indicates dominant Umklapp process of phonon scattering arising from 3rd order anharmonic term of potential energy expansion causing thermal resistivity. T^{-1} behaviour is common in other heavy elements and recently is also experimentally observed in bulk Te. The low values of κ_l in 2D Te compared to for example $MoSe_2$ or MoS_2 originates from reduced group velocity due to heavy mass of Te, which gets further influenced by the unique feature of phonon dispersion namely the low frequency optical mode TO_x overlapping with acoustic mode causing increase of phonon-phonon scattering rate. As is seen in Fig 7.6, applied strain softens the in-plane (TA and LA) modes, while it stiffens the out-of-plane ZA mode. Under tensile strain, ZA mode is seen to deviate from its quadratic nature around Γ point even with the application of huang condition. For a sufficiently large strain, the ZA modes becomes linear (cf Fig 7.6) suppressing κ_l. Such a trend has been seen in 2H $MoTe_2$.[47] This observation has been evident from our calculated κ_l at δ=1, with $\kappa_l^{xx} = 0.144$ and $\kappa_l^{yy} = 0.815$ $Wm^{-1}K^{-1}$ at $T = 300$K.

7.3.6 Figure of merit and TE conversion efficiency

Figure of merit ZT is determined from computed power factor and total thermal conductivity. Temperature dependence of ZT for the unstrained Te ML is shown in Fig. 7.8(a). ZT of the unstrained structure, which shows a monotonic increase with temperature, is found to be largest for p-doping along the y or armchair direction with $ZT_{yy}^h = 2.85$ at T=800K. We find that ZT decreases slightly with corrected ZA mode using huang invariance condition. ZT_h^{yy} decreases from 0.76 to 0.64 at T = 300 K and 2.33 to 2.12 at T = 700 K.

TE performance can be evaluated by computing their TE conversion efficiencies, related to Carnot efficiency and ZT value,

$$\eta = \frac{T_h - T_c}{T_h} \frac{\sqrt{1+ZT}-1}{\sqrt{1+ZT}+T_c/T_h} \tag{7.5}$$

where T_h and T_c are the hot and cold end of the TE devices, respectively and Carnot efficiency is given by $\frac{T_h - T_c}{T_h}$. Taking T_c = 300 K and T_h ranging from 300 to 800 K, calculated η values of unstrained structure is shown in inset of Fig. 7.8(a), which shows $\eta_h^{yy} = 25.1\%$ at 800 K.

The monotonic increase of ZT with temperature as well as dominance of p-type TE along arm-chair direction is found to hold good even for the strained structures. However, both ZT and η are found to be enhanced significantly by tensile strain. At room temperature (300K) the ZT_h^{yy} is found to show about 84% increase, with the value crossing 1(1.18), for tensile strain of $\delta = 1.0$ while slight increase of 6% is evident under compressive strain of δ = -1.5. The effect is found

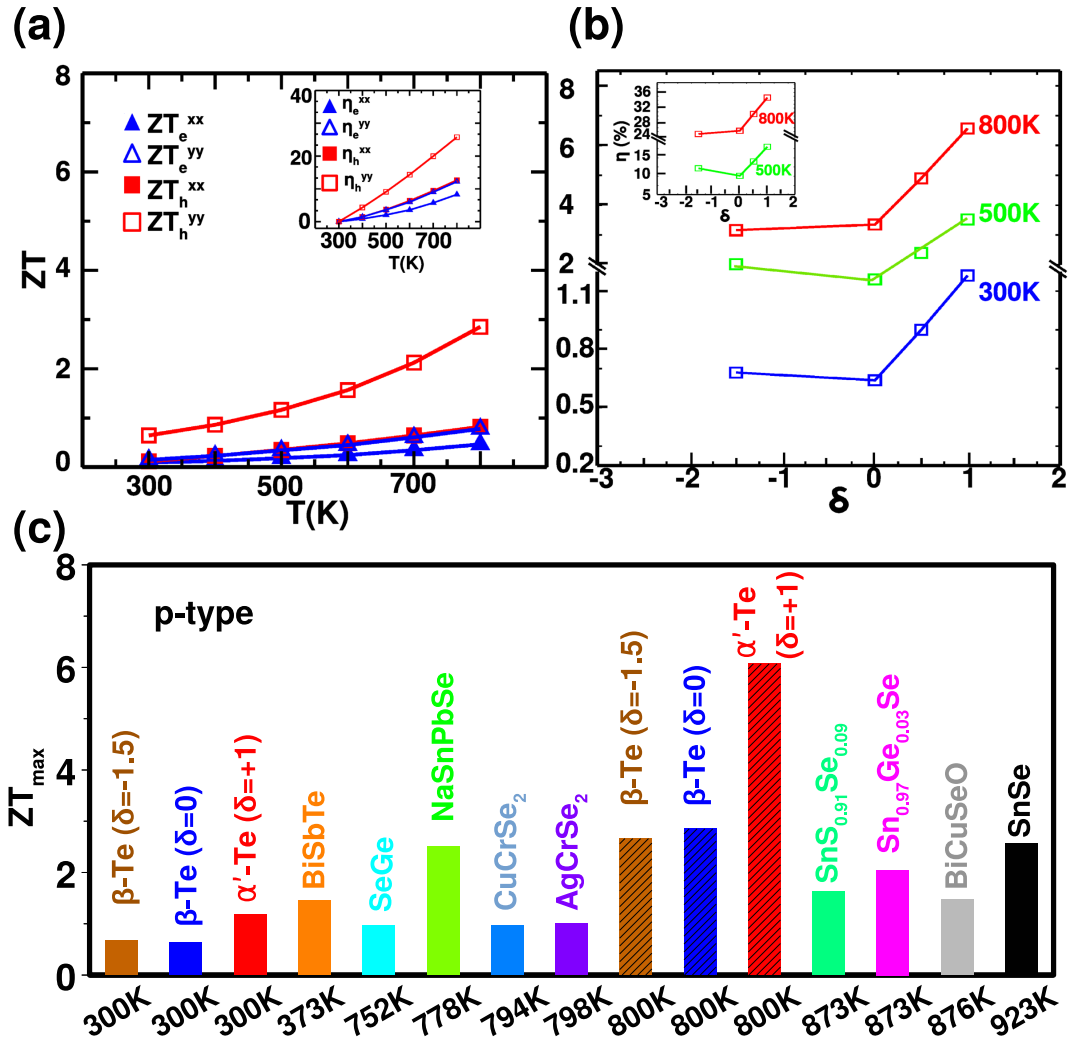

Figure 7.8: (a) The temperature variation of ZT and TE efficiency (inset) of unstrained Te monolayer, for chosen carrier concentration of 10^{13}cm^{-2}. (b) The variation of ZT_h^{yy} with strain at T = 300 K, 500 K and 800 K. The inset shows the corresponding variation of TE efficiency at 500 K and 800 K. (c) Comparison of TE perfomance of strained and unstrained Te monolayer with other known p-type layered materials.

to be more spectacular at high temperature (T=800K) for tensile strain. For δ = 1.0, ZT_h^{yy} found to reach 6.07, amounting to 113% enhancement with respect to unstrained ZT_h^{yy} while under compressive strain of δ=-1.5, ZT_h^{yy} becomes 2.66 of about 7% decrease than that of unstrained case. The variation of ZT_h^{yy} with respect to biaxial strain at T = 300K, 500K and 800K is shown in Fig. 7.8(b). Tensile strain is found to cause a sharp increase in ZT values, found to be above 2 for $T >$ 400 K. Interestingly, following the trend of ZT, maximum efficiency also shows an increase upon the application of tensile strain, as shown in inset of Fig. 7.8(b) with value of 34.2 % at T= 800 K for δ=1. The strategy of strain engineering to increase ZT was also found to be effective for γ- phase of ML tellurene [48] which showed that upon 4% tensile strain ZT of n-type ML γ Te can increse to 71% and 39% compared to that of calculated with unstrained structure at T = 300 K and 700 K respectively.

Finally, the thermoelectric performance, namely the p-type ZT values of strained and unstrained ML Te are shown in Fig. 7.8(c) in comparison to that of known p-type layered compounds. As is seen, performance of 1% tensile strained or -1.5% compressive strained Te ML as elemental thermoelectric is comparable to ternary compound BiSbTe [49] at room temperature, while its performance at high temperature (800 K) is far superior compared to other p-type binary or ternary layered thermoelectrics like NaSnPbSe[50] or SnSe[51] or Ag(Cu)CrSe$_2$[52, 53], BiCuSeO[54], $Sn_{0.97}Ge_{0.03}Se$[55] etc.

7.4 Conclusion

In conclusion, employing first-principles DFT calculations and Boltzmann transport theory, we investigate the role of strain on thermoelectric properties of monolayer tellurene,[20] brought into attention recently due to its fascinating properties including environmental stability, piezoelectric effect, high carrier mobility, photoresponse etc.[4–6] We consider realistics estimates of compressive as well as tensile strain values, that may be imparted through heterostructuring with known 2D materials, like graphene or transition metal dichalcogenides. We find interesting structural transition from centrosymmetric to noncentrosymmetric helical chain structure under tensile strain that has important bearing on the elastic properties. Although the band gap is not found to be show a significant variation, a direct to indirect band gap transition is observed for large compressive strain of 2%, with electrical conductivity, and power factor showing more than one and two order of magnitude enhancement under tensile strain, driven by the changes in mobility. The thermal conductivity dominated by heat transport by charge carriers, which is the lowest for tellurene among known 2D Materials, is increased under compressive strain. The delicate balance between electrical and thermal transport results in enhanced thermoelectric figure of merit for tensile strain,

with a value exceeding 1.0 at room temperature, comparable to BiSbTe.[49] For strained structures, the ZT value remains above 2 beyond temperature of 400 K and shoots up to 6.07 at 800 K, much higher than other binary and ternary layered thermoelectrics like $SnS_{0.91}Se_{0.09}$[56], SnSe[51], or $Sn_{0.97}Ge_{0.03}Se$[55] or BiCuSeO[54]. These findings underline the prospect of the strained tellurene as high-performance thermoelectric at moderate temperature.

References

[1] Z. Gao, F. Tao, and J. Ren, "Unusually low thermal conductivity of atomically thin 2D tellurium," *Nanoscale*, vol. 10, no. 27, pp. 12997–13003, 2018.

[2] A. A. Balandin, S. Ghosh, W. Bao, I. Calizo, D. Teweldebrhan, F. Miao, and C. N. Lau, "Superior thermal conductivity of single-layer graphene," *Nano letters*, vol. 8, no. 3, pp. 902–907, 2008.

[3] X. Gu and R. Yang, "Phonon transport in single-layer transition metal dichalcogenides: A first-principles study," *Applied Physics Letters*, vol. 105, no. 13, p. 131903, 2014.

[4] Y. Wang, G. Qiu, R. Wang, S. Huang, Q. Wang, Y. Liu, Y. Du, W. A. Goddard, M. J. Kim, X. Xu, *et al.*, "Field-effect transistors made from solution-grown two-dimensional tellurene," *Nature Electronics*, vol. 1, no. 4, pp. 228–236, 2018.

[5] M. Amani, C. Tan, G. Zhang, C. Zhao, J. Bullock, X. Song, H. Kim, V. R. Shrestha, Y. Gao, K. B. Crozier, *et al.*, "Solution-synthesized high-mobility tellurium nanoflakes for short-wave infrared photodetectors," *ACS nano*, vol. 12, no. 7, pp. 7253–7263, 2018.

[6] T. I. Lee, S. Lee, E. Lee, S. Sohn, Y. Lee, S. Lee, G. Moon, D. Kim, Y. S. Kim, J. M. Myoung, *et al.*, "High-power density piezoelectric energy harvesting using radially strained ultrathin trigonal tellurium nanowire assembly," *Advanced Materials*, vol. 25, no. 21, pp. 2920–2925, 2013.

[7] C. Lin, W. Cheng, G. Chai, and H. Zhang, "Thermoelectric properties of two-dimensional selenene and tellurene from group-vi elements," *Physical Chemistry Chemical Physics*, vol. 20, no. 37, pp. 24250–24256, 2018.

[8] D. K. Sang, T. Ding, M. N. Wu, Y. Li, J. Li, F. Liu, Z. Guo, H. Zhang, and H. Xie, "Monolayer β-tellurene: a promising p-type thermoelectric material via first-principles calculations," *Nanoscale*, vol. 11, no. 39, pp. 18116–18123, 2019.

[9] R. DSouza, S. Mukherjee, and S. Ahmad, "Strain induced large enhancement of thermoelectric figure-of-merit (ZT$\sim$ 2) in transition metal dichalcogenide monolayers ZrX_2 (X= S, Se, Te)," *Journal of Applied Physics*, vol. 126, no. 21, p. 214302, 2019.

[10] X. Zhao, G. Tang, Y. Li, M. Zhang, and Y. Nie, "Biaxial strain improving

the thermoelectric performance of a two-dimensional MoS_2/WS_2 heterostructure," *ACS Applied Electronic Materials*, vol. 3, no. 7, pp. 2995–3004, 2021.

[11] J. P. Perdew, K. Burke, and M. Ernzerhof, "Generalized gradient approximation made simple," *Physical review letters*, vol. 77, no. 18, p. 3865, 1996.

[12] G. Kresse and J. Hafner, "Ab initio molecular dynamics for liquid metals," *Physical review B*, vol. 47, no. 1, p. 558, 1993.

[13] H. J. Monkhorst and J. D. Pack, "Special points for brillouin-zone integrations," *Physical review B*, vol. 13, no. 12, p. 5188, 1976.

[14] G. K. Madsen, J. Carrete, and M. J. Verstraete, "Boltztrap2, a program for interpolating band structures and calculating semi-classical transport coefficients," *Computer Physics Communications*, vol. 231, pp. 140–145, 2018.

[15] A. Togo and I. Tanaka, "First principles phonon calculations in materials science," *Scripta Materialia*, vol. 108, pp. 1–5, 2015.

[16] W. Li, J. Carrete, N. A. Katcho, and N. Mingo, "Shengbte: A solver of the boltzmann transport equation for phonons," *Computer Physics Communications*, vol. 185, no. 6, pp. 1747–1758, 2014.

[17] Z. Zhu, X. Cai, S. Yi, J. Chen, Y. Dai, C. Niu, Z. Guo, M. Xie, F. Liu, J.-H. Cho, *et al.*, "Multivalency-driven formation of te-based monolayer materials: a combined first-principles and experimental study," *Physical review letters*, vol. 119, no. 10, p. 106101, 2017.

[18] Y. Xiang, S. Gao, R.-G. Xu, W. Wu, and Y. Leng, "Phase transition in two-dimensional tellurene under mechanical strain modulation," *Nano Energy*, vol. 58, pp. 202–210, 2019.

[19] J. Qiao, Y. Pan, F. Yang, C. Wang, Y. Chai, and W. Ji, "Few-layer tellurium: one-dimensional-like layered elementary semiconductor with striking physical properties," *Science bulletin*, vol. 63, no. 3, pp. 159–168, 2018.

[20] B. Wu, X. Liu, J. Yin, and H. Lee, "Bulk β-te to few layered β-tellurenes: indirect to direct band-gap transitions showing semiconducting property," *Materials Research Express*, vol. 4, no. 9, p. 095902, 2017.

[21] K. Wu, H. Ma, Y. Gao, W. Hu, and J. Yang, "Highly-efficient heterojunction solar cells based on two-dimensional tellurene and transition metal dichalcogenides," *Journal of Materials Chemistry A*, vol. 7, no. 13, pp. 7430–7436, 2019.

[22] W. Hu and J. Yang, "First-principles study of two-dimensional van der waals heterojunctions," *Computational Materials Science*, vol. 112, pp. 518–526, 2016.

[23] W. Hu, T. Wang, R. Zhang, and J. Yang, "Effects of interlayer coupling and electric fields on the electronic structures of graphene and MoS_2 heterobilayers," *Journal of Materials Chemistry C*, vol. 4, no. 9, pp. 1776–1781, 2016.

[24] W. Hu, T. Wang, and J. Yang, "Tunable schottky contacts in hybrid graphene–phosphorene nanocomposites," *Journal of Materials Chemistry C*,

vol. 3, no. 18, pp. 4756–4761, 2015.

[25] H.-P. Komsa and A. V. Krasheninnikov, "Electronic structures and optical properties of realistic transition metal dichalcogenide heterostructures from first principles," *Physical Review B*, vol. 88, no. 8, p. 085318, 2013.

[26] X. Li, S. Yu, S. Wu, Y. Wen, S. Zhou, and Z. Zhu, "Structural and electronic properties of superlattice composed of graphene and monolayer mos2," *The Journal of Physical Chemistry C*, vol. 117, no. 29, pp. 15347–15353, 2013.

[27] X. Wu, V. Varshney, J. Lee, Y. Pang, A. K. Roy, and T. Luo, "How to characterize thermal transport capability of 2d materials fairly?–sheet thermal conductance and the choice of thickness," *Chemical Physics Letters*, vol. 669, pp. 233–237, 2017.

[28] A. Cepellotti, G. Fugallo, L. Paulatto, M. Lazzeri, F. Mauri, and N. Marzari, "Phonon hydrodynamics in two-dimensional materials," *Nature communications*, vol. 6, no. 1, pp. 1–7, 2015.

[29] G. Qin, Z. Qin, W.-Z. Fang, L.-C. Zhang, S.-Y. Yue, Q.-B. Yan, M. Hu, and G. Su, "Diverse anisotropy of phonon transport in two-dimensional group iv–vi compounds: A comparative study," *Nanoscale*, vol. 8, no. 21, pp. 11306–11319, 2016.

[30] X. Gu and R. Yang, "Phonon transport in single-layer transition metal dichalcogenides: A first-principles study," *Applied Physics Letters*, vol. 105, no. 13, p. 131903, 2014.

[31] F. Q. Wang, J. Yu, Q. Wang, Y. Kawazoe, and P. Jena, "Lattice thermal conductivity of penta-graphene," *Carbon*, vol. 105, pp. 424–429, 2016.

[32] X. Wu, V. Varshney, J. Lee, T. Zhang, J. L. Wohlwend, A. K. Roy, and T. Luo, "Hydrogenation of penta-graphene leads to unexpected large improvement in thermal conductivity," *Nano letters*, vol. 16, no. 6, pp. 3925–3935, 2016.

[33] W. Xu, G. Zhang, and B. Li, "Thermal conductivity of penta-graphene from molecular dynamics study," *The Journal of chemical physics*, vol. 143, no. 15, p. 154703, 2015.

[34] J. Qiao, X. Kong, Z.-X. Hu, F. Yang, and W. Ji, "High-mobility transport anisotropy and linear dichroism in few-layer black phosphorus," *Nature communications*, vol. 5, no. 1, pp. 1–7, 2014.

[35] S. Bruzzone and G. Fiori, "Ab-initio simulations of deformation potentials and electron mobility in chemically modified graphene and two-dimensional hexagonal boron-nitride," *Applied Physics Letters*, vol. 99, no. 22, p. 222108, 2011.

[36] G. Fiori and G. Iannaccone, "Multiscale modeling for graphene-based nanoscale transistors," *Proceedings of the IEEE*, vol. 101, no. 7, pp. 1653–1669, 2013.

[37] H. Kim, B. Anasori, Y. Gogotsi, and H. N. Alshareef, "Thermoelectric properties of two-dimensional molybdenum-based mxenes," *Chemistry of Mate-*

rials, vol. 29, no. 15, pp. 6472–6479, 2017.

[38] Y. Pei, A. LaLonde, S. Iwanaga, and G. J. Snyder, "High thermoelectric figure of merit in heavy hole dominated PbTe," *Energy & Environmental Science*, vol. 4, pp. 2085–2089, 2011.

[39] H. Zhang, S. Lu, J.-l. Zheng, J. Du, S. Wen, D. Tang, and K. Loh, "Molybdenum disulfide (mos 2) as a broadband saturable absorber for ultra-fast photonics," *Optics express*, vol. 22, no. 6, pp. 7249–7260, 2014.

[40] A. Berkdemir, H. R. Gutiérrez, A. R. Botello-Méndez, N. Perea-López, A. L. Elías, C.-I. Chia, B. Wang, V. H. Crespi, F. López-Urías, J.-C. Charlier, *et al.*, "Identification of individual and few layers of WS_2 using raman spectroscopy," *Scientific reports*, vol. 3, no. 1, pp. 1–8, 2013.

[41] W.-X. Zhou and K.-Q. Chen, "First-principles determination of ultralow thermal conductivity of monolayer WSe_2," *Scientific reports*, vol. 5, no. 1, pp. 1–8, 2015.

[42] J. Carrete, W. Li, L. Lindsay, D. A. Broido, L. J. Gallego, and N. Mingo, "Physically founded phonon dispersions of few-layer materials and the case of borophene," *Materials Research Letters*, vol. 4, no. 4, pp. 204–211, 2016.

[43] M. Born and K. Huang, *Dynamical Theory of Crystal LatticesMax Born and Kun Huang*. Clarendon P, 1954.

[44] F. Eriksson, E. Fransson, and P. Erhart, "The hiphive package for the extraction of high-order force constants by machine learning," *Advanced Theory and Simulations*, vol. 2, no. 5, p. 1800184, 2019.

[45] S. Sharma, N. Singh, and U. Schwingenschlögl, "Two-dimensional tellurene as excellent thermoelectric material," *ACS Applied Energy Materials*, vol. 1, no. 5, pp. 1950–1954, 2018.

[46] D. Liu, A. G. Every, and D. Tománek, "Continuum approach for long-wavelength acoustic phonons in quasi-two-dimensional structures," *Physical Review B*, vol. 94, no. 16, p. 165432, 2016.

[47] A. Shafique and Y.-H. Shin, "Strain engineering of phonon thermal transport properties in monolayer 2H-$MoTe_2$," *Physical Chemistry Chemical Physics*, vol. 19, no. 47, pp. 32072–32078, 2017.

[48] J. Ma, F. Meng, J. He, Y. Jia, and W. Li, "Strain-induced ultrahigh electron mobility and thermoelectric figure of merit in monolayer α-te," *ACS Applied Materials & Interfaces*, vol. 12, no. 39, pp. 43901–43910, 2020.

[49] B. Poudel, Q. Hao, Y. Ma, Y. Lan, A. Minnich, B. Yu, X. Yan, D. Wang, A. Muto, D. Vashaee, *et al.*, "High-thermoelectric performance of nanostructured bismuth antimony telluride bulk alloys," *Science*, vol. 320, no. 5876, pp. 634–638, 2008.

[50] Y. K. Lee, Z. Luo, S. P. Cho, M. G. Kanatzidis, and I. Chung, "Surface oxide removal for polycrystalline SnSe reveals near-single-crystal thermoelectric performance," *Joule*, vol. 3, no. 3, pp. 719–731, 2019.

[51] L.-D. Zhao, S.-H. Lo, Y. Zhang, H. Sun, G. Tan, C. Uher, C. Wolverton,

V. P. Dravid, and M. G. Kanatzidis, "Ultralow thermal conductivity and high thermoelectric figure of merit in snse crystals," *nature*, vol. 508, no. 7496, pp. 373–377, 2014.

[52] F. Gascoin and A. Maignan, "Order–disorder transition in $AgCrSe_2$: A new route to efficient thermoelectrics," *Chemistry of Materials*, vol. 23, no. 10, pp. 2510–2513, 2011.

[53] S. Bhattacharya, R. Basu, R. Bhatt, S. Pitale, A. Singh, D. Aswal, S. Gupta, M. Navaneethan, and Y. Hayakawa, "$CuCrSe_2$: a high performance phonon glass and electron crystal thermoelectric material," *Journal of Materials Chemistry A*, vol. 1, no. 37, pp. 11289–11294, 2013.

[54] Y. Liu, L.-D. Zhao, Y. Zhu, Y. Liu, F. Li, M. Yu, D.-B. Liu, W. Xu, Y.-H. Lin, and C.-W. Nan, "Synergistically optimizing electrical and thermal transport properties of BiCuSeO via a dual-doping approach," *Advanced Energy Materials*, vol. 6, no. 9, p. 1502423, 2016.

[55] S. Chandra and K. Biswas, "Realization of high thermoelectric figure of merit in solution synthesized 2D SnSe nanoplates via Ge alloying," *Journal of the American Chemical Society*, vol. 141, no. 15, pp. 6141–6145, 2019.

[56] W. He, D. Wang, H. Wu, Y. Xiao, Y. Zhang, D. He, Y. Feng, Y.-J. Hao, J.-F. Dong, R. Chetty, *et al.*, "High thermoelectric performance in low-cost $SnS_{0.91}Se_{0.09}$ crystals," *Science*, vol. 365, no. 6460, pp. 1418–1424, 2019.

Chapter 8

Summary and Outlook

The primary objective of the present thesis is based on the modeling and simulation of two broad classes of materials that are technologically important and indigenous. The first class of materials is molecular complexes and coordination polymers exhibiting spin-crossover (SCO) properties which have been discussed in chapters 3 to 5. In chapters 3 and 4, we study the light-induced excited spin state trapping (LIESST) phenomena in Fe(II) based complexes which require an accurate description of both ground and excited states. Considering a model SCO system, we first test the applicability of wave function and density functional theory (DFT) based approaches in such situations in Chapter 3. With that knowledge in Chapter 4, we employ the time-dependent density functional theory (TDDFT) based scheme with a suitable choice of exchange-correlation (XC) functional to explain the observed trend in the relaxation rate of LIESST process for a range of Fe(II) SCO complexes. In Chapter 5, we provide the microscopic understanding of thermally activated Spin transition observed in the tetrazole-based coordination polymer following the model Hamiltonian approach proposed by Banerjee et al. Chapters 6 and 7 deal with the other class namely layered two-dimensional (2D) materials displaying thermoelectric properties. We first discuss the thermoelectric properties of double transition metal carbide compound MXene with complex alloyed structure in Chapter 6 and then elemental 2D material Tellurene in Chapter 7 within the framework of Boltzmann transport theory taking input from DFT band structure.

In the present chapter, we summarize the main findings described in the previous chapters that emerge from our study. We then discuss the future possibilities to extend on our present work.

8.1 Summary

8.1.1 Chapter 3: Light-Induced Excited Spin State Trapping in Spin Crossover Model System

In Chapter 3, we investigate the LIESST problem considering a hypothetical SCO model system built from a real complex [Fe(abpt)$_2$(NCS)$_2$] (where abpt = 4-amino-3,5-bis(pyridin-2-yl)-1,2,4-triazole) using two complementary techniques namely time-dependent density functional theory (TDDFT) with choice of different XC functional, and multi-reference approach of complete active space self-consistent field (CASSCF) and complete active-space second-order perturbation (CASPT2) theory. The findings are summarized below,

- Comparing the electronic energy difference between the ground High spin (HS) and Low spin (LS) state (ΔE^0_{HL}), we find that CASSCF gives rise to unphysical stabilization of the HS state over the LS state. This contradicts the SCO behavior of LIESST material. But DFT with different choices of functionals captures the right stability.
- CASPT2 calculations which include the effect of dynamical correlation, make the unphysical stabilization of HS state over LS state much less severe, compared to that in CASSCF, stressing the importance of inclusion of dynamical effect.
- Within the d-d excitation-deexcitation scenario and Franck-Condon theory, we compute the relaxation rates of possible LIESST mechanisms, as suggested by the two approaches.
- Based on our findings, we conclude that rates are captured in a reasonable manner by TDDFT making it a suitable approach to estimate the relaxation rates of real complexes, consisting of several tens to several hundreds of atoms, given its computationally inexpensive nature compared to that of the multi-reference approaches.

8.1.2 Chapter 4: Trend in Light-Induced Excited-State Spin Trapping in Fe(II)-based Spin Crossover Systems

Exercise made in Chapter 3 makes us believe that TDDFT with a suitable choice of XC functional is a potential tool for the microscopic understanding of the variation in the low-temperature rate constant of LIESST process for a range of Fe(II) complexes. In Chapter 4, we explore this possibility by considering four different LIESST complexes with the following ligands of varying degree of size

and complexity, 1-propyltetrazole (ptz), 2-picolylamine (pic), tris4-[(6-methyl)-2-pyridyl]-3-aza-butenylamine ((mepy)$_3$tren), 2,2'-bipyridine. The choice of the specific ligands is primarily based on the relative stability of their charge-transfer and ligand-field electronic states. These complexes, studied by Hauser et al[1], exhibit 14 orders of magnitude variation in rate constant, posing a challange for theoretical calculation. The major findings are:

- By carefully examining 21 different XC functionals from the broad catagory of the GGA, meta-GGA, hybrid, range-separated hybrid, hybrid meta-GGA, and double-hybrid types, a consistent description of ΔE^0_{HL} of the four compounds are established by comparing computed estimate of ΔE_{HL} with experimental estimates drawn from knowledge of $T_{1/2}$ and ΔS^0_{HL}.

- Within the d-d excitation-deexcitation, calculated low-temperature relaxation rate constants of ptz and pic complexes are found to be in excellent agreement with measured values. It is noteworthy that the measured relaxation rates from the four complexes vary over a range of nine orders of magnitude with $\sim 4{\times}10^{-5}$ for ptz to 10^4 for bipy.

- Both the HS-LS energy gap and nuclear contribution of rate constant are found to contribute to this trend being coupled to the ligand field effect and metal-ligand bond stiffness. The metal-ligand covalency, quantified through the integrated value of crystal orbital Hamiltonian population (ICOHP), reveals clear correspondence with the low-temperature rate constant.

- This, in turn, establishes the progressive stabilization of the charge-transfer and ligand-field states from 1-propyltetrazole to 2,2-bipyridine utilizing an increasing degree of covalency.

  Our study underlines the relationship between the geometry of the ligands and the relaxation rate. The microscopic understanding, thus provided, may be useful in rational designing of the ligands, with desired LIESST properties.

8.1.3 Chapter 5: Trend in cooperativity in spin-crossover of metal-organic polymers

In Chapter 5, we investigate the microscopic origin of cooperativity in three Fe(II) tetrazole-based polymeric compounds showing different thermal spin transition behavior. The tetrazole-based bridging ligand of the polymers is differed by the number of carbon atoms present in the linker between two tetrazole rings leading to the formation of 1D and 2D coordination networks. Following the

model Hamiltonian approach proposed by Banerjee et al., we calculate the spin-dependent elastic interaction (E_v) and magnetic exchange interaction (J) among Fe(II) centers of associated polymers. Our findings, as listed below, show

- The elastic exchange, E_v for all the compounds are of an anti-ferroelastic type and hence cooperative behavior is determined by magnetic exchange J.
- J turns out to be anti-ferromagnetic for all compounds.
- E_v is found to decrease as one move from two to four and six C- linker-based ligand compounds and J shows a similar trend as that of E_v.
- This in turn explains the decrease of hysteresis width ($\Delta T_{1/2}$) in six C-linker based (2K) ligand compounds than that of two C-linker based (29K) ones.
- We predict that the Four C-linker-based Fe(II) compounds must show spin transition accompanied by hysteresis which is yet to be validated from the experiment.

8.1.4 Chapter 6: First-principles Prediction of Enhanced Thermoelectric Properties of Double Transition Metal MXenes: $Ti_{3-x}Mo_xC_2T_2$ (x =0.5, 1, 1.5, 2, 2.5, T = -OH/-O/-F)

In Chapter 6, we investigate the stability, electronic, magnetic, and transport properties of Ti-Mo-based MXene compounds considering five ordered alloyed structures $Ti_{3-x}Mo_xC_2$ with x = 0.5, 1, 1.5, 2, 2.5 in two possible ordered forms i.e., I-MXene and O-MXene, employing first-principles density functional theory and Boltzmann transport formalism.

- First, we study the relative stability of unpassivated structures between the I- and O- phases. This uncovers the role of magnetism in chemical ordering stabilizing the I-phase over the O-phase.
- To capture the realistic situation, we next consider the structures passivated by -O or -F or -OH, which is found to stabilize the O-phases.
- Passivated Ti-Mo MXenes show an antiferromagnetic AFM-1 ground state with ferro ordering of TMs along the a-axis, antiferro ordering of TMs along the b-axis, and ferro ordering of TMs along the c-axis.
- Among all the studied MXenes, $Ti_2MoC_2F_2$, $TiMo_2C_2F_2$, and $TiMo_2C_2(OH)_2$ are found to be semiconducting, opening up the possible use of these compounds as thermoelectric materials.

- In order to validate our scheme of transport calculation with experiment, we calculate the electrical transport properties of passivated n-type $TiMo_2C_2$ with uniform as well as mixed passivation by -O or -F or -OH.
- The calculated results are found to show good agreement with experimental data for the choice of passivation with O and OH.
- We find that Ti_2MoC_2 show superior electrical transport properties compared to $TiMo_2C_2$ with a power-factor of 10^4 $\mu Wcm^{-1}K^{-2}$ at 300 K for a p-type carrier density of $10^{19}cm^{-3}$.
- This leads to an exceptional thermoelectric figure of merit of ZT of 1.5 at 300 K, and 3.1 at 800 K, the latter with a 27 % efficiency.

  Our theoretical prediction should motivate the study of passivated Ti_2MoC_2 compounds, exploring their usage as potential thermoelectric materials.

8.1.5 Chapter 7: High-performance Thermoelectric Properties of Strained Two-Dimensional Tellurium

In Chapter 7, we investigate the influence of biaxial strain on Tellurene, which had been discussed already for its potential in thermoelectric applications. We demonstrate that the structural, electrical, and thermal transport properties of monolayer (ML) orthorhombic β-Te can get strongly influenced by strain. The summary of our main findings are,

- To get a realistic estimate of strain ($\sim< 2\%$), we construct the van der Waals hetero-structure of β-Te with other known 2D materials like graphene, MoS_2, $MoSe_2$, WS_2 and WSe_2. We notice that substrate MoS_2, $MoSe_2$, and WS_2 lead to compression on β-Te ML whereas graphene and WSe_2 lead expansion.
- We find that under tensile strain, centrosymmetric β-phase of 2D Te spontaneously transforms to non-centrosymmetric $\alpha\prime$-phase with a helical chain-like structure at tensile strain $\geq 0.5\%$, while structural symmetry remains unaltered under compressive strain.
- Following the structural changes of 2D Te under strain, the anisotropy in elastic properties of 2D Te is found to show interesting evolution, which had an important bearing on the mobility of the charge carriers that depend on stretching modulus, deformation potential, and effective mass.
- Although the band gap remains essentially unchanged ($\sim$1 eV) upon straining, which keeps the Seeback coefficient unchanged, more than an order of magnitude enhancement in electrical conductivity is observed under tensile strain, driven by changes in mobility and hence relaxation time.

- This drives the power factor (PF) $S^2\sigma$ for holes along armchair direction (10^4 μWcm^{-1}K^{-2}) about two order of magnitude larger for 2D Te under tensile strain.
- Under tensile strain, heat transport by the holes shows more than an order of magnitude enhancement compared to that in an unstrained structure whereas the lattice component shows an order of magnitude decrease.
- We find that compressive strain increases lattice thermal conductivity.
- The delicate balance between electrical and thermal transport results in an enhanced thermoelectric figure of merit for tensile strain, with a value exceeding 1.0 at room temperature, comparable to BiSbTe.
- For strained structures, the ZT value remains above 2 beyond the temperature of 400 K and shoots up to 6.07 at 800 K, much higher than other binary and ternary layered thermoelectrics like $SnS_{0.91}Se_{0.09}$, SnSe, or $Sn_{0.97}Ge_{0.03}Se$ or BiCuSeO.

  Above findings underline the prospect of the strained tellurene as a high-performance thermoelectric at moderate temperatures.

8.2 Outlook

8.2.1 SCO molecular materials and coordination polymers

In chapters 3 and 4, we studied the LIESST phenomena of Fe(II) complexes with the help of the Relaxation model proposed by Hauser et al. Here, electronic states are modeled as 1D potential energy curves (PECs). Structure-wise, spin crossover is accompanied by drastic change within the first coordination sphere of the complexes leading to considerable elongation of the iron-ligand bond length during LS→HS transition. Hence we consider the PECs as a function of the average bond length of Fe(II)N_6 octahedra ($< R_{Fe-N} >$) only. Our analysis may be improved on following aspects.

- We have assumed that the LIESST mechanism is limited to the d-d excitation-deexcitation scenario. This assumption holds good when the d manifold is widely separated from the metal-ligand charge transfer (MLCT) manifold. While this is a simplistic approach, this is a pragmatic approach given the complexity and diversity of the actual complexes. A more involved and sophisticated approach considering explicit nuclear quantum dynamics[2] has been applied in the context[3–15] of model systems. Although It will be a computational challenge to apply such an approach to real complexes, it is worth investigating its effect on case like [Fe(2,2'-bipyridine)$_3$]$^{2+}$.

- As discussed in Chapter 1, the main disadvantage of the LIESST phenomena is that the trapping in photoinduced HS state occurs only at cryogenic temperature and there is a rapid increase of the HS $\rightarrow$ LS relaxation rate constant above $\sim$50K. Above a certain critical temperature defined as $T_c(LIESST)$[16], the system overcomes the energy barrier between the two spin states and relaxes to the LS state. This prohibits the potential applications of LIESST compounds in any electronic devices. Although there are several strategies proposed by Hauser to circumvent the situations [17] discussed in the following, it still remains an open problem to the community. In this respect, the following may be worth exploring.

  a) To manifest LIESST at higher temperatures requires designing compounds with larger HS-LS metal-ligand bond difference (ΔR_{HL}). Phosphine-based Fe(II) complex with $\Delta R_{HL} \sim 0.27\mathring{A}$ reported to have $k_{HL}(T \rightarrow 0)$ one order of magnitude smaller than that of the complexes with nitrogen donors by Wu et al.[18] and the $T_c(LIESST)$ turned out to be relatively large as $\sim$80 K.

  b) Light-induced bistability exhibited by $[Fe(etz)_6](BF_4)$[19] could be another possible strategy. Hauser suggested that irradiation inside the hysteresis of a thermal spin transition may result in switching between two spin states of the crystal with a large lifetime. Such experiments on systems with thermal hysteresis at elevated temperatures have not yet been done successfully. Hence computational modeling of this situation could be useful.

  c) A secondary photochemical process triggered by the light-induced population of the HS state could be a promising strategy. Here the HS$\rightarrow$LS relaxation rate of a system is determined by an intramolecular ligand exchange[20] instead of intersystem crossing making the process two orders of magnitude slower. Renz et al.[21] obtained a long-lived metastable HS state for the LS system $[Fe(terpy)_2]^{2+}$ doped into an inert manganese host.

- It is also worth mentioning that, Letard et al[16] compared the photomagnetic properties of a series of Fe(II) compounds in the high-temperature region, determined corresponding $T_c(LIESST)$ values, and correlated them with their thermal properties. Variation of $T_c(LIESST)$ vs $T_{1/2}$ for 22 compounds were shown to be represented by parallel lines of the equation of the form $T_c(LIESST) = T^0 0.3 T_{1/2}$, where T^0 expected to vary with the associated cooperativity of the compounds. Previously, a similar correlation was suggested by Hauser et al where they demonstrated that the logarithm of the lifetime of the metastable LIESST state is inversely proportional to $T_{1/2}$, known as inverse gap law. Microscopic understanding of such correlation is important because it may help to tune the LIESST properties in

the desired range of temperatures.

In Chapter 5, we discuss the microscopic origin of thermally activated spin transition for three different tetrazole-based Fe(II) polymeric compounds using the model Hamiltonian setup proposed by Banerjee et al. Currently, we will solve the constructed Hamiltonian using a Monte Carlo simulation based on a standard Metropolis algorithm. Spin-dependent elastic interactions and magnetic exchange interactions for different compounds extracted from DFT calculation will serve as the model parameters and can be used to simulate respective spin transition behavior, which will be taken up shortly.

8.2.2 Layered 2D thermoelectric materials

In chapters 6 and 7, we studied the transport properties of materials within the semi-classical Boltzmann transport theory. There are several future directions.

- More sophisticated methods involving quantum transport techniques like non-equilibrium green function formalism[22] could be employed to calculate the transport properties as done by Lu et al.[23] and Xu et al.[24] to calculate thermal transport in grain boundaries of graphene, and graphene junctions and quantum dots, respectively.

- As suggested by Li et al.[25], there are two possible research approaches in order to achieve high-performance thermoelectric materials by tailoring their interconnected transport properties. Both mechanisms provide a chance to disconnect the linkage between thermal and electrical transport by introducing some new scattering mechanisms and enhancing the figure of merit ZT. One approach is to explore new materials with complex crystalline structures such as skutterudites[26], clathrates[27], and Zintl compounds[28]. In skutterudites, clathrates compounds, the *rattling* motion of loosely bonded atoms within a large cage generates strong scattering against lattice phonon propagation but has less impact on the transport of electrons. As a consequence, the thermal conductivity can be reduced greatly while maintaining the electrical conductivity unaltered. Zintl compounds with a large unit cell such as $Yb_{14}MnSb_{11}$, $Yb_{11}GaSb_9$, $Ca_{11}GaSb_9$ and $SrZnSb_2$ have also been reported to possess an intrinsically low lattice thermal conductivity due to the high fraction of low-velocity optical phonon modes[29].

- On the other hand, another approach would be to reduce the dimensions of the materials. When any of the dimensions of a system decreases and approaches a length scale comparable to the characteristic length of an electron (e.g. mean free path, de Broglie wavelength) in the same direction, the density of states (DOS) is increased significantly due to quantum

confinement[30], resulting in the enhancement of the Seebeck coefficient. The thermal conductivity is also reduced because the surface strongly scatters the propagation of phonons (boundary scattering), as the corresponding dimension becomes less than the average free path of phonons. Bi_2Te_3-based films prepared by pulsed laser deposition show κ values of 0.3-0.4 $Wm^{-1}K^{-1}$, which are 25% lower than in the bulk[31]. It has also been reported that a silicon nanowire with a diameter of 10-20 nm presents amazingly low thermal conductivity with a $\kappa_{bulk}/\kappa_{nanowire}$ ratio of as high as 25-150 near room temperature[32].

- In the above context, recently monolayer and few-layer Ti_3C_2 MXene nanodots with lateral sizes below 10 nm and nanoribbons have been fabricated in the laboratory.[33, 34] Nanoribbons terminated along different orientations usually exhibit unique electronic properties different from their 2D counterparts and can be useful to design desired transport properties. Hence we expect that the thermoelectric properties can be further improved by reducing their dimension to the nanoribbon limit.

- As discussed in Chapter 7, the thermoelectric figure of merit (ZT) of ML tellurene is found to be improved on the application of biaxial strain where realistic estimates of strain are achieved from the construction of van der Waal heterostructure of tellurene with other 2D materials like MoS_2, $MoSe_2$, WS_2, WSe_2, Graphene. Thermoelectric properties of such heterostructure may be different from that of ML. Unless the ML of tellurene can be used selectively in the TE measurement, the TE properties of the bottom layer constituting other 2D material will also contribute. Depending on the device geometry, the bottom layer may also undergo some amount of strain. Also, other than the geometrical effect, namely strain, there can be chemical effects like the charge transfer between the component MLs, which may influence the transport properties and thereby the TE properties of the heterojunctions. It is an intriguing issue whether thermoelectric properties can be inherited when extended to the case of van der Waal heterostructures.

References

[1] A. Hauser, A. Vef, and P. Adler, "Intersystem crossing dynamics in fe (ii) coordination compounds," *The Journal of chemical physics*, vol. 95, no. 12, pp. 8710–8717, 1991.

[2] M. Pápai, "Photoinduced low-spin to high-spin mechanism of an octahedral fe (ii) complex revealed by synergistic spin-vibronic dynamics," *Inorganic chemistry*, vol. 60, no. 18, pp. 13950–13954, 2021.

[3] C. Sousa, M. Llunell, A. Domingo, and C. de Graaf, "Theoretical evidence for the direct 3 mlct-hs deactivation in the light-induced spin crossover of fe (ii)–polypyridyl complexes," *Physical Chemistry Chemical Physics*, vol. 20, no. 4, pp. 2351–2355, 2018.

[4] C. Sousa, C. de Graaf, A. Rudavskyi, and R. Broer, "Theoretical study of the light-induced spin crossover mechanism in [fe (mtz) 6] 2+ and [fe (phen) 3] 2+," *The Journal of Physical Chemistry A*, vol. 121, no. 51, pp. 9720–9727, 2017.

[5] G. Vanko, A. Bordage, M. Pápai, K. Haldrup, P. Glatzel, A. M. March, G. Doumy, A. Britz, A. Galler, T. Assefa, *et al.*, "Detailed characterization of a nanosecond-lived excited state: X-ray and theoretical investigation of the quintet state in photoexcited [fe (terpy) 2] 2+," *The Journal of Physical Chemistry C*, vol. 119, no. 11, pp. 5888–5902, 2015.

[6] T. J. Penfold, E. Gindensperger, C. Daniel, and C. M. Marian, "Spin-vibronic mechanism for intersystem crossing," *Chemical reviews*, vol. 118, no. 15, pp. 6975–7025, 2018.

[7] C. Sousa, C. de Graaf, A. Rudavskyi, R. Broer, J. Tatchen, M. Etinski, and C. M. Marian, "Ultrafast deactivation mechanism of the excited singlet in the light-induced spin crossover of [fe (2, 2'-bipyridine) 3] 2+," *Chemistry–A European Journal*, vol. 19, no. 51, pp. 17541–17551, 2013.

[8] G. Capano, T. Penfold, M. Chergui, and I. Tavernelli, "Photophysics of a copper phenanthroline elucidated by trajectory and wavepacket-based quantum dynamics: a synergetic approach," *Physical Chemistry Chemical Physics*, vol. 19, no. 30, pp. 19590–19600, 2017.

[9] S. Gómez, M. Heindl, A. Szabadi, and L. González, "From surface hopping to quantum dynamics and back. finding essential electronic and nuclear degrees of freedom and optimal surface hopping parameters," *The Journal of Physical Chemistry A*, vol. 123, no. 38, pp. 8321–8332, 2019.

[10] M. Pápai, "Toward simulation of fe (ii) low-spin to high-spin photoswitching by synergistic spin-vibronic dynamics," *Journal of chemical theory and computation*, vol. 18, no. 3, pp. 1329–1339, 2022.

[11] M. Kondo and K. Yoshizawa, "A theoretical study of spin–orbit coupling in an fe (ii) spin-crossover complex. mechanism of the liesst effect," *Chemical physics letters*, vol. 372, no. 3-4, pp. 519–523, 2003.

[12] Y. Shiota, D. Sato, G. Juhász, and K. Yoshizawa, "Theoretical study of thermal spin transition between the singlet state and the quintet state in the [fe (2-picolylamine) 3] 2+ spin crossover system," *The Journal of Physical Chemistry A*, vol. 114, no. 18, pp. 5862–5869, 2010.

[13] M. Papai, G. Vanko, C. De Graaf, and T. Rozgonyi, "Theoretical investigation of the electronic structure of fe (ii) complexes at spin-state transitions," *Journal of chemical theory and computation*, vol. 9, no. 1, pp. 509–519, 2013.

[14] C. Sousa, A. Domingo, and C. de Graaf, "Effect of second-order spin–orbit

coupling on the interaction between spin states in spin-crossover systems," *Chemistry–A European Journal*, vol. 24, no. 20, pp. 5146–5152, 2018.

[15] M. Alías-Rodríguez, M. Huix-Rotllant, and C. de Graaf, "Quantum dynamics simulations of the thermal and light-induced high-spin to low-spin relaxation in fe (bpy) 3 and fe (mtz) 6," *Faraday Discussions*, 2022.

[16] J.-F. Létard, L. Capes, G. Chastanet, N. Moliner, S. Létard, J.-A. Real, and O. Kahn, "Critical temperature of the liesst effect in iron (ii) spin crossover compounds," *Chemical physics letters*, vol. 313, no. 1-2, pp. 115–120, 1999.

[17] J. F. Létard, P. Guionneau, and L. Goux-Capes, *Spin Crossover in Transition Metal Compounds I-III: Gütlich, P., Goodwinpp, H.* Springer: Berlin, Germany, 2004.

[18] C.-C. Wu, J. Jung, P. K. Gantzel, P. Gütlich, and D. N. Hendrickson, "Liesst effect studies of iron (ii) spin-crossover complexes with phosphine ligands: Relaxation kinetics and effects of solvent molecules," *Inorganic chemistry*, vol. 36, no. 23, pp. 5339–5347, 1997.

[19] A. Hauser, R. Hinek, H. Spiering, and P. Gütlich, "The [fe (etz) 6](bf4) 2 spin-crossover system-part two: Hysteresis in the liesst regime," *Chemistry–A European Journal*, vol. 2, no. 11, pp. 1435–1439, 1996.

[20] S. Schenker, P. C. Stein, J. A. Wolny, C. Brady, J. J. McGarvey, H. Toftlund, and A. Hauser, "Biphasic behavior of the high-spin to low-spin relaxation of [fe (btpa)](pf6) 2 in solution (btpa= n, n, n ', n '-tetrakis (2-pyridylmethyl)-6, 6 '-bis (aminomethyl)-2, 2 '-bipyridine)," *Inorganic chemistry*, vol. 40, no. 1, pp. 134–139, 2001.

[21] F. Renz, H. Oshio, V. Ksenofontov, M. Waldeck, H. Spiering, and P. Gütlich, "Strong field iron (ii) complex converted by light into a long-lived high-spin state," *Angewandte Chemie International Edition*, vol. 39, no. 20, pp. 3699–3700, 2000.

[22] J.-S. Wang, B. K. Agarwalla, H. Li, and J. Thingna, "Nonequilibrium greens function method for quantum thermal transport," *Frontiers of Physics*, vol. 9, pp. 673–697, 2014.

[23] Y. Lu and J. Guo, "Thermal transport in grain boundary of graphene by non-equilibrium greens function approach," *Applied Physics Letters*, vol. 101, no. 4, p. 043112, 2012.

[24] Y. Xu, X. Chen, J.-S. Wang, B.-L. Gu, and W. Duan, "Thermal transport in graphene junctions and quantum dots," *Physical Review B*, vol. 81, no. 19, p. 195425, 2010.

[25] J.-F. Li, W.-S. Liu, L.-D. Zhao, and M. Zhou, "High-performance nanostructured thermoelectric materials," *NPG Asia Materials*, vol. 2, no. 4, pp. 152–158, 2010.

[26] B. Sales, D. Mandrus, and R. K. Williams, "Filled skutterudite antimonides: a new class of thermoelectric materials," *Science*, vol. 272, no. 5266, pp. 1325–1328, 1996.

[27] G. Nolas, J. Cohn, G. Slack, and S. Schujman, "Semiconducting ge clathrates: Promising candidates for thermoelectric applications," *Applied Physics Letters*, vol. 73, no. 2, pp. 178–180, 1998.

[28] S. M. Kauzlarich, S. R. Brown, and G. J. Snyder, "Zintl phases for thermoelectric devices," *Dalton Transactions*, no. 21, pp. 2099–2107, 2007.

[29] E. S. Toberer, A. F. May, and G. J. Snyder, "Zintl chemistry for designing high efficiency thermoelectric materials," *Chemistry of Materials*, vol. 22, no. 3, pp. 624–634, 2010.

[30] L. Hicks and M. Dresselhaus, "Use of quantum-well superlattices to obtain a high figure of merit from nonconventional thermoelectric materials," *MRS Online Proceedings Library (OPL)*, vol. 326, 1993.

[31] R. S. Makala, K. Jagannadham, and B. C. Sales, "Pulsed laser deposition of bi 2 te 3-based thermoelectric thin films," *Journal of Applied physics*, vol. 94, no. 6, pp. 3907–3918, 2003.

[32] A. I. Hochbaum, R. Chen, R. D. Delgado, W. Liang, E. C. Garnett, M. Najarian, A. Majumdar, and P. Yang, "Enhanced thermoelectric performance of rough silicon nanowires," *Nature*, vol. 451, no. 7175, pp. 163–167, 2008.

[33] T. Zhang, X. Jiang, G. Li, Q. Yao, and J. Y. Lee, "A red-phosphorous-assisted ball-milling synthesis of few-layered ti3c2tx (mxene) nanodot composite," *ChemNanoMat*, vol. 4, no. 1, pp. 56–60, 2018.

[34] Q. Xue, H. Zhang, M. Zhu, Z. Pei, H. Li, Z. Wang, Y. Huang, Y. Huang, Q. Deng, J. Zhou, *et al.*, "Photoluminescent ti3c2 mxene quantum dots for multicolor cellular imaging," *Advanced Materials*, vol. 29, no. 15, p. 1604847, 2017.